An Experimental and Theoretical Study of Surfactant Dynamics at Microscale Interfaces

Submitted in partial fulfillment of the requirements for

the degree of

Doctor of Philosophy

in

the Department of Chemical Engineering

Nicolas J. Alvarez

B.S., Chemical Engineering, University of Florida

Carnegie Mellon University
Pittsburgh, PA

April, 2011
Doctor of Philosophy

ACKNOWLEDGEMENTS

I would first like to thank my thesis advisors, Professors Lynn M. Walker and Shelley L. Anna, for their unwavering guidance and pushing me to achieve my full potential. It was their willingness and openness to tackle new research questions that made this thesis possible. A great deal of thanks goes to their patience and allowing me to explore and be creative in the laboratory. It is this freedom that made my time at Carnegie Mellon University some of the greatest years of my life.

My gratitude goes to my committee members, Professors Stephen Garoff, Dennis Prieve, and Jim Schneider, for helpful discussions and for always leaving their door open. You made me feel like I had five advisors by always giving me opportunities in the classroom (teaching) and laboratory that challenged me to be a better scientist. Particularly I would like to thank Steve Garoff for all the help and long discussions concerning the mystery of light and its interactions with nanoscopic metal particles. Even though this work never made it into the thesis, the knowledge I gained from you is invaluable.

This work was financially supported by a National Science Foundation Graduate Fellowship, the John and Claire Bertucci Fellowship, the department of Chemical Engineering, and partially funded by NSF award CBET-0730727.

To all the professors and students in the Complex Fluids Group at Carnegie Mellon University, the collaborative environment that we have created is unparalleled and I am honored to be a part of it. I want to thank specifically past and present members of the Anna and Walker groups: Gordon, Shahab, and

Danny for showing me the ropes and passing on their knowledge of equipment and analysis techniques; Wingki for working with me on the oil-water studies and helpful discussions concerning surfactant dynamics; Viet for all of our discussions especially the passionate ones, I learned more from these discussions than reading the relevant literature; Doug for all the help with the microtensiometer, your hard working attitude will take you far; Nick L. for all your help on the pendant drop/bubble apparatus; Anthony for all those morning coffee breaks, I can think of no better way to start a morning; Sourav, Matt, Sharon, Vicki, Jenny, Todd, and others, thank you for making the office such a friendly and entertaining atmosphere. I cannot think of another time in my life when I had so much fun "working".

Special thanks go to A. Kerem Uguz for being a wonderful mentor and friend throughout the years. Your clear thinking and analytical approach is refreshing and I look forward to the many years of collaboration. And to Professor Ranga Narayanan, my undergraduate advisor, I cannot put into words the gratitude I have for your guidance and mentoring. You helped me to see what I wanted to do with my life and gave me the tools to do it.

Finally, I want to thank my loving family and friends for supporting me through the years and giving me the confidence and diligence to aim high and see things through: especially my mother who always encouraged me when I was young and fought to give me the best education possible and my father who gave me a love for science all those years ago on our Saturday trips to the sugar mill. The two of you are the rock that I build my life upon. To my loving wife,

Michelle, thank you for your patience and understanding: especially on those nights that I didn't come home from lab. You are unquestionably a large "part of" this work and words cannot describe my gratitude for the sacrifices and support that you have given me throughout the years. Without you I would truly be lost!

To everyone above and the countless others that I have missed, this work would not have been possible without you. THANK YOU!!!

ABSTRACT

Surfactants are important in countless fields of research and industrial processing. Their value is inherently dependent on our ability to characterize their fundamental transport parameters, such as diffusion coefficients and kinetic rate constants, and thus predict their dynamic and equilibrium behavior in a wide range of applications. However, current techniques of measuring and analyzing surfactant transport to fluid-fluid interfaces are confounded by the inability to decouple kinetics and diffusion. This thesis outlines a new methodology of analyzing surfactant dynamics using a time scale analysis that definitively identifies the relevant transport mechanisms. A new device is designed and implemented, which measures surface tension at microscale interfaces in order to validate the scaling analysis. The device has several advantages over conventional techniques: namely measures surface tension *in-situ*, performs faster, and requires significantly less volume. Concentration, radius of the interface, and convection are shown to be important parameters in observing a transition from diffusion-limited to kinetic-limited dynamics. Measuring kinetic-limited dynamics is necessary to accurately measure kinetic rate coefficients of surfactants. The scaling analysis is demonstrated on a family of nonionic surfactants, C_iE_8 at the air-water and oil-water interface. The analysis and instrumentation introduced in this thesis will be instrumental in characterizing new and innovative surfactant molecules; as well as furthering our understanding of the relationship between molecular structure and fundamental transport parameters.

TABLE OF CONTENTS

LIST OF TABLES

LIST OF FIGURES

"At length being at Clapham, where there is on the common a large pond which I observed one day to be very rough with the wind, I fetched out a cruet of oil and dropped a little of it on the water. I saw it spread itself with surprising swiftness upon the surface; but the effect of smoothing the waves was not produced; for I had applied it first on the leeward side of the pond where the waves were greatest; and the wind drove my oil back upon the shore. I then went to the windward side where they began to form; and there the oil, though not more than a teaspoonful, produced an instant calm over a space several yards square which spread amazingly and extended itself gradually till it reached the lee side, making all that quarter of the pond, perhaps half an acre, as smooth as a looking glass."

- A letter from Benjamin Franklin to William Brownigg, 1773

CHAPTER 1

INTRODUCTION

There are two mechanisms governing transport of surfactants to interfaces: diffusion and kinetics. The fundamental transport parameters associated with these mechanisms, namely the diffusion coefficient and kinetic rate constants, are important to predicting, designing, and controlling surfactant induced phenomenon. The transport of surfactant to fluid-fluid interfaces is characterized by measuring surface tension as a function of time. However, since diffusion and kinetics are serial processes, it is difficult to decouple the two and thus quantitatively analyze dynamic surface tension data. Often analysis of dynamic surface tension data considering both diffusion and kinetics results in unphysical trends in best fit parameters, such as a concentration dependent diffusion coefficient and/or adsorption and desorption rate constant.

Recently, a time scale analysis predicted that measuring dynamic surface tension using a radius below a critical intrinsic length scale would yield kinetic-dominated dynamics and allow for direct measurements of kinetic rate constants. This argument came from a time scale analysis showing that the rate of diffusion, unlike kinetics, is dependent on the radius of curvature of the interface. The goal of this thesis is to test this hypothesis and measure the effect of curvature on surfactant dynamics, to characterize the transition from diffusion-limited to kinetic-limited transport, and to directly measure kinetic rate parameters for surfactants.

The first step is to confirm, experimentally and theoretically, the diffusion time scale to a spherical interface. A detailed analysis of the diffusion time scale proposed in the literature reveals that the functional form does not capture the correct asymptotic behavior for increasing bubble radius and concentration. Therefore, we derive a new diffusion time scale that correctly captures these trends. In Chapter 4, a new time scale is presented and validated using a scaling analysis, numerical simulations, and experimental data. The development of a new instrument was necessary to experimentally confirm the dependence of the diffusion time scale on radius of curvature.

There are no techniques reported in the literature that explicitly examine the dependence of dynamic surface tension on interface radius. Therefore, a new apparatus, a microtensiometer, was developed and validated (described in Chapter 5) which has the ability to measure surfactant dynamics at microscale radii ranging from tens to hundreds of micrometers. Experimental validation of the diffusion time scale is shown in Chapter 6 using a well-characterized surfactant at the air-water interface. Aside from elucidation of surfactant transport mechanisms, this device also provides a tool for rapid measurements of interfacial properties using a significantly smaller volume of sample and measures surface tension *in-situ*.

Using the validated spherical diffusion time scale, the transition from diffusion-limited to kinetic-limited dynamics was predicted for several surfactants. In Chapter 4, an operating diagram shows how radius and concentration are two control parameters used to observe a transition from one

transport mechanism to another. Using values of rate constants reported in the literature, a nonionic polyoxyethylene surfactant, $C_{12}E_8$ was predicted to be likely to show a transition from diffusion-limited to kinetic-limited dynamics at experimentally feasible concentrations and radii. The microtensiometer is used to characterize the dynamic surface tension of $C_{12}E_8$ at various concentrations and bubble radii at the air-water interface. The effects of both concentration and bubble radius on $C_{12}E_8$ dynamics are discussed in Chapter 6.

The key to observing kinetic-dominated dynamics is to reduce the time scale for diffusion without altering the rate of kinetic transport. It is well known that convection reduces the length over which diffusion must occur and therefore increases the rate of diffusion. In Chapter 8, the effect of low Reynolds number flow across a spherical interface is examined theoretically and experimentally. The microtensiometer is configured with a flow cell, described in Chapter 5, which introduces low Reynolds number flow across the fluid-fluid interface while measuring surface tension. The effect of Peclet number on the rate of diffusion transport is measured for different surfactants as a function of radius and concentration at the air-water interface.

Chapters 6 and 8 describe a new methodology of determining the dominant transport mechanisms in surfactant dynamics by determining the effect of interface radius and low Reynolds number. Together these tools can definitively confirm the importance of kinetic transport and thus aid in the analysis of dynamic surface tension to accurately and quantitatively determine transport parameters such as kinetic rate constants.

Detailed surfactant transport studies have typically been restricted to the air-water interface. This is mainly due to the lack of experimental devices and techniques available to study liquid-liquid interfaces. As a result, there is a lack of relevant data and understanding of surfactant behavior in microfluidic studies and emulsion applications. In Chapter 7, using a novel shape fitting algorithm for pendant drop/bubble measurements capable of handling fluids of similar densities (described in Chapter 3), we measure dynamic surface tension as a function of bulk concentration at the silicone oil-water interface for a homologous series of surfactants previously studied at the air-water interface in Chapters 6 and 8. The results are analyzed in the context of the scaling analysis described in Chapters 4 and 6 and the relevant transport mechanisms are identified. Comparisons are made between air-water and oil-water dynamics.

The microtensiometer has a number of advantages that allow for the study of surface active species that normally could not be studied using conventional techniques. For example, polymer grafted nanoparticles stabilize emulsions at very low weight fractions: a considerable advantage over bare particle stabilized emulsions. However, the extremely slow transport of particles to planar and large radius interfaces makes it considerably difficult to measure transport of these species to fluid-fluid interfaces. In Chapter 9, the microtensiometer is used to characterize the transport of polymer grafted nanoparticles to the air-water and xylene-water interface in order to better understand their stabilization mechanism. Furthermore, the microtensiometer is configured to measure interfacial elasticity

through a forced sinusoidal oscillation of the interface to determine if a correlation exists between dilatational modulus and emulsion stability.

Ideally only diffusion and kinetics govern transport of surfactants to interfaces. However there are other transport mechanisms that affect surfactant dynamics. Another mechanism that is well understood but often neglected is depletion. Depletion occurs when the available surface area is large enough such that adsorption of surfactant molecules to the surface decreases the bulk concentration, i.e. the bulk concentration is depleted of surfactant. While this is not a new idea, a concise quantification is not found in the literature. Appendix analyzes the effects of depletion on equilibrium and dynamic surface tension for the case of surfactant transport to fluid-fluid interfaces. Equations are derived in terms of an arbitrary geometry and for a spherical drop. The impact of depletion is described by a single parameter, a ratio of volumes. A transport model is used to determine a criterion for when depletion is important. This criterion is validated using experimental results.

The results presented in this thesis denote a major shift in our understanding of surfactant dynamics. For many years it was thought that the only handle on characterizing surfactant transport to fluid-fluid interfaces was concentration. The diffusion time scale clearly shows that concentration is neither the only nor the most relevant to characterize kinetic-limited dynamics and thus directly measure kinetic rate constants. Instead it is more significant to probe surfactant dynamics as a function of radius and/or Peclet number. The tools developed here, the microtensiometer and its various alterations, will change the

way that surfactants are analyzed and will lead to direct and definitive identification of relevant transport mechanisms and quantification of the corresponding transport parameters: improving our modeling and understanding of surfactant induced phenomenon.

CHAPTER 2

BACKGROUND

2.1 SURFACTANTS AND SURFACE TENSION

Surface active agents, surfactants, are one of the most versatile molecules of the chemical industry. Products ranging from pharmaceuticals to motor oils to cleaning supplies and laundry detergents all utilize surfactants. Furthermore, surfactants are used in high tech industries such as micro-electronics, biotechnology, and magnetic recording.

A surfactant is a molecule that has a hydrophilic head group that likes water and a hydrophobic (lipophilic) tail that does not like water. Due to this structure, it is favorable for surfactant molecules to adsorb to surfaces (air-liquid) and interfaces (liquid-liquid) and thus lower the interfacial free energy. The interfacial free energy is the minimum amount of work required to create an interface and is directly related to the surface or interfacial tension.

The surface or interfacial tension, γ, is the amount of work, W, required to create a unit area, ΔA, of an interface, $W = \gamma \cdot \Delta A$. The greater the dissimilarity between the two phases, the larger the interfacial or surface tension between them. It is this tension that acts to counter the force of gravity and allow certain bugs to walk on water and paperclips to float on the surface of a stagnant air-water interface. Surfactants adsorb to available interfaces and lower the interfacial free energy by reducing the surface or interfacial tension between the two phases.

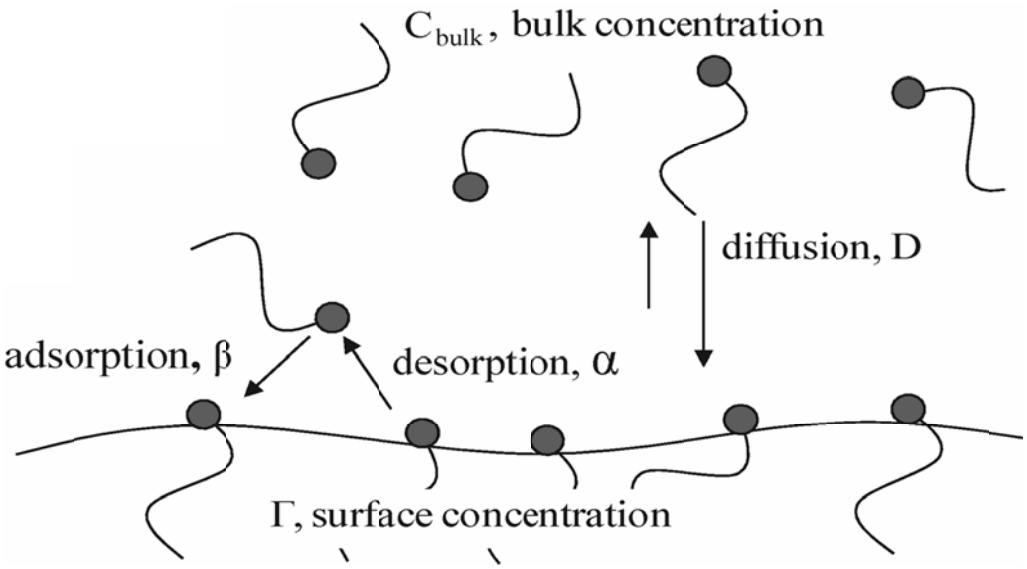

Figure 2.1. Schematic illustration of the three fundamental transport processes (diffusion, adsorption, and desorption) governing surfactant dynamics at an interface.

The transport of surfactant to an initially clean spherical or planar interface is understood to follow three simultaneous transport processes [1-5]. Surfactant molecules near the interface undergo adsorption and desorption from the bulk to the interface due to an entropic driving force. The interfacial tension decreases with adsorption of surfactant to the interface. In the absence of convective transport, the surfactant that is depleted near the interface is repopulated with surfactant from the bulk diffusing along the established concentration gradient. The surfactant molecule may also undergo reorientation at the interface. The surface tension stops changing when the interface reaches equilibrium with the bulk surfactant concentration, i.e., the surface concentration, Γ, is constant ($\Gamma = \Gamma_{eq}$, the equilibrium surface concentration). The process is illustrated in Figure 2.1. Note that although these processes are occurring

simultaneously, the relative importance of each process will depend on its individual time scale compared with all other time scales.

At low concentrations, the free energy of the solution is such that surfactants are present as monomers, i.e. single molecules. At elevated concentrations the free energy of solubilizing large quantities of hydrophobic tails becomes large enough to induce the self-assembly of surfactant molecules into capsules, often spherical, with a hydrophobic core and a hydrophilic shell. These self-assembled aggregates are called micelles and the concentration of surfactant at which the transition from free monomer to micelle formation occurs is called the critical micelle concentration, cmc. The cmc and shape of the aggregate strongly depends on the type and structure of the surfactant molecule.

There are three predominant classifications of surfactants: ionic, zwitterionic, and nonionic. Nonionic surfactants are amphiphilic molecules that do not dissociate into ions and therefore have no charge near neutral pH. Nonionic surfactants make up a quarter of the world's total surfactant production and are counted as the most diverse type of surfactants with respect to structure, composition, and surface properties. Nonionic surfactants, with few exceptions, are classified into four categories: alcohols, polyethers, esters, or their combinations. A good review of nonionic surfactants is [6].

One important class of commercially available nonionic surfactants is polyethers, called polyoxyethylene alcohols, formed by reacting ethers with an alcohol. The length of the polyoxyethylene head group and the type of alcohol used in the reaction determine the applications of these versatile compounds. One

of the reasons that these compounds are so widely used is because they are not harmful to the environment and are readily biodegradable. Some are approved by the FDA for *in-vitro* applications. The homologous series of surfactants with chemical structure $(C_iH_{2i+1}O(CH_2CH_2O)_jH$ abbreviated C_iE_j or C_iEO_j are some of the most studied surfactants in the literature [1, 4, 7-17].

The solubility of a given surfactant depends on the relative measure of hydrophilic groups to hydrophobic (lipophilic) groups or the hydrophilic-lipophilic balance (HLB). Numerous methods are available for calculating the HLB value. Griffin's method for nonionic surfactants is derived from a purely empirical relationship. Davies' method uses information about the chemical structure and is more rigorous because it takes into account the hydrophobicity of the individual molecular groups [18].

The range of HLB values and their classification are given in Table 2.1. The value of HLB for a given molecule is given by

$$HLB = 7 + \sum n_{H,j}\chi_{H,j} - \sum n_{L,i}\chi_{L,i}\,, \tag{2.1}$$

where $n_{H,j}$ is the number of hydrophilic species j, $\chi_{H,j}$ is the value of the hydrophilic species j, $n_{L,i}$ is the number of hydrophobic species i, and $\chi_{L,i}$ is the value of the hydrophobic species i. For the C_iE_j series of surfactants, the HLB number is given by $HLB = 7 + 0.33 \cdot j + 1.3 + 1.9 - 0.475 \cdot i$. As an example, $C_{12}E_8$ has an HLB=7.14. When the HLB value is less than 6, the surfactant is no longer soluble in water and is often referred to as an insoluble surfactant. In this work we only consider water soluble surfactants.

HLB values	Application
3.5-6	Water in Oil emulsification
7-9	Wetting Agent
8-18	Oil in Water emulsification
13-15	Detergent
15-18	Solubilization

Table 2.1. Classification of emulsifiers for different HLB values taken from [18].

2.2 RELATIONSHIP BETWEEN SURFACE TENSION AND SURFACE CONCENTRATION

An interface or surface with adsorbed water soluble molecules is called a Gibbs monolayer after Josiah Willard Gibbs who first described the relationship between number of soluble surfactant molecules adsorbed and the surface tension [19]. Gibbs derived a thermodynamic relationship between the surface concentration of surfactant species and the surface tension using the concept of the Gibbs dividing surface/plane, which is placed such that the chemical potential of the solvent is zero. To obtain this relationship we start with the Gibbs-Duhem expression, derived from the first law of thermodynamics,

$$SdT + \sum n_i d\mu_i + Ad\gamma - VdP = 0, \qquad (2.2)$$

where S is the entropy of the surface, P is the pressure, n_i is the number of molecules of species i, and μ_i is the chemical potential of species i. For a single surfactant system at constant pressure and temperature Eqn (2.2) reduces to,

$$Ad\gamma = -n_1 d\mu_1 \tag{2.3}$$

or

$$\Gamma \equiv \frac{n_1}{A} = -\frac{d\gamma}{d\mu}, \tag{2.4}$$

where Γ is defined as the number of molecules per unit surface area. If we assume an ideal solution, then the chemical potential in terms of bulk concentration, C_{bulk}, is given by

$$d\gamma = RTd\ln C_{bulk} \tag{2.5}$$

where R is the gas constant and T is the temperature. Substitution of Eqn (2.5) into Eqn (2.4) yields the well-known Gibbs' adsorption equation,

$$\Gamma = \frac{1}{RT}\frac{\partial\gamma}{\partial\ln C_{bulk}}. \tag{2.6}$$

The Gibbs' adsorption equation gives a relationship between surface concentration, bulk concentration, and surface tension. If the relationship between Γ and C_{bulk}, i.e. the isotherm, is known, then a relationship between γ and Γ can be derived using Eqn (2.6). This relationship is known as an equation of state. The Langmuir isotherm is the simplest isotherm that has been shown to work for several surfactants and is given by

$$\frac{\Gamma}{\Gamma_\infty} = \frac{C_{bulk}}{C_{bulk} + a}, \tag{2.7}$$

where Γ_∞ is the maximum surface concentration of surfactant, a is the ratio of the desorption, α, to adsorption, β, rate constant. Substitution of Eqn (4.6) into Eqn (2.6) yields the Langmuir equation of state

$$\gamma = \gamma_0 + RT\Gamma_\infty \ln\left(1 - \frac{\Gamma}{\Gamma_\infty}\right). \tag{2.8}$$

Eqn (2.8) relates the surface tension to the number of surfactant molecules adsorbed to the interface per unit area.

There are numerous methods of measuring surface tension. Direct measurements rely on force balances using microbalances to determine the surface or interfacial tension of an interface, e.g. Du Nouy ring, Wilhelmy Plate, etc. Indirect measurements rely on measuring capillary pressure or a balance between capillary forces and gravity, e.g. pendant drop/bubble, sessile drop, maximum bubble pressure, drop volume, capillary rise, growing drop, etc. A review of these methods can be found in the "Encyclopedia of Surface and Colloids Science" [20].

The study of surfactant transport to and from interfaces requires the accurate measurement of surface tension as a function of time. This type of measurement is restricted to indirect measurements because of the long measurement times for direct measurements. This thesis is concerned with the measurement of surfactant adsorption dynamics and thus restricts discussion to indirect methods.

2.3 ANALYZING SURFACTANT TRANSPORT TO FLUID-FLUID INTERFACES

The evolution of surface tension is studied to determine the fundamental transport properties (diffusion, adsorption, and desorption) that dictate how surfactants populate fluid-fluid interfaces. The coefficients of these transport properties are fundamental parameters of the surfactant solution and do not

depend on the measurement technique or experimental apparatus. The need to determine these coefficients with certainty is of great importance to many active fields of research, namely surfactant chemistry, interfacial science, and fluid dynamics. In addition, surfactant transport is important in applications involving emulsion stability [21], drop spreading [22], drop impact [23], and drop breakup [24, 25]. The ability to quantitatively measure these fundamental parameters will yield a means to catalogue and organize surfactants into classes with particular properties. Furthermore, a better understanding of how changes in surfactant molecular structure influence the kinetic coefficients of adsorption and desorption will assist in the advancement and design of efficient surfactants.

Surfactant transport to a spherical interface from a semi-infinite bulk volume is modeled using Fick's law of diffusion in spherical coordinates

$$\frac{\partial C}{\partial t} = \frac{D}{r^2}\frac{\partial}{\partial r}\left(r^2 \frac{\partial C}{\partial r}\right), \tag{2.9}$$

subject to a flux balance at the interface and a Dirichlet condition far from the interface given by

$$\frac{\partial \Gamma}{\partial t} = D\frac{\partial C}{\partial r}\bigg|_{r=b} \tag{2.10}$$

and

$$\lim_{r\to\infty} C \to C_{bulk} \tag{2.11}$$

In order to solve this problem, a relationship is needed between Γ and C_{bulk}, such as Eqn (4.6). Isotherms are by definition restricted to equilibrium situations. However, as described above kinetic barriers can have an effect on the rate of

surfactant transfer to and from the bulk volume. A rate equation more appropriately describes this situation and the Langmuir kinetic rate equation is given by

$$\frac{\partial \Gamma}{\partial t} = \beta C_s \Gamma_\infty \left(1 - \frac{\Gamma}{\Gamma_\infty}\right) - \alpha \Gamma \,, \tag{2.12}$$

where C_s is the concentration of surfactant immediately adjacent to the interface.

If Eqns (3.7) and (2.12) are solved subject to (8.6) and (2.11), all modes of surfactant transport to the interface are described. Two special cases of this solution are diffusion-limited and kinetic-limited dynamics. The diffusion-limited case can be described by simultaneously solving Eqns (3.7) and (4.6), which is analogous to solving Eqns (3.7) and (2.12) where the right hand side of Eqn (2.12) is set equal to zero. In other words, at all time steps the subsurface and the interface concentrations are in equilibrium. The kinetic-limited case can be solved by integrating Eqn (2.12) only.

To describe surfactant transport to a freshly formed interface, we use the following initial conditions,

$$\Gamma(t=0) = 0 \text{ and } C(t=0,r) = C_{bulk} \,. \tag{2.13}$$

To describe surfactant transport onto an expanded or compressed interface we use the following initial conditions,

$$\Gamma(t=0) = \Gamma_{eq}(C_{bulk}) \text{ and } C(t=0,r) = C_{bulk} \,. \tag{2.14}$$

The current state of the art in surfactant analysis has been developed by Maldarelli, Lin, and others [4, 5, 11, 13]. The method consists of fitting an equation of state, such as Eqn (2.8), to equilibrium data, testing the equation of

state against bubble expansion data [1], and finally fitting the full adsorption model to dynamic data allowing diffusion coefficient and rate constants to be fitting parameters [11]. Although this has worked well for some surfactants, other surfactants show behavior that is not accounted for by the above model. In fact, to characterize the surfactant behavior either the diffusion coefficient of the surfactant or another parameter, usually the adsorption rate constant, must be a function of concentration [4]. This arises because this methodology allows both the diffusion coefficient and the rate constants to be fitting parameters. The ratio of rate constants is fixed and determined from the fit of the equation of state to equilibrium data. Since both the value of the adsorption rate constant and the diffusion coefficient affect the functional form of dynamic surface tension in the same manner, there is no unique solution to this methodology.

2.4 RELATIVE IMPORTANCE OF KINETICS AND DIFFUSION

There exists a characteristic time scale for the diffusion process and a characteristic time scale for the kinetic process of adsorption/desorption. The ratio of these time scales yields valuable information about the mechanism governing surfactant transport. The diffusion time scale in planar coordinates is defined to be $\tau_{D,p} = \Gamma^2 / \left({C_{bulk}}^2 D \right)$, where C_∞ is the bulk surfactant concentration [25]. The kinetic time scale for the Langmuir kinetic model for any geometry is shown to be $\tau_k = \left(\beta C_{bulk} + \alpha \right)^{-1}$. A ratio of $\tau_{D,p}$ to τ_k is given by,

$$\Lambda = \Gamma^2 \left(\beta C_{bulk} + \alpha \right) / {C_{bulk}}^2 D \,. \tag{2.15}$$

This ratio is known as the Damkoehler number in reaction literature, and is a measure of the controlling mechanism for surfactant adsorption dynamics for a planar system. When $\Lambda >> 1$ the adsorption dynamics are diffusion-limited and when $\Lambda << 1$ the adsorption dynamics are kinetic-limited. Between these two limits, the system follows both mechanisms and is best described by the full transport model.

From the two limits of dilute and concentrated surfactant concentrations, we can see how the kinetic-limited adsorption becomes important at increasing concentration. In the dilute limit where $\beta C_\infty << \alpha$, Λ is independent of surfactant concentration. However, in the concentrated limit where $\beta C_\infty >> \alpha$, Λ scales as $1/C_\infty$, signifying that as surfactant concentration increases, kinetics become increasingly important.

Ideally, one would like to directly probe the kinetic-limited regime of adsorption dynamics as it does not depend on the diffusion of molecules from the bulk. It would be straightforward to test kinetic models directly using kinetic-limited dynamic data and determine congruency between kinetic rate coefficients determined from equilibrium data and dynamic data. However, accessing the kinetic regime by increasing concentration has the disadvantage of decreasing the time constant of adsorption requiring a very fast measuring tool of dynamic surface tension (i.e. millisecond time scales). Since most dynamic surface tension measurement techniques are restricted to measurements on the order of seconds, probing the kinetic regime at high concentrations is challenging.

Recently, Jin et al. suggested that the kinetic-limited regime might instead be accessed by controlling the curvature of a spherical interface [2]. For a spherical interface the diffusion time scale is known to depend on the radius of the interface. From a scaling analysis one can see theoretically that it might be possible to reduce the size of the interface enough to restrict the dynamics to a kinetically controlled regime. From a scaling of the diffusion equation in spherical coordinates, the diffusion time scale takes the form of $\tau_{D,s} = l^2 / D$, where l is the characteristic length scale over which diffusion occurs. Lin et al. suggest that the scaling should come from the boundary condition on the bubble surface and thus, $l^2 = h_p b = (\Gamma b) / C_\infty$ [4], where h_p is the planar depletion depth [25].

For a spherical geometry, $\Lambda = \Gamma b \left(\beta C_{bulk} + \alpha \right) / D C_{bulk}$, and if we assume a Langmuir adsorption isotherm for Γ, then $\Lambda = \Gamma_\infty \beta b / D$ for all concentrations. We can now recast Λ as a ratio of length scales, $\Lambda = b / R_{DK}$ where $R_{DK} = D / \left(\beta \Gamma_\infty \right)$. Therefore, if $b >> R_{DK}$ the dynamics are diffusion controlled and if $b << R_{DK}$ then the dynamics are kinetically controlled [2]. Table 2.2 shows a list of properties for the C_iE_j family of surfactants and their corresponding R_{DK} values. It should be noted that β values are estimated from dynamic surface tension data and therefore the values of R_{DK} are estimated values.

	Γ_∞ $(mol/m^2)x10^{-6}$	β $(m^3/mol/s)$	D $(m^2/s)x10^{10}$	R_{DK} (μm)
$C_{12}E_6$	3.50	4.0	6.0	43
$C_{14}E_8$	6.80	5.4	8.7	24
$C_{12}E_8$	2.70	4.6	8.0	65
$C_{10}E_8$	3.00	6.9	6.5	31
n-decanol	6.50	6.7	7.7	18

Table 2.2 The values of R_{DK} for well-studied surfactants assuming a Langmuir isotherm [2, 11, 26].

This scaling analysis suggests that measuring dynamic surface tension as a function of curvature rather than concentration is potentially more efficient at measuring kinetic-limited surfactant transport. This thesis examines the role of curvature on dynamic surface tension and re-examines the scaling analysis suggested by Jin *et al.*

2.5 IMPACT OF FLOW ON SURFACTANT TRANSPORT

The mobility of a fluid-fluid interface determines the feasibility of a wide range of applications. Mobile interfaces are advantageous in thermocapillary migration of neutrally buoyant drops and bubbles and increase mass transfer across interfaces [28, 29]. Immobile interfaces promote foam retention [30], emulsion stability [31], and are preferred for foam based control of oil-recovery [32]. The mobility of a fluid-fluid interface is strongly dependent on the presence of surface active species, i.e., surfactants and amphiphilic polymers [33-36]. For

example, when surfactants are present, a falling drop or rising bubble follows Stokes law instead of the Hadamard-Rybczynski result for a clean fluid-fluid interface [36, 37].

The mechanism by which surfactants can immobilize fluid-fluid interfaces is well understood. In the presence of flow, adsorbed surfactant molecules are swept to the stagnation region of a drop/bubble where surface flows converge. When desorptive and diffusive resistances hinder repopulation of the interface, surfactant molecules accumulate near the stagnation region; forming a gradient of surface tension along the interface [36-40]. This difference in surface pressure or Marangoni stress acts in the opposite direction of the imposed flow and retards the surface velocity [36, 37].

The impact of surface velocity on drop deformation, breakup, and coalescence has been the focus of intensive research. For example, the effects of surfactants on drop deformation and breakup in simple rheological flows at low Reynolds numbers have been extensively studied theoretically [41-43] and experimentally [24, 38, 44-48]. Furthermore, several studies have examined the impact of surface velocity on drop coalescence [31, 49]. One general conclusion from the above studies is that drop deformation, breakup, and coalescence are strongly dependent on the relative rate of surfactant transport to and from the interface compared to convective transport along the interface. For example, it has been shown that a fluid-fluid interface with adsorbed surfactant can be remobilized when the rate of desorption is faster than the convective rate along the interface and the concentration of surfactant is sufficiently high to eliminate a

resistance due to a diffusion boundary layer [38, 39]. Under these conditions, the surface concentration is uniform, the Marangoni stresses are irrelevant and the surface velocity is not impeded [38].

It is evident from these studies and others that the fundamental transport parameters that describe rates of adsorption desorption, and diffusion must be properly characterized, if the results of fundamental surfactant studies are to be useful in real engineering applications. As described above, the measurement of fundamental transport parameters such as kinetic rate coefficients and the diffusion coefficient are performed by fitting dynamic surface tension data to a surfactant transport model [4, 5, 10]. The measurable transport parameters are dependent on the relevant transport mechanisms. In some cases, the rate of kinetics is much faster than the rate of diffusion and the kinetic rate coefficients are not measurable: limiting our ability to model surfactant induced phenomena [35, 50].

It is well known that low Reynolds number flow across an interface induces a velocity boundary layer. The velocity boundary layer decreases the length scale over which diffusion occurs, the diffusion boundary layer, and subsequently increases the rate of diffusion. The diffusion boundary layer depends on the Peclet number, $\mathrm{Pe} = U_0 b/D$, where U_0 is the fluid velocity far from the interface and D is the diffusion coefficient [37, 51]. The diffusion boundary layer and thus τ_D decrease with increasing Pe number.

The number of studies that examine surfactant dynamics in the presence of bulk convection is limited [52, 53]. Svitova *et al.* measured dynamic surface

tension using a pendant bubble apparatus, while mixing the external bulk solution. The device was used to examine the reversibility of low molecular weight nonionic and ionic surfactants as well as large polymeric surfactants and proteins [53]. Using a flow cell to exchange the bulk concentration of surfactant for pure deionized water, the authors were able to observe the desorption rates of polymers and surfactants from equilibrated interfaces. Fainerman *et al.* used the same configuration as that presented in Svitova *et al.* to measure dynamic surface tension of proteins to an initially clean interface [52]. The authors compare dynamic surface tension with and without forced convection. However, in neither case do the authors present a quantitative analysis on the dependence of dynamic surface tension on bulk convection.

The measurement of mass transport of butanol to a mineral oil-water interface in the presence of flow in a microfluidic tensiometer was described previously [54]. Surface tension is measured at discrete intervals in space by measuring the deformation of flowing oil droplets through periodic contractions in a microchannel. The surface age of an oil droplet is determined by the flow rate and distance traveled down the microchannel. The authors find that butanol follows a kinetic-diffusion model for transport to the mineral oil-water interface in the presence of flow. Using tracer particles, the mobility of the interface is determined. The authors find that at low surfactant concentrations the interface is rigid and at high concentrations the interface is remobilized. Dynamic surface tension data is compared to a kinetic-diffusion transport model.

[1] R.N. Pan, J. Green, and C. Maldarelli, "Theory and experiment on the measurement of kinetic rate constants for surfactant exchange at an air/water interface," Journal of Colloid and Interface Science, 205 (1998), 213-230.

[2] F. Jin, R. Balasubramaniam, and K.J. Stebe, "Surfactant adsorption to spherical particles: The intrinsic length scale governing the shift from diffusion to kinetic-controlled mass transfer," Journal of Adhesion, 80 (2004), 773-796.

[3] J. Eastoe and J.S. Dalton, "Dynamic surface tension and adsorption mechanisms of surfactants at the air-water interface," Advances in Colloid and Interface Science, 85 (2000), 103-144.

[4] S.Y. Lin, et al., "Adsorption kinetics of C12E8 at the air-water interface: Adsorption onto a clean interface," Langmuir, 12 (1996), 6530-6536.

[5] S.Y. Lin, K. Mckeigue, and C. Maldarelli, "Diffusion-Controlled Surfactant Adsorption Studied by Pendant Drop Digitization," AIChE Journal, 36 (1990), 1785-1795.

[6] N.M.v. Os, *Nonionic surfactants: organic chemistry* (Marcel Dekker, New York, 1998).

[7] L. Liggieri, et al., "Molecular reorientation in the adsorption of some CiEj at the water-air interface," Colloids and Surfaces a-Physicochemical and Engineering Aspects, 156 (1999), 455-463.

[8] Y.C. Lee, et al., "Adsorption and desorption kinetics of CmE8 on impulsively expanded or compressed air-water interfaces," Colloids and Surfaces A-Physicochemical and Engineering Aspects, 220 (2003), 139-150.

[9] Y.C. Lee, H.S. Liu, and S.Y. Lin, "Adsorption kinetics of C10E4 at the air-water interface: consider molecular interaction or reorientation," Colloids and Surfaces a-Physicochemical and Engineering Aspects, 212 (2003), 123-134.

[10] S.Y. Lin, Y.C. Lee, and M.M. Shao, "Adsorption kinetics of C12E6 at the air-water interface," Journal of the Chinese Institute of Chemical Engineers, 33 (2002), 631-643.

[11] S.Y. Lin, et al., "Surface equation of state of nonionic CmEn surfactants," Langmuir, 19 (2003), 3164-3171.

[12] P.G. Nilsson, H. Wennerstrom, and B. Lindman, "Structure of Micellar Solutions of Non-Ionic Surfactants - Nuclear Magnetic-Resonance Self-Diffusion and Proton Relaxation Studies of Poly(Ethylene Oxide) Alkyl Ethers," Journal of Physical Chemistry, 87 (1983), 1377-1385.

[13] R.Y. Tsay, et al., "Adsorption kinetics of C12E8 at the air-water interface: Desorption from a compressed interface," Langmuir, 13 (1997), 3191-3197.

[14] M.W. Yang, et al., "A study of C12E4 adsorption kinetics-considering pendant bubble shape," Colloids and Surfaces a-Physicochemical and Engineering Aspects, 317 (2008), 462-472.

[15] R. Miller, et al., "Effect of surfactant interfacial orientation/aggregation on adsorption dynamics," Abstracts of Papers of the American Chemical Society, 215 (1998), U415-U415.

[16] R. Miller, et al., "Effect of the reorientation of oxyethylated alcohol molecules within the surface layer on equilibrium and dynamic surface pressure," Langmuir, 15 (1999), 1328-1336.

[17] R. Miller, V.B. Fainerman, and H. Mohwald, "Adsorption behavior of oxyethylated surfactants at the air/water interface," Journal of Colloid and Interface Science, 247 (2002), 193-199.

[18] J.T. Davies, "A quantitative kinetic theory of emulsion type I. Physical chemistry of the emulsifying agent," Proceedings of 2nd international Congress of Surface Activity, (1957), 426-438.

[19] J.W. Gibbs, *The collected works of J. Willard Gibbs* (Longmans, Green and Co., New York, 1928).

[20] A.T. Hubbard, *Encyclopedia of surface and colloid science* (Marcel Dekker, New York, 2002).

[21] Y.H. Kim, K. Koczo, and D.T. Wasan, "Dynamic film and interfacial tensions in emulsion and foam systems," Journal of Colloid and Interface Science, 187 (1997), 29-44.

[22] P.G. Degennes, "Wetting - Statics and Dynamics," Reviews of Modern Physics, 57 (1985), 827-863.

[23] A.L. Yarin, "Drop impact dynamics: splashing, spreading, receding, bouncing..." Annual Review of Fluid Mechanics, 38 (2006), 159-192.

[24] S.L. Anna and H.C. Mayer, "Microscale tipstreaming in a microfluidic flow focusing device," Physics of Fluids, 18 (2006), 121512.

[25] F. Jin, N.R. Gupta, and K.J. Stebe, "The detachment of a viscous drop in a viscous solution in the presence of a soluble surfactant," Physics of Fluids, 18 (2006), 022103

[26] A.F.H. Ward and L. Tordai, "Time-Dependence of Boundary Tensions of Solutions .1. The Role of Diffusion in Time-Effects," Journal of Chemical Physics, 14 (1946), 453-461.

[27] Y.C. Lee, S.Y. Lin, and H.S. Liu, "Role of equation of state on studying surfactant adsorption kinetics," Langmuir, 17 (2001), 6196-6202.

[28] Y.L. Lee, "Surfactants effects on mass transfer during drop-formation and drop falling stages," AIChE Journal, 49 (2003), 1859-1869.

[29] J.N. Chen and K.J. Stebe, "Surfactant-induced retardation of the thermocapillary migration of a droplet," Journal of Fluid Mechanics, 340 (1997), 35-59.

[30] A. Saint-Jalmes, Y. Zhang, and D. Langevin, "Quantitative description of foam drainage: Transitions with surface mobility," European Physical Journal E, 15 (2004), 53-60.

[31] B. Dai and L.G. Leal, "The mechanism of surfactant effects on drop coalescence," Physics of Fluids, 20 (2008).

[32] D.H. Smith, *Surfactant-based mobility control: progress in miscible-flood enhanced oil recovery* (American Chemical Society, Washington, DC, 1988).

[33] Y. Yoon, A. Hsu, and L.G. Leal, "Experimental investigation of the effects of copolymer surfactants on flow-induced coalescence of drops," Physics of Fluids, 19 (2007).

[34] J. Boussinesq, "Application of superficial viscosity grade on a surface of spherical liquid drop, falling slowly, a movement becoming uniform, at the heart of an infinite mass fluid in dormancy, of a least specific weight," Annales De Chimie Et De Physique, 29 (1913), 357-364.

[35] N.J. Alvarez, L.M. Walker, and S.L. Anna, "A Microtensiometer To Probe the Effect of Radius of Curvature on Surfactant Transport to a Spherical Interface," Langmuir, 26 (2010), 13310-13319.

[36] V.G. Levich and V.S. Krylov, "Surface-Tension-Driven Phenomena," Annual Review of Fluid Mechanics, 1 (1969), 293-&.

[37] V.G. Levich, *Physicochemical hydrodynamics: Veniam G. Levich; translated by Scripta Technica Inc* (Prentice-Hall, Englewood Cliffs, N.J., 1962).

[38] K.J. Stebe, S.Y. Lin, and C. Maldarelli, "Remobilizing Surfactant Retarded Fluid Particle Interfaces .1. Stress-Free Conditions at the Interfaces of Micellar Solutions of Surfactants with Fast Sorption Kinetics," Physics of Fluids a-Fluid Dynamics, 3 (1991), 3-20.

[39] K.J. Stebe and C. Maldarelli, "Remobilizing Surfactant Retarded Fluid Particle Interfaces .2. Controlling the Surface Mobility at Interfaces of Solutions Containing Surface-Active Components," Journal of Colloid and Interface Science, 163 (1994), 177-189.

[40] D.A. Edwards, H. Brenner, and D.T. Wasan, *Interfacial transport processes and rheology* (Butterworth-Heinemann, Boston, Mass., 1991).

[41] C.D. Eggleton and K.J. Stebe, "An adsorption-desorption-controlled surfactant on a deforming droplet," Journal of Colloid and Interface Science, 208 (1998), 68-80.

[42] C.D. Eggleton, Y.P. Pawar, and K.J. Stebe, "Insoluble surfactants on a drop in an extensional flow: a generalization of the stagnated surface limit to deforming interfaces," Journal of Fluid Mechanics, 385 (1999), 79-99.

[43] H.A. Stone and L.G. Leal, "Breakup of Concentric Double Emulsion Droplets in Linear Flows," Journal of Fluid Mechanics, 211 (1990), 123-156.

[44] W.J. Milliken, H.A. Stone, and L.G. Leal, "The Effect of Surfactant on the Transient Motion of Newtonian Drops," Physics of Fluids a-Fluid Dynamics, 5 (1993), 69-79.

[45] J.J.M. Janssen, A. Boon, and W.G.M. Agterof, "Influence of Dynamic Interfacial Properties on Droplet Breakup in Simple Shear-Flow," AIChE Journal, 40 (1994), 1929-1939.

[46] Y.T. Hu, D.J. Pine, and L.G. Leal, "Drop deformation, breakup, and coalescence with compatibilizer," Physics of Fluids, 12 (2000), 484-489.

[47] R.A. Debruijn, "Tipstreaming of Drops in Simple Shear Flows," Chemical Engineering Science, 48 (1993), 277-284.

[48] W. Lee, L.M. Walker, and S.L. Anna, "Role of geometry and fluid properties in droplet and thread formation processes in planar flow focusing," Physics of Fluids, 21 (2009), -.

[49] S.D. Hudson, A.M. Jamieson, and B.E. Burkhart, "The effect of surfactant on the efficiency of shear-induced drop coalescence," Journal of Colloid and Interface Science, 265 (2003), 409-421.

[50] N.J. Alvarez, L.M. Walker, and S.L. Anna, "Diffusion-limited adsorption to a spherical geometry: The impact of curvature and competitive time scales," Physical Review E, 82 (2010).

[51] P.O. Brunn, "Heat or Mass-Transfer from Single Spheres in a Low Reynolds-Number Flow," International Journal of Engineering Science, 20 (1982), 817-822.

[52] V.B. Fainerman, et al., "Adsorption kinetics of proteins at the solution/air interfaces with controlled bulk convection," Colloids and Surfaces a-Physicochemical and Engineering Aspects, 282 (2006), 217-221.

[53] T.F. Svitova, M.J. Wetherbee, and C.J. Radke, "Dynamics of surfactant sorption at the air/water interface: continuous-flow tensiometry," Journal of Colloid and Interface Science, 261 (2003), 170-179.

[54] J.D. Martin and S.D. Hudson, "Mass transfer and interfacial properties in two-phase microchannel flows," New Journal of Physics, 11 (2009), 115005.

CHAPTER 3

METHODS AND MATERIALS

3.1 ANALYSIS OF PENDANT DROP/BUBBLE IMAGES

3.1.1 INTRODUCTION

The pendant drop method is one of the most widely used techniques to measure the surface tension between gas-liquid and liquid-liquid interfaces. The method consists of fitting the Young-Laplace equation to the digitized shape of a drop suspended from the end of a capillary tube. The first use of digital computers to solve this problem utilized nonlinear least squares fitting and since then numerous subroutines and algorithms have been reported for improving efficiency and accuracy. However, current algorithms which rely on gradient based methods have difficulty converging for almost spherical drop shapes (i.e. low Bond numbers). We present a non-gradient based algorithm based on the Nelder-Mead simplex method to solve the least squares problem. The main advantage of using a non-gradient based fitting routine is that it is robust against poor initial guesses and works for almost spherical bubble shapes. We have tested the algorithm against theoretical and experimental drop shapes to demonstrate both the efficiency and the accuracy of the fitting routine for a wide range of Bond numbers. Our study shows that this algorithm allows for surface tension measurements corresponding to Bond numbers previously shown to be ill suited for pendant drop measurements.

3.1.2 BACKGROUND

When a fluid is suspended from a capillary and surrounded by another fluid such that gravity acts along the axis of the capillary to distend the nominally spherical interface, the shape of the interface depends on the surface tension, γ, the characteristic size of the bubble or drop, R_0, and the density difference between the two fluids, $\Delta\rho$. The Bond number, given by

$$Bo = \Delta\rho g R_0^2 / \gamma, \tag{3.1}$$

is a dimensionless group describing the relative magnitude of forces due to gravity and surface tension. If the density difference between the fluids is known and the size can be measured, then the surface tension can be determined from a measurement of the interface shape. This method of measuring surface tension, first realized by Andreas and coworkers [1], has come to be known as the pendant drop method. The method was suggested earlier by Worthington [2, 3] and Ferguson [4], but measurements of drop coordinates proved difficult at that time. Andreas *et al* overcame these issues by reformulating the Young-Laplace equation in a new coordinate system.

Using the formulation of Andreas *et al*, the Young-Laplace equation is integrated to obtain a theoretical drop shape, which is then compared with an experimental drop shape to determine the surface tension between the two fluids. Before the availability of digital computers, drop shapes were analyzed by examining the ratio of radii of the drop at different axial positions, whose values were tabulated along with corresponding surface tension values [5]. This analysis, known as the selected plane method, is still carried out today when

rough estimates (i.e. within 1 mN/m) of surface tension are of interest. However, when accuracy is required it is necessary to solve a nonlinear least-squares problem to fit a calculated drop shape to a measured drop shape. In addition, the selected plane method only works for drops that fall within a selected range of Bond numbers.

Although the particulars of the nonlinear least-squares fitting algorithms found in the literature might differ, the general procedure for each method remains the same. For instance, an image is first recorded by a CCD camera and digitized. An edge detection method is used to extract the shape of the drop interface. The coordinates of the interface are then used to calculate the error between computed theoretical shapes and the measured shape. The error is computed via an objective function, defined as the shortest distance between an experimental point and a point on the calculated interface. The procedure is repeated until the theoretical shape corresponding to the minimum error is found. The parameters that result from the fitting analysis are then assumed to be the parameters governing the shape of the experimental drop.

The most extensively utilized fitting routine for pendant and sessile drop studies is known as Axisymmetric Drop Shape Analysis (ADSA) [6]. Since the initial publication of this approach, there have been many improvements and adaptations for different applications [7, 8]. The first version used a Newton-Raphson routine with incremental loading, a method that systematically increments the parameter space after each Newton-Raphson iteration. However, this algorithm was found to be computationally expensive and convergence is not

guaranteed, especially when starting from a poor guess [7]. To improve convergence, del Rio *et al.* combined the Newton-Raphson method with the Levenberg-Marquardt algorithm which helped improve the likelihood of convergence. However, major limitations to the ADSA algorithm remain, as summarized recently by Hoorfar and Neumann [8]. For example, the authors found that ADSA-based algorithms are ill-suited for certain drop shapes that are close to spherical. A spherical drop of water analyzed using the ADSA algorithm yields a surface tension value near 79.32 mN/m, compared with the expected value of 72.28 mN/m [8]. The discrepancy between these two values is relatively large compared with typical pendant drop measurements, which are normally within 0.5 mN/m of the expected value at optimum conditions. To mitigate these discrepancies, a shape parameter, which is a measure of how close the shape is to spherical, is used to determine whether ADSA can be appropriately applied to a given drop. Generally speaking, the minimum Bond number at which the ADSA algorithm can be successfully applied is approximately $Bo \approx 0.2$.

Although improvements on these methods continue to be developed, there are fundamental limitations to gradient-based techniques such as ADSA. For instance, the convergence of gradient optimization methods assumes a continuous objective function. Although continuity of the error equation may be assumed for theoretical drops with no distortion in the pixel positions, the assumption may not be valid for experimental drop shapes where pixel positions may be shifted due to threshold effects, imperfect edge detection routines, and random noise [9].

The inability of pendant drop measurements to be conducted below $\beta \approx 0.2$ places a significant restriction on interfacial tension measurements for liquid-liquid pairs. For example, in the case of silicone oil and water, the density difference, $\Delta\rho \approx 10^{-2}$ g/cm^3. To achieve a Bond number greater than $\beta \approx 0.2$ would require a drop size on the order of centimeters. While this might not represent significant impedance for static measurements, the time scale to reach equilibrium in dynamic studies of surfactant adsorption scales with drop radius, and a centimeter-scale drop will increase the time scale by an order of magnitude compared with typical pendant drop measurements [10]. In addition, in experiments where microgravity is simulated using density matched fluids $\Delta\rho \approx 10^{-3}$ g/cm^3, which further limits both static and dynamic studies as the drop would have to be extremely large and time scales to reach equilibrium very long. Therefore, an algorithm that can avoid the restriction on Bond number would facilitate studies of liquid-liquid interfaces that are currently too difficult to measure.

The present section describes a new, non-gradient-based algorithm that utilizes the Nelder-Mead simplex method for the determination of surface tension from the measured shape of a pendant drop or bubble. Numerous test cases are constructed to validate the efficiency and robustness of the algorithm, even when only poor initial guesses are available. Efficiency of the algorithm is tested extensively in lieu of its use in dynamic studies where many frames (i.e. 100-1000) need to be studied. Furthermore, we demonstrate the ability of the new

algorithm to fit nearly spherical drop shapes, both theoretically and experimentally, overcoming a major limitation of existing algorithms.

3.1.3 RELATIONSHIP BETWEEN SURFACE TENSION AND THE SHAPE OF A PENDANT DROP

The pressure jump ΔP across a fluid interface at any point is a function of the two principal radii of curvature, given by the Young-Laplace equation, $\Delta P = \gamma\left(1/R_1 + 1/R_2\right)$, where γ is the interfacial tension, and R_1 and R_2 are the two principle radii of curvature. If gravity is the only additional force acting on the drop, then the pressure jump is given by $\Delta P = \Delta P_0 + \Delta\rho g z$, where $\Delta\rho$ is the density difference between the two fluids. Using geometrical arguments and a change of coordinate system, illustrated schematically in Figure 3.1, the Young-Laplace equation becomes a set of three ordinary differential equations [1],

$$\begin{aligned} \frac{dx}{ds} &= \cos\varphi, \\ \frac{dz}{ds} &= \sin\varphi, \\ \frac{d\phi}{ds} &= 2 - Bo \cdot z - \frac{\sin\phi}{x}, \end{aligned} \tag{3.2}$$

where x is the horizontal coordinate, z the vertical coordinate, φ is the angle of rotation measured from the apex, and s is the arc length. Eqns (3.2) are subject to the initial conditions

$$x\left(s=0\right) = z\left(s=0\right) = \varphi\left(s=0\right) = 0 \tag{3.3}$$

where Bo is the Bond number defined earlier, Eqn (3.1) , in which R_0 is taken to be the radius of curvature at the apex.

Numerous techniques, summarized by del Rio and Neumann [7], have been employed to solve the system of differential equations given by Eqn (3.2) subject to (3.3). In this section, we have chosen to use a version of the well-known Runge-Kutta approach, specifically the fourth and fifth order Runge-Kutta-Dormand-Prince pair, which is an efficient solver allowing for intermediate step sizes to be calculated with almost no increase in computational time [11]. This scheme increases the accuracy of the fitting routine without increasing computational time for the numerous integrations that are performed, as described in the following section. Note that a 4^{th} order Runge-Kutta integrator was initially attempted, however the computation time for convergence for the fitting routine was on the order of minutes. This was unsatisfactory for dynamic studies. We now discuss a new approach to the fitting of a drop shape to measured experimental drop interface coordinates, which incorporates methods from algorithms reported in the literature and new methods developed in our laboratory to formulate an improved algorithm that can fit small Bond number drop shapes.

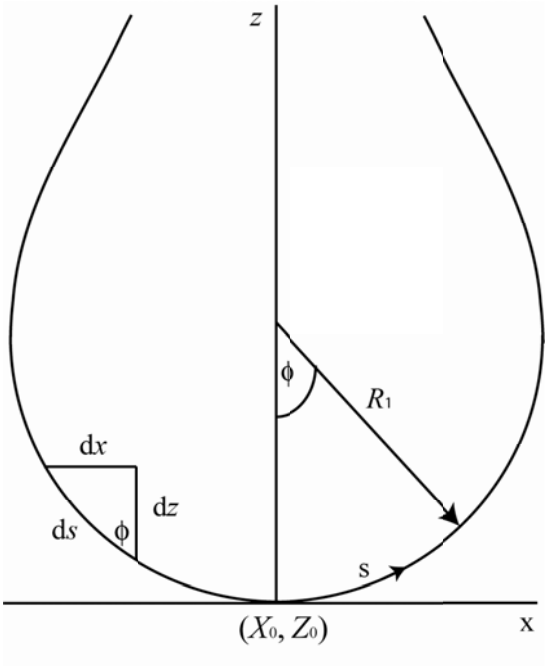

Figure 3.1. The coordinate system for a pendant drop, where x is the horizontal coordinate, z is the vertical coordinate, φ is the angle of rotation from the apex (X_0, Z_0), and s is the arc length. R_1 is the principal radius of curvature in the plane of the page and R_2 is the principal radius of curvature in a plane perpendicular to the page and the axis of symmetry, such that $R_2 = x / \sin\varphi$.

3.1.4 ALGORITHM FOR ANALYZING A DIGITIZED PENDANT DROP SHAPE

To determine the surface tension we compare measured points along the interface of a digitized image of a pendant drop with theoretical drop shapes computed via integration of Eqn (3.2) subject to Eqn (3.3). Although surface tension is the only unknown material parameter, in order to get a reasonable fit we must also optimize several coordinate variables. These parameters include the rotation angle θ of the camera with respect to gravity, the position of the apex of the drop (x_0, z_0), and the radius of curvature at the apex, R_0. This section will

discuss the integration procedure used to obtain the shape of a theoretical drop as well as the specific components of the optimization algorithm.

The experimental measurement of the drop shape results in an array of n interface coordinates (x_n, z_n). The interface shape is obtained by first determining a global threshold calculated by Otsu's method, which assumes that there exist two classes of pixels, foreground and background, and calculates the optimal threshold that separates the two classes [12]. This threshold value converts the image to a binary (black and white) image that is then sent to the edge detection routine developed by Canny [13], which is commonly used in pendant drop analysis [14] to extract the interface coordinates. We note that other edge detection algorithms are also viable for pendant drop analysis including Sobel, Prewitt, and others [8]. Once the interface coordinates are obtained, the magnified coordinates must be scaled by M, where M is the magnification of the camera setup, to obtain the dimensionless coordinates, (X_n, Z_n) in order to compare with the calculated dimensionless coordinates, (X_j, Z_j). In addition, the measured coordinates must also be scaled by a, where a is the aspect ratio between the width and height of the image pixels and rotated by θ. Following Jennings and Pallas this scaling can be written explicitly [15],

$$\begin{aligned} X_n &= \left(\frac{x_n}{M} - x_0\right)\cos\theta + \left(\frac{az_n}{M} - z_0\right)\sin\theta, \\ Z_n &= \left(\frac{az_n}{M} - x_0\right)\cos\theta - \left(\frac{x_n}{M} - z_0\right)\sin\theta. \end{aligned} \tag{3.4}$$

Unlike in prior treatments of the optimization problem, we have found it best to independently calibrate the aspect ratio, *a*, of the imaging system and use the accurately measured diameter of the syringe needle to calculate *M*, instead of requiring these parameters to be optimized. Independent calibration of these parameters reduces the order of the optimization problem and therefore reduces computation time and increases accuracy.

As mentioned above, we use a Runge-Kutta ODE solver to obtain the theoretical drop interface coordinates. Since optimization requires several iterations to converge, it is important that the chosen solver is efficient for low tolerances. To ensure this, we tested the ODE solver for varying numbers of generated points. We found that this solver is quite efficient and that its efficiency is independent of the number of points generated. For example, calculating 200 integration steps requires 0.020 s and calculating 1000 points requires 0.025 s using a Pentium 4 processor with a specified relative tolerance of 10^{-10}. We note that the del Rio and Neumann version of ADSA uses a similar integration scheme known as the fifth and sixth order Verner pair, which is selected due to its ability to allow the calling program to interrupt and continue the integration after any step [7]. This feature is not required in the present algorithm as the error function is approximated as described below.

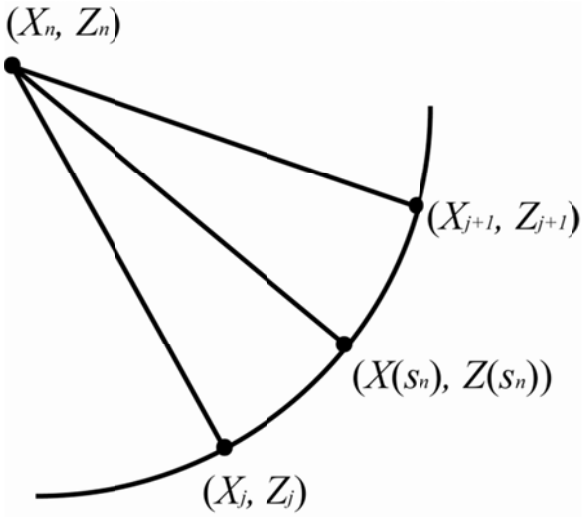

Figure 3.2. A geometrical representation of the approximated normal from the experimental point to the theoretical curve, where (X_n, Z_n) is the n^{th} interfacial coordinate from an experimental drop, and (X_j, Z_j) and (X_{j+1}, Z_{j+1}) are the calculated theoretical points that straddle the point $(X(s_n), Z(s_n))$ that lies on the normal from the experimental interface to the calculated interface.

Now that the two sets of points are scaled in the same manner, it is necessary to define an objective function that can be minimized to yield the best-fit parameters. In pendant drop analysis, attempts to reduce computation time by minimizing only the horizontal distance or only the vertical distance have proven inaccurate since there is uncertainty in pixel position in both directions. Therefore, we define our objective function E as the distance between a measured interface coordinate (X_n, Z_n) and the closest corresponding point on the theoretical curve $(X(s_n), Z(s_n))$, summed over all points,

$$E = \sum_{n=1}^{N} r_i^2 = \sum_{n=1}^{N} \left[\left(X(s_n) - X_n \right)^2 + \left(Z(s_n) - Z_n \right)^2 \right]. \tag{3.5}$$

It can be shown geometrically that the closest corresponding point ($X(s_n)$, $Z(s_n)$), lies on the normal to the measured coordinate (X_n, Z_n), as shown in Figure 3.2. Since the integration of Eqns (3.2) is unlikely to produce the exact points ($X(s_n)$, $Z(s_n)$) corresponding to every data point, we use the interpolation method performed by Jennings and Pallas [15]. From their analysis, the authors show that the distance r_i can be approximated by the triangle formed by the two theoretical points that straddle ($X(s_n)$, $Z(s_n)$) and the interface point (X_n, Z_n) of interest, as illustrated in Figure 3.2. Therefore, r_i is approximated by

$$r_i \cong \frac{\left(Z_j - Z_n\right)\left(X_j - X_{j+1}\right) - \left(X_j - X_n\right)\left(Z_j - Z_{j+1}\right)}{\left[\left(X_j - X_{j+1}\right)^2 + \left(Z_j - Z_{j+1}\right)^2\right]^{\frac{1}{2}}}, \tag{3.6}$$

where (X_j, Z_j) and (X_{j+1}, Z_{j+1}) correspond to the points that straddle ($X(s_n)$, $Z(s_n)$), see Figure 3.2. Although del Rio and Neumann [7] recommend against this approximation, suggesting that it may bring unwanted error into the fitting routine, we have found that any effect on accuracy is compensated by adding intermediate points in the calculated drop shape. Practically, it appears that simply doubling the number of experimental points works well.

We argue that an improvement to existing algorithms will arise from improved optimization of the parameter space. To optimize the parameters Bo, R_0, X_0, Z_0, and θ, we use the Nelder-Mead simplex optimization method [16], which is implemented in the pre-existing MATLAB subroutine *fminsearch* (Mathworks Inc., Natick, MA). The Nelder-Mead simplex method is intended for

nonlinear unconstrained optimization and is therefore applicable to pendant drop analysis. It begins by creating a large simplex, which is an *n*-dimensional polygon, in all dimensions and then steps each vertex of the polygon in the direction of the smallest error in order to shrink the size of the simplex. Convergence is met when the diameter of the simplex falls below the specified tolerance. Since a possible drawback to using the Nelder-Mead simplex algorithm is that it will sometimes converge to a local minimum, we have implemented an additional procedure, which we refer to as a 'reload' algorithm. The reload algorithm re-introduces the previously converged parameter set as a starting guess in a new iteration of the Nelder-Mead algorithm. Since the first step of the method is to create a large simplex, it is straightforward to search for nearby minima that are lower than the current solution. Note if the converged least squared error is greater than 10^{1}, then all initial values are set to zero and the optimization routine is restarted. When the error between subsequent converged parameters is below 10^{-6} the reload algorithm terminates. Although it is not guaranteed that the global minimum will be found by this procedure, this iterative step provides an opportunity for the algorithm to escape a local minimum. For the cases we have tested, we have found that the reload algorithm is effective in locating global minima. Therefore, the reload algorithm results in a solution that is robust against initial guesses, which is a major drawback in other algorithms.

3.1.5 RESULTS AND DISCUSSION

To validate the algorithm described above, we begin by using theoretically calculated interface shapes as the input in place of experimental drop shapes. It is important that the grid spacing between the "experimental" drops and the fitting algorithm are different when testing the algorithm. If they are the same, then the normal will be exact and we will not be testing the ability of the algorithm to minimize the normal distance through the approximation given by Eqn (3.6). Therefore, to ensure that the spacing is different, we use a different solver for the ordinary differential equations known as the Bashford-Adams-Moulton algorithm [17] to create the "experimental" drop shape with the same degree of tolerance, 10^{-10}.

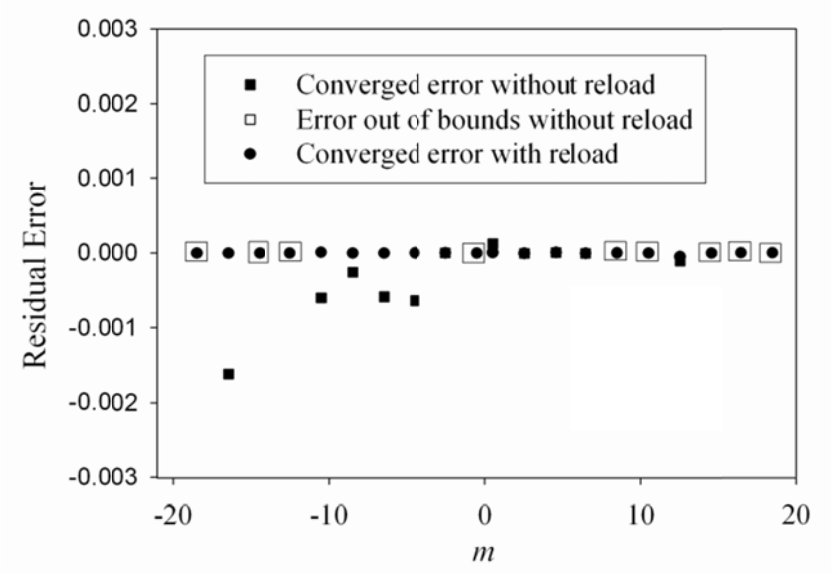

Figure 3.3. Performance of the algorithm as a function of the initial guess. To generate the initial guess, the multiplicative factor m is multiplied by the known drop parameters $Bo = 0.3125$, $R_0 = 1.5$ mm, $X_0 = 1$, $Z_0 = 1$. Error is reported as the fractional difference between the resulting Bond number and the actual Bond number. 516 interface points were fitted. Note that the parameter θ is not perturbed.

To test the sensitivity of the final result to the initial guess, we perturb the five fitting parameters by shifting the guessed values by an amount $m \cdot p$ away from the actual value, where m is the magnitude of the disturbance and p represents the parameter values that define the experimental drop. We selected values of m between -18 and +18 to determine the robustness of the algorithm, where the negative values of m correspond to an initial guess of a sessile drop. We note that initial guesses corresponding to real experiments are rarely as far from the optimum solution as the initial guesses selected here. It is typically possible to obtain initial guess values within 50% of the optimum value. Nevertheless, the present analysis demonstrates the lack of dependence of the converged solution on the initial parameters. Figure 3.3 plots the error in the resulting Bond number, defined as $\left(Bo_a - Bo_c\right)/Bo_a$, as a function of m, where Bo_a is the actual value and Bo_c is the calculated value. The graph shows that the Nelder-Mead algorithm fails to converge with reasonable tolerance for larger values of m and has compromised accuracy for negative values of m. However, when the previously converged solution is reloaded back into the Nelder-Mead algorithm as described in the previous section, where the tolerance for the converged parameters was specified to be 10^{-4}, we find that for all values of m, the solution is significantly closer to the global minimum, with errors in Bo below 10^{-3}, as shown in Figure 3.3. Thus, we have demonstrated that the Nelder-Mead algorithm can overcome local minima and result in fitted parameters that are independent of the initial guess.

The ability of the algorithm to successfully converge even with a poor initial guess is more valuable if the time for convergence is also independent of the initial guess. Figure 3.4 shows that the computation time for all values of *m* fluctuates between 10 and 20 s regardless of the magnitude of the disturbance. Note that the number of fitted interface coordinates is kept fixed at 516 for all fits shown. The computation time ranges from 8 to 27 s, depending on the magnitude of the disturbance. Therefore the algorithm completes in a reasonable computation time for this problem, especially considering the large divergence between the initial guess and the actual parameters used to construct the "experimental drop."

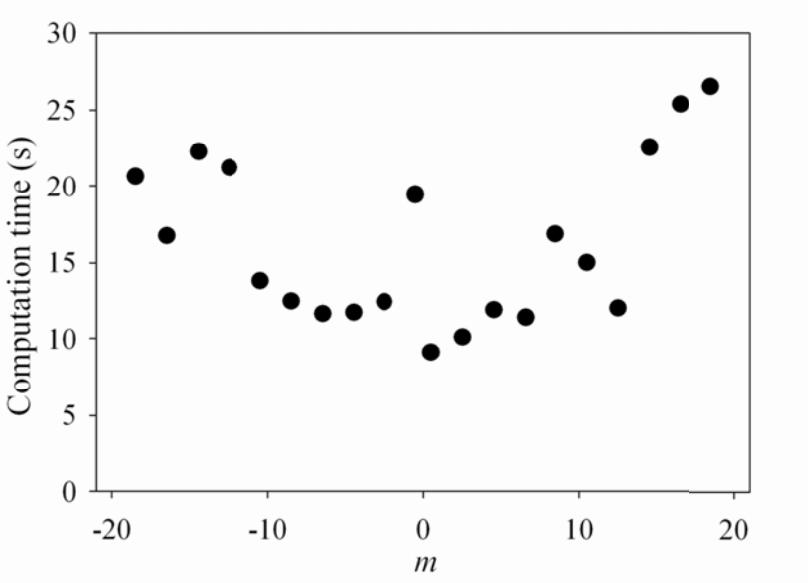

Figure 3.4. Computation time as a function of the multiplicative factor *m*. This plot demonstrates that the computation time is not strongly affected by the quality of the initial guess. 516 points were fitted. The known drop parameters are Bo = 0.3125, R_0 = 1.5 mm.

# points	time (s)	# reload	Bo_{fit}	R_0 (mm)	Residual Error (m)
1522	7.67	1	0.3033	1.50	4.34E-08
762	6.89	2	0.3033	1.50	4.20E-08
508	7.65	3	0.3033	1.50	4.33E-08
382	5.56	2	0.3033	1.50	4.19E-08
306	3.95	1	0.3033	1.50	5.23E-08
254	3.84	1	0.3033	1.50	4.72E-08
140	3.43	1	0.3033	1.50	2.86E-08
96	3.12	1	0.3033	1.50	4.17E-08
74	3.09	1	0.3033	1.50	2.70E-08
60	3.05	1	0.3033	1.50	6.67E-08
52	3.62	1	0.3033	1.50	7.69E-08
44	2.92	1	0.3033	1.50	4.55E-08
40	2.99	1	0.3033	1.50	5.00E-08
34	2.90	1	0.3033	1.50	5.88E-08
32	3.92	2	0.3033	1.50	1.25E-07
28	3.71	2	0.3035	1.50	1.03E-04
26	2.83	1	0.3038	1.50	3.79E-04

Table 3.1.The computation time as a function of the number of points fitted along the interface, as well as the residual error, the calculated Bond number, and the number of reloads. The actual Bond number is $Bo = 0.3033$ and the apex radius is $R_0 = 1.50$. There is no shift in the x or z direction as well as no rotation in θ. These experiments were run with the same initial guess.

Having established that the reload Nelder-Mead scheme leads to convergence to the global minimum regardless of the accuracy of the initial guess, we now examine the effect of the number of fitted interface coordinates on convergence. Ideally, all coordinate points along the interface should be used in the optimization procedure. This is especially true for drop images obtained from experiment, in which the digitized interface coordinates have uncertainty associated with them. In gradient-based methods, using all the available coordinates requires more computation time as the number of integrations increases. Therefore the resulting error for these schemes exhibits a dependence on the number of fitted coordinates along the interface. Using fewer points allows for substantial reductions in the computation time [18]. For the new analysis algorithm described here, Table 3.1 shows the computation time, the least-squares error (LSE), the calculated Bond number, and the number of reloads required as a function of number of fitted interface coordinates. Two main conclusions can be drawn from these results. Firstly, the computation time decreases as the number of fitted points decreases, although not by a significant amount. Secondly, there is a critical value of the number of fitted points at which the LSE begins to increase. Since the computation time does not decrease substantially with the number of fitted points, we use all the available points along the interface so as not to introduce additional error in the optimization. This becomes considerably more important when random errors are present in the drop shape coordinates and selecting specific interface points to be fitted could introduce bias.

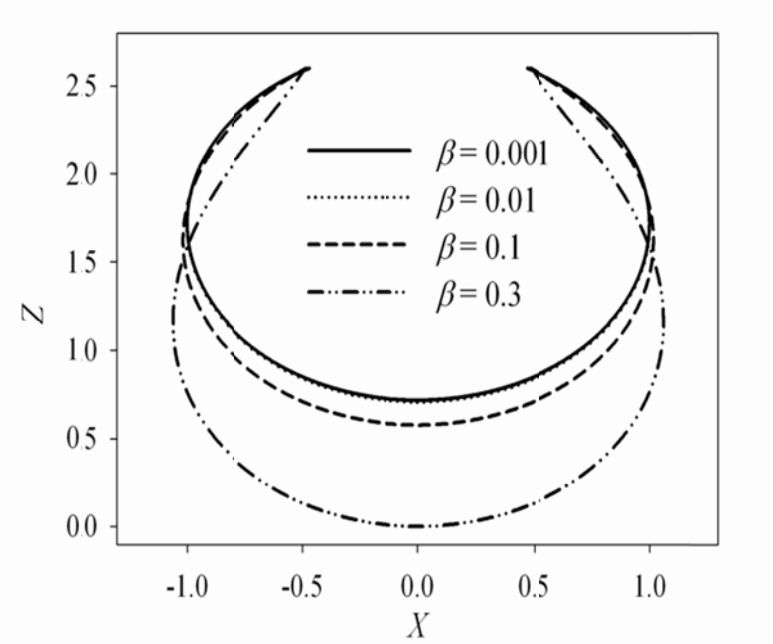

Figure 3.5. Theoretical bubble shapes for different Bond numbers corresponding to a capillary tip with fixed radius.

Bo_{exp}	Bo_{fit}	**Residual Error (m)**
0.001	0.000998	2.00E-03
0.01	0.01000	3.00E-04
0.1	0.1000	8.00E-05
1	1.000	2.00E-06
5	5.0	3.40E-06

Table 3.2. Calculated Bond numbers using the new algorithm for a wide range of actual Bond numbers.

The robustness of the algorithm to initial guesses is important; however the more important improvement using the new formulation is the ability to measure shapes corresponding to small Bond number. We now examine the

ability of the algorithm to handle drop shapes corresponding to a wide range of Bond numbers. Figure 3.5 shows several theoretical interface shapes corresponding to different Bond numbers that would form from a capillary tip with fixed radius. While interface shapes corresponding to larger β values are visually distinct, the low Bond number cases $Bo = 0.001$ and $Bo = 0.01$ exhibit only subtle differences in shape, rendering it exceedingly difficult to fit the correct Bond number to shapes such as these. This is the main reason that pendant drop experiments are typically conducted at Bond numbers greater than $Bo \approx 0.2$ [10]. However, as we discussed earlier, this restriction is limiting for pendant drop experiments in which the two fluids have very similar densities, such as oil and water systems, or those conducted in reduced gravity environments. Table 3.2 shows the results of the optimization procedure for a wide range of Bond numbers. Even for the two smallest Bond number values, the resulting LSE is less than one percent, indicating that the algorithm described here is capable of handling drop shapes corresponding to very small Bond numbers when no error exists in the position of interface coordinates.

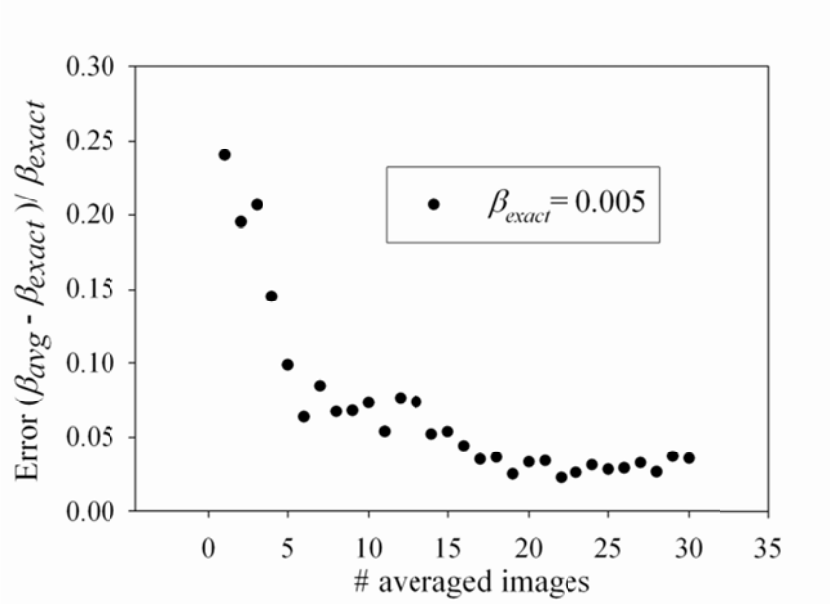

Figure 3.6. Relationship between residual error and the number of averaged drops for a drop corresponding to Bo = 0.005. The residual error decreases the larger the number of drop shapes that are averaged together.

Real digitized experimental images results in pixel positions that contain random errors in the x and z positions arising from a variety of sources including lighting conditions, camera noise, and the image threshold routine. To better understand the bounds that exist when random noise is present, we first tested the algorithm against theoretical drops with random error introduced in the pixel positions. This was done by shifting each interface coordinate normal to the local curvature by a maximum of 1 pixel in a 640x480 image. A similar procedure is described elsewhere [7]. Our results show that for $Bo > 0.01$, the converged solution is within 1% of the known Bond number. However, for lower Bond numbers the converged solution depends strongly on the location of the random errors, see [19]. However, since the noise is random, averaging over multiple drop shapes should reduce the error in the converged solution. This is explicitly

shown in Figure 3.6 for a drop shape corresponding to $Bo = 0.005$, where the error decreases steadily and then reaches a plateau beyond a certain number of averaged drops. Table 3.3 lists the number of averaged drop images required to achieve an error less than 5% for Bond numbers from $0.001 \leq Bo$ 0.01. This table should aid in designing experiments to measure both static and dynamic drop shapes for Bo 0.01. Figure 3.7 shows that the converged error steadily decreases as the Bond number increases.

Bo_{exp}	**# averaged drops**
0.001	-
0.002	26
0.003	22
0.004	20
0.005	16
0.006	11
0.007	11
0.008	6
0.009	4
0.010	1

Table 3.3. The number of averaged drops required to achieve an average error below 5% of the actual Bond number for randomly perturbed interface points. The points were perturbed normal to the local curvature by a maximum of 1 pixel within a 640 x 480 image. 400 points along the interface were fitted.

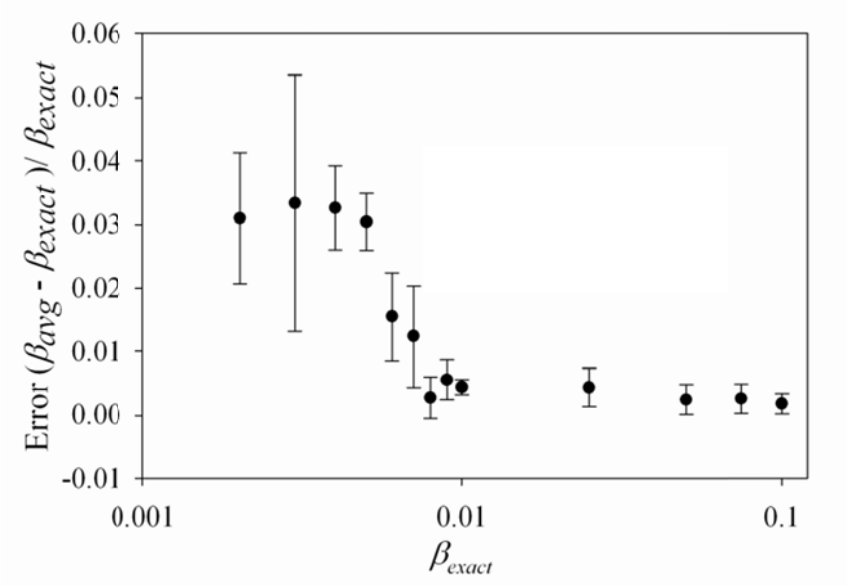

Figure 3.7. Average converged error as a function of Bond number.

Finally, we test the reload Nelder-Mead algorithm using experimental images measured in a pendant bubble apparatus in our laboratory as well as the extracted experimental points given by Jennings and Pallas [15]. First, we measure the surface tension of pure water using a 1.65 mm diameter j-needle (Rame-Hart Inc.). Multiple images captured at 20°C for larger values of Bo yield an average surface tension value of γ = 72.82 ± 0.14 mN/m, which is within 0.1% of the reported value of γ = 72.75 mN/m [20]. In addition, we also tested the algorithm using the experimental data provided by Jennings and Pallas, for which both ADSA and the algorithm presented by these authors yield a surface tension value of 72.10 mN/m. The new algorithm presented here also yields a surface tension value of 72.10 mN/m and Bo =0.3316. These results demonstrate that the reload Nelder-Mead algorithm described here yields surface tension values consistent with existing gradient-based methods for experimental drop shapes.

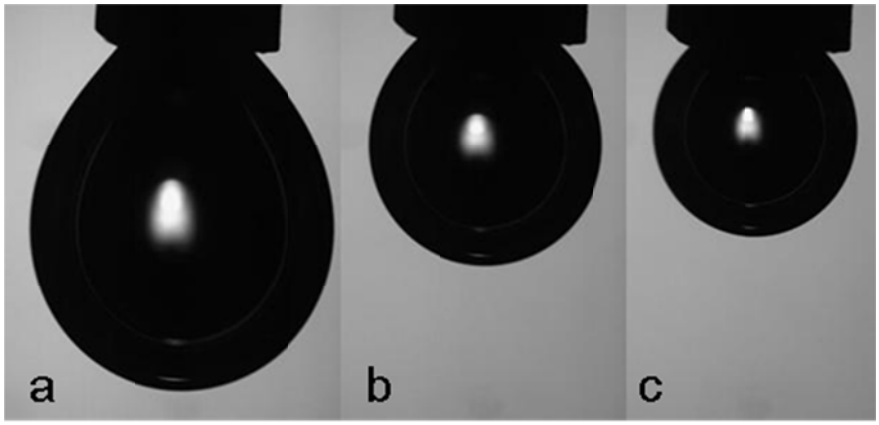

Figure 3.8. Three different sized air bubbles in water corresponding to Bo = 0.228, 0.128, and 0.108 respectively. Note the trend toward a spherical shape as Bond number decreases. The new algorithm results in surface tension values of γ = 72.63, 72.53, and 71.96 mN/m, respectively. Diameter of needle is 1.65 mm.

Finally, we examine the performance of the algorithm for experiments corresponding to very small Bond number values. Figure 3.8 shows three digitized images of air bubbles in water with decreasing Bond number values corresponding to (a) Bo = 0.228, (b) Bo = 0.128, and (c) Bo = 0.108, respectively. Using the reload Nelder-Mead scheme, the calculated surface tension values are (a) γ = 72.63 mN/m, (b) γ = 72.53 mN/m, and (c) γ = 71.96 mN/m, respectively. Gradient-based methods such as ADSA either fail to converge or converge to an erroneous value for nearly spherical drops such as the ones shown in Figure 3.8 b and c.

3.1.6 SUMMARY

We have demonstrated the use of a non-gradient-based algorithm for determining the surface tension from digitized shapes of pendant drops and bubbles. The algorithm is constructed using established fitting and optimization routines allowing for ease in implementation [21]. The major advance that we

have made to this area is the use of the Nelder-Mead algorithm to find the minimum of the objective function, along with a reloading scheme that enables the fitting routine to escape local minima. This has resulted in a robust and efficient algorithm that uses all points along the drop interface and can accurately measure drops with $Bo \geq 0.01$, a lower limit that is a factor of ten or more smaller than the current limit for pendant drop measurements. Furthermore, through the use of averaging the algorithm can be applied to drops with $0.002 \leq Bo \leq 0.01$. For these small bond numbers Table 3.3 shows the number of drops needed to average out the random error. The algorithm has been rigorously tested using theoretical drop shapes with and without introduced random error. In addition, the algorithm has been tested using experimental drop images corresponding to low Bond numbers. Therefore, this algorithm provides a viable alternative for measuring surface tension between liquids of similar density, which is currently impractical in most cases.

3.2 MODELING DYNAMIC SURFACE TENSION: SEMI-INFINITE VOLUME

Surfactant adsorption/desorption to a spherical interface is modeled using Fick's law of diffusion and a kinetic rate equation. Diffusion to a spherical interface is given by

$$\frac{\partial C}{\partial t} = \frac{D}{r^2}\frac{\partial}{\partial r}\left(r^2 \frac{\partial C}{\partial r}\right). \tag{3.7}$$

The kinetic rate equation that is most often used to describe non-ionic surfactants, such as the $C_{12}E_8$ surfactant studied here, is the Generalized Frumkin equation, given by

$$\frac{\partial \Gamma}{\partial t} = \beta C_s \Gamma_\infty \left(1 - \frac{\Gamma}{\Gamma_\infty}\right) - \alpha\Gamma \exp\left(\kappa\left(\frac{\Gamma}{\Gamma_\infty}\right)^n\right), \tag{3.8}$$

where β is the adsorption constant, α is the desorption constant, Γ_∞ is the maximum packing concentration of surfactant at the interface, κ accounts for molecular interactions and n is a fitting parameter accounting for the nonlinearity of the interactions. The relevant boundary conditions are a flux balance at the interface between the surface concentration and the bulk fluid concentration immediately adjacent to the interface. This flux is given by

$$\frac{\partial \Gamma}{\partial t} = D\left.\frac{\partial C}{\partial r}\right|_{r=b}. \tag{3.9}$$

The second boundary condition is such that far from the interface $\lim_{r\to\infty} C \to C_{bulk}$.

If Eqns (3.7) and (3.8) are solved subject to these boundary conditions, all modes of surfactant transport to the interface are described. Two special cases of this solution are diffusion-limited and kinetic-limited dynamics. The diffusion-limited

case can be described by simultaneously solving Eqns (3.7) and (3.8) except that the right hand side of Eqn (3.8) is set equal to zero. In other words, at all time steps the subsurface and the interface concentrations are in equilibrium. The kinetic-limited case can be solved by integrating Eqn (3.8) only. To describe surfactant transport onto a freshly formed interface, we use the following initial conditions,

$$\Gamma\left(t=0\right)=0 \text{ and } C\left(t=0,r\right)=C_{bulk} \ . \tag{3.10}$$

To describe surfactant transport onto an expanded or compressed interface we use the following initial conditions,

$$\Gamma\left(t=0\right)=\Gamma_{eq}\left(C_{bulk}\right) \text{ and } C\left(t=0,r\right)=C_{bulk} \ . \tag{3.11}$$

To solve this problem, we employ a collocation spectral method in which space is discretized using Chebyshev grid points and time is discretized using an implicit Euler scheme [22]. To ensure that convergence is met, we changed the number of grid points and the time step until the solution showed a less than 10^{-6} deviation in $\gamma(t)$ with a change in these parameters. In addition, we validated the numerical procedure, using a similar method described in the literature [23], by integrating the spherical Ward and Tordai equation [24],

$$\Gamma(t)=\Gamma_i+\frac{D}{b}\left[C_{bulk}t-\int_0^t C_s(\tau)d\tau\right]+\left(\frac{4D}{\pi}\right)^{\frac{1}{2}}\left[C_{bulk}\sqrt{t}-\int_0^{\sqrt{t}} C_s(t-\tau)d\sqrt{\tau}\right], \tag{3.12}$$

using the trapezoidal rule, where Γ_i is the initial surfactant coverage on the interface.

3.3 MATERIALS

For most of the work presented in this thesis, we study the transport of nonionic surfactants $C_{10}E_8$, $C_{12}E_8$, and $C_{14}E_8$. The surfactants were purchased from Nikko Chemicals (99% purity) and used as received. The family of C_iE_j molecules has chemical structure $(C_iH_{2i+1}O(CH_2CH_2O)_jH$. Surfactant solutions were prepared using deionized water purified using a Barnstead UV Ultrapure II purification system (resistivity of 18.2 MΩ·cm). Stock solutions are prepared by first melting the pure surfactant at 40°C and then weighing a known amount of pure surfactant. The known mass is diluted to specified concentrations that are below the cmc. Solvents (ACS grade) for cleaning and sample preparation were purchased and used as received.

The diffusion coefficient of $C_{12}E_8$ has been obtained previously using several independent techniques. We take the average value corresponding to several reported values, $D = 3.8\times10^{-10}$ m^2/s [25-27]. The diffusion coefficient for $C_{10}E_8$ and $C_{14}E_8$ were calculated using the diffusion coefficient of $C_{12}E_8$ and the scaling with molecular weight given by $D \sim M^{1/2}$, which has previously been used for low molecular weight surfactants [29]. The values used are $D = 3.9\times10^{-10}$ m^2/s and $D = 3.7\times10^{-10}$ m^2/s, respectively. Silicone oil was purchased from Gelest Inc. and used as received. The measured density of the oil is 960 kg/m^3 and the manufacturer reported viscosity is $\mu/\rho = 50$ cSt ($\mu = 48$ cP). All silicone oil-water experiments were conducted at room temperature, 22 ±1°C.

[1] J.M. Andreas, E.A. Hauser, and W.B. Tucker, "Boundary Tensions by Pendant Drops," Journal of Physical Chemistry, 42 (1939), 1001.

[2] A.M. Worthington, "On Pendent Drops," Proc. Roy. Soc., 32 (1881), 362.

[3] A.M. Worthington, "Note on a Point in the Theory of Pendent Drops," Phil. Mag., 19 (1885), 46.

[4] A. Ferguson, "Photographic Measurements of Pendent Drops," Phil. Mag., 23 (1912), 417-430.

[5] S. Fordham, *On the Calculation of Surface Tension from Measurements of Pendant Drops* Proceedings of the Royal Society of London Series a-Mathematical and Physical Sciences, 194 (1948), 1-16.

[6] Y. Rotenberg, L. Boruvka, and A.W. Neumann, "Determination of Surface Tensions and Contact Angles from the Shape of Axisymmetric Interfaces," Journal of the American Oil Chemists Society, 59 (1982), A297-A297.

[7] O.I. del Rio and A.W. Neumann, "Axisymmetric drop shape analysis: Computational methods for the measurement of interfacial properties from the shape and dimensions of pendant and sessile drops," Journal of Colloid and Interface Science, 196 (1997), 136-147.

[8] M. Hoorfar and A.W. Neumann, "Recent progress in Axisymmetric Drop Shape Analysis (ADSA)," Advances in Colloid and Interface Science, 121 (2006), 25-49.

[9] S.H. Anastasiadis, et al., "The Determination of Interfacial Tension by Video Image Processing of Pendant Fluid Drops," U.S. Army Research Office Technical Reports, (1986).

[10] F. Jin, R. Balasubramaniam, and K.J. Stebe, "Surfactant adsorption to spherical particles: The intrinsic length scale governing the shift from diffusion to kinetic-controlled mass transfer," Journal of Adhesion, 80 (2004), 773-796.

[11] J.R. Dormand and P.J. Prince, "A family of embedded Runge-Kutta formulae," Journal of Computational and Applied Mathematics, 6 (1980), 19-26.

[12] N. Otsu, "Threshold Selection Method from Gray-Level Histograms," IEEE Transactions on Systems Man and Cybernetics, 9 (1979), 62-66.

[13] J. Canny, "A Computational Approach to Edge-Detection," IEEE Transactions on Pattern Analysis and Machine Intelligence, 8 (1986), 679-698.

[14] M.G. Cabezas, J.M. Montanero, and C. Ferrera, "Computational evaluation of the theoretical image fitting analysis - axisymmetric interfaces (TIFA-AI) method of measuring interfacial tension," Measurement Science & Technology, 18 (2007), 1637-1650.

[15] J.W. Jennings and N.R. Pallas, "An Efficient Method for the Determination of Interfacial-Tensions from Drop Profiles," Langmuir, 4 (1988), 959-967.

[16] J.A. Nelder and R. Mead, "A Simplex-Method for Function Minimization," Computer Journal, 7 (1965), 308-313.

[17] L.F. Shampine and M.K. Gordon, "Computer Solution of Ordinary Differential Equations: The Initial Value Problem," (Freeman, San Francisco, 1975).

[18] P. Cheng, et al., "Automation of Axisymmetric Drop Shape-Analysis for Measurement of Interfacial-Tensions and Contact Angles," Colloids and Surfaces, 43 (1990), 151-167.

[19] P. Cheng and A.W. Neumann, "Computational Evaluation of Axisymmetrical Drop Shape Analysis-Profile (ADSA-P)," Colloids and Surfaces, 62 (1992), 297-305.

[20] D.R. Lide and H.P.R. Frederikse, *CRC Handbook of Chemistry and Physics* (CRC Press, Boca Raton, 1995).

[21] *The code has been incorporated into a graphical user interface and can be obtained from the authors upon request.*

[22] L.N. Trefethen, *Spectral methods in MATLAB* (Society for Industrial and Applied Mathematics, Philadelphia, 2000).

[23] R. Miller and G. Kretzschmar, "Numerical-Solution for Mixed Model of Diffusion Controlled Adsorption," Colloid and Polymer Science, 258 (1980), 85-87.

[24] S.Y. Lin, K. Mckeigue, and C. Maldarelli, "Diffusion-Controlled Surfactant Adsorption Studied by Pendant Drop Digitization," AIChE Journal, 36 (1990), 1785-1795.

[25] S.N. Moorkanikkara and D. Blankschtein, "New methodology to determine the rate-limiting adsorption kinetics mechanism from experimental dynamic surface tension data," Journal of Colloid and Interface Science, 302 (2006), 1-19.

[26] B. Faucompre and B. Lindman, "Self-Association of Zwitterionic and Nonionic Surfactants - NMR Self-Diffusion Studies," Journal of Physical Chemistry, 91 (1987), 383-389.

[27] P.G. Nilsson, H. Wennerstrom, and B. Lindman, "Structure of Micellar Solutions of Non-Ionic Surfactants - Nuclear Magnetic-Resonance Self-Diffusion and Proton Relaxation Studies of Poly(Ethylene Oxide) Alkyl Ethers," Journal of Physical Chemistry, 87 (1983), 1377-1385.

CHAPTER 4

DIFFUSION-LIMITED ADSORPTION TO A SPHERICAL GEOMETRY: THE IMPACT OF CURVATURE AND COMPETITIVE TIME SCALES

4.1 INTRODUCTION

Molecules and particles diffuse via Brownian motion along concentration gradients. In many situations such gradients are induced by the removal of material from the bulk to populate a surface. An example is the adsorption of surfactants to liquid or solid interfaces [1, 2]. A characteristic time scale for transport via diffusion can be written as,

$$\tau_D = \frac{l^2}{D}, \tag{4.1}$$

where l is a characteristic length scale across which diffusion must occur and D is the diffusion coefficient. In an unbounded geometry where there is no obvious geometric length scale, a natural length scale is obtained by considering the mass removed to an interface compared with the mass available in a region of the bulk near that interface. Equating the number of molecules of a species accumulated at equilibrium on the interface with the number of molecules of that species available in a volume element of the bulk solution leads to a length scale called the depletion depth, which characterizes the width of the mass transfer boundary layer, or the steepness of the concentration gradient. For example, for surfactant adsorption to a planar interface, Figure 4.1 (a), the number of molecules adsorbed to a unit area of the interface, dA, at equilibrium is given by $\Gamma_{eq} dA$, where Γ_{eq} is the equilibrium surface concentration. The number of molecules in a volume

element adjacent to the interface is given by $C_{bulk} h_p dA$, where h_p is the depletion depth and C_{bulk} is the surfactant concentration in the bulk. Thus, the depletion depth for a planar interface is given by $h_p = \Gamma_{eq} / C_{bulk}$ and the characteristic time scale for diffusion to a planar interface using Eqn (4.1) is given by,

$$\tau_{Dp} = \frac{h_p^2}{D}. \tag{4.2}$$

Since the equilibrium surface concentration is dependent on the bulk concentration through an isotherm, the planar depletion depth h_p is also an intrinsic length scale for the surfactant that depends on bulk concentration and molecular properties of the surfactant.

The characteristic length scale for diffusion to a spherical interface is more complicated than that for a planar interface, since the radius introduces an additional length scale with which to scale the problem. Jin *et al.* [3] recently showed that by scaling the boundary condition for diffusion to a spherical interface, assuming the radius *b* as the relevant length scale, one obtains a characteristic time scale for diffusion given by,

$$\tau_{Dj} = \frac{h_p b}{D} \tag{4.3}$$

suggesting that diffusion is faster for increasing curvature or smaller radius [3]. The radial dependence of the diffusion-limited time scale is due to the increase in the ratio of solution volume to surface area with decreasing radius. In other words, at any given time a smaller radius has a larger number of surfactant molecules adjacent to the interface than a larger interface. Thus a smaller radius

reaches equilibrium faster. Recognizing this radius dependent diffusion time scale represented a change in thinking for the field.

Motivated by the analysis of Jin *et al*., we interpreted experimental data and trends in the context of Eqn (4.3). We found that this scaling is inconsistent with two observations found in the literature. The first inconsistency is that the time scale does not approach that of the planar interface as the radius grows large and the curvature approaches zero, as we would expect. Instead, Eqn (4.3) suggests that the time scale continues to grow without bound as the radius increases. The second inconsistency arises when diffusion competes with other mass transport processes, leading to competing time scales. For example, Jin *et al.* [3] consider the competition between diffusion, which drives surfactant to the interface, and kinetic barriers, which govern the rates at which molecules near the interface adsorb and desorb. Comparing the diffusion time scale given in Eqn (4.3) with a kinetic time scale, τ_k, for ad/desorption at an interface yields a dimensionless ratio analogous to the Damkoehler number used in reaction-diffusion systems [4]. For the case considered by Jin *et al*., the ratio is independent of concentration. A lack of dependence of the dimensionless ratio of time scales on concentration suggests that concentration does not determine the conditions at which the dominant mass transport mechanism shifts from diffusive to kinetic. However, experimental observations described by Pan *et al.* [5] for short chain alcohols and the semi-analytical study performed by Lin *et al.* [6] both show that kinetic processes become increasingly important at high concentration. These observations suggest that a correct time scale for a spherical geometry

should result in a limiting behavior for large radii and a ratio of kinetic to diffusion time scales that is dependent on concentration.

In this chapter, we further develop the scaling analysis presented by Jin *et al.* for diffusion-limited transport to a spherical interface (solid or free) and verify the scaling using both numerical simulations and two distinct experimental data sets using a nonionic surfactant as a test species. This new time scale is then compared with the time scale for kinetics to determine the governing transport mechanism at all radii and concentration conditions. The framework developed here will yield a quantitative means of determining the importance of surfactant kinetic exchange at an interface, i.e., when the kinetic transport is slows enough to alter the overall rates of transport to interfaces.

4.2 DIFFUSION-LIMITED TIME SCALE FOR A SPHERICAL GEOMETRY

To control and understand processes involving mass transport, we need to formulate the correct scaling behavior. This is particularly true when two or more processes compete. Here, we develop a new time scale for the general problem of diffusion mass exchange at spherical interfaces which overcomes the two limitations described earlier. We validate this scaling using numerical simulations solving for diffusion-limited mass transport of surfactant to a spherical interface. The result is an improved scaling which will provide a tool to better design and characterize dynamic surface tension results as well as surfactant-induced phenomena at interfaces, such as tipstreaming [7], detergency [8], and emulsion and film stability [9, 10].

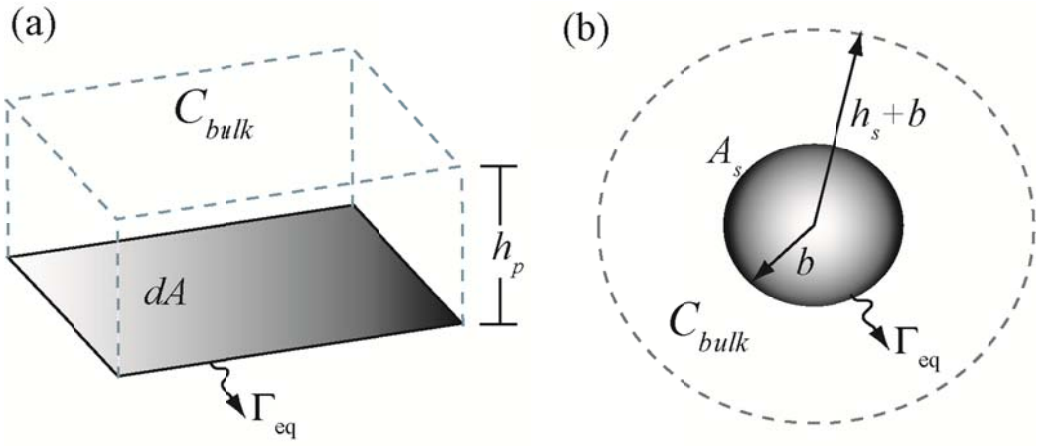

Figure 4.1. Schematic representation of the depletion depth for (a) a planar interface, h_p and (b) a spherical interface, h_s.

Similar to the planar depletion depth, a spherical depletion depth is derived by considering a spherical interface in an unbounded geometry. As shown schematically in Figure 4.1(b), the number of molecules occupying the surface at the equilibrium surface concentration, Γ_{eq}, is given by $4\pi b^2\Gamma_{eq}$. The number of molecules occupying the volume extending a radial distance h_s from the surface of the sphere is given by $\frac{4}{3}\pi C_{bulk}\left(\left(h_s+b\right)^3-b^3\right)$. Combining these two expressions and solving for h_s leads to the expression,

$$\frac{h_s}{h_p}=\left(\frac{b}{h_p}\right)\left[\left(\frac{3h_p}{b}+1\right)^{\frac{1}{3}}-1\right]. \qquad (4.4)$$

The spherical depletion depth depends on both the intrinsic (planar) depletion depth for the surfactant, and the radius of curvature of the depleting interface. In the limit that the radius of curvature is large compared with the intrinsic depletion depth $b >> h_p$, the spherical depletion depth approaches the

planar depletion depth $h_s \to h_p$. In the limit of small radii, $b << h_p$, the spherical depletion depth scales with both the intrinsic depletion depth, h_p, and the radius of curvature, b, such that,

$$h_s \cong \left(3b^2 h_p\right)^{\frac{1}{3}}. \tag{4.5}$$

The behavior of the spherical depletion depth scaled with the intrinsic depletion depth, h_s/h_p, as a function of the dimensionless length scale b/h_p is shown in Figure 4.2. It is notable that the ratio h_s/h_p depends solely on the ratio b/h_p, which contains all of the relevant surfactant conditions including concentration, bubble radius, and surfactant molecular parameters.

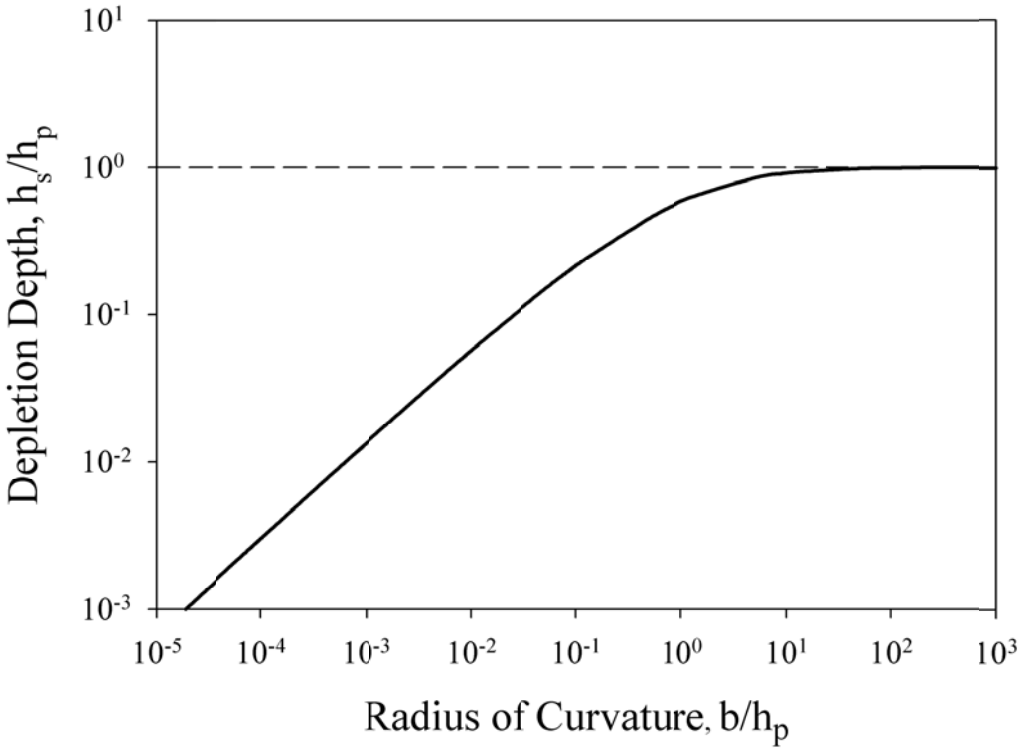

Figure 4.2. Spherical depletion depth scaled by the planar depletion depth as a function b/h_p (solid line). Dashed line represents the planar depletion depth.

4.3 NUMERICAL METHOD

To determine whether the relationship given in Eqn (4.4) is relevant to the diffusion-limited mass transport to a spherical interface, we use numerical simulations to determine the appropriate characteristic time scale. The bulk diffusion of surfactant is modeled using the unsteady form of Fick's law of diffusion in spherical coordinates, $\partial C/\partial t = D/r^2\,\partial/\partial r\left(r^2\,\partial C/\partial r\right)$, subject to a flux condition at the interface, $\partial\Gamma/\partial t = D\,\partial C/\partial r\big|_{r\to b}$ [11]. Far from the interface, a Dirichlet boundary condition applies, $C_{r\to\infty} = C_{bulk}$, and we use the initial

condition $\Gamma(t=0, r=b)=0$, which corresponds to a clean interface. The flux condition is constrained by the Langmuir adsorption isotherm,

$$\frac{\Gamma_{eq}}{\Gamma_{\infty}} = \frac{C_{bulk}}{C_{bulk}+a}, \tag{4.6}$$

where a is the ratio of kinetic constants for adsorption, β, and desorption, α [12]. In this study, the diffusion coefficient is taken to be constant regardless of the proximity of the molecule to the interface. Recent studies on colloidal particles suggest that the diffusion coefficient is not constant as the particle approaches the interface [13, 14]. Although not accounted for here, this type of behavior would introduce new length scales and time scales into the problem.

We solve the governing equations using a spectral analysis method to obtain the complete time-dependent concentration profile for diffusion-limited dynamics [15]. A spectral analysis was performed using Chebyshev grid points and an implicit Euler scheme for discretization in time. Convergence was verified by changing the number of grid points and decreasing the time step until a change in these parameters yielded a change in dynamic surface tension less than a prescribed tolerance, $\Delta\gamma \leq 10^{-6}$ N/m. The spectral algorithm was also verified by comparing the converged solution with the semi-analytical solution to the differential equations described by Mysels [16] and solved by the same methodology as Miller and Kretschmar [17].

4.4 THE DIFFUSION-LIMITED TIME SCALE

Given the general form of the scaling in Eqn (4.1), we expect that the time scale for diffusion to a spherical interface will contain some function of the length scales h_s, h_p and b. In the case of a planar interface, the diffusion time scale has the form of Eqn (4.2). However, for a spherical interface, more than one choice of scaling exists. For example, the scaling given in Eqn (4.3) by Jin *et al.* [3] arises from a scaling of the flux boundary condition using the radius as the characteristic length scale, $r_c = b$. If the flux boundary condition, Eqn (2.10), is instead scaled using the spherical depletion depth, $r_c = h_s$, the characteristic time scale $\tau_1 = h_s h_p / D$ arises. Independently scaling Eqn (2.9), using $r_c = h_s$, yields a characteristic time scale $\tau_2 = h_s^2 / D$. Therefore, the bulk process and the surface flux are governed by different but comparable time scales, τ_1 and τ_2, whereas in the case of the planar geometry only one unique time scale results from the same scaling analysis. Here, we choose a single time scale that is a simple geometric mean of the two time scales τ_1 and τ_2. A similar approach to developing a governing scaling from multiple natural time scales is used in other systems. For example, competitive time scales are seen in the relaxation of an entangled mesh of wormlike micelles, which is governed by both a polymeric reptation time and a breaking and reforming time; in this case a simple geometric mean of the two natural time scales provides a governing time scale that is verified by experiments [18]. In the case of diffusion to a spherical interface, then, we consider the combined time scale given by the geometric mean of τ_1 and τ_2 above, such that,

$$\tau_{D,s} = \left(\tau_1 \tau_2\right)^{1/2} = \frac{\left(h_s^{\,3} h_p\right)^{1/2}}{D}. \tag{4.7}$$

As we previously described, when $b \to \infty$, we see that $h_s \to h_p$ and thus the diffusion time scale reduces to $\tau_{D,s} \to h_p^{\,2}/D$. Therefore, as expected, the time scale given in Eqn (4.7) captures the asymptotic limit corresponding to a planar interface. In the limit of small radii, $b << h_p$, the time scale given by Eqn (4.7) approaches the time scale found by Jin *et al.* [3] Combining Eqn (4.5) and Eqn(4.7), the limiting time scale approaches $\tau_{D,s} \to h_p b/D$ (cf. Eqn (4.3)). Therefore, the results presented in Jin *et al.* can be interpreted as an asymptotic limit of the spherical diffusion time scale presented here.

The effective length scale over which diffusion occurs for a spherical interface (i.e. l from Eqn (4.7)), is given by $l = \left(h_s^{\,3} h_p\right)^{\frac{1}{4}}$. This equation can be rearranged to obtain $l = \left(h_s/h_p\right)^{3/4} h_p$. Using the relationship presented in Eqn (4.4), l can be written as a function of b and b/h_p only. In Figure 5 of Jin *et al*. the following scenario is presented: $b = 10$ μm, $C_\infty = 0.8$ μM and $h_p/b = 210$, leading to a value of $h_s/h_p = 0.0361$, so $l = 1.74\times10^{-4}$ m and $l/b = 17.4$. Even though the spherical depletion depth is much smaller than the planar depletion depth, the effective depletion length scale is larger than the bubble radius. In other words, using a small radius does not ensure that the diffusion length scale is small since the length scale is also dependent on concentration.

It is important to note that this newly derived time scale is independent of the isotherm selected when scaled by the planar time scale. Scaling the spherical diffusion time scale given in Eqn (4.7) by the planar time scale, Eqn (4.2), leads to

$$\frac{\tau_{Ds}}{\tau_{Dp}} = \left(\frac{h_s}{h_p}\right)^{\frac{3}{2}} = \left(\frac{b}{h_p}\right)^{\frac{3}{2}} \left[\left(\frac{3h_p}{b}+1\right)^{\frac{1}{3}} - 1\right]^{\frac{3}{2}}, \tag{4.8}$$

which depends only on the dimensionless quantity b/h_p, (cf. Eqn (4.4)). Although the intrinsic depletion depth, h_p, is determined by the isotherm, varying this quantity only serves to change the relative magnitude of b/h_p. In other words, the isotherm determines where the system conditions fall on the scaling curve, but does not change the shape of the curve. Therefore, any system undergoing diffusion-limited transport to a spherical interface is expected to follow this scaling regardless of the thermodynamic condition that governs its equilibrium.

4.5 NUMERICAL VALIDATION OF TIME SCALE

To validate the scaling given in Eqn (4.8), numerically computed dynamic surface tension curves are analyzed. Using the simulated surface concentration profiles, $\Gamma(t)$, we determine the time, τ_{num}, required to reach a given fraction, ϕ, of the equilibrium surface concentration, $\phi = \Gamma(\tau_{num})/\Gamma_{eq} = const$. The dependence of τ_{num} on b/h_p is then used to test the scaling of the characteristic time for diffusion to within a leading constant. A range of values of b/h_p were obtained by (*i*) considering a fixed radius while varying concentration and (*ii*) considering

a fixed concentration while varying radius. For a planar interface, the time scale obtained for all surface concentration fractions considered, $0.1 \le \phi \le 0.9$, agreed well with the expected scaling given by Eqn (4.2), verifying the technique.

Figure 4.3 compares the time scale resulting from the full diffusion-limited numerical simulations with three different relevant scalings. Note that the numerical time scale has been empirically shifted by a leading constant such that the planar region asymptotically approaches unity for direct comparison with the theoretical scaling. For experimental results, the shift factor is observed to depend on ϕ and the isotherm chosen. In the case of the numerical simulations, the correct isotherm governing the dynamics is known and therefore the shift factor only depends on ϕ. In addition, for all $\phi < 0.90$ the horizontal axis was shifted by dividing the value of b/h_p used in the numerical simulations by ϕ. This scaling is appropriate since only a fraction of the equilibrium coverage is reached at finite values of τ_{num}. Therefore, h_p should be evaluated at the instantaneous surface concentration $\Gamma(\tau_{num})$ and not the equilibrium value Γ_{eq}. In other words, the extracted time scale corresponds to a depletion depth of $h_{p,\tau_{num}} = \Gamma(\tau_{num})/C_{bulk}$ and thus

$$\frac{b}{h_{p,\tau_{num}}} = \frac{bC_{bulk}}{\Gamma(\tau_{num})} = \frac{b}{h_p \phi}, \tag{4.9}$$

such that the time scale corresponds to the fractional coverage and not the equilibrium coverage. Figure 4.3 shows that τ_{num} approaches the planar time scale at large radii and the time scale given by Jin *et al.* [3] at small radii, as

expected from the asymptotic analysis given in Eqn (4.5). The time scale given in Eqn (4.7) captures both this limiting behavior as well as the intermediate scaling for $b/h_p \sim \mathrm{O}(1)$. Therefore, we conclude that a geometric mean of the two comparable time scales for bulk and surface processes does provide the correct characteristic time scale for diffusion-limited transport to a spherical interface.

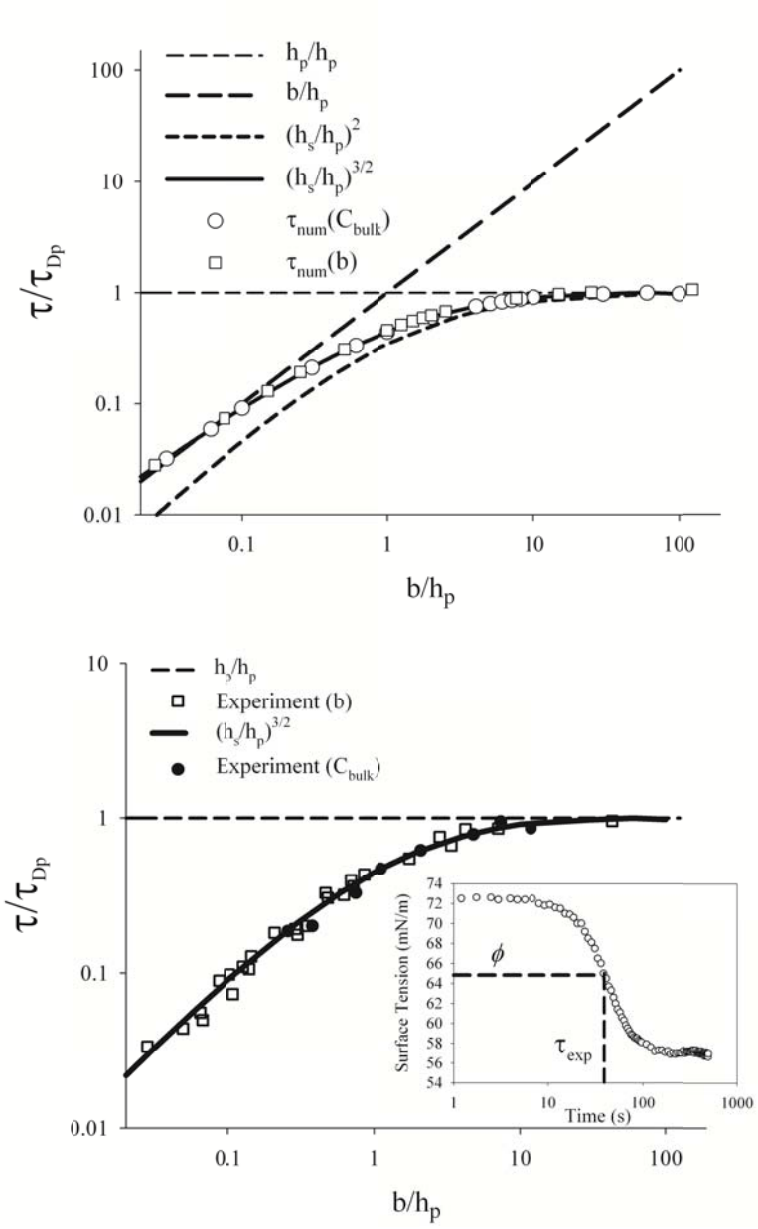

Figure 4.3. (a) Comparison of three possible time scales scaled by the planar time scale as a function of b/h_p. The time scale obtained from numerical simulations is represented by open symbols. The open circles correspond to simulations conducted for changing concentration at fixed radius. The open squares correspond to simulations conducted for changing radius at fixed concentration. Note that the scaling behavior for the characteristic time is the same for both cases. The horizontal line corresponds to the time scale for a planar interface. (b) Comparison of experimental data scaled by the planar time scale as a function of b/h_p. The circles correspond to experiments where the concentration was varied at fixed radius and the squares correspond to experiments where the bubble radius was varied at fixed concentration.

4.6 EXPERIMENTAL VALIDATION OF TIME SCALE

Experimental validation of this time scale was performed by measuring the surfactant dynamics for varying bubble radii and concentration, and conducting a similar analysis to that described in the numerical validation section. Since the time scale is independent of the isotherm governing the equilibrium condition at the interface, any surfactant system can be used to examine the scaling. Conventionally, surfactant dynamics are tested experimentally using shape analysis of a pendant drop of fixed bubble radius and varying bulk concentrations [19]. Results from the literature were used to test our scaling. To test the scaling with varying bubble size at fixed surfactant concentrations, we have built a device in which a bubble is formed at the end of a glass capillary. Capillaries of different radii were used. The surface tension was inferred from a time varying measurement of the pressure jump across the interface and radius of the bubble, the details of which can be found elsewhere [20]. The surfactant used for this study is a nonionic alkyl polyglycolether surfactant, $C_{12}E_8$, for which dynamic surface tension measurements have been reported in the literature [21].

The analysis of the experimental data is performed via the same method described in the numerical validation section, except that the characteristic time scale is extracted from experimental dynamic surface tension curves (Figure 4.3b inset) [20] instead of the dynamic surface concentration curves, which are directly accessible in simulations. Three concentrations were selected, C_{bulk} = 0.0006, 0.0025, and 0.006 mol/m^3, which are all well below the expected critical micelle concentration of 0.1 mol/m^3 [21]. The bubble sizes used for these experiments

were $b =$ 22, 29, 56, 92, 155 μm, and pendant bubble measurements (b~1.5 mm). The selection of different concentrations extended our access to a wider range of b / h_p, due to the limited range of experimentally accessible bubble radii.

The experimental time scales were extracted from the data by choosing $0.6 < \phi < 0.9$, which is converted to the corresponding surface tension using the equation of state for $C_{12}E_8$, [21-23] and extracting the experimental time required to obtain this fractional coverage (i.e., surface tension) for a given concentration. An example is shown in the inset of Figure 4.3b. To determine the dependence of the time scale on concentration, data extracted from Figure 1 of Lin *et al*. [21] was also used. The same technique of determining an experimental time scale was used. Again a constant fractional surface coverage was chosen, $0.6 < \phi < 0.9$, and the governing equation of state was used to calculate the surface tension corresponding to each concentration for the selected fractional coverage. Specifically for $C_{12}E_8$, the Generalized Frumkin isotherm was used to calculate the intrinsic length scale, h_p, and thus the planar diffusion time scale. The parameters for the isotherm were taken from the literature [22], see Table 4.1. Although the isotherm used does not change the scaling, it is important that the isotherm used fits the equilibrium surface tension data and that the same isotherm is used to scale the entire data set.

Surfactant	Γ_∞ [μmol/m^2]	a [mol/m^3]	κ	n	β [m^3/mol/s]	D [10^{10} m^2/s]	R_{DK} [μm]	b [μm]	Model
Butanol [24]	6.7	47	0	0	1.6†	8.8	80	~500	L
Hexanol [24]	6.0	3.7	0	0	35†	7.0	3.4	~500	L
Nonanol [22]	6.4	3.0	-4.97	0.29	100	6.3	1.0	~800	GF
Decanol [25]	7.0	0.97	-5.03	0.26	10	6.0	8.4	~800	GF
Model	6.0	8.0×10^{-6}	0	0	100	7.0			L
$C_{12}E_8$ [23]	5.3	2.3×10^{-6}	13.2	0.50	5.6‡	4.0	14	17-800	GF

†These values were obtained from Joos and Serrien[26]
‡Calculated from scaling limits as explained in text

Table 4.1. Parameters for the surfactants used in this study along with the isotherm employed in the analysis.

The results of the experimental analysis for both varying concentration and varying radius are shown in Figure 4.3b. The scaled data clearly follows the scaling given in Eqn (4.7). Since the diffusion-limited scaling is observed for the entire range of experimental conditions considered for this surfactant, we conclude that the dynamic surface tension response must be diffusion-limited. This is in contrast to many models that have been proposed for this surfactant [21, 22, 27, 28], in which kinetic exchange at the interface is introduced to describe the observed dynamics. In fact, Figure 4.3b suggests that the correct choice of isotherm along with diffusion-limited dynamics should describe the dynamics without having to introduce additional kinetic barriers to exchange at the interface.

These two distinct experimental data sets have further validated the correct time scale for diffusion-limited surfactant transport to a spherical interface. In the next section, we address some of the implications of the results shown in Figure

4.3b on our understanding of surfactant dynamics and on the importance of surfactant kinetics at an interface.

4.7 COMPETING TIME SCALES

Now that the diffusion time scale to a spherical interface has been verified , we can determine the relative impact of competing time scales on transport to interfaces. If the dynamics of a surfactant exhibit a time scale that differs from the form of the diffusion-limited time scale, then it is possible that kinetic exchange at the interface or another process (e.g., convection [29]) is competing with diffusion to the interface. We can determine the relative importance of kinetics and diffusion via the ratio of the characteristic time scales for the processes [30], often referred to as the Damkoehler number in the reaction-diffusion literature. To illustrate this point, consider a surfactant that obeys Langmuirian kinetics [17, 30], where the evolution of surface concentration at a static interface is given by

$$\frac{\partial \Gamma}{\partial t} = \beta C_{bulk} \Gamma_\infty \left(1 - \frac{\Gamma}{\Gamma_\infty} \right) - \alpha \Gamma , \tag{4.10}$$

where β is the adsorption rate constant and α is the desorption rate constant. At equilibrium Eqn (4.10) reduces to the Langmuir isotherm, (cf., Eqn (4.6)). The characteristic kinetic time scale is obtained from the solution to the differential equation in Eqn (4.10), and is given by

$$\tau_k = \frac{1}{\beta C_{bulk} + \alpha} . \tag{4.11}$$

Therefore, the ratio of the two time scales is given by

$$\Lambda = \frac{\tau_{Ds}}{\tau_k} = \frac{\left(h_s^3 h_p\right)^{\frac{1}{2}}}{D}\left(\beta C_{bulk} + \alpha\right). \tag{4.12}$$

A similar analysis was performed by Pan *et al.* who used the planar diffusion time scale to explain the observation that surfactants exhibit kinetic-limited dynamics at high concentrations [5]. Jin *et al.* used the analysis of Pan *et al.* and the scaling given in Eqn (4.3) to demonstrate how curvature affects the relative magnitudes of the two time scales [3]. In particular, Jin *et al.* noted an intrinsic length scale, $R_{DK} = D/\left(\Gamma_\infty b\right)$, at which the two time scales are equal ($\Lambda = 1$) and a transition from diffusion-limited to kinetic-limited transport is expected. Using the corrected scaling for a spherical interface, Eqn (4.12), we determined the critical radius, R_{crit}, at which the kinetic and diffusion time scales are equal by solving

$$\left(R_{crit}\left[\left(\frac{3h_p}{R_{crit}}+1\right)^{\frac{1}{3}}-1\right]\right)^3 h_p\left(\frac{\beta C_{bulk}+\alpha}{D}\right)^2 = 1. \tag{4.13}$$

Solving Eqn (4.13) for R_{crit} and scaling by R_{DK}, the intrinsic surfactant length scale derived by Jin *et al.*, the new critical radius is given by

$$\frac{R_{crit}}{R_{DK}} = \frac{2}{\sqrt{12-3q^2}-3q}\ , \tag{4.14}$$

where $q = \left(R_{DK}/h_p\right)^{1/3}$ is a dimensionless ratio of two intrinsic length scales for the surfactant. Thus, the critical radius now depends on the bulk concentration as well as material properties as experiments and analysis have previously shown [5, 6, 24, 26, 30]. Figure 4.4 shows the dependence of the scaled R_{crit} on the value of

q. The solid line corresponds to the radius at which the two time scales (kinetic and diffusion) are equal. Values far to the left of the solid line correspond to diffusion-limited dynamics and values to the far right correspond to kinetic-limited dynamics. Note that as $q \to 1$, $R_{crit}/R_{DK} \to \infty$. Figure 4.4 is consistent with the expectation that as bubble radius decreases the dynamics become more kinetic-limited. In addition, it captures the experimentally and theoretically observed dependence of the controlling mechanism on surfactant concentration [5, 6, 24, 26, 30]. As concentration increases, q increases and therefore the system moves toward the kinetic-limited regime. The scaling analysis put forth by Jin *et al.* was independent of concentration and therefore inconsistent with these experimental investigations. However, by using the correct diffusion time scale, the scaling analysis is in agreement with both the radius dependence presented by Jin *et al.* and the concentration dependence observed experimentally and discussed in Pan *et al*. It should be noted that Figure 4.4 is general for systems that undergo a Langmuirian kinetic exchange at the interface. A similar analysis could be performed for systems governed by other kinetic models. Such analysis is useful in determining the parameter space in which a transition from diffusion-limited to kinetic-limited transport can be expected.

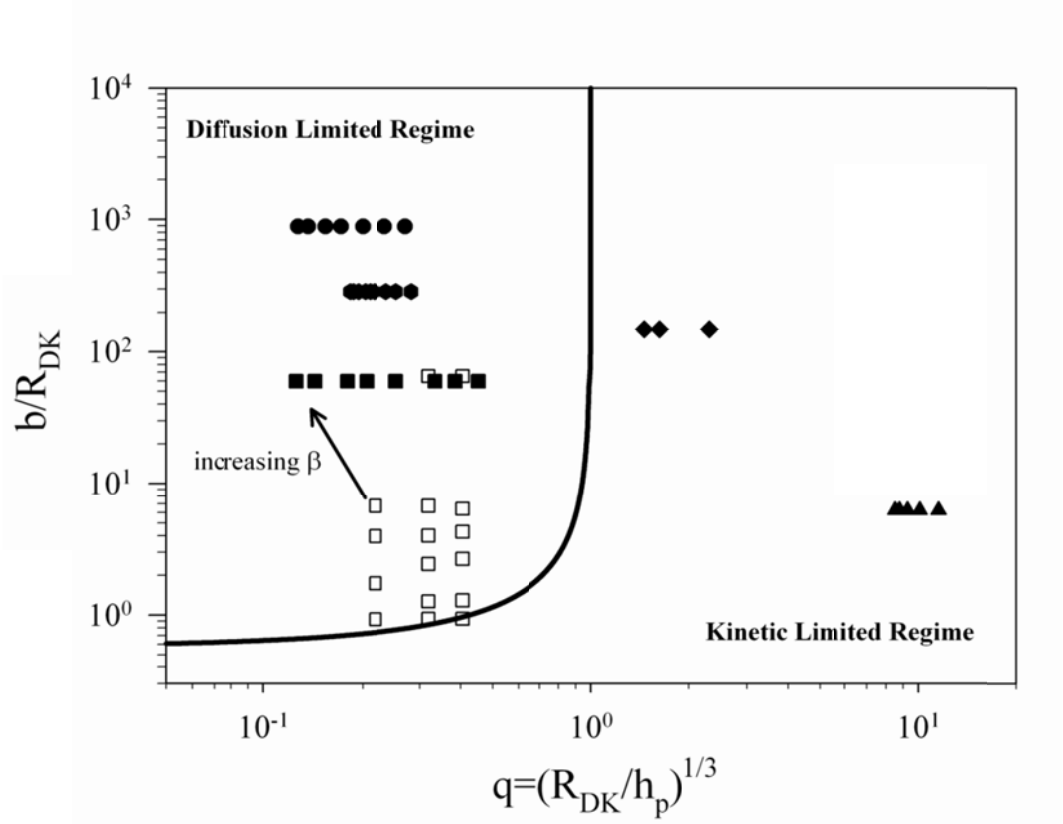

Figure 4.4. The effect of bubble radius and concentration on the governing transport of a soluble adsorbing species following Langmuirian kinetics. The line corresponds to equality of the diffusion time scale and the kinetic time scale. Diffusion-limited dynamics exist far to the left of the line and kinetic-limited dynamics exist far to the right of the line. The points correspond to data extracted from literature (filled symbols) or conducted with varying bubble size (open symbols). ▲ butanol ◆ hexanol ⬣ nonanol ● decanol ■ $C_{12}E_8(C_{bulk})$ and □ $C_{12}E_8(b)$

Among other surfactants, short chain alcohols exhibit kinetic-limited behavior in experiments since high concentrations are needed to achieve appreciable changes in surface tension [5, 24, 26]. We have plotted b/R_{DK} for four short chain alcohols in Figure 4.4, namely butanol, hexanol, nonanol, and decanol, using parameters and dynamic curves extracted from the literature, listed in Table 4.1. The placement of the data on Figure 4.4 suggests that butanol is the

most likely of the surfactants considered to exhibit kinetic-limited behavior. As the tail length increases, the short chain alcohols become more diffusion-limited (i.e. move further to the left of the equality line). From experiments reported in the literature, it is observed that butanol is completely kinetic-limited, while hexanol exhibits mixed dynamics [26]. Nonanol [22] and decanol [25] exhibit little or no observable kinetics. Fainerman and Miller later argued that short chain alcohols are completely governed by diffusion-limited dynamics at the concentrations tested [24]. However, based on the scaling arguments presented here, butanol and hexanol will not exhibit purely diffusion-limited dynamics. To better understand whether short chain alcohols exhibit diffusion-limited, mixed, or kinetic-limited dynamics we return to the spherical depletion depth scaling arguments.

Extracting experimental time scales from published data [24] and plotting in a similar way to the data shown in Figure 4.3, we can determine whether kinetics or diffusion control the dynamics. To compare both the kinetic and diffusion-limited time scales on the same plot, we scale the Langmuir kinetic time scale by the planar diffusion time scale, which leads to

$$\frac{\tau_k}{\tau_{Dp}} = \frac{R_{Dk}}{h_p} = q^3. \tag{4.15}$$

It is notable that this ratio of time scales is given by the same ratio of intrinsic surfactant length scales that defines the transition from diffusion to kinetic-limited transport (cf. Eqn (4.14)). Represented on a log-log plot as a function of b/h_p, Eqn (4.15) yields different functional forms depending on the type of experiment

performed. For fixed bubble size and varying concentration, Eqn (4.15) is a line with slope unity and intercept $I = \log\left(R_{DK}/b\right)$. For fixed concentration and varying bubble radius, Eqn (4.15) is a constant. To test the transition from the spherical diffusion scaling to the kinetic scaling, we used the spectral method to simulate mixed diffusion-kinetic dynamics, substituting Eqn (4.10) for Eqn (4.6) and using model surfactant parameters given in Table 4.1. The simulated time scales are shown in Figure 4.5, demonstrating that the transition in controlling mechanism occurs as expected for each of the two types of experiments described.

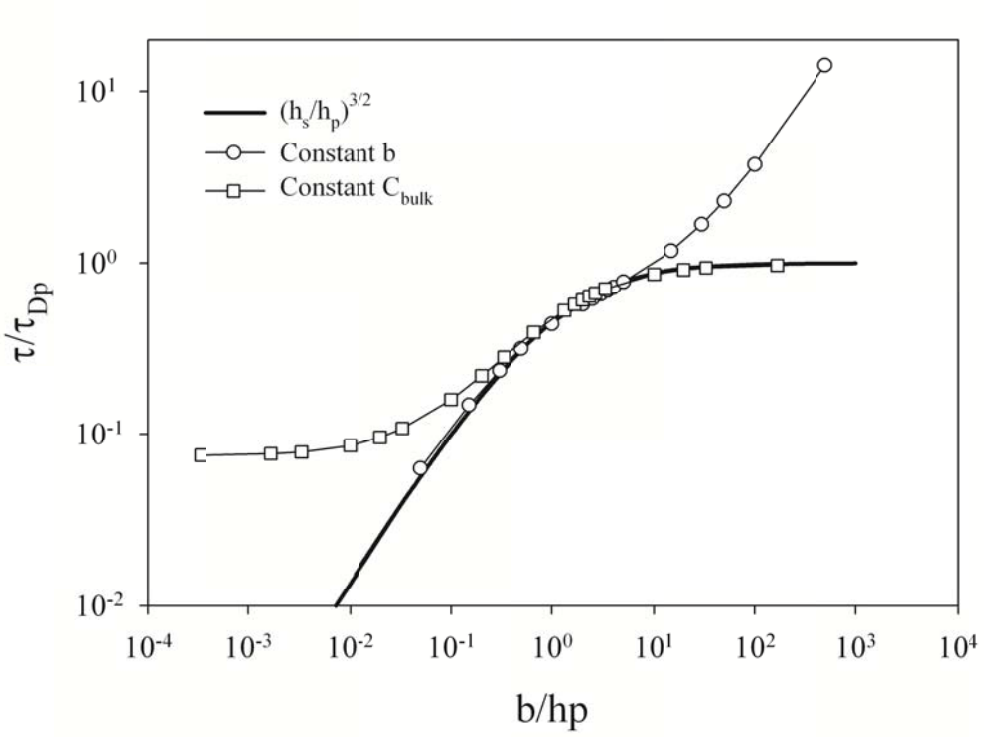

Figure 4.5 Diffusion and kinetic time scales, scaled with the planar depletion depth, as a function of b/h_p for short chain alcohols and $C_{12}E_8$ at the highest concentration for different radii. Butanol and hexanol follow the kinetic time scale, while $C_{12}E_8$ follows the diffusion-limited time scale. Note the difference in the transition to the kinetic time scale depending on whether concentration or bubble size varies.

Returning to the short-chain alcohols considered earlier, recall that the position of the points for both butanol and hexanol in Figure 4.4 indicated that the dynamics should follow the kinetic-limited and not the diffusion-limited scaling. Figure 4.6 shows the dimensionless time scales extracted from the reported dynamic surface tension curves [24]. It is clear from this figure that butanol and hexanol follow the kinetic-limited time scale. In fact, the time scales observed in the experiments are orders of magnitude larger than the diffusion-limited time scale. A kinetic-limited transport is the same result that was concluded by Joos and Serrien by fitting a simple exponential to dynamic surface tension data for both surfactants [26]. On the contrary, Fainerman and Miller concluded that butanol and hexanol show diffusion limited behavior through a short time scaling analysis. The short time scaling analysis is not sufficient to argue whether diffusion or kinetics dominate the transport dynamics. Instead the scaling analysis presented here should be followed.

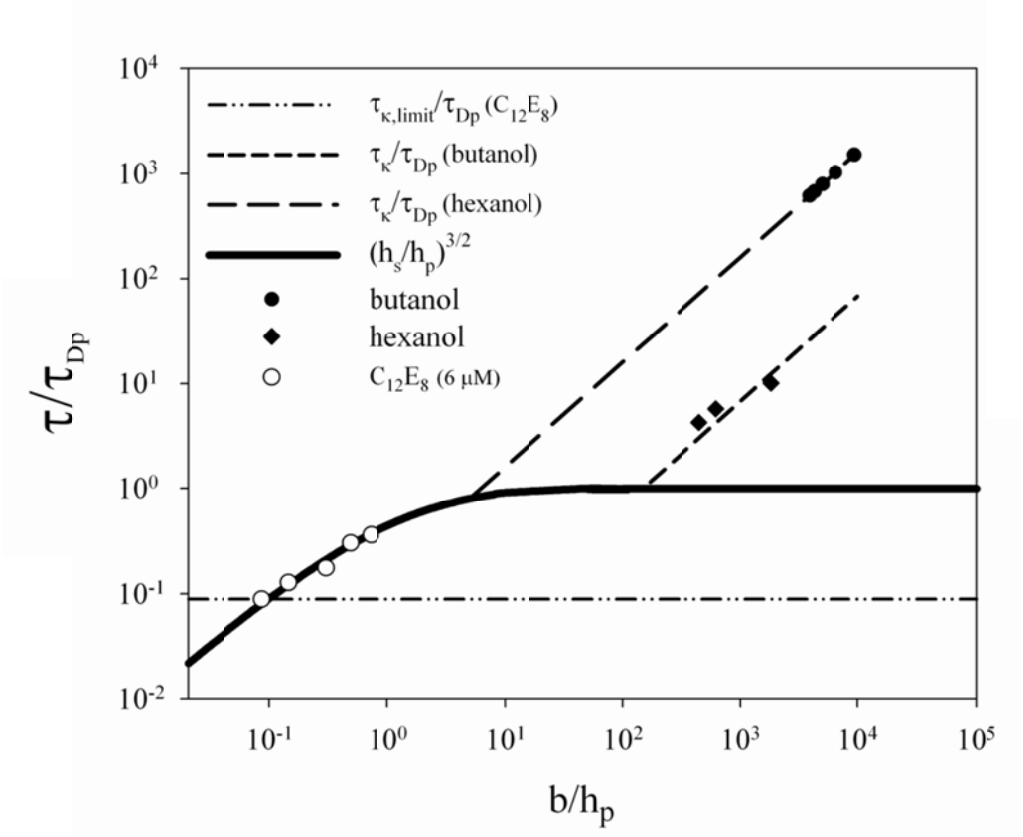

Figure 4.6. Characteristic time scale obtained from mixed kinetic-diffusion simulations (see Table 4.1 Model parameters) scaled by the planar diffusion time scale and plotted as a function of b/h_p. The two different experiments (fixing concentration or bubble radius) exhibit a different form of transition from kinetic-limited dynamics to diffusion-limited dynamics.

A similar analysis was performed on two longer chain alcohols, nonanol and decanol, which closely follow the diffusion-limited time scale at higher concentrations. These data are not shown in Figure 4.6 because deviations are observed at lower concentrations that cannot be due to kinetic or diffusion time scales and are more likely due to other phenomena such as convection [29], evaporation [24], or depletion of surfactant.

Figure 4.6 can also be used to provide physical limits on rate constants. Experiments performed for varying bubble radii at fixed concentration will

exhibit a constant characteristic time scales as the bubble size decreases and the dynamics transition to kinetically controlled. In other words, the kinetic time scale does not depend on the bubble size. For the entire range of bubble radii that we tested, we do not observe a transition to a constant characteristic time scale (cf. open symbols in Figure 4.6). Although we cannot obtain the precise value of the adsorption constant, β, without observing the transition to kinetic-limited dynamics, the limiting time scale corresponding to the smallest bubble radius can provide an upper limit on the kinetic time scale, and therefore, a lower bound on the adsorption rate constant.

The ratio of time scales for this data point yields the inequality $\tau_k / \tau_{Dp} < 0.096$, which leads to $\beta > 5.6$ m^3/(mol·s) through Eqn (4.15). Using the isotherm parameters listed in Table 4.1 along with this minimum value of the adsorption rate constant, we plot the $C_{12}E_8$ data on Figure 4.4. The scaled data appears on the diffusion-limited side of the $\Lambda = 1$ line. Since we used the limiting value of β, this data is forced to lie on the line where the two time scales are equivalent, as expected. The arrow in Figure 4.5 indicates the direction that the experimental points would shift with larger values of β. Note that even though $C_{12}E_8$ follows the Generalized Frumkin isotherm, using a Langmuirian assumption for the kinetic time scale yields qualitative agreement with our experimental observations and yields insight into possible limits on the adsorption rate constant, and subsequently, the desorption rate constant.

4.8 SUMMARY

In summary, we have determined the correct time scale to describe diffusion-limited transport to a spherical interface, which captures the effects of both radius and bulk concentration on the transport of species to the interface, and exhibits the appropriate asymptotic behavior in the limits of both large and small bubble size. The time scale is validated by numerical simulations and experimental data. The new scaling is used to demonstrate a method of analyzing the shift from diffusion-limited to kinetic-limited surfactant dynamics and assessing limiting values of the kinetic rate constants. For example, through a competitive time scale analysis we were able to show that butanol exhibits kinetic-limited behavior as previously suggested, and we have determined limits on the value of the adsorption rate constant for $C_{12}E_8$. In addition, we are able to quantitatively determine the dependence of the dynamics on kinetic transport. In the case of $C_{12}E_8$, the analysis presented suggests that surface kinetics play a less important role in the transport of the surfactant to an interface than previously thought.

Although the scaling analysis presented in this chapter is developed considering the case of surfactant adsorption to interfaces, this scaling applies generally to any physical problem where the flux condition at the spherical interface is solely governed by diffusion and there is no bulk convection. For example, these results could be used to explain why larger drug particles dissolve slower than smaller particles [31]. The simplicity of the scaling will allow more complex kinetic mechanisms to be considered, including the balance of diffusion and reaction in the rapidly growing field of heterogeneous catalysis at

nanoparticle interfaces. As we gain control of nanoscale and microscale interfaces in a wide variety of industrial processes, the elucidation of this fundamental scaling is crucial.

[1] S. Paria and K.C. Khilar, "A review on experimental studies of surfactant adsorption at the hydrophilic solid-water interface," Advances in Colloid and Interface Science, 110 (2004), 75-95.

[2] J. Eastoe and J.S. Dalton, "Dynamic surface tension and adsorption mechanisms of surfactants at the air-water interface," Advances in Colloid and Interface Science, 85 (2000), 103-144.

[3] F. Jin, R. Balasubramaniam, and K.J. Stebe, "Surfactant adsorption to spherical particles: The intrinsic length scale governing the shift from diffusion to kinetic-controlled mass transfer," Journal of Adhesion, 80 (2004), 773-796.

[4] H.S. Fogler, *Elements of chemical reaction engineering* (Prentice Hall PTR, Upper Saddle River, NJ, 2006).

[5] R.N. Pan, J. Green, and C. Maldarelli, "Theory and experiment on the measurement of kinetic rate constants for surfactant exchange at an air/water interface," Journal of Colloid and Interface Science, 205 (1998), 213-230.

[6] S.Y. Lin, H.C. Chang, and E.M. Chen, "The effect of bulk concentration on surfactant adsorption processes: The shift from diffusion-control to mixed kinetic diffusion control with bulk concentration," Journal of Chemical Engineering of Japan, 29 (1996), 634-641.

[7] S.L. Anna and H.C. Mayer, "Microscale tipstreaming in a microfluidic flow focusing device," Physics of Fluids, 18 (2006).

[8] D.L. Carter, et al., "Importance of dynamic surface tension to the residual water content of fabrics," Langmuir, 21 (2005), 10106-10111.

[9] Y.H. Kim, K. Koczo, and D.T. Wasan, "Dynamic film and interfacial tensions in emulsion and foam systems," Journal of Colloid and Interface Science, 187 (1997), 29-44.

[10] C. Stubenrauch and R. Miller, "Stability of foam films and surface rheology: An oscillating bubble study at low frequencies," Journal of Physical Chemistry B, 108 (2004), 6412-6421.

[11] A.F.H. Ward and L. Tordai, "Time-Dependence of Boundary Tensions of Solutions .1. The Role of Diffusion in Time-Effects," Journal of Chemical Physics, 14 (1946), 453-461.

[12] I. Langmuir, "The constitution and fundamental properties of solids and liquids. Part 1. Solids," Journal of the American Chemical Society, 38 (1916), 2221-2295.

[13] Y.Y. Wang, et al., "A study of interfacial dilational properties of two different structure demulsifiers at oil-water interfaces," Journal of Colloid and Interface Science, 270 (2004), 163-170.

[14] T. Bickel, "Hindered mobility of a particle near a soft interface," Physical Review E, 75 (2007).

[15] L.N. Trefethen, *Spectral methods in MATLAB* (Society for Industrial and Applied Mathematics, Philadelphia, 2000).

[16] K.J. Mysels, "Diffusion-Controlled Adsorption-Kinetics - General-Solution and Some Applications," Journal of Physical Chemistry, 86 (1982), 4648-4651.

[17] R. Miller and G. Kretzschmar, "Numerical-Solution for Mixed Model of Diffusion Controlled Adsorption," Colloid and Polymer Science, 258 (1980), 85-87.

[18] M.E. Cates, "Reptation of Living Polymers - Dynamics of Entangled Polymers in the Presence of Reversible Chain-Scission Reactions," Macromolecules, 20 (1987), 2289-2296.

[19] S.Y. Lin, K. Mckeigue, and C. Maldarelli, "Diffusion-Controlled Surfactant Adsorption Studied by Pendant Drop Digitization," AIChE Journal, 36 (1990), 1785-1795.

[20] N.J. Alvarez, L.M. Walker, and S.L. Anna, "A Microtensiometer To Probe the Effect of Radius of Curvature on Surfactant Transport to a Spherical Interface," Langmuir, 26 (2010), 13310-13319.

[21] S.Y. Lin, et al., "Adsorption kinetics of C12E8 at the air-water interface: Adsorption onto a clean interface," Langmuir, 12 (1996), 6530-6536.

[22] H.O. Lee, T.S. Jiang, and K.S. Avramidis, "Measurements of Interfacial Shear Viscoelasticity with an Oscillatory Torsional Viscometer," Journal of Colloid and Interface Science, 146 (1991), 90-122.

[23] S.Y. Lin, et al., "Surface equation of state of nonionic CmEn surfactants," Langmuir, 19 (2003), 3164-3171.

[24] R. Miller, V.S. Alahverdjieva, and V.B. Fainerman, "Thermodynamics and rheology of mixed protein-surfactant adsorption layers," Soft Matter, 4 (2008), 1141-1146.

[25] S.Y. Lin, T.L. Lu, and W.B. Hwang, "Adsorption-Kinetics of Decanol at the Air-Water-Interface," Langmuir, 11 (1995), 555-562.

[26] P. Joos and G. Serrien, "Adsorption-Kinetics of Lower Alkanols at the Air Water Interface - Effect of Structure Makers and Structure Breakers," Journal of Colloid and Interface Science, 127 (1989), 97-103.

[27] L. Liggieri, et al., "Measurement of the surface dilational viscoelasticity of adsorbed layers with a capillary pressure tensiometer," Journal of Colloid and Interface Science, 255 (2002), 225-235.

[28] R. Miller, et al., "Effect of the reorientation of oxyethylated alcohol molecules within the surface layer on equilibrium and dynamic surface pressure," Langmuir, 15 (1999), 1328-1336.

[29] S.N. Moorkanikkara and D. Blankschtein, "Possible Existence of Convective Currents in Surfactant Bulk Solution in Experimental Pendant-Bubble Dynamic Surface Tension Measurements," Langmuir, 25 (2009), 1434-1444.

[30] G. Bleys and P. Joos, "Adsorption-Kinetics of Bolaform Surfactants at the Air Water Interface," Journal of Physical Chemistry, 89 (1985), 1027-1032.

[31] M.T. Crisp, et al., "Turbidimetric measurement and prediction of dissolution rates of poorly soluble drug nanocrystals," Journal of Controlled Release, 117 (2007), 351-359.

CHAPTER 5

DESCRIPTION OF MICROTENSIOMETER, FLOW CELL, AND INTERFACIAL RHEOMETER

5.1 MICROTENSIOMETER APPARATUS

5.1.1 BACKGROUND

In a static drop or bubble suspended in a liquid at the end of a capillary tube, the capillary pressure jump across the interface is proportional to the local curvature of the interface and the surface tension. Hydrostatic pressure variations modify the force balance if the bubble is large enough. The Young-Laplace equation describes this normal stress balance,

$$p_i - p_o = (\rho_o - \rho_i) gh + \gamma \nabla \cdot n, \tag{5.1}$$

where p_i is the absolute pressure inside the bubble, p_o is the absolute pressure outside the bubble within the surfactant solution, ρ_i is the density of fluid inside the drop or bubble, ρ_o is the density of the surfactant solution, γ is the interfacial tension, g is the acceleration due to gravity, h is the z-position along the interface and $\nabla \cdot n$ is the curvature of the interface. For a spherical bubble, the curvature of the interface is constant, such that $\nabla \cdot n = 2/R$, where R is the radius of the sphere. If we scale Eqn (5.1) by normalizing the curvature by the inverse radius of the capillary tube, $1/R_C$, the interface position by the radius of the capillary tube, and the pressure by a characteristic capillary pressure, γ/R_C, we obtain the dimensionless expression,

$$\Delta \bar{p} = B_o \bar{h} + \nabla \cdot \bar{n}, \qquad (5.2)$$

where $B_o = \Delta\rho g R_C^2 / \gamma$ is the Bond number, which describes the relative importance of gravity compared with capillary forces. Eqn (5.2) shows that the interface shape is unique for a given value of the Bond number.

For a drop or bubble pinned at the end of a needle submerged in another fluid at moderate values of the Bond number, the interface shape is no longer spherical and depends only on $\Delta\rho$, $R_c = R_0$, the radius of curvature at the apex, and γ. If both $\Delta\rho$ and R_0 are known, then the only unknown is surface tension. The pendant drop technique, commonly used to measure surfactant dynamics for both initially clean interfaces and compressed or expanded interfaces, uses this principle to calculate the surface tension from digitally captured drop/bubble shapes [1-3]. For typical pendant bubble experiments $R_0 \approx 1.5$ mm and thus $B_o \approx 0.3$ for an air-water interface. This value of the Bond number is sufficient to perturb the bubble shape away from spherical but not sufficient to detach the bubble from the capillary. The Bond number is usually restricted to a value greater than 0.15 due to limitations of the fitting algorithms [4]. Even though a new algorithm has recently been documented that can accurately measure surface tension from drop shapes an order of magnitude below this limit [2], the range of bubble sizes (for an air-water interface) is no smaller than 600 μm using the pendant drop technique $B_o \approx 0.01$.

When the Bond number is small $B_o << 0.01$, gravitational forces do not strongly influence the interface shape, and the bubble remains nearly spherical,

$R_C = b$. In this case, Eqn (5.2) is simplified and the pressure jump across the bubble is given by

$$\Delta p = \frac{2\gamma}{b}, \tag{5.3}$$

where b is the radius of curvature. $B_o << 0.01$ when either the density of the inner and outer fluids are similar, common in oil-water systems, the radius of the interface is small (note the squared dependence of Bond number on radius). For a microscopic, clean air-water interface, where $b = 150$ μm, the value of $B_o = 0.003$ makes the first term in Eqn (5.2) negligible. At this value of B_o the interface is spherical and the pressure jump calculated using Eqn (5.3) for a clean air-water interface is $\Delta P = 973$ Pa. Measuring both the pressure jump across the interface and the radius of the spherical interface, the surface tension is calculated directly using Eqn (5.3). On the basis of these estimates we have custom-built a "microtensiometer" which allows the measurement of dynamic surface tension from direct measurements of the pressure jump across the interface and the radius of the interface.

The use of the Laplace equation (Eqn (5.3)) to measure surface tension is not a new concept. The maximum bubble technique measures the maximum pressure required to push a bubble from the tip of a capillary. Since the maximum pressure will occur when the radius of the interface is approximately the radius of the capillary, the radius at this pressure is known and the surface tension is calculated using Eqn (5.3) [5, 6]. The pressure derivative method uses a pressure transducer to measure the pressure jump across the interface and an independent

measure of the radius to compute the equilibrium interfacial tension between two pure fluids [7]. This method relies on multiple points taken at different radii of a growing drop to determine the interfacial tension. The growing drop technique uses the instantaneous radius of the drop and pressure jump across the interface to compute the interfacial tension using Eqn (5.3) [8]. Both the pressure derivative method and the growing drop method use a syringe pump to deliver a constant flow rate of the inner fluid. All these methods are applied to bubbles ranging from 0.3 to 2 mm in radius and have not assessed the dependence of dynamic surface tension on the curvature of the interface.

Other experiments have reported the measurement of dynamic surface tension and equilibrium surface tension using microscopic interfaces. For example, using a constant pressure, Lee *et al.* constrain a gas-liquid interface inside a tapered glass capillary [9]. A second glass capillary delivers a surfactant solution to the interface within the tapered glass capillary. By measuring the radius of the interface and knowing the applied pressure, the surface tension of the interface is determined from the Young-Laplace equation. The authors used this method to measure dynamic surface tension of phospholipids and qualitatively note differences compared with pendant drop measurements [9]. This observation motivated us to fully characterize the impact of radius of curvature on surfactant transport to interfaces. To date, no quantitative study of dynamic surface tension dependence on interface curvature has been performed. The confinement of the interface within the capillary complicates the modeling and characterization of the mass transport of surfactant species since the geometry is finite and depletion

effects may become important [10]. Microfluidic methods have also been developed to measure interfacial tension at microscale interfaces, but these methods require the presence of convective bulk flow, which also complicates modeling and characterization [11]. The microtensiometer used in this study considers a simpler geometry, that of a spherical cap immersed in a semi-infinite surfactant solution, and limits measurements to transport by diffusion only.

5.1.2 DESCRIPTION OF DEVICE

The key features of the microtensiometer apparatus are shown schematically in Figure 5.1. The sample cell is fabricated by permanently bonding parts (B), (C), and (D) using radio frequency ionizing plasma [12]. The capillary, (F), is then inserted into the prefabricated hole in (B) and is connected using polyethylene tubing to a three-way solenoid valve, (H). The pressure transducer (G) and pressure source (I) are also connected to the three-way valve. The sample cell is designed to fit squarely on a custom horizontal microscope stage. Parts (A) and (E) correspond to the condenser and objective of a Nikon T-300 inverted light microscope.

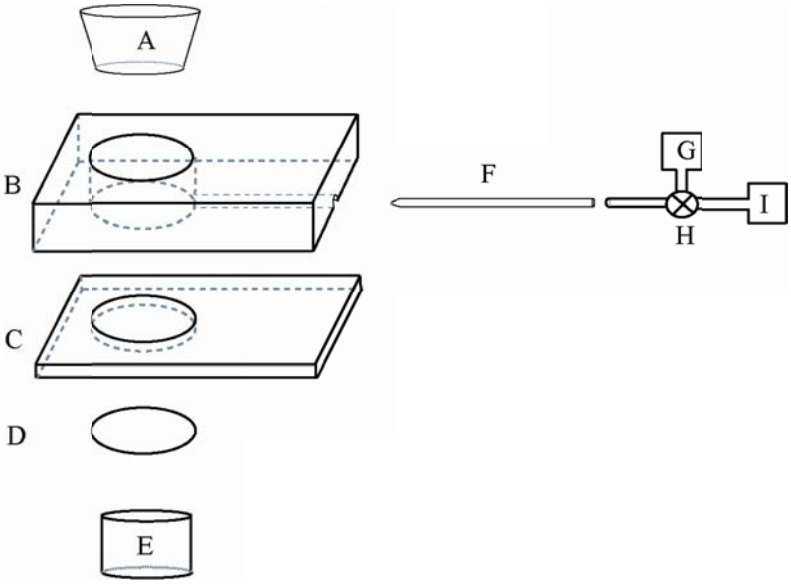

Figure 5.1. Schematic diagram of the microtensiometer apparatus. Parts include (A) microscope condenser, (B) PDMS well and holder, (C) PDMS spacer, (D) #1 cover slip, (E) objective and image analysis, (F) glass capillary, (G) pressure transducer, (H) 3-way solenoid valve, and (I) constant pressure head.

The sample cell (parts (B) – (D)) is simple and could be fabricated from essentially any material and the dimensions adjusted within some constraints. Cross-linked polydimethylsiloxane (PDMS) is chosen for parts (B) and (C) due to its availability and ease of use. The PDMS is fabricated using a standard kit containing liquid silicone and curing agent in a 10:1 ratio by mass (Dow Sylgard 184 PDMS Kit, purchased from Essex Brownell). The device is formed in a custom mold fabricated from epoxy resin. The overall length and width of part (B) is 2.5 x 1.5 inches and the depth is between 0.3-0.5 inches. The variation in depth allows for different solution volumes. The diameter of the well is 1.25 cm and the groove on the bottom is 1 mm in diameter. The dimensions of the well are chosen to ensure that adsorption of surfactant to solid-liquid interfaces (PDMS and glass) does not deplete enough surfactant to significantly reduce the bulk

concentration. Part (C) is a copy of part (B) except that the depth is between 1-3 mm and there is no groove. The depth of Part (C) is adjustable to ensure a semi-infinite solution volume surrounding the interface. Experiments are performed at different depths of the capillary until the dynamic response is observed to be independent of distance from the bottom glass cover slip (D). Part (D) is a #1 1-inch circular glass cover slip (Warner Instruments, Hamden, CT). The same type of cover slip is also used to cover the top of the cell during experiments to minimize the effects of evaporation and convection.

The capillary, (F), is either purchased or fabricated using custom settings on a P-80 capillary puller (Sutter Instrument Co., Novato, CA) or a PMP-100 capillary puller (Micro Data Instrument Inc., South Plainfield, NJ). Capillary diameters ranging from 12 to 300 μm are used in the experiments reported here. Capillaries used for pulling are thin-walled capillaries purchased from WPI Inc., (Sarasota, FL), with dimensions of I.D. = 0.75 mm, O.D. = 1 mm and L = 4 in. To avoid wetting issues the capillaries are cleaned by first submerging them in sulfuric acid and then rinsing with acetone. This process is repeated until an air bubble can be pinned at the edge of the capillary tip. The capillaries are also tested for axisymmetry by measuring the radius of a bubble suspended at the tip at different angles of rotation about the longitudinal axis of the capillary. Capillaries with excessive asymmetry, indicated by a difference in surface tension greater than 1 mN/m as a function of rotation, are discarded.

5.1.3 MEASURING SURFACE TENSION

The bubble or drop is suspended at the end of the capillary using a constant pressure head. The pressure head is generated using a column of water attached by polyethylene tubing to the three-way solenoid valve. The pressure head is measured using two strain-gauge pressure transducers: an Omega Model PX409-001GV for pressures up to 1 psi (6895 Pa) and a Cole Parmer Model EW-68075-10 for pressures up to 5 psi (34,474 Pa). The pressure transducers are calibrated using a water column with an accuracy of 0.063 in. of H_2O (15 Pa). The pressure readings are recorded using a National Instruments Fieldpoint Module AI-100.

The interface is imaged using a Diagnostic Instruments Spot RT Monochrome digital camera connected to the side port of the microscope. Nikon ELWD Plan Fluoro microscope objectives are used with magnifications of 10X, 20X, and 40X. The camera and optical setup are calibrated for all microscope objectives using a calibration slide with 10 μm graduations. The 10X, 20X and 40X objectives are measured to have calibration factors of 5.0 ± 0.09, 9.8 ± 0.2 and 19.4 ± 0.3 pixels/μm, respectively. The image is captured using a custom Labview subroutine and subsequently analyzed *in-situ* by fitting a circle to the extracted interface image. The National Instruments Vision toolbox is used for interface detection and fitting.

Pressure and radius are measured simultaneously and surface tension is calculated using

$$\gamma(t) = \frac{1}{2}\Delta P(t) R(t), \tag{5.4}$$

where $\Delta P(t)$ is the pressure jump across the interface. The pressure jump is computed by subtracting the hydrostatic pressure head of the solution acting at the capillary tip from the measured constant pressure head. The maximum frame rate and corresponding data acquisition rate is 6.5 frames/s. Although we are currently restricted to 6.5 frames/s, by using a high speed camera the data acquisition rate could be increased up to 100,000 frames/s. Bubbles can be formed on millisecond time scales in either the microtensiometer or a pendant drop apparatus; however, at the length scales of the pendant drop apparatus, this would lead to significant convection, complicating dynamic surface tension measurements[13]. The length scales in the microtensiometer apparatus should alleviate this problem. Therefore, the microtensiometer has the ability to measure sub-second dynamic surface tension, allowing for faster dynamics to be characterized.

The microtensiometer apparatus is validated using dynamic surface tension measurements of well-characterized pure fluid-fluid systems. For example, the measured surface tension at the interface of an air bubble in clean water is (73.2 ± 0.4) mN/m and that of an air bubble in clean ethanol is (22.7 ± 0.3) mN/m. The results given represent average values of several measurements taken as a function of time using capillaries of different radii (40 to 150 μm) at 20^{o}C. The reported values of the interfacial tension for both liquids are 72.9 and 22.4 mN/m [14] . The uncertainty in the calculated surface tension is less than

$\Delta\gamma < \pm 0.5\,\text{mN/m}$ for the two measured fluid-liquid pairs and represents the expected error for dynamic measurements involving surfactants.

Analysis of the propagation of errors shows that the largest random errors occur at the smallest (17 μm) and largest (150 μm) capillary radii. The uncertainty for the smallest capillaries is dominated by random errors associated with fitting the interface radius, while the random errors in the pressure measurement are most important for the largest capillaries. The estimated uncertainty for the smallest radius is ±0.2 mN/m. The estimated uncertainty for the largest radius is ±0.5 mN/m. Note that the measured experimental random error is similar to the error contributions estimated from propagation of error analysis, suggesting that there are no major contributions to error other than pressure and radius.

For this apparatus, because the bubble is maintained using a constant pressure head, the change in surface tension is primarily accounted for by a change in radius; the radius of the interface continuously changes in a dynamic experiment. The dynamics depend on radius and therefore to properly model the behavior observed in the experiments the changing radius must be taken into account. We account for this effect in numerical modeling that we will describe in a later section. The flow generated by the changing radius is neglected. The maximum velocity corresponding to the changing radius is estimated from experimental data and is less than $v_{max} < 1\times10^{-6}\,\text{m/s}$. The maximum velocity occurs at the apex of the spherical cap. This calculation is performed using the height equation for a spherical cap and the maximum velocity is estimated from

the change in height of the cap with time. The minimum velocity occurs at the fixed contact line where the bubble is pinned at the edge of the capillary tube. The experimental velocity reported above is estimated by tracking the height of the observed spherical interface as a function of time and then computing the derivative of the time-dependent height. The estimated velocities are small enough that we conclude convection effects due to changing radius are negligible.

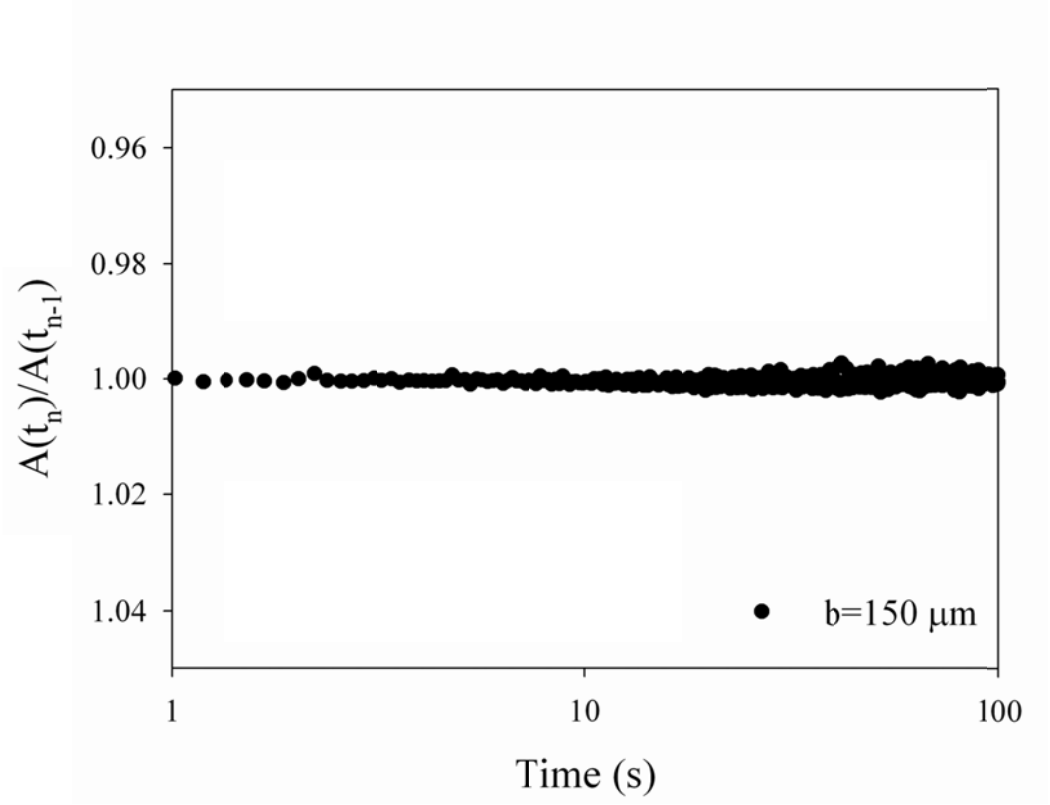

Figure 5.2. Ratio of change in area as a function of time for an dynamic surface tension experiment conducted on a 150 μm radius bubble and $C_{bulk} = 6.0\ \mu\text{M}$. The ratio is essentially unity for all times.

If the bubble radius continuously changes during an experiment, then so does the interfacial area. Experimental data are used to estimate whether the changing surface area significantly influences the evolution of the surface concentration. Figure 5.2 shows the ratio of the surface area at a given time to the surface area for the previous time step as a function of time for the capillary tip with the largest radius (150 μm) and a relatively large surfactant concentration (6.0 μM). The area is calculated using the equation for the surface area of a spherical cap pinned at the end of a capillary of fixed radius. The results shown in Figure 5.2 demonstrate that the change in area is less than 0.1% for any given time step. Therefore, even though the change in radius is taken into account

because diffusion to the interface depends on the magnitude of the interface radius, c.f. Eqn (4.8), we conclude that there is no appreciable effect on the surface concentration evolution, and the change in surface area is neglected in our theoretical analysis.

5.1.4 SUMMARY

This chapter depicts a microtensiometer apparatus for measuring dynamic and equilibrium surface tension at microscopic interfaces. The apparatus works on the principle of the Laplace equation and measures surface tension by simultaneously measuring pressure and interfacial radius. This device will be extensively used in this thesis to probe surfactant dynamics at the air-water and oil-water interface. The following two sections describe modifications to this device to allow for dynamic surface tension measurements in the presence of flow and for measurements of dilatational elasticity.

5.2 MICROTENSIOMETER WITH FLOW CELL CONFIGURATION

5.2.1 BACKGROUND

The microtensiometer apparatus described above is used to measure dynamic surface tension in the absence of bulk convection. This section describes the development of a flow cell configuration of the microtensiometer apparatus that allows for the measurement of surfactant dynamics in the presence of controlled laminar bulk convection. The concept behind this device is to use bulk convection to increase the rate of diffusion and expose kinetic limited dynamics, i.e. allow for the direct measurement of the kinetic rate constants of adsorption and desorption.

The number of studies that examine surfactant dynamics in the presence of bulk convection are limited [15, 16]. Svitova *et al.* measured dynamic surface tension using a pendant bubble apparatus, while mixing the external bulk solution. The device was used to examine the reversibility of low molecular weight nonionic and ionic surfactants (NP9 and CTAB) as well as large polymeric surfactants and proteins (Pluronic F108 and BSA) [16]. Fainerman *et al.* used the same configuration as that presented in Svitova *et al.* to measure dynamic surface tension of proteins HSA, BSA, BLG, and β-casein to an initially clean interface. The authors compare dynamic surface tension with forced convection with no forced convection. However, in neither case do the authors present a quantitative analysis of dependence of dynamic surface tension on bulk convection. In addition, Svitova *et al.* complain

The purpose of this chapter is to describe the components that make up the microtensiometer modified with a flow cell. Characterization of the flow field is presented using particle tracking velocimetry measurements.

5.2.2 DESCRIPTION OF THE FLOW CELL

The key features of the microtensiometer apparatus are shown schematically in Figure 5.3. The assembled sample cell (C) is the same described in Figure 5.1 with the exception two holes in the sidewalls of the PDMS chamber to allow for two 21-gauge needles (H) to be introduced to the bulk solution. The needles (H) are connected to a peristaltic pump (B) using polypropylene tubing. The capillary, (F) in Figure 5.1 (not shown in Figure 5.3) is inserted into the prefabricated hole in (C) and is connected using polyethylene tubing to a three-way solenoid valve (E). The pressure transducer (D) and pressure source (F) are also connected to the three-way valve. The sample cell is designed to fit squarely on a custom horizontal microscope stage. Parts (A) and (G) correspond to the condenser and objective of a Nikon T-300 inverted light microscope.

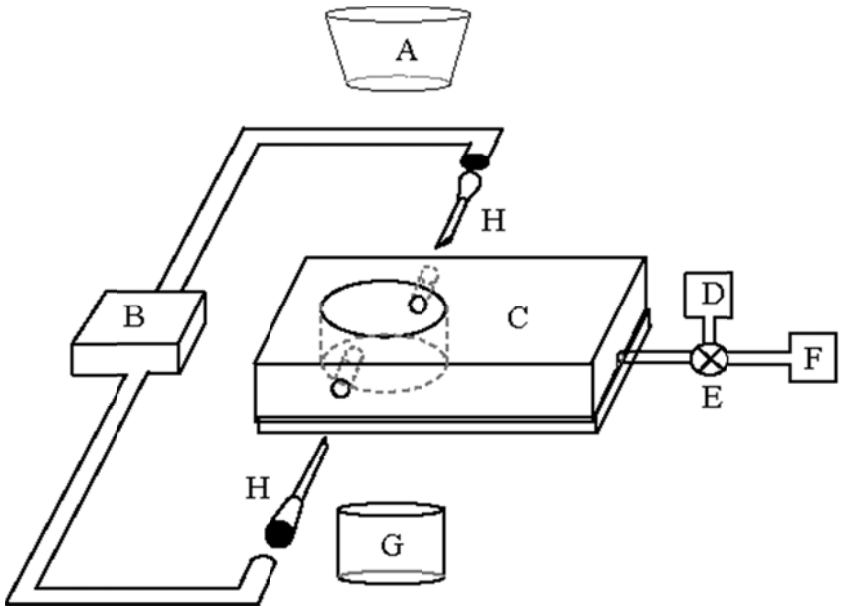

Figure 5.3 Schematic diagram of the microtensiometer apparatus setup for bulk convection. Parts include (A) microscope condenser, (B) peristaltic pump, (C) microtensiometer apparatus described in Figure 5.1, (D) Pressure Transducer, (E) 3-way solenoid valve, (F) constant pressure head, (G) objective and image analysis (H) 21-gauge needles.

The flow field is generated using a Cole-Parmer® (Vernon Hills, Illinois) peristaltic pump (B) Model 7553-30 with L/S-15 pump head Model 7015-20 and controller Model 7553-71 with silicone Masterflex® pump tubing (Cole-Parmer®) for pump head L/S-15. The silicone pump tubing is cut to a length of 10-15 inches and placed into the pump head. The inlet and outlet of the silicone tubing is connected to polypropylene tubing via luer-lock tubing connectors. The polypropylene tubing is connected to the two 21-gauge needles (H) with luer-lock tubing connectors. The pump can generate both forward and reverse flow. The pump is primed with clean DI water or a surfactant solution prior to connection to the needles in order to minimize air bubbles in the pump tubing. The presence of

air bubbles negatively impacts pump performance by introducing vibrations and oscillations in the sample cell volume. The vibrations complicate image analysis of the interface curvature and the oscillations in volume impact the hydrostatic pressure acting on the outside of the interface.

The pump has ten speed settings. Settings 1-5 were used for the experiments presented in Chapter 8. Settings above setting 6 caused the solution in the sample cell to splash out of the cell. The flow rate of the setup was determined by measuring mass of DI water collected in a given time with all components connected except the sample cell. This was done because the flow rate of a peristaltic pump depends on the resistance in tubing and connections. The density of water used was 996 kg/m^3. Figure 5.4 shows the dependence of volumetric flow rate on pump speed setting.

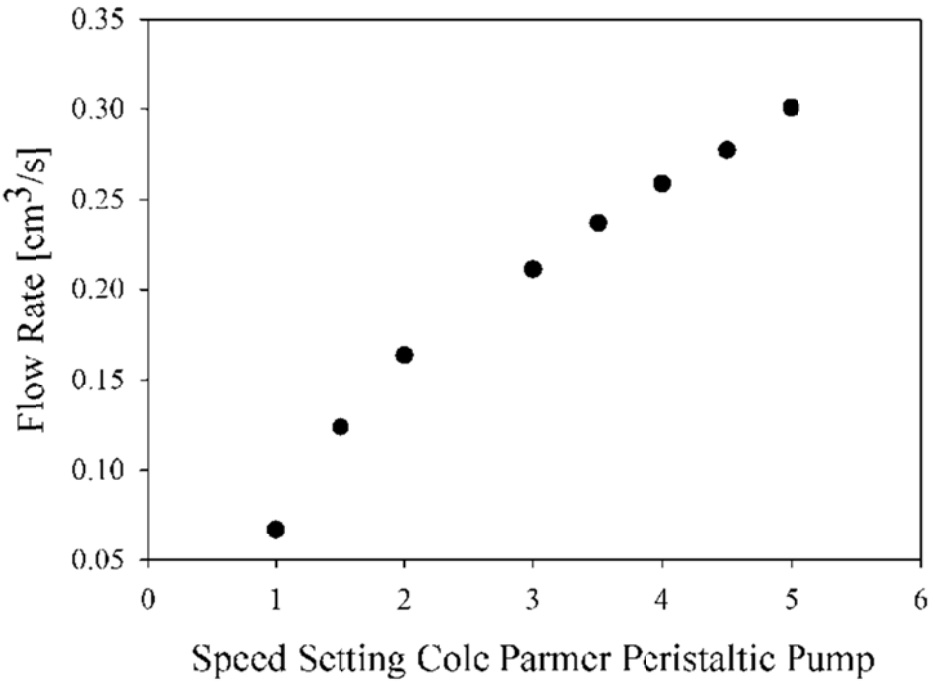

Figure 5.4. Flow rate as a function of speed setting for Cole Parmer peristaltic pump.

The velocity generated for a given pump flow rate was measured using particle tracking image analysis. The particle tracking analysis is described more in depth at the end of this section. Figure 5.5 shows measured particle velocities for different pump flow rates. Particle velocities at different locations inside the sample cell are presented. The velocities are characterized by a steady and unsteady regime. The steady regime is observed to be low Reynolds # unidirectional flow across the interface. The unsteady regime is characterized by changes in direction, i.e. accelerating and decelerating, of the flow field with some periodicity. This transition is most likely due to the high Reynolds number at high flow rates (velocities). There are two Reynolds numbers that can be defined for this system. The first is defined for the sample cell $\mathrm{Re}_C = \rho U_0 R_{S.C.} / \mu$,

where ρ is the density of the solution, U_0 is the far field velocity, $R_{S.C.}$ is the radius of the sample cell, and μ is the viscosity of the solution. This yields a critical $\mathrm{Re}_C = 762$. The second Reynolds number is defined for flow past the interface $\mathrm{Re}_i = \rho U_0 b/\mu = 1.98$ for the largest radius studied (185 μm). In this case the large Reynolds number in the sample cell causes the flow to become unsteady.

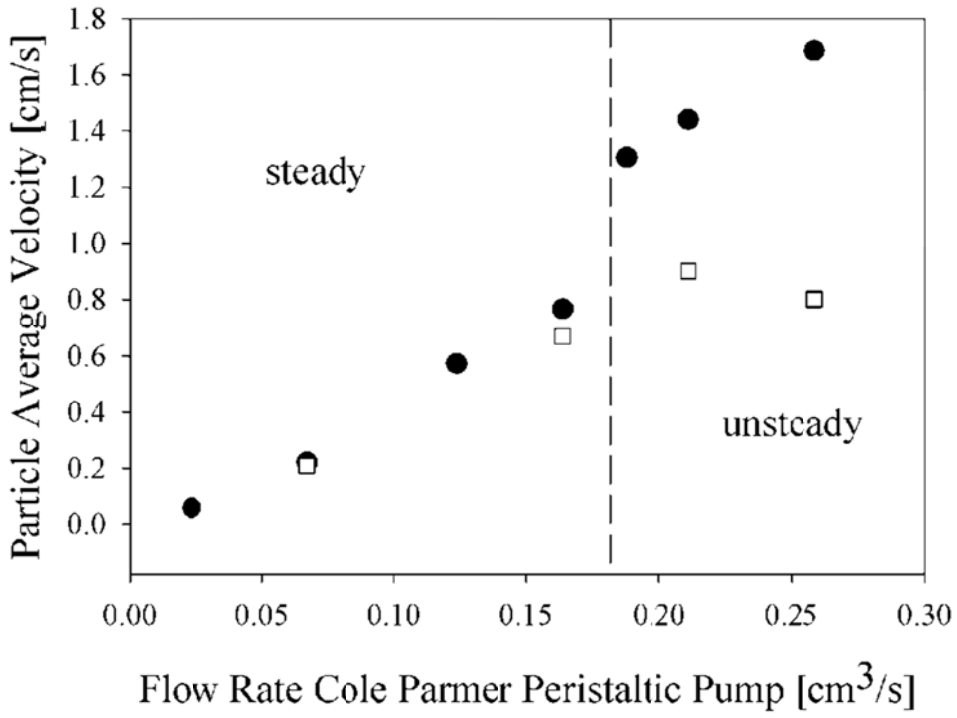

Figure 5.5. Particle Velocity as a function of pump flow rate. □ represent velocities measured near the bubble interface and ● represent velocities measured in the middle of the sample cell.

5.2.3 MEASURING SURFACE TENSION IN PRESENCE OF FLOW FIELD

Similar to the description in section 5.1.3, a bubble or drop is suspended at the end of the capillary using a constant pressure head. The pressure head is generated using a column of water attached by polyethylene tubing to the three-way solenoid valve. The pressure head is measured using an Omega Model PX409-001GV pressure transducer with a range of up to 1 psi (6895 Pa). The pressure transducer was calibrated using a water column with an accuracy of 0.063 in. of H_2O (15 Pa). The pressure readings are recorded using a National Instruments USB-6009 data acquisition module.

After all components in Figure 5.3 are attached and setup for viewing under the microscope, the sample cell (C) is filled with a solution to be measured. Before beginning any experiments, the pump in its slowest speed settings is run forward and then in reverse until all air bubbles are removed from needles. This is to prevent introduction of air bubbles into the pump tubing, which considerably alter performance. Once the lines are cleared the setup is ready for measurement. Dynamic surface tension is measured for different pump speed settings.

Dynamic surface tension is measured in the exact same way as explained in section 3.2 using Eqn (5.3). To ensure that the flow did not have a measureable impact on the pressure outside of the drop/bubble therefore impacting $\Delta P(t)$ in Eqn (5.3), measurements were made on deionized water to ensure that the flow does not impact the measurement on surface tension. Figure 5.6 shows surface tension as a function of time for a 30 μm radius interface in the presence of no bulk convection (filled symbol) and bulk convection induced by the peristaltic

pump with volumetric flow rate 0.32 cm^3/s (open symbol). It is clear from Figure 5.6 that the flow induced by the pump is not strong enough to alter the pressure jump across the interface. The surface tension of deionized water is unchanged whether the pump is running or whether the solution is stagnant.

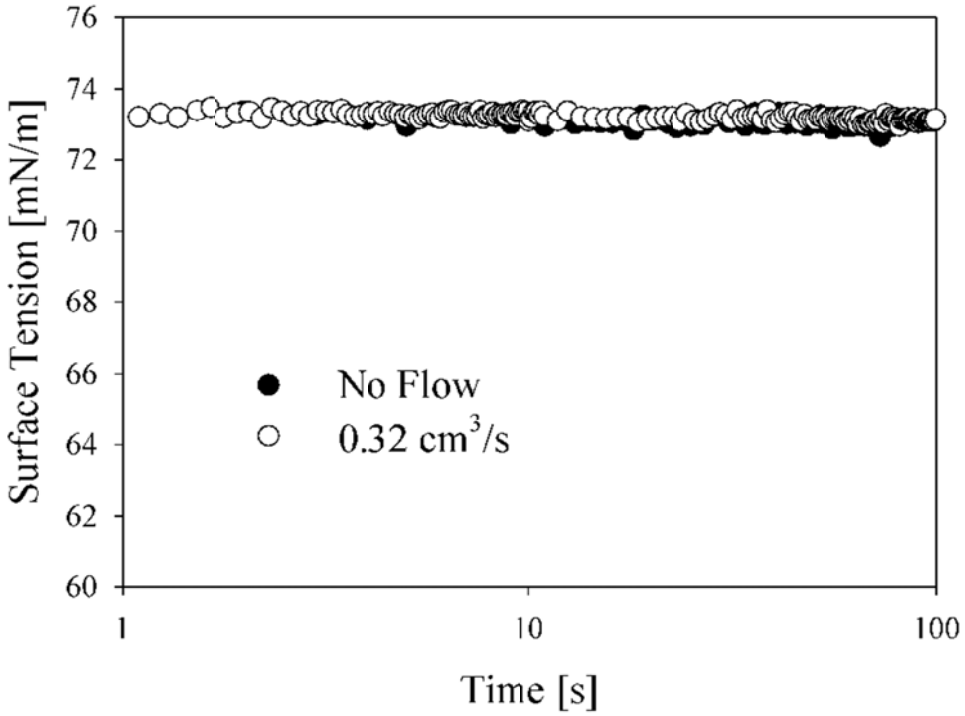

Figure 5.6. Surface tension as a function of time for a 30 μm radius bubble in the presence of no bulk convection and bulk convection induced by a volumetric flow rate of 0.32 cm^3/s.

The experimental protocol for measurements concerning surfactants was to prime the sample cell and tubing with a high concentration, near critical micelle concentration. It is important to prime the system with a solution below the cmc in order to use equilibrium surface tension to determine if the system has reached equilibrium. This was necessary because of the large surface area available for

the surfactant to adsorb. The pump was then left to mix the sample for 30 minutes to 1 hour. This was done to allow the walls plenty of time to reach equilibrium with the bulk surfactant concentration. The surface area to volume ratio is such that depletion of the bulk surfactant concentration is anticipated, c.f. Appendix. After the mixing period, multiple surface tension measurements were taken to ensure that the equilibrium surface tension value was no longer changing. If the equilibrium surface tension value was constant with time, then the system had reached equilibrium.

Once the system has reached equilibrium 2.5 ml of solution was removed from the sample cell and replaced with 2.5 ml of D.I. Water. The pump was used to mix the sample cell until equilibrium was achieved. Equilibrium was determined using surface tension measurements. Titration was repeated until the equilibrium surface tension, which correlates to a bulk surfactant concentration through the isotherm, was achieved. At this point, the system is at equilibrium and the bulk surfactant concentration will not be a function of time. Note that attempting to reach a stable bulk surfactant concentration by titrating the bulk concentration upwards requires a great deal of time: since depletion of the bulk surfactant concentration is drastic at low surfactant concentrations (see Appendix). For a given bulk surfactant concentration, dynamic surface tension measurements were made at various fluid velocities.

5.2.4 SUMMARY

This chapter depicts the setup and implementation of a microtensiometer modified with a flow cell. The velocity field is well characterized using particle

tracking image analysis. Also presented is a detailed procedure for conducting dynamic surface tension measurements in the presence of bulk convection. This apparatus will be used heavily in Chapter 8 to probe the kinetics of surfactant exchange at the air-water interface.

5.2.5 PARTICLE TRACKING

Two micron polystyrene particles were added to the flow cell in order to characterize the flow field. Measurements of particle speed at different locations in the flow cell were performed by recording particles moving at a fixed field of view in the flow field with a high speed camera (Phantom). Particle velocities were determined by image analysis. The images were analyzed using matlab versions of IDL code written by John C. Crocker and Eric R. Weeks converted by Daniel Blair and Eric Dufresne. A typical flow experiment is shown in Figure 5.7 using streak lines obtained by overlaying multiple images.

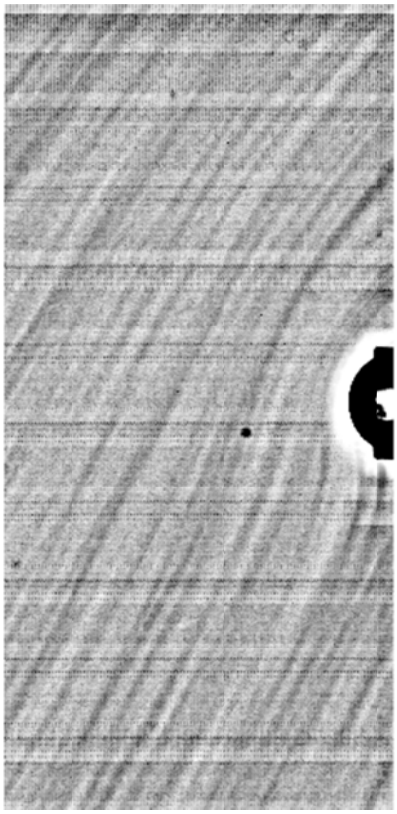

Figure 5.7. Steak lines of 2 μm polystyrene particles in the flow cell moving at ~0.01 m/s. Image is created by overlaying multiple frames and adjusting contrast between particle and background.

5.3 MICROTENSIOMETER AS AN INTERFACIAL RHEOMETER

5.3.1 BACKGROUND

There are two rheological properties of a fluid-fluid interface: interfacial shear viscosity and the dilatational or Gibbs elasticity [17]. The shear viscosity is measured by applying a rheological flow to the interface in an analogous fashion to that performed in bulk rheological measurements [9, 18-20]. In this measurement, the area of the interface is kept constant [17]. Dilatational elasticity measurements are made by measuring the change in stress due to a change in the surface area of the interface [17]. This section concentrates on the measurement of dilatational elasticity using the microtensiometer apparatus described in section 5.1.

A number of instruments have been developed to measure dilatational elasticity [9, 17, 21-24]. The first measurements were performed by Gibbs on soap films. Gibbs showed that the elasticity of a soap film is related to the change in surface pressure with a change in surface area of the interface. The Gibbs elasticity is defined as

$$E_G = 2\frac{\partial \gamma}{\partial \ln A}, \tag{5.5}$$

where γ is the surface tension and A is the surface area. The factor of two is because there are two interfaces for a soap film. For a bubble, the Gibbs elasticity is given by $E_G = \partial\gamma/\partial \ln A$.

The Gibbs elasticity is traditionally measured by imposing a sinusoidal oscillation to the surface area of a drop or bubble. The response in surface tension is recorded. If the strain is small, i.e. $\Delta A/A_0 << 0.10$, then Eqn (5.5) reduces to

$$E_G = \frac{\partial \gamma}{\partial \ln A} \approx \frac{\Delta \gamma}{\Delta A / A_0}, \tag{5.6}$$

where A_0 is the initial or mean area of the sinusoidal disturbance. This section depicts the construction of an attachment to the microtensiometer that facilitates sinusoidal oscillations of the interfacial area.

5.3.2 DESCRIPTION OF INTERFACIAL RHEOMOETER

A schematic of the microtensiometer is shown on the left side of Figure 5.8. The microtensiometer operates by applying a constant pressure head (5) to the end of a glass capillary (1), which is submerged in a cured PDMS sample cell (2). The applied pressure is measured with a pressure transducer (4). The radius is measured using a camera connected to a Nikon microscope with condenser (1) and 10x, 20x, and 40x objectives (9). The surface tension is measured by a simultaneous measurement of radius, b, and pressure jump, ΔP, across the interface of the fluid-fluid interface suspended at the tip of the capillary and the Laplace equation

$$\gamma(t) = \frac{\Delta P(t) b(t)}{2}. \tag{5.7}$$

The details of measuring surface and interfacial tension are discussed in section 5.1.3 [25].

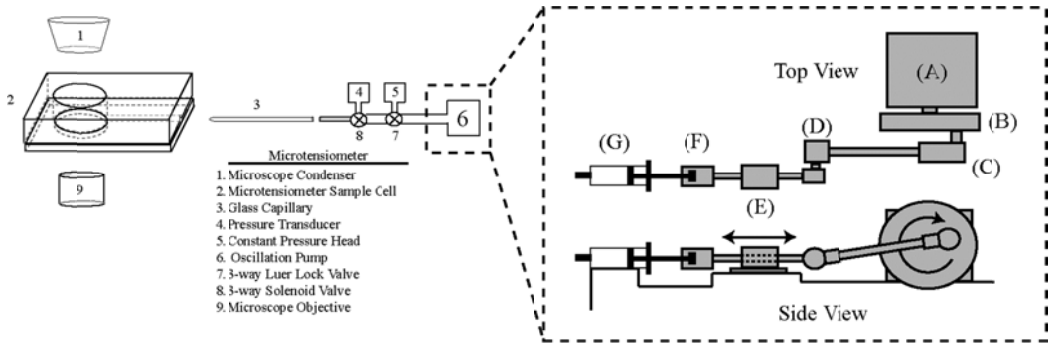

Figure 5.8. Sketch of oscillating apparatus. (A) Oriental DC motor Model , (B) Rotating wheel attached to motor axel, (C) Universal rod joint, (D), Universal joint, (E) PTFE lined pillow block, (F) Custom syringe plunger holder, (G) Syringe.

Once the interface has reached equilibrium, the luer lock valve (7) was switched from the constant pressure head (5) to the custom built oscillation pump (6). A sketch of the oscillation pump is shown on the left of Figure 5.8. The pump works by applying a voltage to a DC motor (Oriental Motors Inc.) Model AXHM230KC-GFH which through a series of universal joints and a pillow block applies a sinusoidal oscillation to a syringe filled with water (G) held in place by (F). The syringe applies a sinusoidal oscillation to the static pressure inside the tubing, which in turn causes the interface at the tip of the glass capillary to undergo oscillations in area. The amplitude of the sinusoidal pressure disturbance is determined by the inner bore diameter of the syringe and the placement of (C) from the center point of (B). Placement of (C) directly at the center of (B) corresponds to zero amplitude. Twice the distance of (C) to the center of (B) is the stroke length of the plunger.

5.3.3 MEASURING DILATATIONAL ELASTICITY

There are two types of devices that are predominately used to measure dilatational elasticity. One is based on a nonlinear fit of the Young-Laplace equation to the shape of a drop/bubble suspended at the end of a capillary tip to determine surface tension as a function of surface area, see Chapter 5, section 5.1 [26-28]. The other relies on the use of pressure transducers to measure capillary pressure and determine surface tension using the simpler Laplace equation [21]. In this apparatus, the oscillating bubble technique operates by imposing a sinusoidal volume change in a closed chamber.

The apparatus described in this section is most like that of Fruhner and Wantke, except that the interface is oscillated by applying a pressure oscillation to the inside phase. This eliminates many of the complications encountered when oscillating the outside volume, such as complicated relationships between pressure and surface tension. We apply a pressure oscillation of the form,

$$P_i = P_A \sin(\omega t) + P_{i0}, \tag{5.8}$$

where P_A is the induced amplitude of the pressure, P_i is the internal pressure of the drop/bubble interface, P_{i0} is the initial pressure inside the drop when the surface tension has reached equilibrium, and ω is the frequency of the oscillation. The change in pressure induces a change in the radius of the interface and the sinusoidal response of the radius is recorded,

$$b = b_A \sin(\omega t + \varphi) + b_0, \tag{5.9}$$

where b_A is the amplitude of the measured radius response, b_0 is the initial radius of the interface at equilibrium, φ is the phase angle between the radius and

pressure measurement. The change in area is determined using the equation for a spherical cap given by,

$$A = 2\pi b\left(b - \sqrt{b^2 - R_c^2}\right) = A_A \sin\left(\omega t + \varphi\right) + A_0 \text{ , or} \tag{5.10}$$

$$A = 2\pi\left(b_A \sin(\omega t + \varphi) + b_0\right)^2 \left(1 - \frac{\sqrt{\left(b_A \sin(\omega t + \varphi) + b_0\right)^2 - R_C^2}}{b_A \sin(\omega t + \varphi) + b_0}\right), \tag{5.11}$$

where R_c is the radius of the capillary tip, A_A is the amplitude of the measured area response, and A_0 is the initial area of the interface at equilibrium. The measured surface tension Eqn (5.4) becomes,

$$\gamma(t) = \frac{\Delta P(t) b(t)}{2} = \frac{\left(P_A \sin(\omega t) + P_{i0} - P_h\right)\left(b_A \sin(\omega t - \varphi) + b_0\right)}{2}, \text{ or} \tag{5.12}$$

$$\gamma(t) = \gamma_A \sin(\omega t) + \gamma_{eq}, \tag{5.13}$$

where P_h is the hydrostatic pressure outside the interface, γ_A is the amplitude of the measured response in surface tension, and γ_{eq} is the equilibrium surface tension. Finally, the dilatational modulus is determined by the ratio of the measured amplitude in surface tension to the amplitude in area or

$$\varepsilon = A_0 \frac{\Delta\gamma}{\Delta A} = A_0 \frac{\gamma_A}{A_A} \tag{5.14}$$

[1] Y. Rotenberg, L. Boruvka, and A.W. Neumann, "Determination of Surface Tensions and Contact Angles from the Shape of Axisymmetric Interfaces," Journal of the American Oil Chemists Society, 59 (1982), A297-A297.

[2] N.J. Alvarez, L.M. Walker, and S.L. Anna, "A non-gradient based algorithm for the determination of surface tension from a pendant drop: Application to low Bond number drop shapes," Journal of Colloid and Interface Science, 333 (2009), 557-562.

[3] S.Y. Lin, K. Mckeigue, and C. Maldarelli, "Diffusion-Controlled Surfactant Adsorption Studied by Pendant Drop Digitization," AIChE Journal, 36 (1990), 1785-1795.

[4] F. Jin, R. Balasubramaniam, and K.J. Stebe, "Surfactant adsorption to spherical particles: The intrinsic length scale governing the shift from diffusion to kinetic-controlled mass transfer," Journal of Adhesion, 80 (2004), 773-796.

[5] S. Sugden, "The determination of surface tension from the maximum pressure in bubbles," Journal of the Chemical Society, 121 (1922), 858-866.

[6] S. Sugden, "The determination of surface tension from the maximum pressure in bubbles Part II," Journal of the Chemical Society, 125 (1924), 27-31.

[7] A. Passerone, et al., "A New Experimental-Method for the Measurement of the Interfacial-Tension between Immiscible Fluids at Zero Bond Number," Journal of Colloid and Interface Science, 146 (1991), 152-162.

[8] C.A. Macleod and C.J. Radke, "A Growing Drop Technique for Measuring Dynamic Interfacial-Tension," Journal of Colloid and Interface Science, 160 (1993), 435-448.

[9] H.O. Lee, T.S. Jiang, and K.S. Avramidis, "Measurements of Interfacial Shear Viscoelasticity with an Oscillatory Torsional Viscometer," Journal of Colloid and Interface Science, 146 (1991), 90-122.

[10] L.K. Filippov and N.L. Filippova, "Dynamic surface tension and adsorption kinetics in finite systems," Journal of Colloid and Interface Science, 187 (1997), 352-362.

[11] J.D. Martin and S.D. Hudson, "Mass transfer and interfacial properties in two-phase microchannel flows," New Journal of Physics, 11 (2009), 115005.

[12] D.C. Duffy, et al., "Rapid prototyping of microfluidic systems in poly(dimethylsiloxane)," Analytical Chemistry, 70 (1998), 4974-4984.

[13] S.N. Moorkanikkara and D. Blankschtein, "Possible Existence of Convective Currents in Surfactant Bulk Solution in Experimental Pendant-Bubble Dynamic Surface Tension Measurements," Langmuir, 25 (2009), 1434-1444.

[14] A.W. Adamson and A.P. Gast, *Physical chemistry of surfaces* (Wiley, New York, 1997).

[15] R. Miller, V.S. Alahverdjieva, and V.B. Fainerman, "Thermodynamics and rheology of mixed protein-surfactant adsorption layers," Soft Matter, 4 (2008), 1141-1146.

[16] T.F. Svitova, M.J. Wetherbee, and C.J. Radke, "Dynamics of surfactant sorption at the air/water interface: continuous-flow tensiometry," Journal of Colloid and Interface Science, 261 (2003), 170-179.

[17] D.A. Edwards, H. Brenner, and D.T. Wasan, *Interfacial transport processes and rheology* (Butterworth-Heinemann, Boston, Mass., 1991).

[18] J.Q. Ding, et al., "Magnetic needle viscometer for Langmuir monolayers," Langmuir, 18 (2002), 2800-2806.

[19] W.E. Ewers and R.A. Sack, "A New Surface Viscometer," Nature, 168 (1951), 964-964.

[20] A.R. Deemer, et al., "Measuring Liquid-Liquid Interfacial Behavior with the Deep-Channel Surface Viscometer," Journal of Colloid and Interface Science, 78 (1980), 87-99.

[21] H. Fruhner and K.D. Wantke, "A new oscillating bubble technique for measuring surface dilational properties," Colloids and Surfaces A-Physicochemical and Engineering Aspects, 114 (1996), 53-59.

[22] R.L. Kao, et al., "Measurement of the Dynamic Interfacial-Tension and Interfacial Dilatational Viscosity at High-Rates of Interfacial Expansion Using the Maximum Bubble Pressure Method .2. Liquid-Liquid Interface," Journal of Colloid and Interface Science, 148 (1992), 257-260.

[23] L. Liggieri, et al., "Measurement of the surface dilational viscoelasticity of adsorbed layers with a capillary pressure tensiometer," Journal of Colloid and Interface Science, 255 (2002), 225-235.

[24] D.A. Edwards and D.T. Wasan, "Surface Rheology .3. Stress on a Spherical Fluid Surface," Journal of Rheology, 32 (1988), 473-484.

[25] N.J. Alvarez, L.M. Walker, and S.L. Anna, "A Microtensiometer To Probe the Effect of Radius of Curvature on Surfactant Transport to a Spherical Interface," Langmuir, 26 (2010), 13310-13319.

[26] G. Enhorning, "Pulsating Bubble Technique for Evaluating Pulmonary Surfactant," Journal of Applied Physiology, 43 (1977), 198-203.

[27] S.Y. Park, et al., "Dynamic Surface-Tension Behavior of Hexadecanol Spread and Adsorbed Monolayers," Langmuir, 9 (1993), 3640-3648.

[28] K. Lunkenheimer, et al., "Investigations on the Method of the Radially Oscillating Bubble," Colloids and Surfaces, 8 (1984), 271-288.

CHAPTER 6

AN EXPERIMENTAL STUDY ON THE EFFECT OF CURVATURE ON SURFACTANT TRANSPORT TO A SPHERICAL INTERFACE

6.1 INTRODUCTION

As discussed in chapters 4 and Appendix, when the interface is curved, as for a spherical bubble, the characteristic time scale for diffusion-limited adsorption depends on the interface curvature. This is because the ratio of the bubble surface area to the volume surrounding the bubble decreases with decreasing radius. In other words, there are more molecules per unit area available for adsorption near a spherical interface than for a planar interface. This increases the rate of mass transfer to the sphere (i.e. reduces the time scale for diffusion). In Chapter 4, we showed that the correct time scale governing diffusion to a spherical interface is a nonlinear function of the spherical depletion depth, h_s, and the planar intrinsic length scale, $h_p = \Gamma_{eq} / C_{bulk}$,

$$\tau_{Ds} = \frac{\left(h_s^3 h_p\right)^{\frac{1}{2}}}{D}, \tag{6.1}$$

where D is the diffusion coefficient of the molecule and h_s is given by,

$$h_s = b\left(\left(\frac{3h_p}{b}+1\right)^{\frac{1}{3}} - 1\right), \tag{6.2}$$

where b is the bubble radius [1, 2]. The planar diffusion time scale is given by,

$$\tau_{Dp} = \frac{h_p^{\,2}}{D}. \qquad (6.3)$$

The spherical time scale approaches the planar time scale at large bubble radii and also at large concentrations (i.e. the right-hand side of Eqn (6.2) approaches h_p at large radii). The dependence of diffusive transport on interfacial curvature suggested in Eqn (6.1) was only recently confirmed experimentally [2]. Prior to the introduction of this scaling analysis, there has been no systematic study on the dependence of interfacial dynamics on interfacial curvature.

The principal aims of this chapter are to quantitatively validate the dependence of dynamic surface tension on the curvature of the interface. The surfactant chosen for this study is $C_{12}E_8$, a well-characterized nonionic surfactant [3-5]. Two types of experiments are conducted with the microtensiometer described in section 5.1: dynamic surface tension measurements to an initially clean interface and to a suddenly compressed or expanded interface. The dynamic surface tension measurements are interpreted in the context of the time scale for diffusion to a spherical interface and two transport models.

6.2 EXPERIMENTS

The microtensiometer apparatus is described in detail in Chapter 5. Two types of experiments are conducted using the microtensiometer apparatus. The first experiment measures the evolution of surface tension for an initially clean interface $\Gamma_i = 0$ mol/m^2. We interpret the change in surface tension as the result of surfactant populating the interface from the bulk solution. For this experiment air is passed through the needle at a relatively large flow rate to purge any

adsorbed surfactant from the interface. The flow is then stopped and the interface is held at constant pressure while the interface radius is measured as a function of time. The second experiment measures the evolution of surface tension of an interface that is instantaneously expanded or compressed after reaching equilibrium. We interpret the change in surface tension in this case as a re-equilibration of the surface concentration with the bulk surfactant concentration. A solenoid valve is used to subject the interface to a different pressure head, which leads the interface to expand if the pressure is increased or to compress if the pressure is decreased (c.f. Eqn (5.3)). The surface tension is monitored from the instant that the step change in surface area is applied until equilibrium is re-established.

The primary goal of this chapter is to determine the dependence of dynamic surface tension on interfacial radius in the absence of convection and to make a comparison with documented measurements on large radius bubbles [3-9]. Table 6.1 shows literature values of parameters for two isotherms: the generalized Frumkin and reorientation isotherms [3, 9-12].

Generalized Frumkin Isotherm [3, 7]		**Reorientation Isotherm [6]**	
$\boldsymbol{\Gamma_\infty}$ **(10^{-6}) [mol/m^2]**	5.3	$\boldsymbol{\omega_1}$**(10^5) [m^2/mol]**	10.0
a **(10^{-6}) [mol/m^3]**	2.33	$\boldsymbol{\omega_2}$**(10^5) [m^2/mol]**	3.42
κ	13.2	**b_o(10^3) [m^3/mol]**	2.34
n	0.503	**α_o**	2.75

Table 6.1. Literature parameters for $C_{12}E_8$ for the Generalized Frumkin and reorientation isotherms at 25°C.

The concentrations presented in this chapter were determined from the isotherm and equation of state using equilibrium surface tension data (see Chapter 2). This is due to the fact, c.f. Appendix, that the specific concentrations that were prepared for the purpose of this discussion were depleted to the walls of the 100 ml volumetric flasks used to store the surfactant solutions, i.e. the value of $3V/\left(h_p A\right) < 10$ (c.f. Appendix). Note that this is why the concentrations do not agree with those presented in the original Langmuir manuscript [13].

6.3 NUMERICAL ANALYSIS

Surfactant transport is modeled as described in Chapter 3 for surfactant transport to the surface of a curved interface from a semi-infinite bulk. Two isotherm models are used in the comparison of dynamic surface tension for different radii of curvature: the generalized Frumkin isotherm and the reorientation isotherm [10]. As explained in the experimental section, the bubble undergoes a change in radius with time during an experiment since pressure is kept relatively constant during a dynamic surface tension measurement. The

dynamics are highly dependent on curvature and this changing radius should be accounted for to correctly model the experimental data. The experimental pressure data are introduced in the numerical solution in order to accomplish this. First, a spline curve is fit to the measured transient pressure data. Then the numerical calculation is initiated using the initial radius of the experiment, and the surface tension is calculated at the subsequent time step, t_n. The resulting surface tension coupled with the corresponding pressure interpolated at the given time step, t_n, is used to calculate the radius, b, at the current time step. This radius is then used to calculate the surface concentration at the next time step, t_{n+1}. This process is repeated until the surface tension reached equilibrium or the loop is terminated at a specified time. The numerical analysis presented here will be compared to our experimental results.

6.4 RESULTS

Relaxation of surface tension with time due to adsorption of $C_{12}E_8$ is measured using the microtensiometer for an initially clean air-water interface and the results are shown in Figure 6.1. Figure 6.1a shows the surface tension evolution as a function of time for a fixed C_{bulk} = 0.6 μM (0.6% CMC) and different capillary radii: b = 17, 30, 45, 70, 130 μm, and a pendant bubble (b~1.5 mm). Note that the radius of the capillary, since the radius of the interface is a function of pressure. Pendant bubble measurements are taken using a separate device (c.f. Chapter 3) [14]. Clean bubbles are formed by pushing a steady stream of air out of the capillary so that all dynamic surface tension curves start at

the clean interfacial tension value for air and water, γ_0 = (73.2 ± 0.25) mN/m, and decrease to an equilibrium surface tension value of γ_{eq} = (62.4 ± 0.3) mN/m. The radius of the pendant bubble is approximately 1200 μm. Both devices yield the same equilibrium surface tension values, to within the expected uncertainty observed in our experiments. The time scales for reaching equilibrium change significantly with bubble radius. As bubble radius decreases, the dynamics become faster and the time to reach equilibrium is reduced. For example, it takes approximately 1000 seconds for the surface tension to reach the halfway point (68 mN/m) in the pendant bubble apparatus, and only 50 seconds to reach the same point for the 17 μm radius microtensiometer experiments.

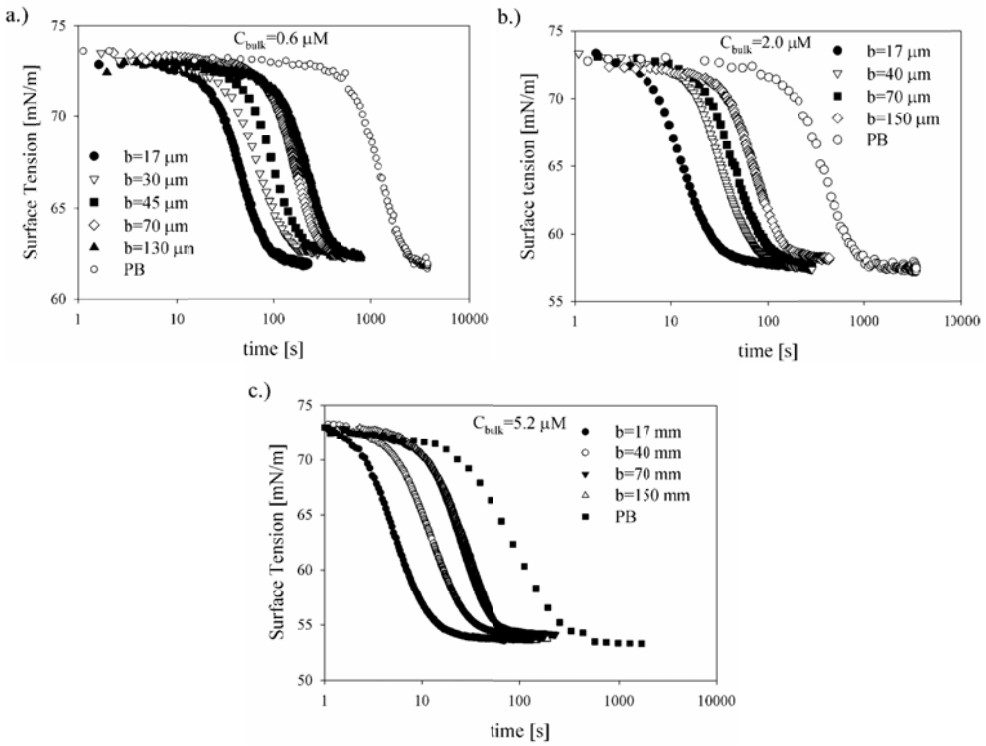

Figure 6.1. Surface tension as a function of time for different radii of curvature at fixed surfactant concentrations. a.), b.), and c.) correspond to experiments at bulk concentrations of 0.6, 0.20, and 5.2 μM, respectively. PB refers to pendant bubble experiments.

Figure 6.1b shows the surface tension as a function of time for C_{bulk} = 2.0 μM (2.0% CMC) measured at capillary radii o f b = 17, 40, 70, 150 μm, and a pendant bubble. As before, the curves begin at the clean interfacial tension value and decrease to an equilibrium value of γ_{eq} = (57.8 ± 0.3) mN/m. Comparing Figure 6.1a to Figure 6.1b, it is observed that the equilibrium surface tension decreases as the bulk concentration increases, as expected. In addition, the dynamics become faster as concentration increases. Figure 6.1c shows the surface tension as a function of time for C_{bulk} = 5.2 μM (5.2% CMC) measured at capillary radii of b = 17, 40, 70, 150 μm, and a pendant bubble. The equilibrium surface tension value for this concentration is γ_{eq} = (53.8 ± 0.3) mN/m. It is evident Figure 6.1a-c that the surface tension evolves significantly faster for bubbles tens of micrometers in diameter compared with millimeter-scale bubbles. The equilibration time is reduced by an order of magnitude from the largest radius, 1200 μm, to the smallest radius, 17 μm.

By allowing the interface to achieve equilibrium and then rapidly increasing or decreasing the interfacial area, the relaxation of surface tension due to a perturbation about the equilibrium surface concentration is probed. Figure 6.2 shows the relaxation of the normalized surface tension,

$$\theta = \left(\gamma(t) - \gamma_{eq}\right) \Big/ \left(\gamma_0 - \gamma_{eq}\right). \tag{6.4}$$

The expansion experiments correspond to positive displacements from equilibrium, while the compression experiments correspond to negative displacements. Expansion of the interface results in a reduced surface concentration since the area of the interface increases while the number of

adsorbed molecules stays the same. The opposite is true for compression experiments, where the area decreases and the number of molecules stays the same. Three bulk concentrations are shown in the figure, corresponding to C_{bulk}= 0.4, 2.0, and 5.0 μM from left to right for both expansion and compression experiments. A wide range of experiments are conducted at various bubble radii and surfactant concentrations. The results shown here are experiments conducted at a fixed expansion and compression ratio. The radii used for the expansion experiments are 22, 38, and 38 μm from left to right; for compression 24, 45, and 24 μm from left to right. For the fixed radius expansion and compression experiments performed at 38 μm and 24 μm respectively, as concentration decreases the relaxation of surface tension is slower for both types of experiments, so that the curves shift to the right as concentration decreases. For the expansion experiments the change in surface area is A_0/A = 0.833, 0.832, and 0.827 respectively. The compression area ratios are A_0/A = 1.27, 1.25, and 1.23 respectively.

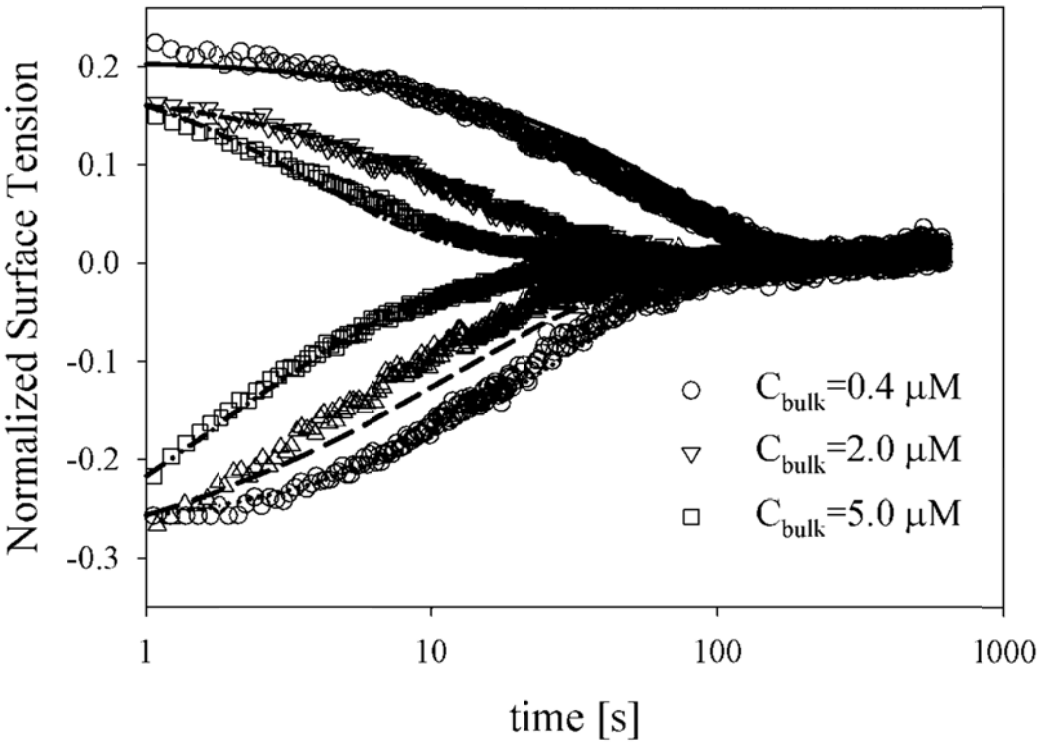

Figure 6.2. Normalized compression/expansion experiments for different concentrations and bubble radii. Compression experiments correspond to a relaxation from a negative normalized surface tension and expansion experiments correspond to positive values. The bulk surfactant concentration corresponding to each curve from left to right are C_{bulk}= 0.4, 2.0, and 5.0 μM. The expansion experiments correspond to a change in surface area of A_0/A = 0.833, 0.832, and 0.827 from left to right. The compression area ratios are A_0/A = 1.27, 1.25, and 1.23 from left to right. The lines correspond to model predictions. The molecular diffusion coefficient, $D = 3.8\times10^{-10}$ m^2/s and the Generalized Frumkin isotherm are used for these predictions.

This new apparatus is successfully used to measure the dependence of surfactant dynamics on bubble radius for initially clean interface dynamics as well as measure dynamic re-equilibration after a sudden expansion or compression. The initially clean interface measurements show a strong dependence of surfactant dynamics on radius of curvature. Namely, as radius decreases, the equilibration time decreases. There is good agreement between the equilibrium

surface tension values obtained with the microtensiometer and the pendant bubble apparatus. However, the microtensiometer uses significantly less volume than the pendant bubble and equilibrium is reached more rapidly.

Characteristic time scales for each dynamic surface tension experiment are shown in Figure 6.3. For each experiment, the time corresponding to a given surface coverage $\phi = \Gamma/\Gamma_{eq}$ is extracted from the data shown in Figure 6.1a-c. The open symbols correspond to a surface coverage of $\phi = 0.6$ and the closed symbols to $\phi = 0.1$. The experiment time is normalized by the characteristic time for diffusion to a planar interface (Eqn (6.3)), and is plotted as a function of the capillary radius normalized by the intrinsic depletion depth h_p. To scale the data, an isotherm is required to calculate the depletion depth and the planar diffusion time scale. The Generalized Frumkin isotherm with the fitted parameters corresponding to our measured data as given in Table 1 is used to perform the scaling analysis. In Figure 6.3, the solid line represents the normalized characteristic time scale for diffusion to a spherical interface (Eqn (6.1)), and the dashed line corresponds to that of a planar interface. The data and analysis presented in Figure 6.3 is previously presented [2], but here the data are presented to emphasize the dependence on bubble radius and concentration for each data set. Figure 6.3 shows that as the concentration increases the experiment time scale approaches the planar time scale, and as the radius decreases the experiment time scale is smaller than the planar time scale, i.e. the dynamics are faster for smaller radii.

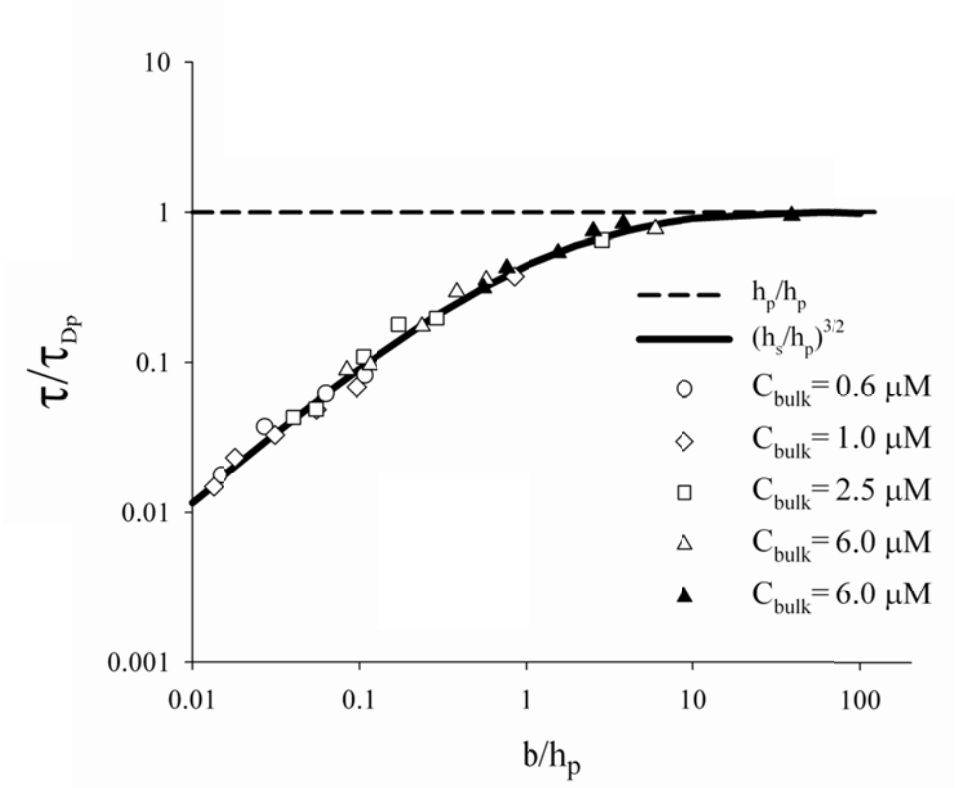

Figure 6.3. Scaled experimental time as a function of b/h_p for different concentrations and bubble radii. The symbols correspond to experimental time scales extracted from Figure 6.1.

The scaled data shows very good agreement with the time scale for diffusion to a spherical interface. If kinetic processes of adsorption and desorption are important then there will be a deviation from the diffusion time scaling [2]. The agreement between the experimental data and the diffusion time scale in Figure 6.3 strongly suggests that $C_{12}E_8$ undergoes diffusion-limited transport for all experimental conditions considered here. This result is contrary to current literature and shows that kinetic exchange at the interface does not need to be invoked to capture the dynamics of this surfactant. The advantage of knowing that the surfactant dynamics follow diffusion-limited transport is that a lower limit on β, the adsorption coefficient, can be determined from asymptotic analysis.

This analysis is further explained in Chapter 4 (Alvarez *et al*.) [2]. For example, for $C_{12}E_8$, we previously found that $\beta_{Limit} = 5\,\mathrm{m}^3/\mathrm{mol/s}$ [2].

From Chapter 4, the ratio of the diffusion time scale to the kinetic time scale (assuming Langmuirian kinetics for simplicity) is set equal to unity, and the radius, R_{crit} , where the time scales are equal, is determined by solving

$$\left(R_{crit}\left[\left(\frac{3h_p}{R_{crit}} + 1 \right)^{\frac{1}{3}} - 1 \right] \right)^3 h_p \left(\frac{\beta C_{bulk} + \alpha}{D} \right)^2 = 1 \qquad (6.5)$$

,

for R_{crit}. Scaling by $R_{DK} = D/\left(\beta\Gamma_\infty\right)$, an intrinsic length scale introduced by Jin *et al.* [1], the new critical radius is given by

$$\frac{R_{crit}}{R_{DK}} = \frac{2}{\sqrt{12 - 3q^2} - 3q} \qquad (6.6)$$

,

where $q = \left(R_{DK}/h_p\right)^{1/3}$. Figure 6.4 shows an operating diagram for dynamic surface tension measurements in terms of bubble radius and the bulk concentration of surfactant. The critical radius denoting the transition from diffusion-limited to kinetic-limited transport is plotted using Eqn (6.6) for different values of the kinetic adsorption constant. Note that the values chosen for β span the bounds put forth in previous studies [15]. The solid lines correspond to the radius at which the two time scales are equal for a given surfactant concentration. Values far to the left of the solid line correspond to diffusion-limited dynamics and values far to the right correspond to kinetic-limited dynamics. Figure 6.4 shows the expected trend that kinetic exchange at the interface plays a more important role in the rate of transport of species to the

interface as bubble radius decreases. In addition, the figure captures the experimentally and theoretically investigated dependence of the controlling mechanism on surfactant concentration. As concentration increases, the system moves toward the kinetic-limited regime.

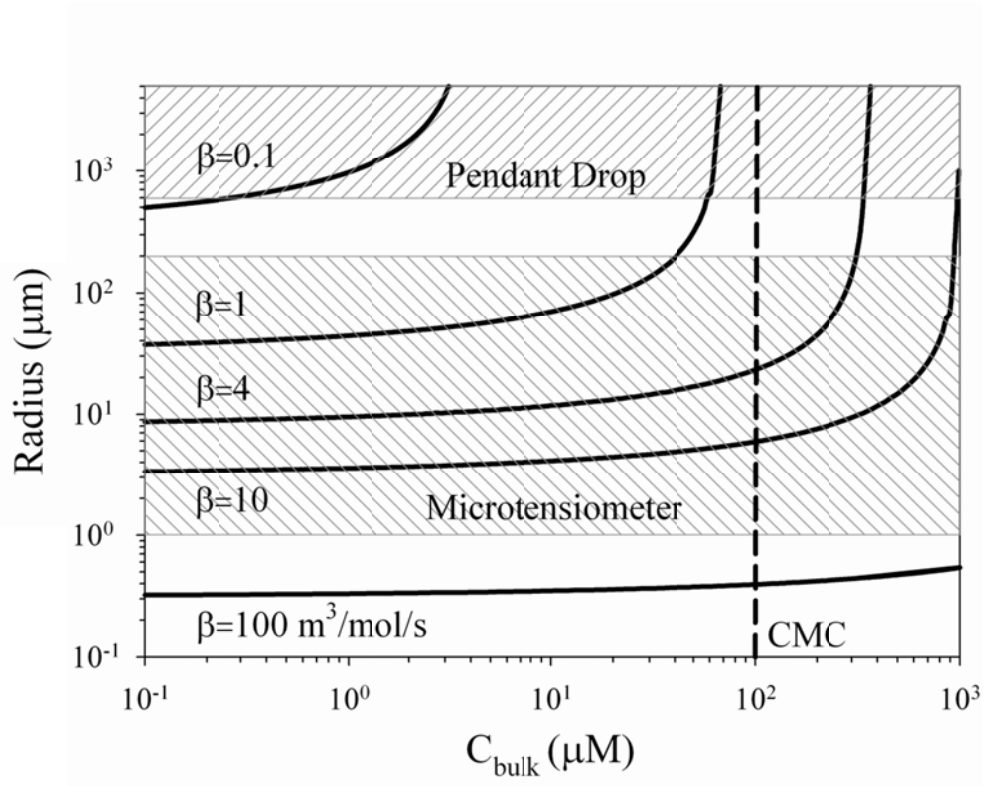

Figure 6.4. Operating diagram showing bubble radius and bulk surfactant concentration. The solid lines correspond to the points when the kinetic and diffusion time scales are equal for a given adsorption constant, β. Far to the left of the solid line defines diffusion-limited dynamics and far to the right of the line defines kinetic-limited dynamics. The two shaded regions correspond to the experimental operating regimes for the pendant drop/bubble and the microtensiometer apparatus.

The two shaded regions in Figure 6.4 correspond to the physical operating space for the pendant drop/bubble apparatus and the microtensiometer device presented in this chapter. From this figure, we conclude that the pendant drop/bubble apparatus cannot easily be used to observe kinetic-limited dynamics

except for cases when the adsorption coefficient is very small (i.e. $\beta \leq 0.1$ m^3/mol/s). Experiments could be conducted at high concentrations, but the dynamics become too fast to observe and the critical micelle concentration acts as an upper limit for concentration, beyond which dynamics are complicated by the existence of micelles in the bulk solution. Therefore, it is advantageous to work with microscale interfaces and moderately dilute concentrations to observe kinetic-limited transport. Although the results from this study reveal that the dynamics for $C_{12}E_8$ do not diverge from diffusion-limited dynamics, Figure 6.4 yields information concerning the lower limit on the adsorption coefficient β that can be tested in a given apparatus (i.e. for $C_{12}E_8$ $\beta \leq 4\,m^3$/mol/s for the microtensiometer and $\beta \leq 0.1$ m^3/mol/s for the pendant drop/bubble apparatus).

The scaling analysis presented previously [2] is used to show that $C_{12}E_8$ follows diffusion-limited dynamics for all radii and concentrations tested using the pendant drop/bubble apparatus and the microtensiometer. This is made clear by the excellent agreement between the scaled experimental data and the spherical diffusion-limited time scaling. Therefore, to correctly describe the evolution of the surface tension dynamics for $C_{12}E_8$, a diffusion model is required and kinetic exchange at the interface does not need to be considered. In the next section, we compare experiments with a diffusion-limited transport model.

6.5 PREDICTION OF DYNAMIC SURFACE TENSION

To determine whether the diffusion-limited Generalized Frumkin (GF) model correctly predicts the dynamic surface tension response of $C_{12}E_8$ at different concentrations and radii, we used the numerical procedure discussed earlier. Here, we have chosen to use a fixed value of the diffusion coefficient that corresponds to the molecular diffusion coefficient. NMR studies performed on C_8E_4 determined that the self-diffusion coefficient for this molecule is $(4.83\pm0.12)\times10^{-10}$ m^2/s in D_2O [16]. Using the relationship that the diffusion coefficient scales with $M^{-1/2}$, where M is the molecular weight of the surfactant molecule and accounting for viscosity and temperature differences between D_2O and water, the diffusion coefficient for $C_{12}E_8$ is $(3.93\pm0.12)\times10^{-10}$ m^2/s. This value is consistent with a previous study in which the authors state that the diffusion coefficient for $C_{12}E_8$ monomer is 3.5×10^{-10} m^2/s in D_2O at 25^oC [17]. Using the Stokes-Einstein relationship and accounting for both the temperature and the viscosity, the diffusion coefficient of $C_{12}E_8$ is 3.8×10^{-10} m^2/s in H_2O at 20^oC. The value obtained from the short time analysis of dynamic surface tension yields a diffusion coefficient of $(3.67\pm1.6)\times10^{-10}$ m^2/s [15]. The diffusion coefficient used in the present study is $D = 3.8\times10^{-10}$ m^2/s at 20^oC, based on an average of the estimated values from all these studies.

The first comparison is made between measurements of dynamic surface tension at initially clean interfaces and predictions using the molecular diffusion coefficient and the GF isotherm numerical model. Figure 6.5 compares experiments and predictions for three different radii for each surfactant

concentration. Figure 6.5a shows predictions for three bubble radii, b=17, 130 μm, and a pendant bubble at fixed C_{bulk} = 0.6 μM. At this concentration, the GF model predicts the dynamics for b=17 μm well, but deviates from the experimental curves for larger radii. Figure 6.5b and Figure 6.5c compare model predictions with experiments for b=17, 150 μm, and a pendant bubble at fixed C_{bulk} = 2.0 μM and C_{bulk} = 5.2 μM, respectively. In both cases, the GF model predicts much slower dynamics for b=17 μm than observed. For the larger radii, b=150 μm and a pendant bubble, both models predict similar equilibration time scales to those observed in the experiments, but differ in shape. Note that in all predictions, the equilibration time, i.e. the time it takes for the dynamics to reach γ_{eq}, is close to the measured equilibrium time even though the shapes of the predicted and measured curves may differ.

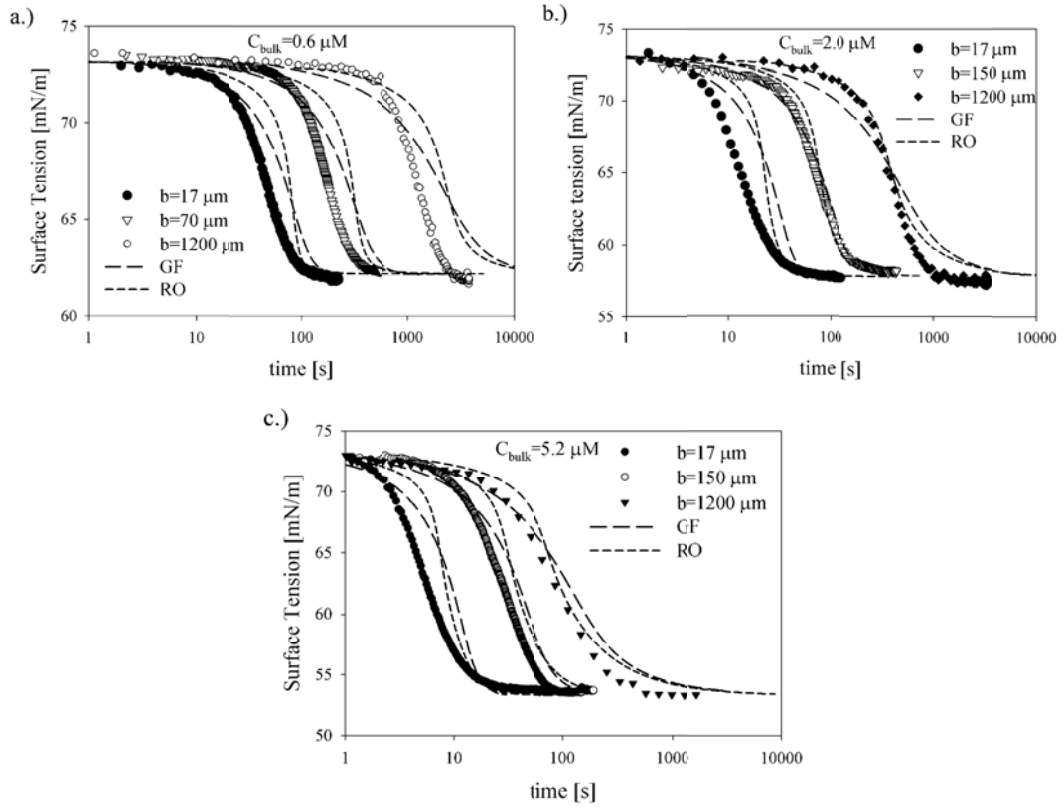

Figure 6.5. Experimental surface tension as a function of time for selected bubble radii compared with diffusion-limited model predictions using the molecular diffusion coefficient, $D = 3.8\times10^{-10}$ m^2/s and the Generalized Frumkin isotherm.

One possible source of the discrepancy in these comparisons is that the selected isotherm is not adequate to capture the dynamics. To examine this possibility we tested another isotherm given in the literature, known as the "reorientation isotherm," which has been suggested to be appropriate for $C_{12}E_8$ [6]. A numerical analysis is conducted using the reorientation model [18] coupled with transport equations outlined in Chapter 3. The relevant parameters are given in Table 6.1. As shown by the dashed lines in Figure 6.5a-c, use of the reorientation model did not lead to improved agreement between the predictions and data. We also note the agreement cannot be improved by introducing

adsorption/desorption kinetic barriers in the model. For a fixed molecular diffusion coefficient, introducing kinetic barriers would change the shape of the curve, shifting the calculated dynamics further to the right of the experimental curves and increasing the predicted equilibration times. One possible reason that a single isotherm cannot capture the observed dynamics is that there is a phase transition from a gas-like to liquid-like state at low surface concentrations [19, 20].

A situation like this could be avoided by using compression-expansion experiments to perturb the interface about the equilibrium concentration. In a compression experiment, the adsorbed species are further pushed into a liquid regime and therefore no transition of states is expected. In an expansion experiment, as long as the surface concentration is not pushed too far from equilibrium, then the surfactant at the interface should also remain in a liquid state. Thus, compression-expansion can be modeled by any single phase isotherm that accurately fits the measured equilibrium surface tension as a function of bulk concentration. An additional advantage of this type of experiment is that changes in radius are small since the surface tension is only changing by a few mN/m for a given expansion or compression ratio.

Figure 6.2 compares three expansion and compression experiments for different concentrations and bubble radii with dynamics predicted using the GF isotherm. From this figure it is evident that the GF isotherm captures the initial surface tension value that results from compressing or expanding the interface. This is a similar analysis, although not as rigorous, as that previously performed

to test the equation of state using the pendant bubble apparatus [7, 8, 19]. In addition, using the molecular value of the diffusion coefficient, the model captures the re-equilibration dynamics quantitatively for different radii and concentrations.

This result is important for two reasons. First, the agreement between model and experiments indicates that diffusion-limited transport can correctly predict the dynamics from expansion and compression experiments using a molecular diffusion coefficient for several different radii and concentrations (i.e., kinetic exchange at the interface is much faster than transport via diffusion). Second, since an expansion experiment only requires a small number of surfactants from the bulk to re-establish equilibrium, diffusion from the bulk is less important than for initially clean interfaces. This is most important for small radii, which have a smaller area to volume ratio and thus more surfactants adjacent to the interface than for larger radii. The fact that the diffusion-limited model works well is further evidence that there is no measurable kinetic barrier in the surfactant transport of $C_{12}E_8$.

6.6 SUMMARY

Using a newly developed microtensiometer apparatus, we have measured the dependence of surfactant dynamics on radius of curvature. The spherical time scale derived in Chapter 4 was validated using different radii and concentrations of a well characterized surfactant $C_{12}E_8$. Transport of surfactant to an interface is faster for a larger radius of curvature, i.e. smaller radii. The agreement between experimental time scales and the diffusion time scale suggest that diffusion is the

dominant transport mechanism for all radii and concentrations studied. Two types of experiments were performed: measurement of dynamic surface tension to initially clean interfaces and to suddenly expanded or contracted interfaces.

The agreement between the experimental time scale and the theoretical diffusion time scale eliminates the need to consider other transport processes such as kinetics. A comparison between two diffusion-limited transport models (the generalized Frumkin and the reorientation isotherm) using the molecular diffusion coefficient and dynamic surface tension data for both an initially clean and a suddenly compressed or expanded interface is presented. A comparison of the transport model to experiments for initially clean interface show qualitatively agreement. Quantitatively the model over predicts the experimental data. Comparison of the model to experiments to suddenly compressed and expanded interfaces shows quantitative agreement. Confirming both that the kinetic exchange at the interface is too fast for this surfactant method to measure with the smallest radii presented here and that the molecular diffusion coefficient appropriately described transport of $C_{12}E_8$ for all surfactant concentrations.

[1] F. Jin, R. Balasubramaniam, and K.J. Stebe, "Surfactant adsorption to spherical particles: The intrinsic length scale governing the shift from diffusion to kinetic-controlled mass transfer," Journal of Adhesion, 80 (2004), 773-796.

[2] N.J. Alvarez, L.M. Walker, and S.L. Anna, "Diffusion-limited Adsorption to a Spherical Geometry: The Impact of Curvature and Competitive Time scales," Physical Review E, (2010).

[3] S.Y. Lin, et al., "Adsorption kinetics of C12E8 at the air-water interface: Adsorption onto a clean interface," Langmuir, 12 (1996), 6530-6536.

[4] R.Y. Tsay, et al., "Adsorption kinetics of C12E8 at the air-water interface: desorption from a compressed interface," Langmuir, 13 (1997), 3191-3197.

[5] L. Liggieri, et al., "Molecular reorientation in the adsorption of some CiEj at the water-air interface," Colloids and Surfaces A-Physicochemical and Engineering Aspects, 156 (1999), 455-463.

[6] R. Miller, V.B. Fainerman, and H. Mohwald, "Adsorption behavior of oxyethylated surfactants at the air/water interface," Journal of Colloid and Interface Science, 247 (2002), 193-199.

[7] S.Y. Lin, et al., "Surface equation of state of nonionic CmEn surfactants," Langmuir, 19 (2003), 3164-3171.

[8] Y.C. Lee, S.Y. Lin, and H.S. Liu, "Role of equation of state on studying surfactant adsorption kinetics," Langmuir, 17 (2001), 6196-6202.

[9] Y.C. Lee, et al., "Adsorption and desorption kinetics of CmE8 on impulsively expanded or compressed air-water interfaces," Colloids and Surfaces A-Physicochemical and Engineering Aspects, 220 (2003), 139-150.

[10] V.B. Fainerman, et al., "Adsorption isotherm and surface tension equation for a surfactant with changing partial molar area .1. Ideal surface layer," Journal of Physical Chemistry, 100 (1996), 7669-7675.

[11] V.B. Fainerman, et al., "Comparison of various models describing the adsorption of surfactant molecules capable of interfacial reorientation," Journal of Colloid and Interface Science, 261 (2003), 180-183.

[12] R. Miller, et al., "Effect of the reorientation of oxyethylated alcohol molecules within the surface layer on equilibrium and dynamic surface pressure," Langmuir, 15 (1999), 1328-1336.

[13] N.J. Alvarez, L.M. Walker, and S.L. Anna, "A Microtensiometer To Probe the Effect of Radius of Curvature on Surfactant Transport to a Spherical Interface," Langmuir, 26 (2010), 13310-13319.

[14] N.J. Alvarez, L.M. Walker, and S.L. Anna, "A non-gradient based algorithm for the determination of surface tension from a pendant drop: Application to low Bond number drop shapes," Journal of Colloid and Interface Science, 333 (2009), 557-562.

[15] S.N. Moorkanikkara and D. Blankschtein, "New methodology to determine the rate-limiting adsorption kinetics mechanism from experimental dynamic surface tension data," Journal of Colloid and Interface Science, 302 (2006), 1-19.

[16] B. Faucompre and B. Lindman, "Self-Association of Zwitterionic and Nonionic Surfactants – NMR Self-Diffusion Studies," Journal of Physical Chemistry, 91 (1987), 383-389.

[17] P.G. Nilsson, H. Wennerstrom, and B. Lindman, "Structure of Micellar Solutions of Non-Ionic Surfactants - Nuclear Magnetic-Resonance Self-Diffusion and Proton Relaxation Studies of Poly(Ethylene Oxide) Alkyl Ethers," Journal of Physical Chemistry, 87 (1983), 1377-1385.

[18] V.B. Fainerman, A.V. Makievski, and R. Miller, "Surfactant adsorption isotherms considering molecular reorientation or aggregation at liquid/fluid interfaces," Reviews in Chemical Engineering, 14 (1998), 373-407.

[19] R.N. Pan, J. Green, and C. Maldarelli, "Theory and experiment on the measurement of kinetic rate constants for surfactant exchange at an air/water interface," Journal of Colloid and Interface Science, 205 (1998), 213-230.

[20] J.K. Ferri and K.J. Stebe, "Soluble surfactants undergoing surface phase transitions: A Maxwell construction and the dynamic surface tension," Journal of Colloid and Interface Science, 209 (1999), 1-9.

CHAPTER 7

THE EFFECT OF ALKANE TAIL LENGTH OF C_lE_8 SURFACTANTS ON TRANSPORT TO THE SILICONE OIL-WATER INTERFACE

7.1 INTRODUCTION

The transport of surfactants to the oil-water interface is important in many processes and applications such as the formulation, stabilization and production of pesticides, cosmetics, and foods. Surfactant transport is typically characterized using the measurement and analysis of dynamic surface tension. Dynamic surface tension studies have been conducted using a number of fluid-water/surfactant pairs and various measurement techniques [1, 2]. However, relatively few studies involving oil-water interfaces exist due to measurement limitations when fluid densities are similar.

Surfactant transport to an interface is characterized by the measurement of surface tension as a function of time. The surface tension is related to the number of molecules per unit area on the interface through the Gibbs' adsorption equation [3] assuming a nonionic surfactant and an ideal solution,

$$\Gamma = \frac{1}{RT}\frac{\partial \gamma}{\partial \ln\left(C_{bulk}\right)}\bigg|_{T}, \tag{7.1}$$

where γ is the interfacial tension, Γ is the surface concentration, R is the ideal gas constant, T is the temperature, and C_{bulk} is the bulk surfactant concentration..

In the absence of bulk flow, surfactants undergo transport onto an interface via two primary mechanisms: diffusion from the bulk to the interface

and kinetic exchange at the interface. For an initially clean interface ($\Gamma = 0$), the surface tension starts at the clean interfacial tension value for the two immiscible fluid pair, and decreases to an equilibrium surface tension value ($\Gamma = \Gamma_{eq}$) that depends on C_{bulk} and molecular transport parameters. Equilibrium surface tension is attained when the rates of adsorption and desorption are equal and the bulk surfactant concentration is spatially uniform. For a given surfactant/fluid-fluid pair and a given surfactant concentration, the dynamics can be classified as diffusion-limited, kinetic-limited, or a mixture of the two mechanisms.

Even though dynamic surface tension studies have been conducted at the oil-water interface [4-15], the number of possible oil-water/surfactant combinations is immense. Therefore, researchers interested in surfactant induced phenomena, e.g. droplet coalescence [16, 17] and tipstreaming [18, 19], usually must measure both the fundamental surfactant transport parameters as well as the induced phenomenon for each new surfactant-water/oil pair of interest.

The goal of this chapter is to parameterize the kinetic constants for a series of nonionic C_iE_j surfactants with structure $C_iH_{2i+1}\left(CH_2CH_2O\right)_j OH$. Specifically, for this study j=8 and we consider the surfactants $C_{10}E_8$, $C_{12}E_8$, and $C_{14}E_8$ solubilized in water at the silicone oil interface. The hydrophilic head group is the same for all three surfactants, while the number of carbons in the hydrophobic tail varies. Silicone oil is used in microfluidic studies and is available in different viscosities. This series of surfactants has been extensively studied at the air-water interface and a detailed analysis has been presented in the previous chapters [1, 20-23]. We anticipate that the parameters obtained from this

study will be of use to those modeling surfactant mediated events in applications such as microfluidics and emulsification and demulsification processes. The analysis presented here relies heavily on the scaling analysis presented in Chapter 4 [24].

7.2 METHODS

7.2.1 PENDANT DROP APPARATUS

Different techniques have been developed for oil-water studies such as the growing drop technique [25, 26], the drop volume method [11], the controlled drop tensiometer [27], a microchannel flow tensiometer [28], and the pendant drop technique [6, 12, 29]; each has advantages and disadvantages. The pendant drop technique is chosen for this study for its use of a static drop shape with no bulk convection.

The pendant drop technique measures the surface tension by fitting the Young-Laplace equation to the interface shape of a drop or bubble that is pinned at the end of a capillary and distended from a spherical shape [30, 31]. The distended shape is parameterized by the Bond number, which describes the relative magnitude of gravity compared with surface tension and is defined by

$$Bo = \frac{\Delta\rho g R^2}{\gamma}, \tag{7.2}$$

where $\Delta\rho$ is the density difference between the two fluids, g is the acceleration due to gravity, R is the radius of curvature at the apex of the drop or bubble interface, and γ is the interfacial tension at the fluid–fluid interface.

Most pendant drop shape fitting algorithms require $Bo > 0.15$ in order to accurately fit the Young-Laplace equation to the extracted interfacial edge coordinates [31-33]. Therefore, studies at the silicone oil-water interface ($\gamma = 40$ mN/m and $\Delta\rho = 40\,\text{kg/m}^3$) require a drop size of $R > 4$ mm to remain within the Bo constraint. A drop this size requires long formation times and a large volume of surfactant solution to maintain a constant surfactant concentration within the sample well, i.e. minimal depletion of surfactant from the bulk. However, our group has recently developed a non-gradient based algorithm that can accurately measure surface tension for $Bo > 0.01$ [31], which allows for the use of a traditional $R = 1 - 2$ mm drop for silicone oil-water interfaces. The details of the algorithm are discussed elsewhere [31].

The experiments are performed using a custom-built pendant drop apparatus similar to a previously reported design [34]. The droplets of oil are formed at the tip of a 1.65 mm J-needle (Rame-Hart Inc.) submerged in a 2.5 cm by 2.5 cm glass cell (4G, Sterna Cell Inc.). The oil is pushed through PEEK capillary tubing I.D. 0.030 in. (Small Parts Inc.) using a glass syringe (Hamilton) attached to a syringe pump (Braintree Scientific Inc.). The flow rate of oil is kept small (850 μL/min) in order to reduce convective flow in the cell. Images of the interface are captured using a CCD camera with 640x480 pixel resolution (Cohu) during the evolution of the drop from a clean interface to an equilibrium surface shape corresponding to $\gamma_{eq}\left(\Gamma_{eq}\right)$. The system is floated on an optical bench to reduce vibration. The drop is backlit using a light source with a diffuse optical filter. The interface shape as a function of time is extracted from the captured

image sequence. The fitting routine is used to obtain surface tension as a function of time. The dynamic surface tension profiles are measured as a function of bulk concentration below the critical micelle concentration [cmc] and then analyzed in the context of a reaction-diffusion model.

7.2.2 DATA ANALYSIS

The analysis scheme in this chapter follows four steps. First, isotherm parameters are estimated from a nonlinear least squares fit to equilibrium surface tension data. Second, using a scaling analysis presented previously [24, 35], we determine the dominating transport mechanism for each measured dynamic surface tension curve. Diffusion-limited dynamics are coupled with equilibrium data to determine a unique set of isotherm parameters that capture both data sets. Third, a check is performed on the scaling analysis to assess whether the best-fit isotherm parameters results in a shift in the governing transport mechanism. Finally, if dynamics that are not diffusion limited are observed, then kinetic parameters are determined from a one parameter nonlinear fit to the dynamic surface tension data. If the dynamics are diffusion-limited, then a sensitivity analysis is performed and a lower limit on the adsorption constant, β, is determined.

For the surfactants considered here, the Generalized Frumkin isotherm is chosen because it has been shown to agree quantitatively with dynamic surface tension studies at the air-water interface involving $C_{10}E_8$ [1, 23], $C_{12}E_8$ [20, 23, 36], and $C_{14}E_8$ [21-23]. The generalized Frumkin isotherm has four unknown parameters and is given by,

$$\frac{\Gamma}{\Gamma_\infty} = \frac{C_{bulk}}{C_{bulk} + a\exp\left(\kappa\left(\frac{\Gamma}{\Gamma_\infty}\right)^n\right)}, \tag{7.3}$$

where a is the ratio of the kinetic rate constant of desorption, α, and adsorption, β, such that $a = \alpha/\beta$, κ is a surface van der Waals interaction term, Γ_∞ is the maximum surface concentration, and n is a nonlinear fitting parameter. Note that this isotherm reduces to the Frumkin isotherm when $n = 1$ and to the Langmuir isotherm when $\kappa = 0$. This isotherm is often fit by allowing all four parameters to vary [20, 22, 23, 37]. A multi-parameter fit can lead to multiple best-fit solutions that depend on the initial guess, often resulting in very different parameter values. To reduce the number of fitting parameters, it is possible to determine Γ_∞ directly from the asymptotic slope of equilibrium surface tension data at high concentrations using Eqn (7.1) [4, 5, 15]. This chapter follows the latter methodology.

Using the isotherm parameters obtained from the fit described above, a scaling analysis is performed in order to determine the dominant mechanism of surfactant transport for each set of conditions considered. The scaling analysis is performed by determining the experimental time, $\tau_{\exp}$, required to reach a specified fractional surface coverage, $\phi = \Gamma\left(\tau_{\exp}\right)/\Gamma_{eq}$, for each bulk surfactant concentration. This experimental time scale is normalized by the planar diffusion time scale, $\tau_{Dp} = h_p^{\,2}/D$, and plotted as a function of the dimensionless bubble radius, b/h_p, where $h_p = \Gamma_{eq}/C_{bulk}$, b is the bubble radius, and D is the diffusion

coefficient. We compare the normalized experimental transport time with the spherical diffusion time scale,

$$\tau_{Ds} = \frac{\left(h_s{}^3 h_p\right)^{\frac{1}{2}}}{D}, \tag{7.4}$$

where h_s is the spherical depletion depth given by [24],

$$h_s = b\left[\left(\frac{3h_p}{b}+1\right)^{1/3} - 1\right]. \tag{7.5}$$

We have demonstrated previously that diffusion-limited dynamics follow the scaling with bubble size and concentration given in Eqns (7.4) and (7.5), and that when kinetics become significant the normalized time scale deviates from this scaling [24]. Therefore, we can determine the governing transport mechanisms for each concentration.

Once the dominant mechanism is established, it is possible to determine the relevant transport parameters. For example, if diffusion is the dominant mechanism, then the only unknown, the diffusion coefficient, can be fit to the dynamic surface tension data and compared with the molecular value obtained by other techniques such as NMR [38]. Alternatively, the molecular diffusion coefficient can be assumed and diffusion-limited dynamic surface tension data can be used as further input to the multi-parameter isotherm fit. Previous studies have demonstrated the complexity of determining correct isotherm parameters by solely fitting equilibrium data [21, 23, 39]. This has led to the development of numerous experimental techniques designed to probe the isotherm in more detail, e.g. compression/expansion experiments [40]. Diffusion-limited surface tension

experiments are also a useful tool to test the isotherm, since the surface is assumed to be in equilibrium with the concentration of surfactant immediately adjacent to the interface, i.e. the isotherm is probed as a function of time. Therefore, once the scaling analysis reveals which dynamic surface tension curves are diffusion-limited, the isotherm parameters are fit by minimizing the error between equilibrium data and the diffusion-limited dynamic data simultaneously. The result of this fitting procedure is a unique set of best-fit isotherm parameters.

We note that the scaling analysis depends on the isotherm parameters. Since the isotherm parameters may change when fitting the diffusion-limited dynamic and equilibrium surface tension data simultaneously, it is important to check that the new isotherm parameters do not shift the time scales. In other words, the chosen concentration for fitting diffusion-limited dynamics should still follow the diffusion-limited scaling.

If the scaling analysis reveals experimental conditions that do not follow diffusion-limited dynamics, then additional transport parameters can be determined. For example, if the dynamics are fully kinetic-limited then the only unknown is the adsorption rate constant. In this case, the rate constant is obtained from a one parameter nonlinear fit using the dynamic surface tension data corresponding to this limit and a kinetic-limited transport model. Similarly, if the dynamics are in transition between the two limits, then the adsorption rate constant is determined from a nonlinear fit using a full transport model incorporating both diffusion and kinetics. In either case, the one parameter fit assumes that the isotherm parameters are obtained previously. Finally, in the

event that all experiments exhibit diffusion-limited dynamics, then a sensitivity analysis is performed and a lower limit on the adsorption rate constant is determined. A similar sensitivity analysis has been performed previously [1]. Note that all analyses above assume that the diffusion coefficient is known.

7.2.3 NUMERICAL SCHEME

Fitting the dynamic surface tension data requires a transport model. Mass transport from the bulk is modeled using Fick's Law in spherical coordinates $\partial C/\partial t = D/r^2\ \partial(r^2 \partial C/\partial r)/\partial r$. A flux boundary condition is imposed at the interface, $\partial\Gamma/\partial t = D\,\partial C/\partial r$ and a Dirichlet condition is specified far from the boundary, $C\big|_{r\to\infty} = C_{bulk}$. The mass balance governing transport from the bulk solution adjacent to the interface onto the interface is given by either a kinetic mass rate equation or an isotherm model. The rate equation used in this study is the Generalized Frumkin rate equation given by

$$\frac{d\Gamma}{dt} = \beta C_s \Gamma_\infty \left(1 - \frac{\Gamma}{\Gamma_\infty}\right) - \alpha\Gamma \exp\left(\kappa\left(\frac{\Gamma}{\Gamma_\infty}\right)^n\right), \qquad (7.6)$$

where C_s is the concentration of surfactant adjacent to the interface, β is the adsorption constant, α is the desorption constant, κ is an interaction parameter, and n is a fitting parameter. When $\partial\Gamma/\partial t = 0$, Eqn (7.6) reduces to the Generalized Frumkin isotherm, Eqn (7.3). A collocation (spectral) method is used to solve the governing equations for mass transfer to a fluid-fluid interface. Time is discretized using an implicit Euler scheme. Convergence is defined when

there is less than 10^{-6} deviation in $\gamma(t)$. The validation of this numerical scheme is discussed elsewhere [24].

7.3 MATERIALS

Solvents (ACS grade) for cleaning and preparation were purchased and used as received. The nonionic surfactants $C_{10}E_8$, $C_{12}E_8$, and $C_{14}E_8$ were purchased from Nikko Chemicals (99% purity) and used as received. Surfactant solutions are prepared using deionized water purified using a Barnstead UV Ultrapure II purification system (resistivity of 18.2 MΩ·cm). Stock surfactant solutions are prepared by first melting the pure surfactant at 40°C and then weighing a known mass of surfactant in liquid form. The known mass is diluted to specified concentrations that are below the cmc. The diffusion coefficient of $C_{12}E_8$ has been obtained previously using several independent techniques. We take the average value corresponding to several reported values, $D = 3.8\times10^{-10}$ m^2/s [38, 41, 42]. The diffusion coefficient for $C_{10}E_8$ and $C_{14}E_8$ were calculated using the diffusion coefficient of $C_{12}E_8$ and the scaling with molecular weight given by $D \sim M^{1/2}$, which has previously been used for low molecular weight surfactants[29]. The values used are $D = 3.9\times10^{-10}\,m^2/s$ and $D = 3.7\times10^{-10}\,m^2/s$, respectively. Silicone oil was purchased from Gelest Inc. and used as received. The measured density of the oil is 960 kg/m^3 and the manufacturer reported viscosity is $\mu/\rho = 50$ cSt ($\mu = 48$ cP). All experiments were conducted at room temperature, 22 ±1°C.

In most previously reported oil-water studies, a direct comparison with air-water dynamic surface tension is complicated by partitioning of surfactant into the oil phase. Assuming the rate of partitioning is driven by diffusion in the oil phase, the rate of partitioning is reduced by approximately a factor of 50 in the experiments presented here due to the relatively high viscosity of silicone oil compared with oils used in previous studies. In addition, since the oil is significantly more viscous than water, the time scale for partitioning is an order of magnitude slower than adsorption to the interface. Partitioning of surfactant from the water to the oil phase would be evident in a change in the measured critical micelle concentration (CMC). The fact that the same CMC is observed in the equilibrium data for silicone oil-water as in air-water (c.f. Figure 5) suggests that the series of polyoxyethylene surfactants studied here are relatively insoluble in silicone oil. Both arguments suggest that partitioning is not a relevant process in our dynamic surface tension measurements. Therefore, we do not include it in the transport model.

7.4 RESULTS AND DISCUSSION

Figure 7.1 shows the measured surface tension as a function of time for three different nonionic surfactants ($C_{10}E_8$, $C_{12}E_8$, and $C_{14}E_8$) dissolved in water at the interface of an initially clean pendant drop of silicone oil. Figure 7.1a shows the dynamic surface tension for $C_{10}E_8$ for four surfactant concentrations ranging from 4 μM to 25 μM (cmc = 1200 μM [1]). Figure 7.1b shows the dynamic surface tension for $C_{12}E_8$ at bulk concentrations ranging from 0.6 μM to 100 μM (cmc = 100 μM [20]). Finally, Figure 7.1c shows the dynamic surface tension

measurements for $C_{14}E_8$ at bulk concentrations ranging from 0.6 to 13 μM (cmc = 10 μM [21]). In all cases, the radius of the drop is fixed at $b = 1.9$ mm. Note that the time scale to reach equilibrium decreases with increasing concentration for all three surfactants. The length of the tail of the surfactant molecule also impacts the dynamics by requiring a longer time to reach equilibrium as the tail length increases for the same surfactant concentration (c.f. 0.6 μM, Figure 7.1b and c). In other words, increasing tail length decreases the rate of transport.

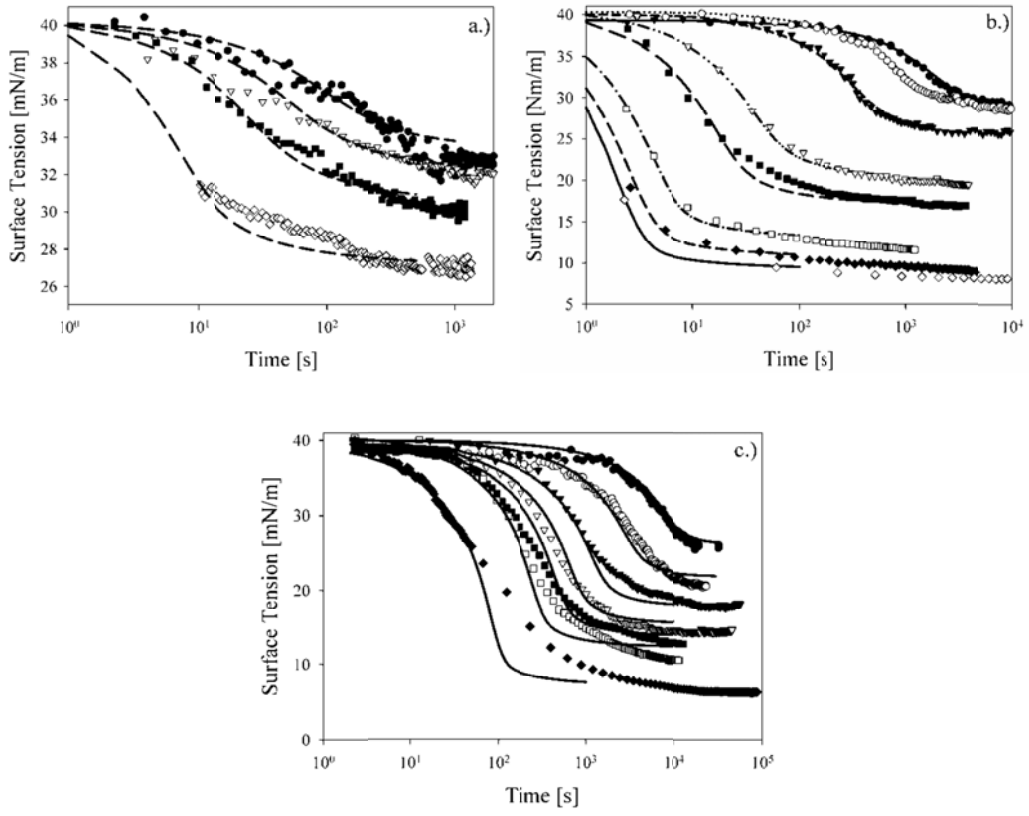

Figure 7.1. Surface tension as a function of time at different bulk surfactant concentrations for a.) $C_{10}E_8$, b.) $C_{12}E_8$, and c.) $C_{14}E_8$. Concentrations for $C_{10}E_8$ correspond to ● 4 μM, ▽ 6 μM, ■ 10 μM, and ○ 25 μM. Concentrations for $C_{12}E_8$ correspond to: ● 0.6 μM, ○ 1.0 μM, ▼ 2.2 μM, ▽ 10.0 μM, ■ 17.82 μM, □ 50 μM, ◆75 μM, and ◇ 100 μM. Concentrations for $C_{14}E_8$ correspond to : ● 0.6 μM, ○ 1.0 μM, ▼ 2.2 μM, ▽ 3.2 μM, ■ 4.3 μM, □ 6.6 μM, and ◆13 μM. Lines correspond to predictions using the full transport model. Experiments are conducted at fixed bubble radius, $b = 1.9$ mm.

Figure 7.2 shows the equilibrium surface tension as a function of concentration for all three surfactants considered. The equilibrium value is determined from the long time asymptotic value of the dynamic surface tension shown in Figure 7.1. The solid lines represent the best-fit Generalized Frumkin isotherm for each surfactant. The best-fit parameters are given in Table 7.1. We reduce the fitting to three parameters by first extracting the value of Γ_∞ from the slope of the isotherm data shown in Figure 7.2 using Eqn (7.1). For $C_{10}E_8$, $C_{12}E_8$ and $C_{14}E_8$, the values of Γ_∞ obtained this way are $(2.05\pm0.20)\times10^{-6}$, $(2.16\pm0.12)\times10^{-6}$, and $(2.36\pm0.16)\times10^{-6}$ mol/m^2, respectively. These three values are equivalent within experimental error, suggesting that Γ_∞ is not a strong function of tail length. Therefore, for all three surfactants we assume a constant value of $\Gamma_\infty = 2.20\times10^{-6}$ mol/m^2, given by the average of the three individual values.

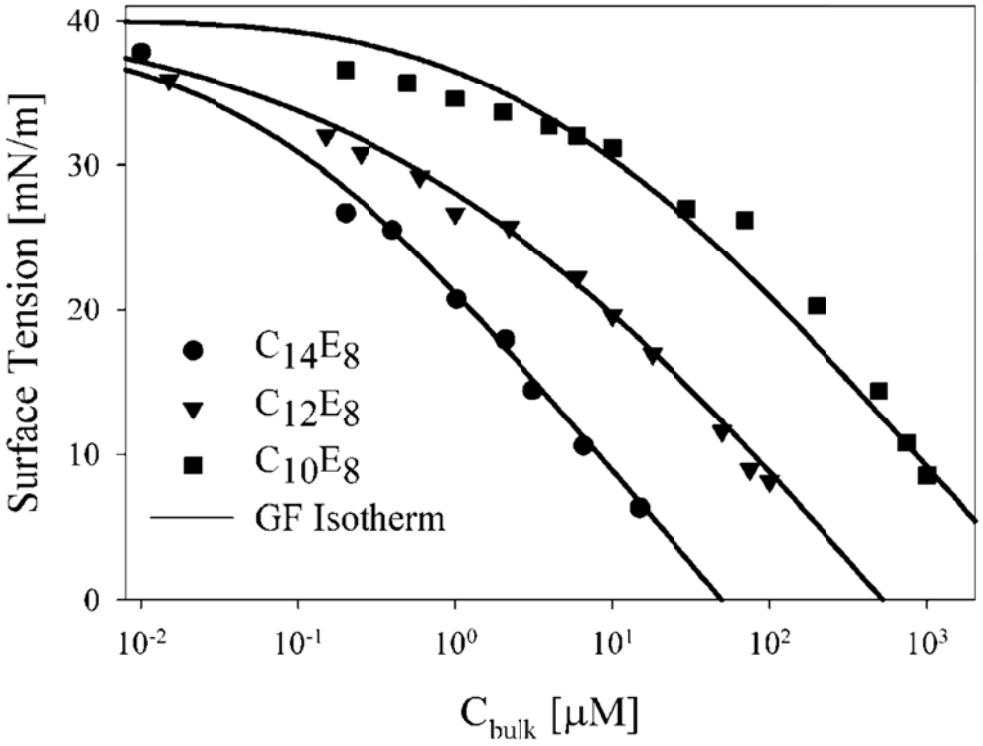

Figure 7.2. Equilibrium surface tension as a function of concentration for $C_{10}E_8$, $C_{12}E_8$, and $C_{14}E_8$. The lines correspond to the best-fit isotherm.

Characteristic dimensionless time scales obtained from the dynamic surface tension experiments shown in Figure 7.1 are plotted in Figure 7.3 as a function of dimensionless drop radius b/h_p. For each experiment, the time corresponding to a specified surface coverage $\phi = \Gamma/\Gamma_{eq}$ is determined from the data shown in Figure 7.1. The experimental time scales for $C_{10}E_8$, $C_{12}E_8$, and $C_{14}E_8$ are obtained for $\phi = 0.85$, $\phi = 0.99$, and $\phi = 0.93$, respectively. The experimental time is determined by using the equation of state and the isotherm parameters in Table 1 to determine the surface tension corresponding to the specified ϕ value for each concentration. This experimental time is normalized by

the planar diffusion time scale and plotted against the dimensionless drop radius b/h_p corresponding to that experiment. The solid line represents the normalized spherical diffusion time scale given by Eqn (7.4). If the experiment time scales agree with the spherical diffusion time scale, then the dynamics are assumed to be diffusion limited. At low surfactant concentrations, Figure 7.3 shows that all three surfactants follow diffusion-limited dynamics. However, at higher surfactant concentrations, $C_{12}E_8$ and $C_{14}E_8$ deviate from the spherical diffusion time scale. The deviation from the diffusion-limited scaling exhibited by $C_{12}E_8$ and $C_{14}E_8$ is characteristic of a shift from diffusion to kinetics as the controlling mechanism [24]. Therefore, kinetic parameters are obtained through a one parameter fit, as discussed previously.

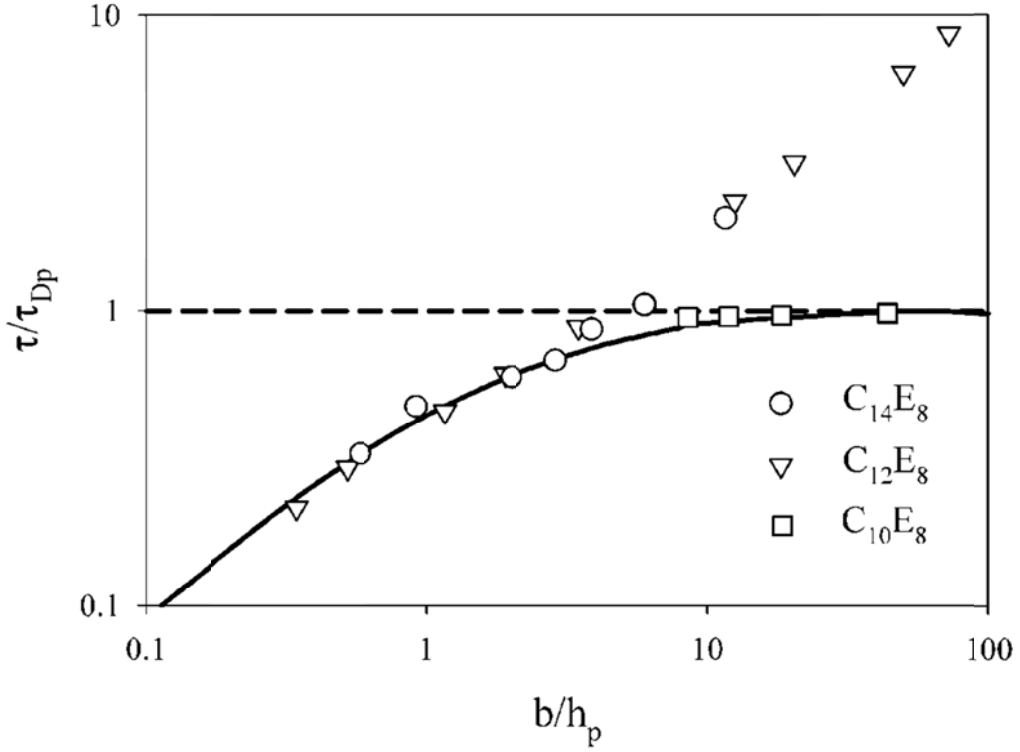

Figure 7.3. Scaled experimental time as a function of b/h_p for different concentrations and fixed bubble radius for $C_{10}E_8$, $C_{12}E_8$, and $C_{14}E_8$

Using a non-gradient fitting routine, the full transport model is fit to the dynamic surface tension curves that deviate from the diffusion-limited scaling. The best-fit adsorption rate constant is shown in Figure 7.4 as a function of bulk concentration for $C_{12}E_8$ and $C_{14}E_8$. The solid lines represent the averages of the best-fit values for each surfactant, corresponding to 22.1±2.3 and 9.42±4.27 $m^3/(mol \cdot s)$, respectively. The shaded regions correspond to the 95% confidence region for the respective mean value. From Figure 7.4 it is clear that the adsorption constants for $C_{12}E_8$ and $C_{14}E_8$ are statistically different. The adsorption constant for $C_{10}E_8$ is not presented in Figure 7.4 since the dynamics follow diffusion-limited transport for all concentrations considered, and the

kinetics are too rapid to observe. However, using the same one parameter fitting routine, we determine a lower limit on the adsorption rate constant for this surfactant. A similar approach to determining the lower limit for the kinetic rate constant has been presented previously [1]. We find a lower limit for $C_{10}E_8$ of $\beta > 50\ m^3/(mol \bullet s)$. In other words, at a value of $\beta = 50\ m^3/(mol \bullet s)$, the dynamics become independent of the value of β. The transport parameters for each surfactant are summarized in Table 7.1.

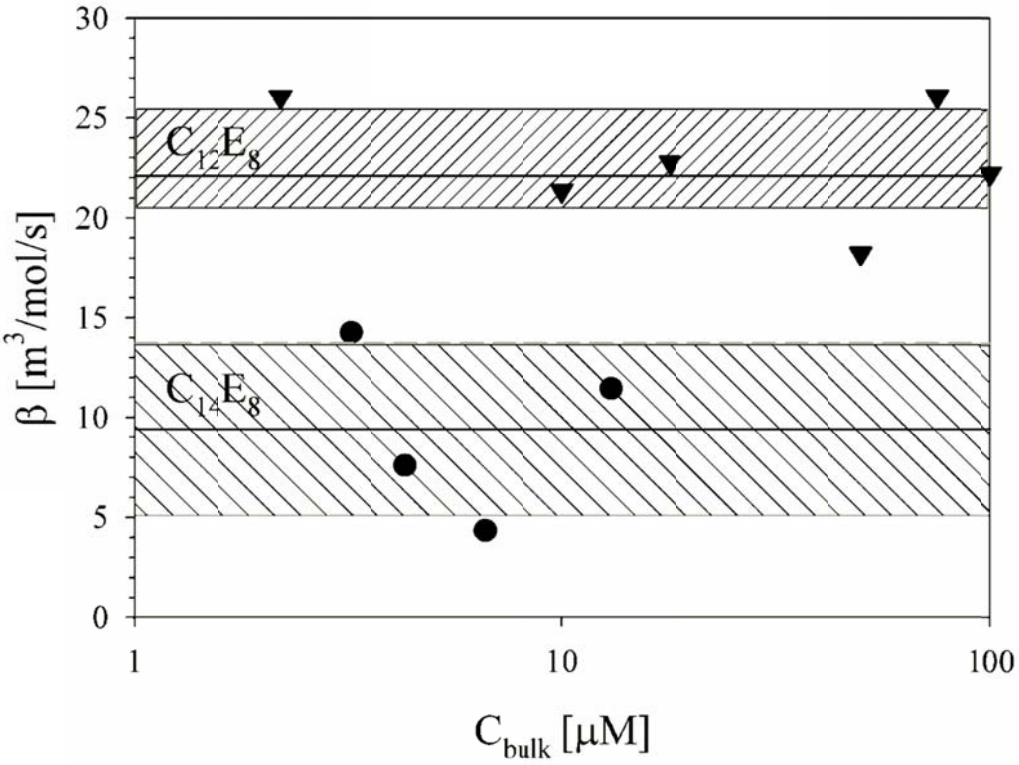

Figure 7.4. Best-fit adsorption rate constant obtained from a one parameter nonlinear fit. Shaded regions refer to 95% confidence region of average value (solid line).

Best-Fit Isotherm Parameters						
	$\Gamma_\infty \times 10^6$ [mol/m^2]	a [mol/m^3]	κ	n	β [m^3/mol/s]	α [1/s]
$C_{10}E_8$	2.25	5.00×10^{-4}	4.00	1.00	>50.0	2.50×10^{-2}
$C_{12}E_8$	2.25	3.10×10^{-7}	10.3	0.460	21.5	6.67×10^{-6}
$C_{14}E_8$	2.25	2.70×10^{-9}	10.8	0.130	9.40	2.54×10^{-8}
Literature Values for Air-Water Isotherms[22]						
$C_{10}E_8$	3.42	2.13×10^{-5}	12.2	0.385	-	-
$C_{12}E_8$	5.28	2.33×10^{-6}	13.2	0.532	-	-
$C_{14}E_8$	4.95	1.13×10^{-7}	10.9	0.556	-	-

Table 7.1**.** Parameters obtained from literature (air-water) and from fitting of the Generalized Frumkin Isotherm to equilibrium data and diffusion-limited dynamic data simultaneously (oil-water).

We check the goodness of fit by comparing the model predictions with the experimental dynamic surface tension results. The solid and dashed lines in Figure 7.1 correspond to predictions for each surfactant concentration using the best-fit transport parameters. The model and the experiments agree well for $C_{10}E_8$ and $C_{12}E_8$. For $C_{14}E_8$, there is good agreement at low concentrations. However, for $C_{14}E_8$ at high concentrations the model under predicts the experiments at intermediate times. One possible explanation for the mismatch between theory and experiments for $C_{14}E_8$ at high concentration is that these concentrations are close to the cmc and the dynamics could be complicated by the presence of micelles in solution.

Now that the transport parameters are specified for the silicone oil-water interface, it is instructive to compare the behavior of the C_iE_8 surfactants at the oil-water interface with the behavior at the air-water interface, for which there is abundant data available in the literature. Typical air-water isotherm parameters obtained from the literature for the three surfactants studied are shown in Table 1. Figure 7.5 compares the isotherms obtained using literature values from air-water studies and the best-fit parameters obtained here for silicone oil and water. To directly compare the two interfacial systems, the data is presented in terms of the surface pressure, $\Pi = \gamma_0 - \gamma_{eq}$, where γ_0 is the clean interfacial tension of each system and γ_{eq} is the equilibrium surface tension at a given concentration.

Figure 7.5 shows that the isotherms for the two interfaces are different. Examining the high concentration limit, it is clear that the values of Γ_∞ are different since the slopes of the isotherm curves are different (c.f. Eqn (7.1)). Based on the values for Γ_∞ given in Table 1, it appears that the maximum number of molecules that can adsorb onto the oil-water interface is less than half the maximum number that can adsorb onto the air-water interface, see Table 1. This is consistent with the observation that the same bulk concentration lowers the surface tension more at the air-water interface than at the oil-water interface. The smaller maximum packing concentration observed at the oil-water interface is consistent with a previous equilibrium study conducted at multiple oil-water interfaces for different $C_{12}E_j$ surfactants [43], as well as a previous study comparing equilibrium isotherm data at air-water and oil-water interfaces using different types of surfactants, e.g. Triton X-100 [11].

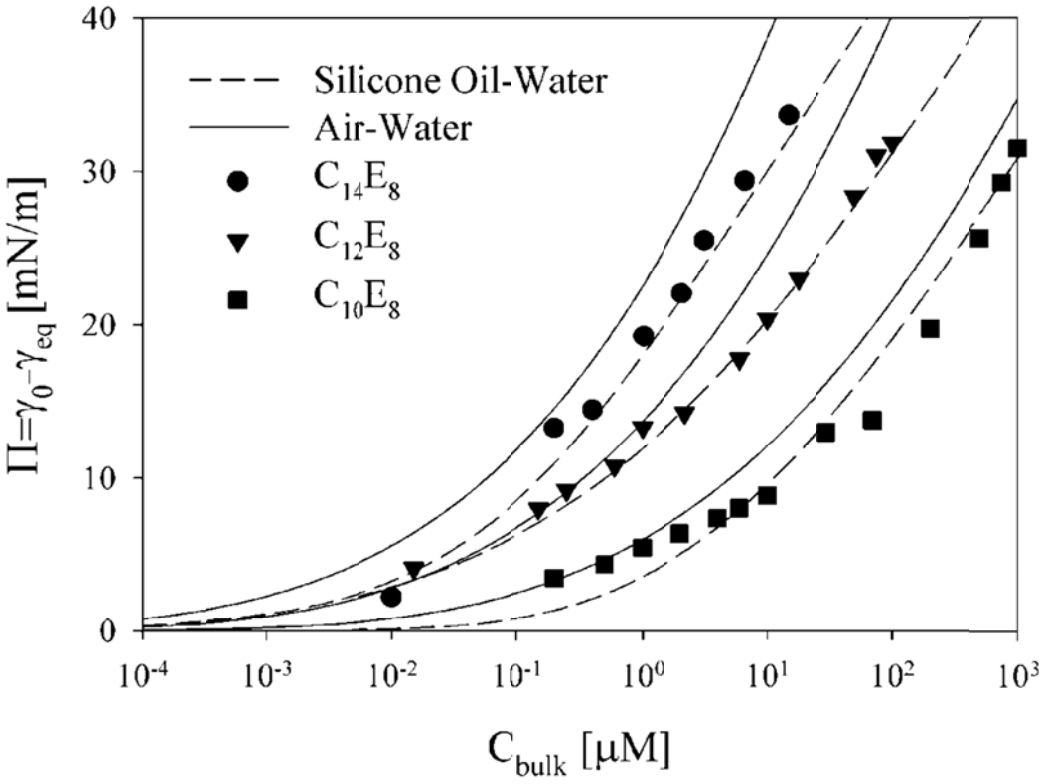

Figure 7.5. Comparison between isotherm data for air-water and oil-water interfaces for $C_{10}E_8$, $C_{12}E_8$, and $C_{14}E_8$. The symbols correspond to experimental data at the oil-water interface.

In addition to a difference in equilibrium, there is also a difference in the governing transport mechanism for $C_{12}E_8$. As shown in Figure 7.3, $C_{12}E_8$ exhibits a shift in the governing transport mechanism with increasing surfactant concentration. This result is very different from the observed dynamics at the air-water interface. For a similar series of concentrations, the scaling for the dynamics at the air-water interface shows that $C_{12}E_8$ follows diffusion-limited dynamics over all concentrations [35]. This suggests that the rate of adsorption is slower at the oil-water interface than at the air-water interface. In other words, the magnitude of the kinetic barrier depends on the fluids that form the interface.

This result is consistent with the results of a dynamic surface tension study investigating Triton X405 at the hexane-water interface [4]. Triton X405 exhibits purely diffusion-limited behavior at the air-water interface and a mixture of diffusion and kinetics at the hexane-water interface. The agreement between these studies suggests that kinetics at oil-water interfaces are generally slower than at air-water interfaces.

With these results a comparison between kinetic constants determined from this study with the same surfactant at the oil-water interface can be made. For example, in a review article the adsorption constants for $C_{10}E_8$, $C_{12}E_8$, and $C_{14}E_8$ at the air-water interface are reported as 6.9, 4.6, and 5.4 $m^3/(mol \cdot s)$, respectively [20]. It would appear that the kinetic constants obtained from oil-water dynamics show larger rate constants. However, since the diffusion coefficient was not a fixed parameter in the air-water studies and was overall higher than the molecular diffusion coefficient used in this study, a direct comparison is not easily made. If a smaller diffusion coefficient were used in the analysis of air-water dynamic surface tension measurements, then the resulting kinetic rate constant would have been larger than that reported or in some cases not measurable. For example, the air-water dynamic surface tension measurements for $C_{12}E_8$ used to determine the value of 4.6 $m^3/(mol \cdot s)$ was shown to follow diffusion-limited dynamics [35]. Therefore the kinetic exchange at the interface is faster than the diffusion process and determining absolute value of the adsorption/desorption rate constant is not possible. Instead the most that could be determined is a lower bound.

7.5 SUMMARY

We have presented a new analysis approach that uses scaling arguments to determine the relevant transport mechanisms for the evolution of surface tension at an oil-water interface for a series of homologous C_iE_8 surfactants. For the surfactants $C_{12}E_8$ and $C_{14}E_8$, the scaling analysis shows that the governing transport mechanism shifts from diffusion-limited at low concentration to kinetic-limited at high concentration. $C_{10}E_8$ is diffusion limited for all concentrations tested. The diffusion-limited dynamics are coupled with equilibrium data to obtain the best-fit isotherm parameters. The resulting isotherm parameters are coupled with a full transport model to determine the adsorption rate constant. The full transport model and the best-fit parameters are compared with the experimental dynamic data and show good agreement for most conditions.

For this homologous series of surfactants at the silicone oil-water interface, both the adsorption and desorption rate constants decrease with increasing tail length, suggesting that the rate of adsorption and desorption decrease with increasing tail length. In addition, the surfactants ability to reduce the surface tension is greater at the air-water interface than the oil-water interface due to the larger maximum surface concentration observed at the air-water interface. The agreement between the model parameters and the experimental data suggest that the new analysis approach presented here is effective for determining appropriate isotherm and kinetic parameters for modeling surfactant behavior.

[1] S.Y. Park, et al., "Dynamic Surface-Tension Behavior of Hexadecanol Spread and Adsorbed Monolayers," Langmuir, 9 (1993), 3640-3648.

[2] J. Eastoe and J.S. Dalton, "Dynamic surface tension and adsorption mechanisms of surfactants at the air-water interface," Advances in Colloid and Interface Science, 85 (2000), 103-144.

[3] J.W. Gibbs, et al., *The collected works of J. Willard Gibbs* (Longmans, Green and co., New York, 1928).

[4] J. Vanhunsel and P. Joos, "Adsorption-Kinetics at the Oil-Water Interface," Colloids and Surfaces, 24 (1987), 139-158.

[5] J. Vanhunsel, G. Bleys, and P. Joos, "Adsorption-Kinetics at the Oil-Water Interface," Journal of Colloid and Interface Science, 114 (1986), 432-441.

[6] G. Tomoaia, et al., "Kinetic study of adsorption of some biocompounds at the oil/water interface," Central European Journal of Chemistry, 3 (2005), 347-360.

[7] O.S. Sudah, G. Chen, and Y.C. Chiew, "Adsorption of single component and binary mixtures of protein and surfactants at the oil-water interface," Colloids and Surfaces B-Biointerfaces, 13 (1999), 195-202.

[8] S.A. Zholob, V.B. Fainerman, and R. Miller, "Dynamic adsorption behavior of polyethylene glycol octylphenyl ethers at the water/oil interface studied by a dynamic drop volume technique," Journal of Colloid and Interface Science, 186 (1997), 149-159.

[9] P. Joos, et al., "Adsorption kinetics of some carotenoids at the oil/water interface," Colloids and Surfaces B-Biointerfaces, 37 (2004), 83-91.

[10] L. Liggieri, et al., "Adsorption kinetics of alkylphosphine oxides at water/hexane interface .2. Theory of the adsorption with transport across the interface in finite systems," Journal of Colloid and Interface Science, 186 (1997), 46-52.

[11] J.G. Gobel and G.R. Joppien, "Dynamic interfacial tensions of aqueous triton X-100 solutions in contact with air, cyclohexane, n-heptane, and n-hexadecane," Journal of Colloid and Interface Science, 191 (1997), 30-37.

[12] M. Ferrari, et al., "Adsorption kinetics of alkylphosphine oxides at water/hexane interface .1. Pendant drop experiments," Journal of Colloid and Interface Science, 186 (1997), 40-45.

[13] V.B. Fainerman, S.A. Zholob, and R. Miller, "Adsorption kinetics of oxyethylated polyglycol ethers at the water-nonane interface," Langmuir, 13 (1997), 283-289.

[14] S.R. Deshiikan, et al., "SDS, Brij58 and CTAB at the dodecane-water interface," Colloids and Surfaces A-Physicochemical and Engineering Aspects, 136 (1998), 133-150.

[15] G. Bleys and P. Joos, "Adsorption-Kinetics of Bolaform Surfactants at the Air Water Interface," Journal of Physical Chemistry, 89 (1985), 1027-1032.

[16] Y.H. Kim, D.T. Wasan, and P.J. Breen, "A Study of Dynamic Interfacial Mechanisms for Demulsification of Water-in-Oil Emulsions," Colloids and Surfaces A-Physicochemical and Engineering Aspects, 95 (1995), 235-247.

[17] K. Giribabu and P. Ghosh, "Adsorption of nonionic surfactants at fluid-fluid interfaces: Importance in the coalescence of bubbles and drops," Chemical Engineering Science, 62 (2007), 3057-3067.

[18] W. Lee, L.M. Walker, and S.L. Anna, "Role of geometry and fluid properties in droplet and thread formation processes in planar flow focusing," Physics of Fluids, 21 (2009).

[19] S.L. Anna and H.C. Mayer, "Microscale tipstreaming in a microfluidic flow focusing device," Physics of Fluids, 18 (2006), 121512.

[20] S.Y. Lin, et al., "Adsorption kinetics of C12E8 at the air-water interface: Adsorption onto a clean interface," Langmuir, 12 (1996), 6530-6536.

[21] S.Y. Lin, et al., "A study on surfactant adsorption kinetics: The role of the data of equation of state gamma(Gamma) for C14E8," Journal of Colloid and Interface Science, 244 (2001), 372-376.

[22] Y.C. Lee, et al., "Adsorption and desorption kinetics of CmE8 on impulsively expanded or compressed air-water interfaces," Colloids and Surfaces A-Physicochemical and Engineering Aspects, 220 (2003), 139-150.

[23] S.Y. Lin, et al., "Surface equation of state of nonionic CmEn surfactants," Langmuir, 19 (2003), 3164-3171.

[24] N.J. Alvarez, L.M. Walker, and S.L. Anna, "Diffusion-limited adsorption to a spherical geometry: The impact of curvature and competitive time scales," Physical Review E, 82 (2010).

[25] C.A. Macleod and C.J. Radke, "A Growing Drop Technique for Measuring Dynamic Interfacial-Tension," Journal of Colloid and Interface Science, 160 (1993), 435-448.

[26] C.A. Macleod and C.J. Radke, "Surfactant Exchange Kinetics at the Air-Water-Interface from the Dynamic Tension of Growing Liquid-Drops," Journal of Colloid and Interface Science, 166 (1994), 73-88.

[27] R. Nagarajan, et al., "Controlled Drop Tensiometer for Measuring Dynamic Interfacial and Film Tension," AIChE Journal, 41 (1995), 915-923.

[28] J.D. Martin and S.D. Hudson, "Mass transfer and interfacial properties in two-phase microchannel flows," New Journal of Physics, 11 (2009), 115005.

[29] P. Reis, et al., "Lipases at interfaces: Unique interfacial properties as globular proteins," Langmuir, 24 (2008), 6812-6819.

[30] Y. Rotenberg, L. Boruvka, and A.W. Neumann, "Determination of Surface Tensions and Contact Angles from the Shape of Axisymmetric Interfaces," Journal of the American Oil Chemists Society, 59 (1982), A297-A297.

[31] N.J. Alvarez, L.M. Walker, and S.L. Anna, "A non-gradient based algorithm for the determination of surface tension from a pendant drop: Application to low Bond number drop shapes," Journal of Colloid and Interface Science, 333 (2009), 557-562.

[32] F. Jin, R. Balasubramaniam, and K.J. Stebe, "Surfactant adsorption to spherical particles: The intrinsic length scale governing the shift from diffusion to kinetic-controlled mass transfer," Journal of Adhesion, 80 (2004), 773-796.

[33] M. Hoorfar and A.W. Neumann, "Recent progress in Axisymmetric Drop Shape Analysis (ADSA)," Advances in Colloid and Interface Science, 121 (2006), 25-49.

[34] S.Y. Lin, K. Mckeigue, and C. Maldarelli, "Diffusion-Controlled Surfactant Adsorption Studied by Pendant Drop Digitization," AIChE Journal, 36 (1990), 1785-1795.

[35] N.J. Alvarez, L.M. Walker, and S.L. Anna, "A Microtensiometer to Probe the Effect of Radius of Curvature on Surfactant Transport to a Spherical Interface," Langmuir, 26 (2010), 13310-13319.

[36] R.Y. Tsay, et al., "Adsorption kinetics of C12E8 at the air-water interface: Desorption from a compressed interface," Langmuir, 13 (1997), 3191-3197.

[37] S.Y. Lin, Y.C. Lee, and M.M. Shao, "Adsorption kinetics of C12E6 at the air-water interface," Journal of the Chinese Institute of Chemical Engineers, 33 (2002), 631-643.

[38] B. Faucompre and B. Lindman, "Self-Association of Zwitterionic and Nonionic Surfactants - NMR Self-Diffusion Studies," Journal of Physical Chemistry, 91 (1987), 383-389.

[39] Y.C. Lee, S.Y. Lin, and H.S. Liu, "Role of equation of state on studying surfactant adsorption kinetics," Langmuir, 17 (2001), 6196-6202.

[40] R.N. Pan, J. Green, and C. Maldarelli, "Theory and experiment on the measurement of kinetic rate constants for surfactant exchange at an air/water interface," Journal of Colloid and Interface Science, 205 (1998), 213-230.

[41] S.N. Moorkanikkara and D. Blankschtein, "New methodology to determine the rate-limiting adsorption kinetics mechanism from experimental dynamic surface tension data," Journal of Colloid and Interface Science, 302 (2006), 1-19.

[42] P.G. Nilsson, H. Wennerstrom, and B. Lindman, "Structure of Micellar Solutions of Non-Ionic Surfactants - Nuclear Magnetic-Resonance Self-Diffusion and Proton Relaxation Studies of Poly(Ethylene Oxide) Alkyl Ethers," Journal of Physical Chemistry, 87 (1983), 1377-1385.

[43] M.J. Rosen and D.S. Murphy, "Effect of the Nonaqueous Phase on Interfacial Properties of Surfactants .2. Individual and Mixed Nonionic Surfactants in Hydrocarbon Water-Systems," Langmuir, 7 (1991), 2630-2635.

CHAPTER 8

USING BULK CONVECTION TO REACH KINETIC-LIMITED SURFACTANT DYNAMICS: THEORY AND EXPERIMENTS

8.1 INTRODUCTION

As explained in Chapter 2, there are two processes governing surfactant transport to an interface (reorientation at the interface is ignored). Molecules adsorb and desorb to and from the interface via a kinetic mechanism and molecules diffuse to and from the interface along concentration gradients. We showed in Chapter 4 and 6 that current techniques that measure surfactant dynamics at interfaces operate in a regime where diffusion is the dominating transport mechanism and the kinetic exchange at the interface is too fast to measure. Even using a microtensiometer which reduces the importance of diffusion by measuring surfactant transport to microscale interfaces, see Chapter 4, 5, and 6, a well characterized surfactant $C_{12}E_8$ showed only diffusion-limited behavior [1].

The same surfactant, however, exhibited both kinetic and diffusion dominated dynamics at the silicone oil-water interface, see Chapter 7. In this chapter we introduce bulk convection into the sample cell of the microtensiometer in order to further reduce the length of the diffusion boundary layer and thus the time scale for diffusion. A short background on our current understanding of the impact of convection on adsorbed surfactant molecules and the transport of surfactants to fluid-fluid interfaces is given in Chapter 2. A

Reduction in the time scale for diffusion increases the relevant importance of kinetic transport and potentially leads to measurable kinetic parameters.

In Chapter 4 and 6, we showed through a time scale analysis that a ratio of the diffusion time scale to the kinetic time scale yields a phase diagram that depends on bubble radius and bulk surfactant concentration. Kinetic transport becomes more important at high surfactant concentrations and/or small radii. This scaling analysis is useful in identifying the dominant transport mechanism in dynamic surface tension data.

In the present Chapter, we measure dynamic surface tension as a function of Peclet number for two surfactants, $C_{12}E_8$ and $C_{14}E_8$. We show that the presence of flow near an air-water interface further decreases the characteristic length scale for diffusion, increases the time scale for diffusion, and increases the range of measurable kinetic processes. Dynamic surface tension measurements are compared with a simplified convection-diffusion transport model for both a rigid and a mobile interface. The measured transport parameters at the air-water interface are compared with kinetic parameters previously measured for air-water and silicone oil-water interfaces [2].

8.2 MATERIALS AND METHODS

The microtensiometer has been modified to allow for flow to be generated in the sample cell. The key features of the microtensiometer apparatus are shown schematically in Figure 5.3. A linear fit to the steady velocity data in Figure 5.5 is used to calculate the characteristic velocity in our analysis for all flow rates considered. We show later that the analysis of surfactant dynamics in the

presence of bulk convection does not depend on the specifics of the flow field. Section 5.2.3 describes how experiments are performed and demonstrates that the measurement of surface tension is accurate over all Peclet numbers studied.

Solvents (ACS grade) for cleaning and preparation were purchased and used as received. The nonionic surfactants $C_{12}E_8$ and $C_{14}E_8$ were purchased from Nikko Chemicals (99% purity) and used as received. Surfactant solutions are prepared using deionized water purified using a Barnstead UV Ultrapure II purification system (resistivity of 18.2 MΩ·cm). Stock surfactant solutions are prepared by first melting the pure surfactant at 40°C and then weighing a known mass of surfactant in liquid form. The known mass is diluted to specified concentrations that are below the cmc.

8.3 MODELING MASS TRANSPORT TO AN INTERFACE IN THE PRESENCE OF FLOW

We analyze the influence of convection on the transport of soluble surfactants to an initially clean spherical interface using a simplified transport model. Mass transport is governed by the convection-diffusion equation in spherical coordinates,

$$\frac{\partial C}{\partial t} = \frac{D}{r^2}\left(\frac{\partial}{\partial r}\left(r^2\frac{\partial C}{\partial r}\right)+\frac{1}{\sin\theta}\frac{\partial}{\partial\theta}\sin\theta\frac{\partial C}{\partial\theta}\right)-v_r\frac{\partial C}{\partial r}-\frac{v_\theta}{r}\frac{\partial C}{\partial\theta}, \qquad (8.1)$$

Where C is the concentration in the bulk phase, v_r and v_θ are velocities in the radial and azimuthal directions, respectively, and D is the diffusion coefficient of the surfactant molecule. Scaling Eqn (8.1) by $t \equiv \tilde{t}\,\tau_{Adv}$, $v_r \equiv \tilde{v}_r U_0$, $v_\theta \equiv \tilde{v}_\theta U_0$, $C \equiv C_{bulk}\tilde{C}$, $r \equiv \tilde{r}b$, and $\theta \equiv \tilde{\theta}\varphi$, where τ_{Adv} is the

convection-diffusion time scale, U_0 is a characteristic velocity, b is the radius of the interface, C_{bulk} is the bulk surfactant concentration, and φ is the central angle of a spherical cap, leads to the dimensionless form

$$\frac{\partial \tilde{C}}{\partial \tilde{t}} = \frac{1}{\tilde{r}^2}\left(\frac{\partial}{\partial \tilde{r}}\left(\tilde{r}^2 \frac{\partial \tilde{C}}{\partial \tilde{r}}\right) + \frac{1}{\varphi^2 \sin\tilde{\theta}} \frac{\partial}{\partial \tilde{\theta}} \sin\tilde{\theta} \frac{\partial \tilde{C}}{\partial \tilde{\theta}}\right) - \mathrm{Pe}\left(\tilde{v}_r \frac{\partial \tilde{C}}{\partial \tilde{r}} + \frac{\tilde{v}_\theta}{\tilde{r}} \frac{\partial \tilde{C}}{\partial \theta}\right), \qquad (8.2)$$

where $\mathrm{Pe} \equiv \mathrm{U}_0 b/D$ and $\tau_{Adv} = b^2/D$. Our experiments probe the following range of conditions are 0.05 cm/s<U_0< 2 cm/s and 10 μm<b<200 μm and the molecular diffusion coefficient for $C_{12}E_8$ and $C_{14}E_8$ are 3.8×10^{-10} and 3.7×10^{-10} m^2/s, respectively. Thus, the full range of Peclet numbers for our experimental conditions are $13 \le \mathrm{Pe} \le 10000$. At Pe>>1, the concentration boundary layer, δ, depends solely on the radius of curvature and Peclet number.

Analysis of the concentration boundary layer for mass transport coupled with uniform flow past a hard sphere has been described previously by [3, 4]. For surfactant laden interfaces the velocity on the bubble interface is immediately coupled with the number of surfactant molecules adsorbed to the interface, since convection can sweep surfactants along an interface: forming concentration and thus surface tension gradients, i.e., Marangoni effects [3, 5-7]. The Marangoni stresses due to surface tension gradients can counter balance the tangential stresses from the flow and cause an otherwise mobile fluid-fluid interface to become rigid [7-9].

Rather than analyze the full coupled transport problem, we assume that the velocity on the interface will lie somewhere between a fully mobile interface (shear stress = 0, no surfactant) and a rigid interface ($v_i = 0$, Marangoni stresses)

[3]. When $\delta << b$, the effective concentration boundary layer for uniform flow past a rigid sphere ($\mathrm{Re} < 1$) is given by [3],

$$\delta_R \approx \sqrt[3]{\frac{4Db^2}{3U}} = \left(\frac{4}{3Pe}\right)^{\frac{1}{3}} b . \tag{8.3}$$

The effective concentration boundary layer for uniform flow past a mobile interface is given by [3],

$$\delta_M \approx \sqrt{\frac{\pi bD}{3v_0}} = \left(\frac{2\pi}{3Pe}\right)^{\frac{1}{2}} b . \tag{8.4}$$

We examine the influence of concentration on the transport of surfactant to a spherical interface by using the approximations of the boundary layer thickness given in Eqns (8.3) and (8.4) as the length scale over which diffusion occurs. Specifically, we assume that Fick's law is followed within the boundary layer and is given by

$$\frac{\partial C}{\partial t} = \frac{D}{r^2}\frac{\partial}{\partial r}\left(r^2 \frac{\partial C}{\partial r}\right), \tag{8.5}$$

subject to boundary conditions,

$$\frac{\partial \Gamma}{\partial t} = D\left.\frac{\partial C}{\partial r}\right|_{r=b} \tag{8.6}$$

$$C\big|_{r=\delta} = C_{bulk} . \tag{8.7}$$

The Dirichlet condition Eqn (8.7) states that at a distance greater than δ the concentration in the bulk is uniform and equal to the bulk concentration. The value of δ is determined from Eqns (8.3) and (8.4) depending on whether the

interface is approximated as rigid or mobile, respectively. The relationship between surface concentration, Γ, and the concentration immediately adjacent to the interface, $C\big|_{r=b} = C_s$ is given by an isotherm such as the Generalized Frumkin isotherm,

$$\Gamma(t) = \frac{C_s(t)\Gamma_\infty}{C_s(t) + a\exp\left(\kappa\left(\frac{\Gamma}{\Gamma_\infty}\right)^n\right)}. \tag{8.8}$$

Eqns (8.5) and (8.6) are simultaneously solved numerically subject to Eqns (8.7) and (8.8) .

The equations described above consider only convection-diffusion and assumes that the kinetic-exchange of surfactant at the interface is much faster than transport via diffusion. Recall that the goal of this work is to use convection to reduce the boundary layer to increase the importance of kinetic transport and experimentally measure kinetic rate constants. Therefore, it is important to understand the influence of kinetic transport on dynamic surface tension when the boundary layer is reduced to a length scale where the time scale for diffusion and kinetics are comparable [10]. To account for kinetic transport in the convection model described above the kinetic rate equation is substituted for Eqn (8.8) . The generalized Frumkin rate equation is given by,

$$\frac{\partial\Gamma}{\partial t} = \beta C_s(t)\Gamma_\infty\left(1 - \frac{\Gamma}{\Gamma_\infty}\right) - \alpha\Gamma\exp\left(\kappa\left(\frac{\Gamma}{\Gamma_\infty}\right)^n\right). \tag{8.9}$$

To model the full problem where diffusion and kinetics are taken into account, Eqns (8.5) and (8.6) are numerically solved simultaneously subject to Eqns (8.7) and (8.9) .

A collocation (spectral) method is used to solve the governing equations for mass transfer to a fluid-fluid interface discussed above. Time is discretized using an implicit Euler scheme. Convergence is reached/achieved when there is less than 10^{-6} deviation in $\gamma(t)$. The numerical scheme and its validation are discussed elsewhere [10].

8.4 **RESULTS**

Relaxation of surface tension with time due to adsorption of $C_{14}E_8$ to an initially clean interface is measured in the presence of bulk convection using two different bubble radii and a range of flow rates. The results are presented in Figure 8.6. Figure 8.6a shows the surface tension evolution as a function of time for a 60 μm radius, a fixed $C_{bulk} = 0.0025$ mol/m^3 (0.25% CMC), and different pump flow rates. Figure 8.6b shows the surface tension evolution as a function of time for a 185 μm radius, a fixed $C_{bulk} = 0.0025$ mol/m^3 (0.25% CMC), and different pump flow rates. Flow rate increases from left to right. Clean bubbles are formed by pushing a steady stream of air out of the capillary so that all dynamic surface tension measurements start from a clean interfacial tension value for air/water γ_0 = (73.2 ± 0.25) mN/m and decrease to an equilibrium surface tension value of γ_{eq} = (45.0 ± 0.38) mN/m. The time required to reach equilibrium changes significantly with flow rate. In Figure 8.6a, the time is shifted by a factor of two or three from the furthest curve on the right (flow rate = 0) to the furthest on the left (flow rate = 0.28 cm^3/s). In Figure 8.6b, the time is

shifted by a factor of ten from the furthest curve on the right (flow rate = 0) to the furthest on the left (flow rate = 0.30 cm^3/s).

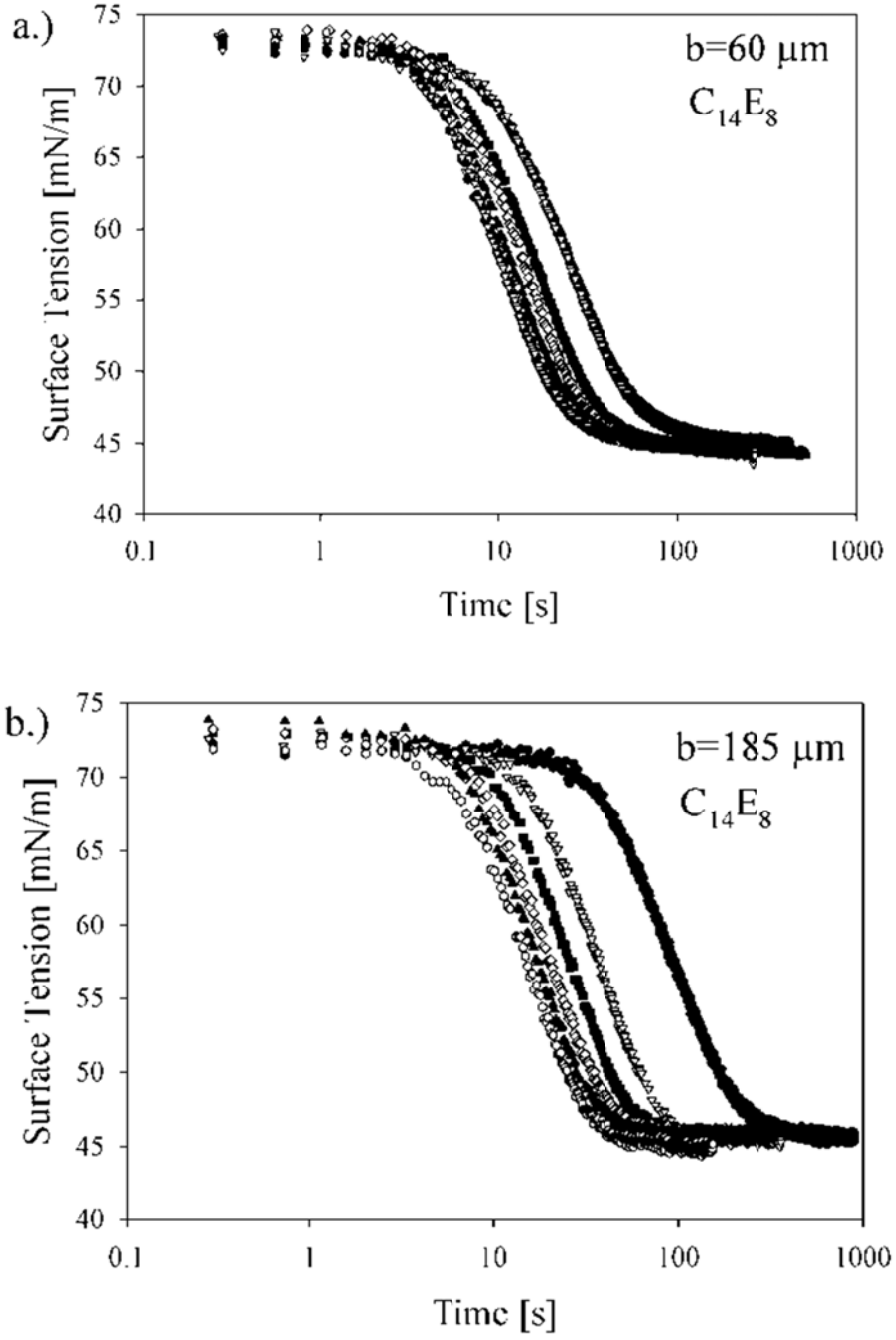

Figure 8.6. Dynamic surface tension for a fixed surfactant concentration, C_{bulk} = 0.0025 mol/m^3, at different flow rates (increasing flow rate from right to left) for a.) b=60 um and b.) b=185 um.

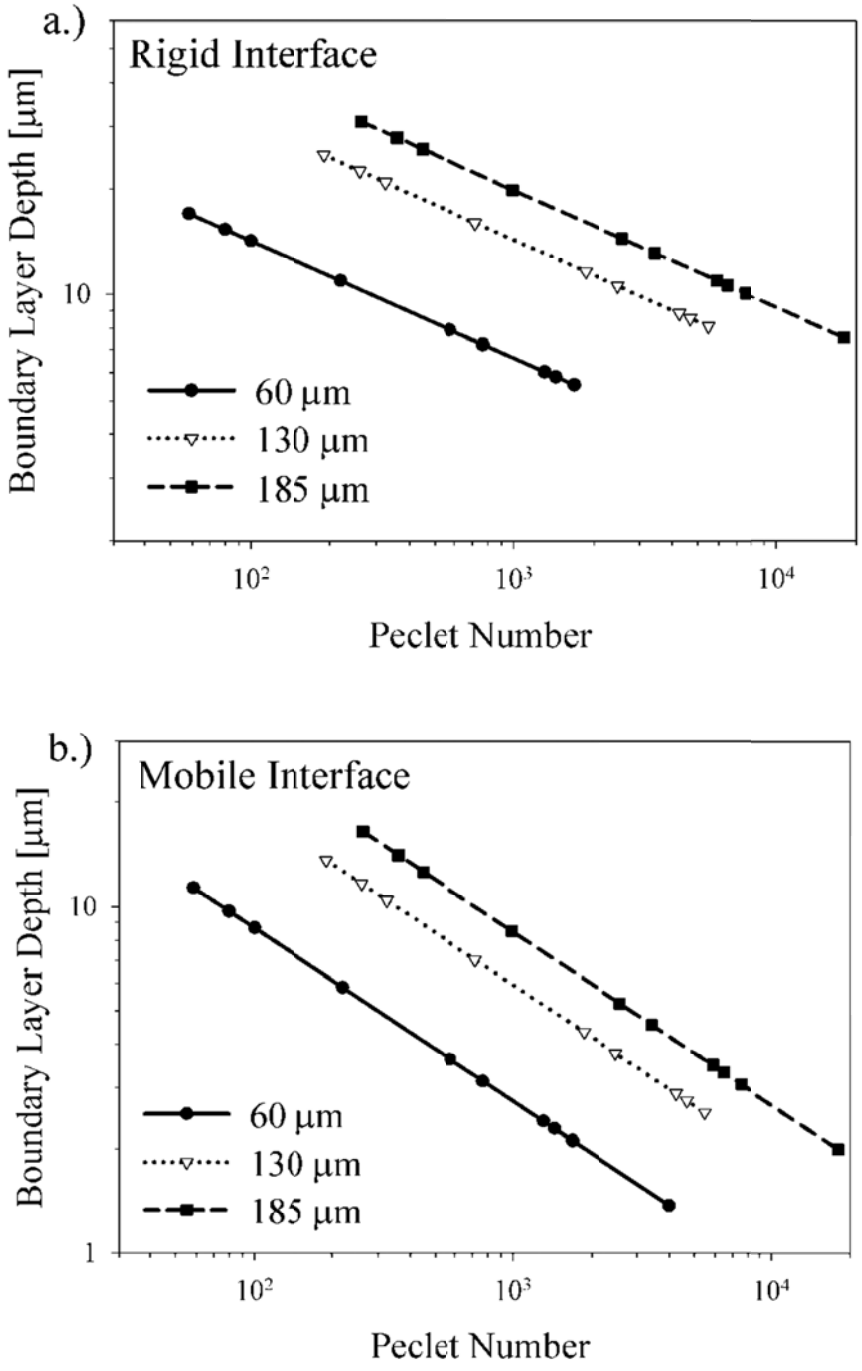

Figure 8.7. Diffusion boundary layer as a function of Peclet number for $C_{14}E_8$ for different interface radii for a rigid (a) and mobile (b) interface using Eqn (8.3) and (8.4) .

Figure 8.7 shows the dependence of the boundary layer on Peclet number for D=4×10^{-10} m^2/s. As expected, the magnitude of the boundary layer is smaller for a mobile interface, Figure 8.7b, than for a rigid interface, Figure 8.7a. The boundary layer follows a power law dependence on Peclet number for both a rigid and mobile interface. Since the diffusion time scale depends explicitly on the length of the boundary layer[10], we expect that dynamic surface tension curves would shift to shorter time scales for increasing Peclet numbers.

Using the convection-diffusion model described above and parameters for $C_{14}E_8$, Figure 8.8 shows dynamic surface tension curves for a range of Peclet numbers. The Peclet numbers correspond to experimentally feasible velocities and bubble radii. Figure 8.8a shows dynamic surface tension curves for a rigid interface. Figure 8.8b shows dynamic surface tension curves for a mobile interface. As expected, there is a shift in the time scale for low Peclet numbers. However, the shift in time scale to reach equilibrium decreases for increasing Peclet number. This is better seen from a plot of the time to reach a given surface tension, γ_t, for the curves in Figure 8.8a and b. Figure 8.9 shows the time to reach γ_t = 60 mN/m for each curve represented in Figure 8.8 . The time scale has a power law dependence in Peclet number as expected from Eqns (8.3) and (8.4) .

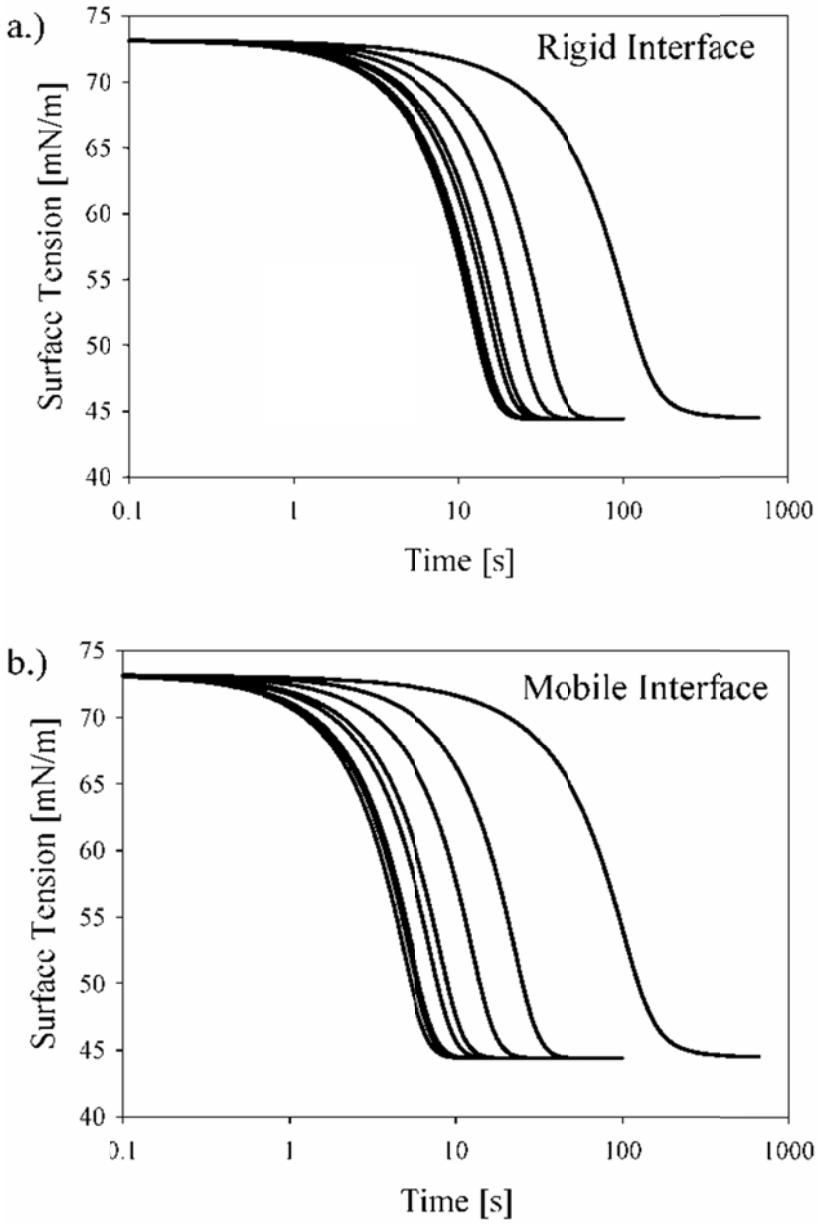

Figure 8.8. Theoretical dynamic surface tension curves for $C_{14}E_8$ calculated using diffusion depths from Peclet # analysis for rigid and mobile interfaces: $b = 60$ μm and $C_\infty = 0.0025$ mol/m^3.

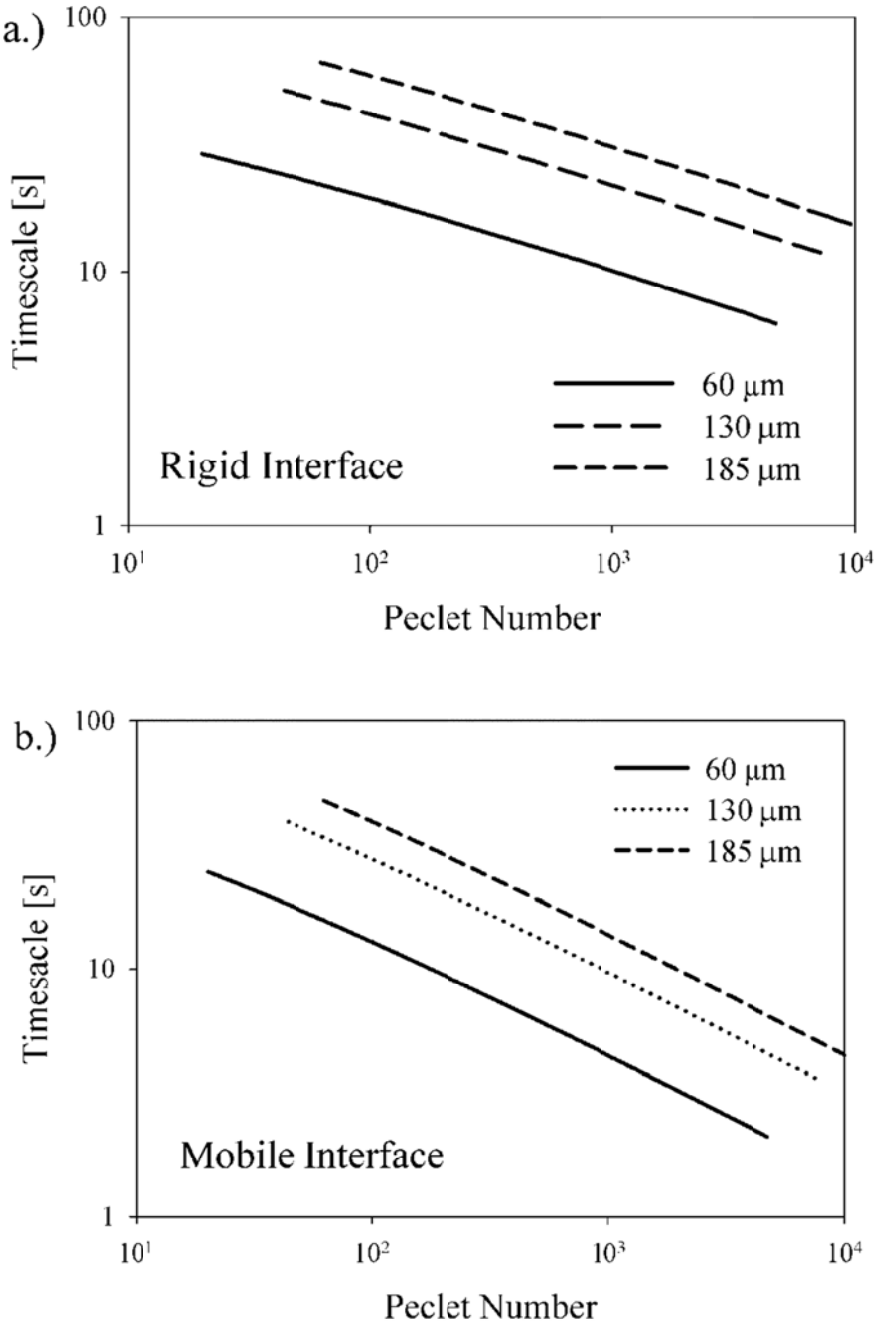

Figure 8.9. Theoretical time scale as a function of Peclet number determined for $\gamma_{eq} = 60$ mN/m for different flow velocities and three different radii for a rigid (a) and mobile (b) interface.

The time required to reach $\gamma_t = 60$ mN/m for the $C_{14}E_8$ experimental data presented in Figure 8.6a and b is plotted in Figure 8.10 as a function of Peclet number. Figure 8.10 shows data for three concentrations and two radii on a log-log scale. Note that the curves have been shifted vertically so that all lie in the same time scale range. In Figure 8.10 the experimental time scale is compared with two convection-diffusion models. The solid lines correspond to the convection-diffusion model for a rigid interface. The dashed lines correspond to the convection-diffusion model for a mobile interface. The experimental data follows the power law dependence of the convection-diffusion time scale for a rigid interface.

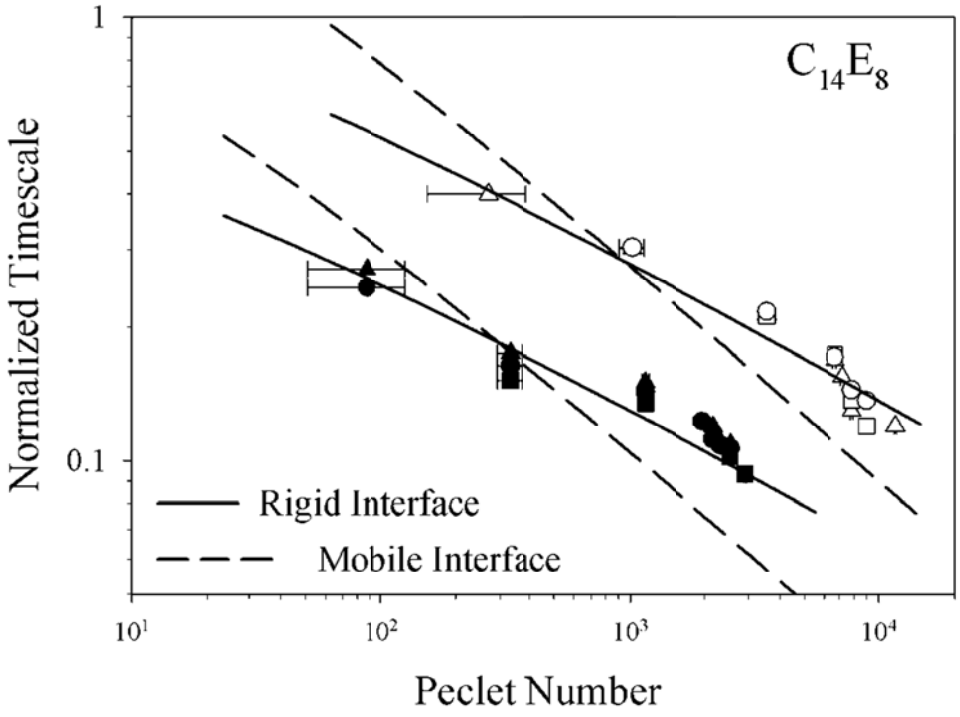

Figure 8.10. Comparison of experimental time scale for three concentrations (● 0.0025 mol/m^3 , ■ 0.003 mol/m^3 , and ▼0.004 mol/m^3) and two radii (filled symbols $b =$ 60 μm and open symbols $b =$ 185 μm) with two convection transport models for a rigid interface and a mobile interface.

Figure 8.11 shows the time scale required to reach $\gamma_t =$ 60.0 mN/m for $C_{12}E_8$ at two radii, 60 and 130 μm, and a concentration of $C_{bulk} = 0.003$ mol/m^3 for both radii and 0.0018, 0.0025, 0.0052, and 0.010 mol/m^3 for $b = 60$ μm as a function of Peclet number. Figure 8.11 compares experimental data with two convection-diffusion models. The solid lines correspond to the convection-diffusion model for a solid interface. The dashed lines correspond to the convection-diffusion model for a mobile interface. The experimental data follows the power law dependence of the convection-diffusion time scale for a rigid interface.

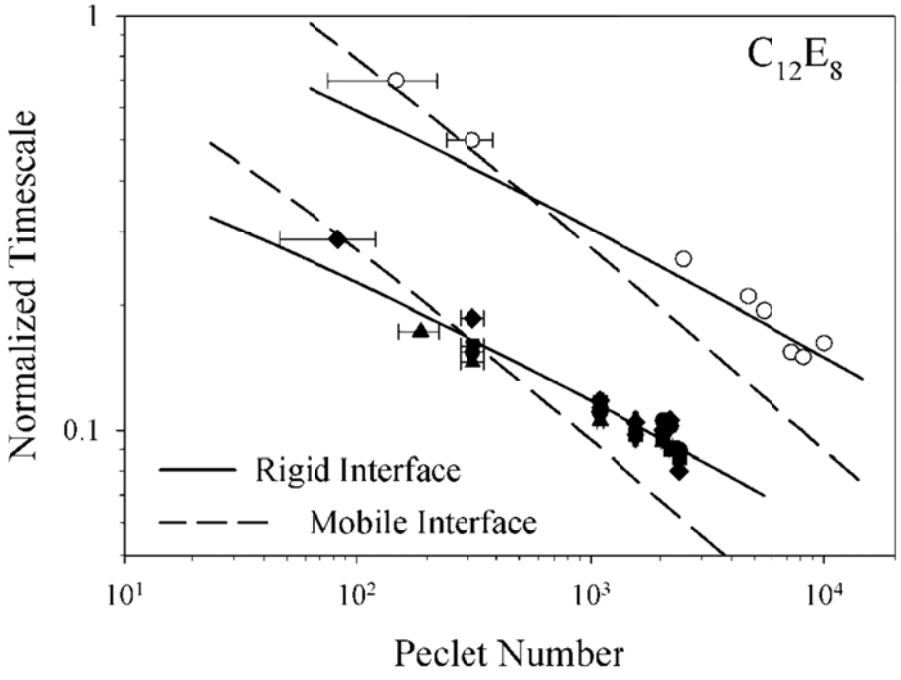

Figure 8.11. Comparison of experimental time scale for five concentrations (▲0.0013 mol/m^3, ▼0.0025 mol/m^3 , ● 0.0037 mol/m^3 , ■ 0.0052 mol/m^3, and ◆ 0.01 mol/m^3) and two radii (filled symbols $b =$ 60 μm and open symbols $b =$ 130 μm) with two convection transport models for a rigid interface and a mobile interface.

Lastly, Figure 8.12 shows the time scale from simulations as a function of Peclet number from Figure 8.9 corresponding to $b = 185$ μm for a rigid and mobile interface and time scales for the mixed kinetic-convection rigid interface model using $C_{14}E_8$ parameters and an adsorption constant, $\beta = 15$ m^3/(mol·s), for two radii $b = 60$ and $b = 185$ μm. Note that the curves in Figure 8.12 have been shifted vertically so that all lie in the same time scale range. Figure 8.12 shows for two radii that the time scale no longer follows a power law dependence when the magnitude of the kinetic time scale is comparable to the convection-diffusion time scale. When the dynamics are kinetic-limited the time scale is independent of Peclet number.

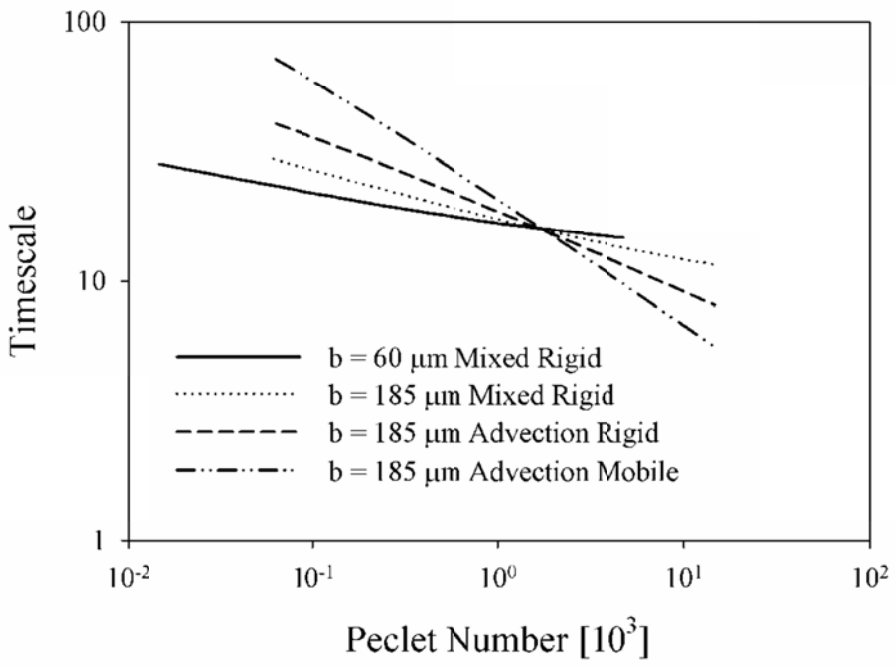

Figure 8.12. Time scale to reach a specific surface tension value as a function of Peclet number for diffusion limited dynamics for a rigid and mobile interface and for mixed dynamics for a rigid interface and two different radii.

8.5 **DISCUSSION**

The simulations presented in Figure 8.8a and b are calculated at the same conditions as the experiments presented in Figure 8.6a, i.e., same bubble radius, concentration, and bulk velocities. A Comparison of numerical simulations with experiments reveals that the trends for both are similar. For example, both simulations and experiments show that as the bulk velocity increases the surface tension dynamics shift to faster time scales. The shift at lower velocities is greater than the shift observed at higher velocities. The dynamic surface tension curves in Figure 8.8a calculated for flow past a rigid interface**,** show quantitative agreement with the dependence of experimental time scales on Peclet number. This suggests that the concentrations are too low and Peclet numbers are too large to observe remobilization of the interface.

Figure 5.5 shows that there is a transition from a steady regime to an unsteady regime in the flow field. A linear fit of the steady velocity region was used to determine the characteristic velocity used in determining the Peclet numbers for the different experiments. From Figure 5.5 it is clear that in the unsteady regime, the measured velocity depends on the location in the cell and the time the measurement is taken (data not shown). Even so, the velocity determined from the best fit line is sufficient to capture the dependence of time scale on Peclet number. This result suggests that the analysis of dynamic surface tension in the presence of flow does not depend strongly on the specifics of the flow field.

Previous studies have reported that both $C_{12}E_8$ and $C_{14}E_8$ have values of $\beta \approx 5$ $m^3/(mol \cdot s)$ [11-13]. However, in a previous study, using the microtensiometer, $\beta > 5$ $m^3/(mol \cdot s)$ [1, 10]. The present study aims to measure kinetic dominated dynamics by reducing the diffusion boundary layer using convection. However, Figure 8.10 and Figure 8.11 show that kinetics is not important at the air/water interface for micron scale radii and large Pe numbers. Thus, the rate constants cannot be quantitatively determined. However, we showed previously that diffusion-limited data can be used to determine a lower limit on β using a one parameter fitting routine [2]. Figure 8.13 shows the best fit parameters for $C_{12}E_8$ and $C_{14}E_8$ determined from a fit of the kinetic rate equation, Eqn (8.9) , to the fastest dynamics, i.e. experiments performed for the smallest bubble radius and largest bulk velocities for a given bulk surfactant concentration. The lines correspond to the lower limit of β for both surfactants, $\beta > 17.1$ and $\beta > 23.3\, m^3/(mol \cdot s)$ for $C_{12}E_8$ and $C_{14}E_8$, respectively.

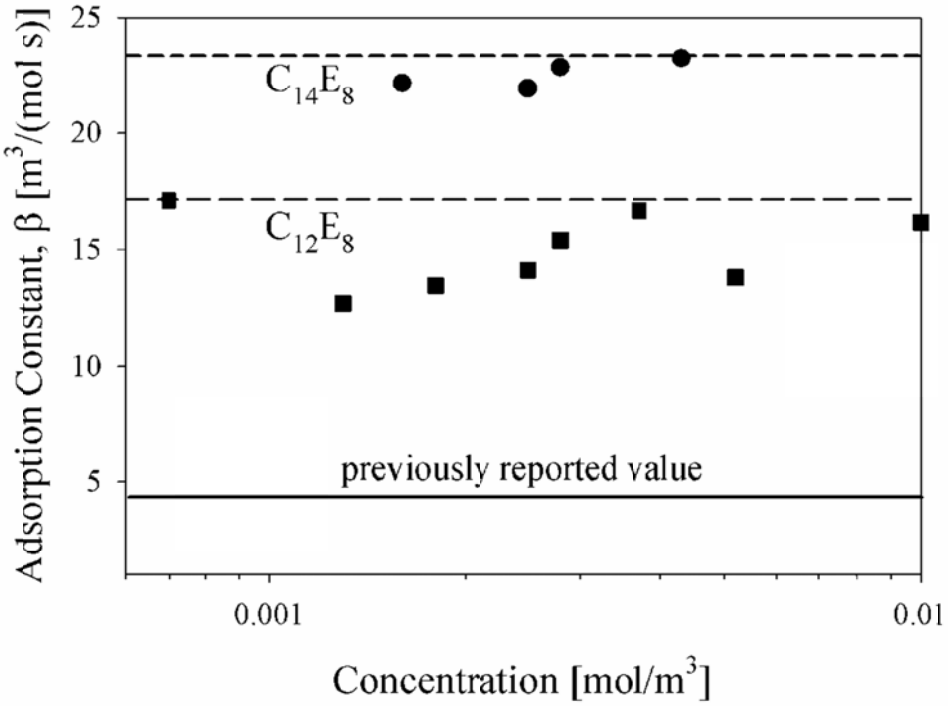

Figure 8.13. Best fit adsorption constant, β, for diffusion-limited experiments at different surfactant concentrations for both $C_{12}E_8$ and $C_{14}E_8$. The dashed lines correspond to the lower limit on β for both surfactants, $\beta > 17.1$ and $\beta > 23.3$ m^3/(mol s), respectively. The solid line corresponds to the previously reported value of β for both $C_{12}E_8$ and $C_{14}E_8$.

There are practical limits to the values of capillary number, Pe number, and the Re number observable in convection experiments: constraining the range of adsorption constants measurable. When the capillary number, $\mathrm{Ca} = \mu U/\gamma$, is large, the interface shape is distorted by the flow field and is no longer spherical. At the highest velocity studied here (U_0=0.025 m/s), $\mathrm{Ca} \approx 0.001$. When Ca>> 0.001, we observed that the drop shape becomes unsteady and is blown from the tip of the capillary. Therefore, the Ca restricts the experimentally feasible velocities. The power law dependence of the effective diffusion boundary layer on Pe also imposes a practical limit. From Figure 8.7, orders of magnitude

changes in Peclet number are required to see a significant reduction in δ. The velocities required to achieve such high Pe would result in Reynolds numbers that violate the assumption of Stokes Flow past a sphere and thus Eqns (8.3) and (8.4) become impracticable. Furthermore, at turbulent conditions it is well known that the effective boundary is larger than the laminar flow case [3]. Thus, it is unlikely that the kinetic rate constants for $C_{12}E_8$ and $C_{14}E_8$ at the air/water interface can be measured using convection experiments because of the large velocities required to increase the range of measurable adsorption constants.

We showed previously that both $C_{12}E_8$ and $C_{14}E_8$ both exhibit measurable kinetics at the silicone oil-water interface [2]. The adsorption rate constants for $C_{12}E_8$ and $C_{14}E_8$ at the silicone oil-water interface were determined from a one parameter fit, $\beta = 22.1 \pm 2.3$ and 9.42 ± 4.27 $m^3/(mol \cdot s)$, respectively. From this study we can conclude that the adsorption rate constant is larger for $C_{14}E_8$ and most likely larger for $C_{12}E_8$ at the air-water interface than at the silicone oil-water interface. This suggests that the kinetic barrier is much smaller for the air-water interface and can be ignored for $C_{12}E_8$ and $C_{14}E_8$ in both diffusion and convection scenarios at air-water interfaces involving micron scale interfaces and moderate fluid velocities. Furthermore, the lower bounds can be used as a lower limit calculation to determine the relative importance of kinetics to diffusion in different experimental scenarios.

8.6 SUMMARY

The presence of bulk convection reduces the thickness of the diffusion boundary layer during dynamic surface tension studies and increases the range of measureable kinetic parameters. No transition from diffusion limited to mixed or kinetic-limited dynamics is observed for $C_{12}E_8$ and $C_{14}E_8$ at the air/water interface for $Pe < 10^5$. Using a kinetic-limited model, lower bounds on the adsorption coefficient were determined for both surfactants. The kinetic adsorption coefficients for $C_{12}E_8$ and $C_{14}E_8$ are greater than $\beta > 17$ and $\beta > 23$ $m^3/(mol \cdot s)$, respectively. These values are considerably larger than the values reported in the literature and suggest that previously reported values are underestimates due to the complexity of extracting kinetic data from diffusion controlled processes.

The experiments and analysis described in this manuscript are instrumental in quantifying the importance of kinetic transport in dynamic surface tension data and increasing the range of measurable kinetic parameters. The results and analysis are not strongly dependent on the specifics of the flow field, suggesting that this technique is easily applicable to microscale techniques and also that convection likely impacts the transport regime experienced in multiphase processes involving surfactants. The observation that liquid-fluid interfaces behave rigidly over a wide range of surface concentrations of adsorbing surfactants confirms the importance of Marangoni stresses in altering the mobility of surfactant-laden interfaces and the need to understand transport of soluble surfactants to these interfaces in processes where interface mobility is critical.

[1] N.J. Alvarez, L.M. Walker, and S.L. Anna, "A Microtensiometer To Probe the Effect of Radius of Curvature on Surfactant Transport to a Spherical Interface," Langmuir, 26 (2010), 13310-13319.

[2] N.J. Alvarez, L.M. Walker, and S.L. Anna, "The Effect of Alkane Tail Length of CiE8 Surfactants on Transport to the Silicone Oil-Water Interface," Journal of Colloid and Interface Science, 355 (2011), 231-236.

[3] V.G. Levich, *Physicochemical hydrodynamics : Veniam G. Levich ; translated by Scripta Technica Inc* (Prentice-Hall, Englewood Cliffs, N.J., 1962).

[4] P.O. Brunn, "Heat or Mass-Transfer from Single Spheres in a Low Reynolds-Number Flow," International Journal of Engineering Science, 20 (1982), 817-822.

[5] C.D. Eggleton and K.J. Stebe, "An adsorption-desorption-controlled surfactant on a deforming droplet," Journal of Colloid and Interface Science, 208 (1998), 68-80.

[6] D.A. Edwards, H. Brenner, and D.T. Wasan, *Interfacial transport processes and rheology* (Butterworth-Heinemann, Boston, Mass., 1991).

[7] H.A. Stone and L.G. Leal, "The Effects of Surfactants on Drop Deformation and Breakup," Journal of Fluid Mechanics, 220 (1990), 161-186.

[8] K.J. Stebe and C. Maldarelli, "Remobilizing Surfactant Retarded Fluid Particle Interfaces .2. Controlling the Surface Mobility at Interfaces of Solutions Containing Surface-Active Components," Journal of Colloid and Interface Science, 163 (1994), 177-189.

[9] K.J. Stebe, S.Y. Lin, and C. Maldarelli, "Remobilizing Surfactant Retarded Fluid Particle Interfaces .1. Stress-Free Conditions at the Interfaces of Micellar Solutions of Surfactants with Fast Sorption Kinetics," Physics of Fluids a-Fluid Dynamics, 3 (1991), 3-20.

[10] N.J. Alvarez, L.M. Walker, and S.L. Anna, "Diffusion-limited adsorption to a spherical geometry: The impact of curvature and competitive time scales," Physical Review E, 82 (2010).

[11] Y.C. Lee, et al., "Adsorption and desorption kinetics of CmE8 on impulsively expanded or compressed air-water interfaces," Colloids and Surfaces A-Physicochemical and Engineering Aspects, 220 (2003), 139-150.

[12] S.Y. Lin, et al., "Adsorption kinetics of C12E8 at the air-water interface: Adsorption onto a clean interface," Langmuir, 12 (1996), 6530-6536.

[13] R.Y. Tsay, et al., "Adsorption kinetics of C12E8 at the air-water interface: Desorption from a compressed interface," Langmuir, 13 (1997), 3191-3197.

CHAPTER 9

TRANSPORT AND INTERFACIAL RHEOLOGY OF GRAFTED NANOPARTICLES AT THE AIR-WATER AND XYLENE-WATER INTERFACE: MECHANISM FOR EMULSION STABILIZATION

9.1 INTRODUCTION

The microtensiometer described in Chapter 3 has a number of advantages over other surface tension measuring techniques. Namely that it requires considerably less volume of solution to make accurate surface tension measurements and increases the rate of transport of species to the interface by measuring surface tension at microscale interfaces. The latter advantage is specifically beneficial for novel macromolecular species that are not available in large quantities. This chapter focuses on quantifying the transport of polymer grafted nanoparticles to the air-water and xylene-water interface. These particles were previously found to be very efficient emulsifiers.

It is well known that finely divided colloidal particles are very effective at stabilizing emulsions against coalescence [1]. These emulsions are referred to as Pickering emulsions. In the case of bare particles, the type and stability of the emulsion formed depends on the contact angle made at the three phase contact line: an obtuse angle against the solid phase facilitates stabilization. The high stability of Pickering emulsions is due to the large adsorption energy of the particle to the interface. The adsorption energy scales with the square of the particle radius. Larger particles are more strongly adsorbed than nanoparticles and therefore micron sized particles are more effective emulsifiers.

Recently it was shown that adsorbing or grafting surface-active polymers to the surface of nanoparticles makes for extremely efficient emulsifiers. Grafted nanoparticle concentrations as low as 0.04wt% are sufficient to stabilize large volume fraction emulsions for many months [2, 3]. The parameter space that impacts the stabilizing properties of polymer grafted nanoparticles is very large and includes temperature, salt concentration, pH, etc. [3]. In this paper, we concentrate on 20 nm diameter silica nanoparticles grafted with poly(2-(dimethyl-amino)ethyl methacrylate), PDMAEMA, in 10 mM NaCl at 20^{o}C and pH 7.5. The particles are synthesized using atom transfer radical polymerization (ATRP) to control the grafting density (chains/nm^2). Two grafting densities are investigated: low density (0.41 chains/nm^2), abbreviated LGD, and high density (1.27 chains/nm^2), abbreviated HGD.

The mechanism of polymer-grafted nanoparticle emulsification has not been examined in detail. Currently, the enhanced emulsification characteristics of polymer grafted nanoparticles relative to bare particles is attributed to the surface activity of the polymer chains. Whereas bare silica particles do not reduce the interfacial (liquid-liquid interface) or surface (liquid-air surface) tension, grafted nanoparticles do lower the surface tension because of the surface active polymer tethered to the surface. This paper focuses on measuring the transport and dilatational elasticity of PDMAEMA grafted silica nanoparticles to the air-water and xylene-water interface and comparisons are made to homopolymer and bare silica particles [4].

We hypothesize that the stability of grafted nanoparticles at very low concentrations can be attributed to the reduction of interfacial tension and the existence of a Gibbs (dilatational) modulus. The reduction in surface tension acts to prevent coalescence due to Ostwalde ripening [5] and the existence of a Gibbs modulus helps to stabilize against coalescence. For two droplets to coalescence, they must get close enough to each other that a thin film forms between them. Whether or not the droplets coalesce depends on whether the thin film between the droplets thins faster than diffusion or convection drives the droplets away from each other. It is known that the film drainage time increases with larger dilatational modulus [6]. Conclusions are drawn by comparing the transport, equilibrium surface tension, and interfacial rheological measurements for free homopolymer and two grafted nanoparticle systems with different grafting densities: LGD and HGD.

The transport of PDMAEMA grafted nanoparticles to the air-water and xylene-water interface is measured using a recently-developed microtensiometer. The details of this device are provided in Chapter 5 [7]. The microtensiometer requires far less volume than traditional surface tension measuring instruments and reduces the time scale to reach equilibrium because of the dependence of diffusion on interface radius [8]. The microtensiometer is configured to measure the dilatational modulus by oscillating the pressure behind the interface

9.2 SURFACE TENSION AND DILATATIONAL MODULUS MEASUREMENTS

There are two rheological properties of a fluid-fluid interface: interfacial shear viscosity and the dilatational or Gibbs elasticity (modulus) [6]. The shear viscosity is measured by applying a rheological flow to the interface in an analogous fashion to that performed in bulk rheological measurements [9-12]. In this measurement, the area of the interface is kept constant [6]. Dilatational elasticity measurements are made by measuring the change in stress due to a change in the surface area of the interface [6]. We focus on the measurement of the dilatational modulus.

A number of instruments have been developed to measure the dilatational modulus [6, 11, 13-16]. The first measurements were performed by Gibbs on soap films. Gibbs showed that the elasticity of a soap film is related to the change in surface tension over a change in surface area of the interface. The Gibbs elasticity is defined as

$$E_G = 2\frac{\partial \gamma}{\partial \ln A}, \tag{9.1}$$

where γ is the surface tension and A is the surface area. The factor of two is because there are two interfaces for a soap film. For a bubble or drop, the dilatational modulus is given by $E_D = \partial\gamma/\partial \ln A$.

The dilatational modulus is traditionally measured by imposing a sinusoidal oscillation to the surface area of a drop or bubble. The response in surface tension is recorded. If the strain is small, i.e. $\Delta A/A_0 << 0.10$, then Eqn (9.1) reduces to

$$E_D = \frac{\partial \gamma}{\partial \ln A} \approx \frac{\Delta \gamma}{\Delta A / A_0}, \tag{9.2}$$

where A_0 is the initial or mean area of the sinusoidal disturbance. The dilatational modulus is measured using an oscillating pressure pump attached to the inside of the capillary. The setup is described in detail in Chapter 5.

9.3 MATERIALS AND METHODS

The high and low grafting density particles were synthesized in a typical surface-initiated ATRP reaction as described previously [3]. Both the high grafting density particles, HGD, and low grafting density particles, LGD, were fully characterized in Ref. [3] and their properties are summarized in Table 1. All HGD and LGD particle solutions were prepared in 10 mM NaCl solutions. NaCl (ACS Grade, Fisher Scientific) was purchased and used as received. Particle diameter and diffusion coefficient were measured from dynamic light scattering measurements. 10 nm diameter bare silica nanoparticles were purchased from Ludox and diluted to a 1 wt% solution (Ludox-SM). All experiments were performed at room temperature, 20^{o}C. All water was purified to a resistivity of 18.2 MΩ·cm using a Barnstead Millipore filtration system. Xylene (mixture of isomers, extra-pure grade) was purchase from Acros Chemicals and used as received. PDMAEMA homopolymer was synthesized via ATRP synthesis with MW= 44000 g/mol and characterized previously [3]. Solutions of PDMAEMA homopolymer were prepared in 10 mM NaCl solutions.

	Grafting Density †	Diam.	MW grafted PDMAEMA†	PD†	Fraction of polymer/particle†	Diff. Coeff.
	(chain/nm^2)	(nm)	(g/mol)		g/g	(m^2/s)
High Grafting Density	1.27	91.4	19,400	1.14	0.875	4.7×10^{-12}
Low Grafting Density	0.41	53.1	16,000	1.25	0.671	8.1×10^{-12}

Table 9.1. Properties and characterization of high and low grafting density particles. † See Ref. [3] for specifics on how these quantities were measured

Two types of experiments will be performed to characterize the transport and stability of PDMAEMA grafted nanoparticles at the air-water and xylene-water interface. Dynamic surface tension measurements, surface tension as a function of time $\gamma(t)$, are made to characterize the transport of particles and homopolymer from the bulk to the interface for different bulk concentrations. Dilatational measurements, surface tension as a function of time and frequency $\gamma(\omega,t)$, are made to determine the dilatational modulus for different concentrations of homopolymer, LGD, and HGD particles.

9.4 EFFECT OF PARTICLES ON DILATATIONAL MODULUS

The change in dilatational elasticity from a homopolymer covered interface to a grafted nanoparticle laden interface can be explained using a model first described by Lucassen [17, 18]. The following derivation is taken from Ref. [17]. If we assume that the applied strain is so small that viscous and inertial forces can be neglected as compared with surface forces and the effect of line tension is ignored, then while the dilational modulus, ε, can vary widely between

the different components of the surface (solid, fluid) the tension, γ, should be uniform at a sufficiently small deformation. If we take the case, where the surface consists of two components 1 and 2, then

$$\gamma_1 = \gamma_2 \tag{9.3}$$

and

$$d\gamma_1 = d\gamma_2 . \tag{9.4}$$

A combination of Eqns (9.3) and (9.4) with the definition of the dilational modulus (9.2) yields

$$\varepsilon_1 \frac{dA_1}{A_1} = \varepsilon_2 \frac{dA_2}{A_2} . \tag{9.5}$$

For a composite surface we then have

$$\varepsilon = \frac{A_{Total} d\gamma}{d\left(A_1 + A_2\right)} \tag{9.6}$$

or

$$\frac{1}{\varepsilon} = \frac{1}{A_{Total}} \left(\frac{dA_1}{d\gamma} + \frac{dA_2}{d\gamma} \right) = \frac{\phi_1}{\varepsilon_1} + \frac{\phi_2}{\varepsilon_2} , \tag{9.7}$$

where ϕ_i represents the area fraction of the surface with dilational modulus ε_i. For the case of spherical particles that are small enough that gravity can be ignored compared with surface forces i.e. small Bond number, the particle will adopt a position at a fluid-fluid interface which is fully determined by the wetting angle, θ. The fractional area occupied by particles when there are n particles per unit surface area is given by,

$$\phi_p = n\pi R^2 \sin^2 \theta , \tag{9.8}$$

where R is the radius of the particle.

The contact angle is related to three surface tensions through Young's law

$$\cos\theta = \frac{\gamma_{SF} - \gamma_{SL}}{\gamma_{LF}}, \tag{9.9}$$

where the subscripts SF, SL and LF represent solid-fluid, solid-liquid, and liquid-fluid. The contact angle determines the area that is occupied by the particle. A change in any three of the surface tensions would cause a change in the contact angle and thus in the area occupied by the particles. In an oscillation experiment, the surface tension is oscillating about the equilibrium surface tension. If we consider that only γ_{LF} changes due to changes in area of the interface, then if we ignore contact angle hysteresis

$$d\theta = \frac{\cos\theta}{\gamma_{LF}\sin\theta} d\gamma_{LF}. \tag{9.10}$$

For an insoluble surfactant or polymer in the interstitial sites of the interface whereby no exchange with the bulk takes place at the frequency of interest, then it is possible to define the change in surface tension in Eqn (9.10) to the tension of the adjoining flat liquid-fluid surface.

Coupling Eqns (9.8) and (9.10) with (9.2) yields a dilatational modulus for the particle covered part of the surface

$$\varepsilon_p = \phi_p \frac{d\gamma_{LF}}{d\phi_p} = \frac{\gamma_{LF}}{2}\tan^2\theta. \tag{9.11}$$

The modulus of the composite surface of particles and the polymer or surfactant in the interstitial sites is given by

$$\frac{1}{\varepsilon} = \frac{2\pi R^2 \cos^2\theta}{\gamma_{LF}} + \frac{1 - n\pi R^2 \sin^2\theta}{\varepsilon_{LF}}, \tag{9.12}$$

or

$$\varepsilon = \frac{\varepsilon_{LF}}{1 + n\pi R^2 \left(\frac{2\varepsilon_{LF} \cos^2 \theta}{\gamma_{LF}} - \sin^2 \theta \right)}, \tag{9.13}$$

where ε_{LF} is the dilatational modulus of the surface in the absence of particles. It is clear from Eqn (9.13) that the presence of partially wetted spherical particles can either increase or decrease the measured dilatational modulus of the entire surface depending on the sign of the term within brackets in Eqn (9.13). When the ratio $\varepsilon_{LF}/\gamma_{LF}$ is very small or when the contact angle is close to $\pi/2$ there will be an increase in the measured modulus in the presence of particles. When the contact angle is close to zero or when $\varepsilon_{LF}/\gamma_{LF}$ is large, the measured dilatational modulus will decrease.

The assumption that the surface tensions of different surface components are the same must be abandoned if the effect of line tension is considered. Instead, if we consider two surface phases, one for the discontinuous phase (particles), $i = 1$, and the surface continuous phase, $i = 2$, where changes in surface tension are measured, then Laplace's law gives the tension difference between the particles and the remaining surface phase

$$\gamma_1 = \gamma_2 - \frac{\tau}{r}, \tag{9.14}$$

where γ_1 and γ_2 are the respective tensions, τ is the line tension, and r is the line's radius of curvature. Substitution of Eqn (9.14) into Eqn (9.7) yields the following equation for the measured dilatational modulus

$$\varepsilon = \frac{\varepsilon_{LF}}{1 + n\pi R^2 \left(\frac{2\varepsilon_{LF} \cos^2\theta}{\gamma_{LF} - \tau / \left(r \tan^2\theta \right)} - \sin^2\theta \right)}. \qquad (9.15)$$

Eqn (9.15) also shows that the measured dilatational elasticity can increase or decrease due to the presence of particles, which again depends on the sign of the bracketed term. When the contact angle is close to $\pi/2$ or when the ratio $\varepsilon_{LF} / \left(\gamma_{LF} - \tau / \left(r \tan^2\theta \right) \right)$ is very small there will be an increase in the measured modulus in the presence of particles. When the contact angle is close to zero or when $\varepsilon_{LF} / \left(\gamma_{LF} - \tau / \left(r \tan^2\theta \right) \right)$ is large, the measured dilatational modulus will decrease.

Equations (9.13) and (9.15) describe expected trends in the measured dilatational modulus measured at fluid-fluid interfaces in the presence of spherical particles. These equations will be used to understand dilatational measurements at the air-water and xylene-water interface.

9.5 RESULTS

9.5.1. AIR-WATER

Dynamic surface tension measurements of 1 wt% bare silica nanoparticle solutions were performed on the microtensiometer. There was no change in surface tension measured. Dilatational measurements also showed no response due to the presence of silica nanoparticles. This confirms the measurements by Okubo on 5-185 nm silica particles made on a completely different apparatus [4]. The elasticity for bare silica nanoparticles are measured as well, but are found to exhibit no measurable dilatational elasticity at the air-water interface.

Figure 9.1 shows surface tension as a function of time for different concentrations of high grafting density, HGD, particles at the air-water interface. At short times, the surface tension is that of clean air-water, 73.2 mN/m. As time progresses and particles adsorb to the interface, the surface tension decreases until the number of molecules on the interface is constant and the process has reached equilibrium. At these times the surface tension is no longer changing with time and we measure the equilibrium surface tension. The rate of change in surface tension with time shifts to faster time scales for larger concentrations of particles. The equilibrium surface tension is not a function of the particle concentration.

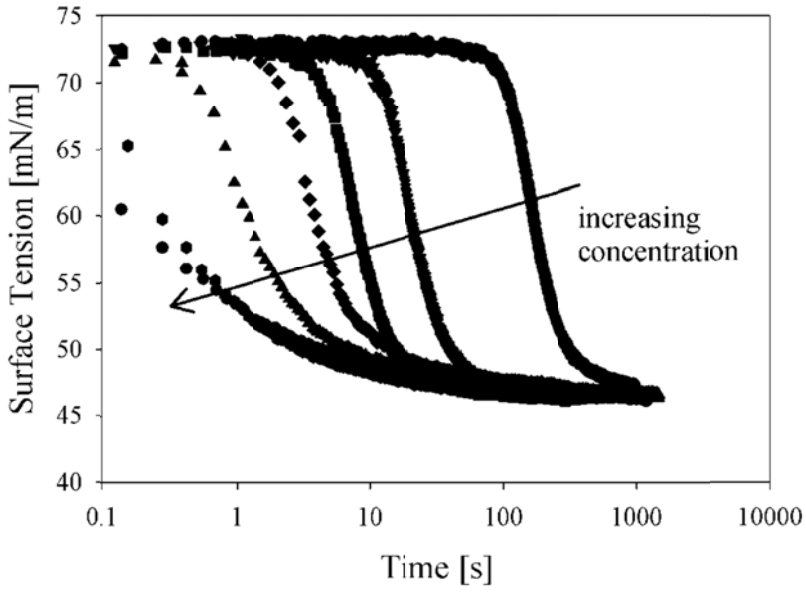

Figure 9.1. Surface tension as a function of time for different concentrations of high grafting density particles at the air-water interface. From left to right the symbols represent ● 0.000515 wt%, ▼ 0.00206 wt%, ■ 0.00413 wt%, ◆ 0.00825 wt%, ▲0.0165 wt%, ⬢ 0.0333 wt%, and ⬢ 0.1 wt%

A comparison of dynamic surface tension for HGD and low grafting density, LGD, particles for different bulk concentrations is shown in Figure 9.2.

Note that the LGD concentrations are significantly higher than HGD particle concentrations. In terms of concentration of PDMAEMA chains, a 0.1 wt% solution of HGD and LGD particles corresponds to a 45 μM solution and 38 μM solution of PDMAEMA, respectively. Even so, the LGD particles show a slower change in surface tension with time and do not achieve the same equilibrium surface tension as the HGD particles. Grafting density affects both the rate of transport and the equilibrium surface tension.

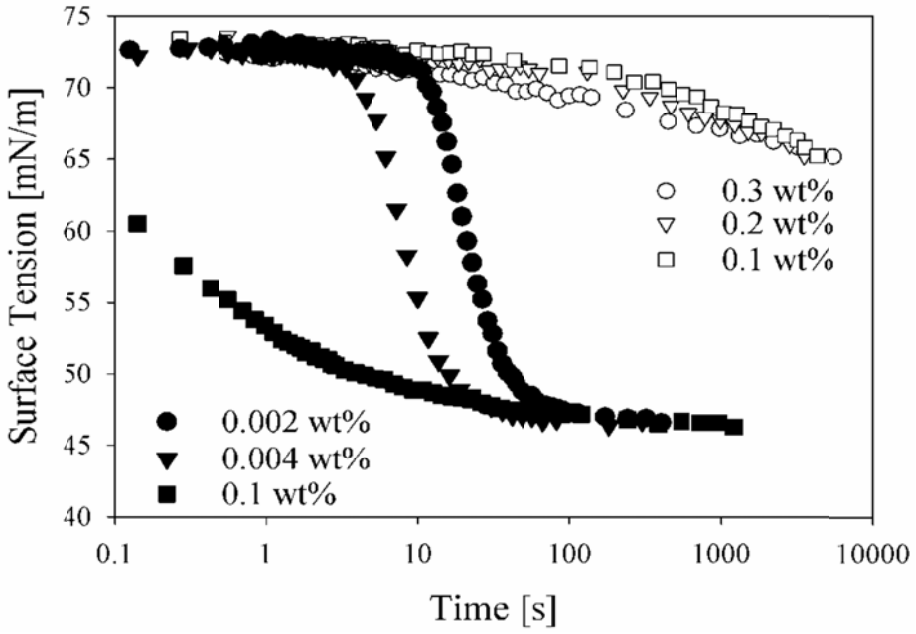

Figure 9.2. Surface tension as a function of time for different concentrations of high grafting density (filled symbols) and low grafting density (open symbols) particles at the air-water interface.

Figure 9.3 shows surface tension as a function of time for different concentrations of PDMAEMA homopolymer at the air-water interface. The dynamic surface tension curves do not all reach the same equilibrium value. As

the concentration of homopolymer increases so does the value of the equilibrium surface tension, which is the opposite of what is typically observed for surfactants and short chain polymers [19, 20]. In addition, the time scale to reach equilibrium is comparable to HGD measurements shown in Figure 9.1 and therefore faster than LGD dynamics.

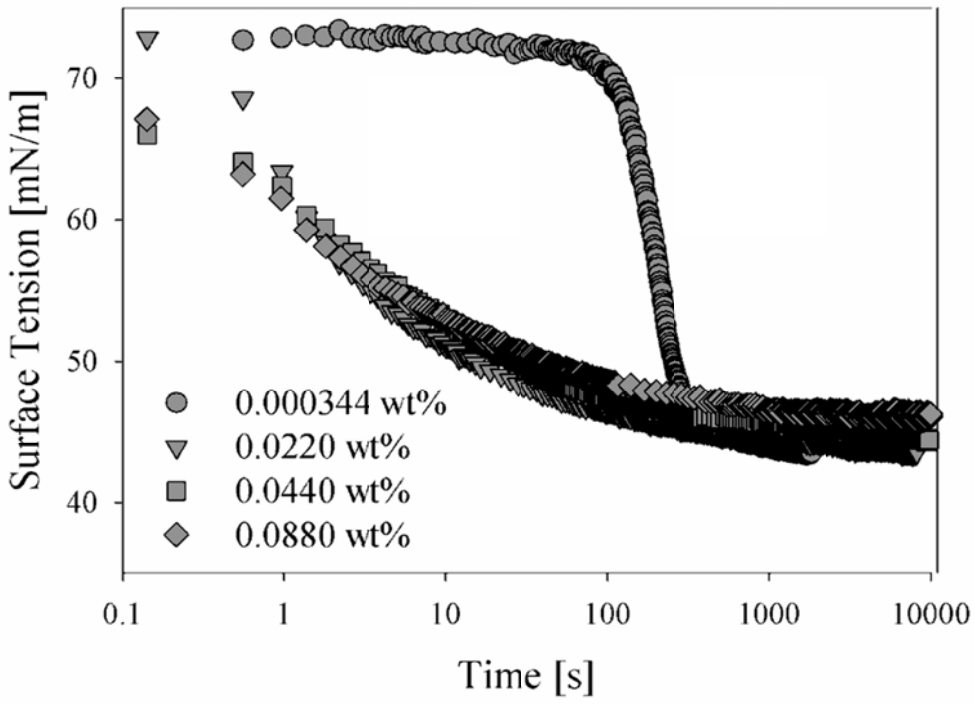

Figure 9.3. Surface tension as a function of time for different concentrations of PDMAEMA homopolymer at the air-water interface.

Figure 9.4 shows surface tension as a function of time for the three different systems at similar weight fractions and similar concentrations of PDMAEMA. The concentration of PDMAEMA for each system in Figure 9.4 is 15.0 μM for HGD, 38.3 μM for LGD, and 20 μM for homopolymer. The surface tension is normalized using

$$\theta = \frac{\gamma(t) - \gamma_{Eq}}{\gamma_0 - \gamma_{Eq}}, \tag{9.16}$$

where γ_0 is the clean surface tension value and γ_{Eq} is the equilibrium surface tension value. Figure 9.4 shows that the transport of HGD particles to the air-water interface is faster than homopolymer and LGD particles. The HGD particles are faster to reach equilibrium than homopolymer eventhough the concentration of PDMAEMA for the homopolymer case is higher. The LGD particles having the highest concentration of PDMAEMA molecules is the slowest to reach equilibrium. Furthermore, the diffusion coefficients for HGD, LGD, and homopolymer are 4.7×10^{-12}, 8.08×10^{-12}, 3.22×10^{-11} m^2/s, respectively. Regardless of having the slowest diffusion coefficient, HGD particles reach equilibrium faster than the other two systems. This suggests that HGD particles are efficient transporters of PDMAEMA to the interface. When one particle adsorbs it brings with it 1600 PDMAEMA to the interface. Even though not all molecules on the surface of the silica nanoparticle have access to the interface, this suggests that enough PDMAEMA chains adsorb to the interface to make up for the diffusion coefficient that is three times smaller than that of the homopolymer.

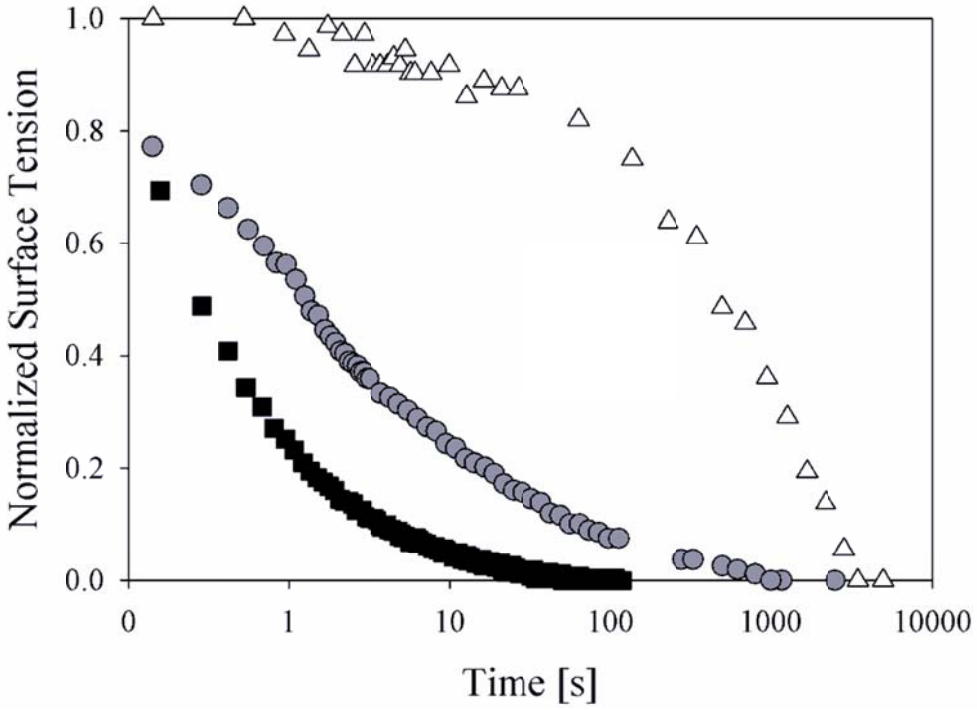

Figure 9.4. Comparison of normalized surface tension as a function of time for high grafting density particles, 0.033 wt% ■, PDMAEMA homopolymer,0.088 wt% ●, and low grafting density particles, 0.1 wt% △, at the air-water interface.

9.5.2. OIL-WATER INTERFACE

We now turn to results at the xylene-water interface. Figure 9.5 shows interfacial tension as a function of time for different concentrations of HGD at the xylene-water interface. At short times, the surface tension is that of the clean value of xylene-water interface, 38.2 mN/m. The interfacial tension for xylene-water is reproted in the literature to vary between 36.1 and 39 mN/m depending on the isomer of xylene [21, 22]. At longer times, the interfacial tension decreases until the dynamics reach equilibrium. The equilibrium interfacial tension depends on the concentration of HGD particles. As the concentration of particles increases, the equilibrium interfacial tension decreases. The change in

equilibrium surface tension is smaller for large concentrations than low concentrations.

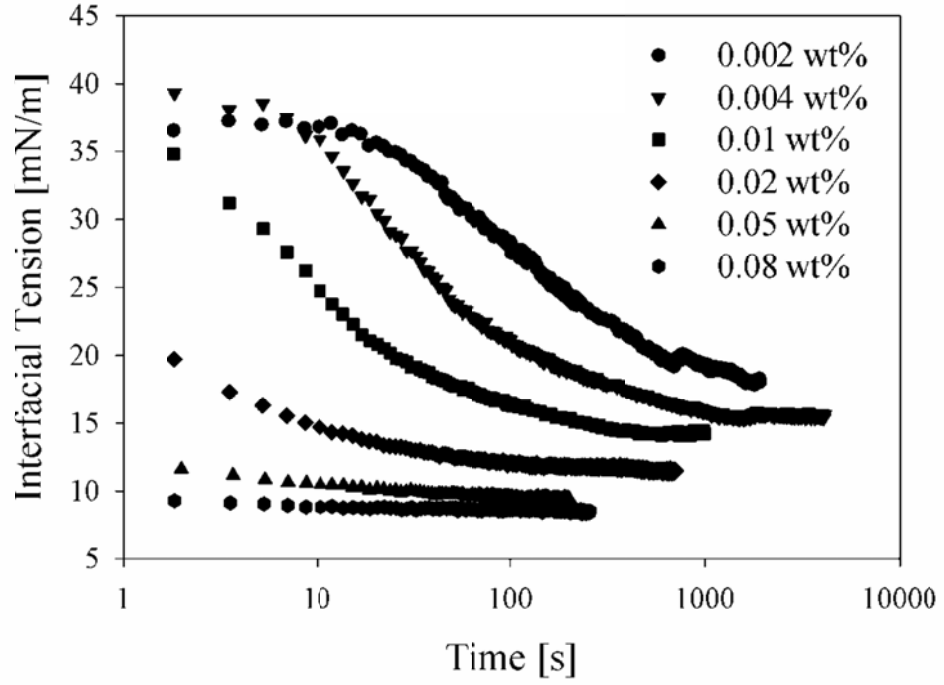

Figure 9.5. Interfacial tension as a function of time for different concentrations of high grafting density particles at the xylene-water interface.

A comparison of dynamic surface tension curves for LGD and HGD particles at the xylene-water interface are presented in Figure 9.6 at almost equal molar concentrations of PDMAEMA. The concentration of PDMAEMA for each system is: 35.7 μM for HGD and 38.3 μM for LGD particles. The LGD particles do not lower the xylene-water interfacial tension as much as the HGD particles even at the same concentration of PDMAEMA. At approximately the same concentration of PDMAEMA, a 0.1 wt% solution of LGD particles reaches equilibrium more slowly (10^5 s) than a 0.08 wt% of HGD particles (10^2 s). The

equilibrium surface tension and the rate of change in surface tension is strongly dependent on the grafting density.

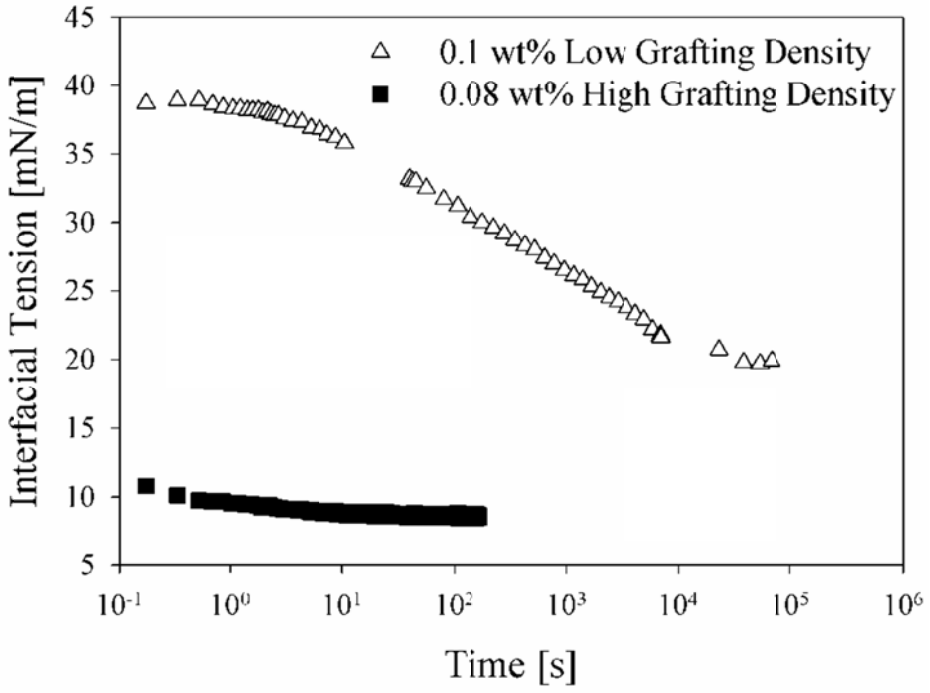

Figure 9.6. Comparison of interfacial tension as a function of time for high grafting density , ■, and low grafting density , △, at the xylene-water interface.

Finally, Figure 9.7 shows dynamic interfacial tension for two concentrations of homopolymer at the xylene-water interface. The equilibrium interfacial tension is again dependent on concentration.

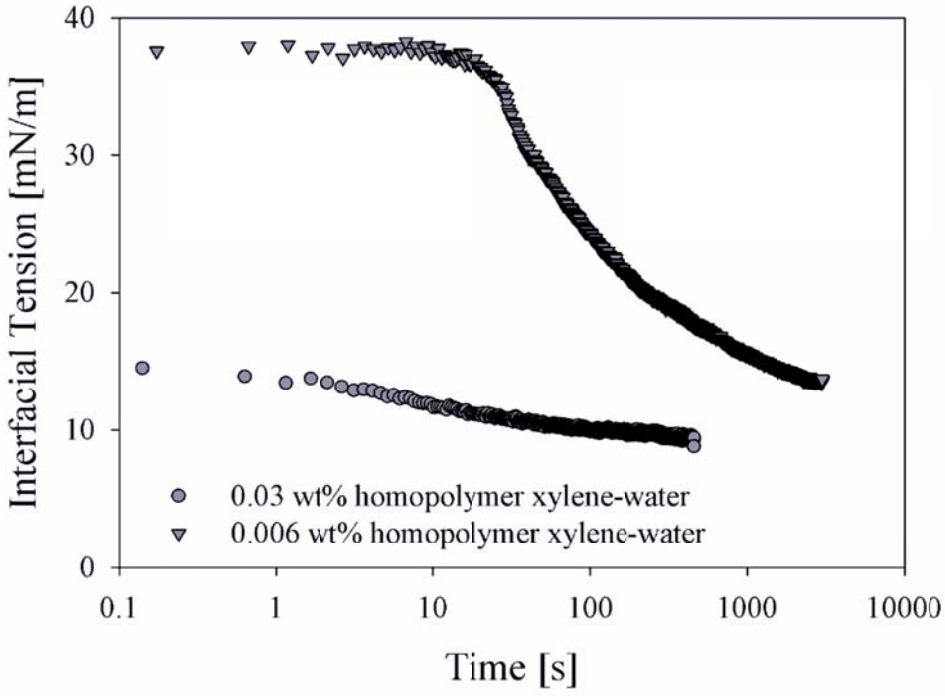

Figure 9.7. Interfacial tension as a function of time for different concentrations of PDMAEMA homopolymer at the xylene-water interface.

9.5.3. COMPARISON OF OIL-WATER AND AIR-WATER RESULTS

The equilibrium surface and interfacial tensions for all systems and concentrations studied are shown in Figure 9.8 for both the air-water and xylene-water interface. From Figure 9.8 it is clear that the equilibrium surface tension at the air-water interface is not dependent on the concentration of homopolymer, LGD or HGD particles. At low concentrations, the lack of dependence of surface tension on homopolymer concentration is in agreement with the response of high MW polyethylene oxide (PEO) at the air-water interface [20, 23]. From Figure 9.8, at high concentrations we observe a slight dependence of equilibrium surface tension of homopolymer on concentration. However, the equilibrium surface

tension increases with increasing bulk concentration, which is opposite of the trend that is observed in a system like PEO.

The equilibrium interfacial tension for all systems studied at the xylene-water interface show a slight dependence on concentration. HGD particles show a decrease in equilibrium interfacial tension for increasing concentration. The same trend is observed for LGD particles. This is a different result than observed for the air-water interface, which showed no dependence of equilibrium surface tension on concentration for either system. Equilibrium surface tension for homopolymer shows the same dependence as HGD and LGD particles at the xylene-water interface, which is different than the slight increase in equilibrium surface tension with concentration observed at the air-water interface.

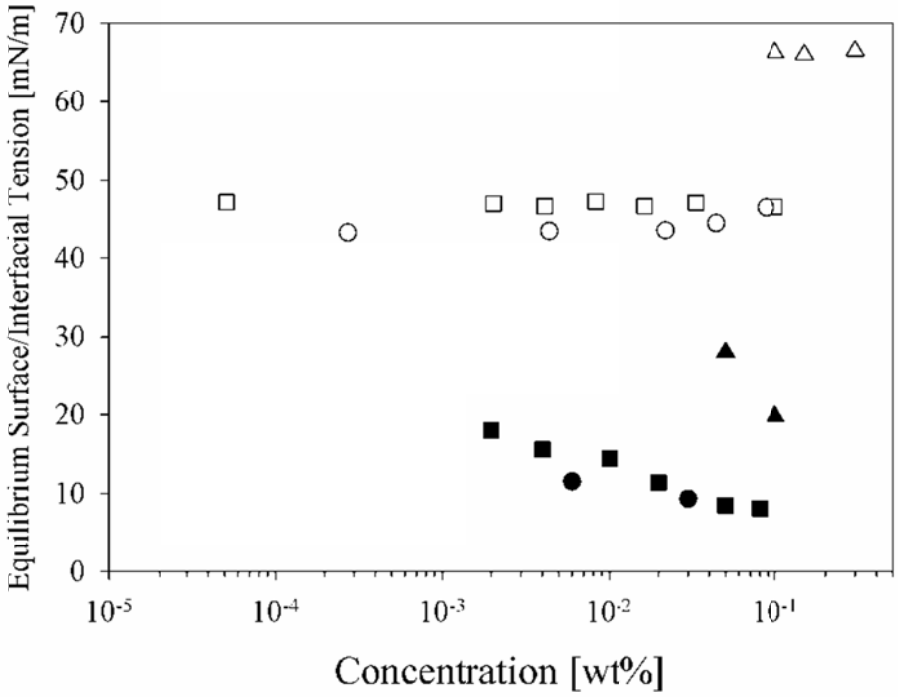

Figure 9.8. Equilibrium surface tension for high grafting density particles, ■□, low grafting density particles, ▲△, and PDMAEMA homopolymer, ●○, at the air-water (open symbols) and xylene-water (closed symbols) interfaces.

The Gibbs Elasticity of all systems studied at the air-water and xylene-water interface are presented in Figure 9.9. For the results at the air-water interface (open symbols) the HGD particles have the lowest measured elasticity and do not show a strong dependence of elasticity on the small range of frequencies tested. The average elasticity for HGD particles at the air-water interface is 10.6±1.0 mN/m. Results for LGD particles at the air-water interface show no dependence on frequency and the average elasticity is 14.2±0.5 mN/m. The highest modulus was measured for homopolymer, which did not change significantly with frequency. The average modulus for homopolymer at the air-water interface is 50.1±3.0 mN/m.

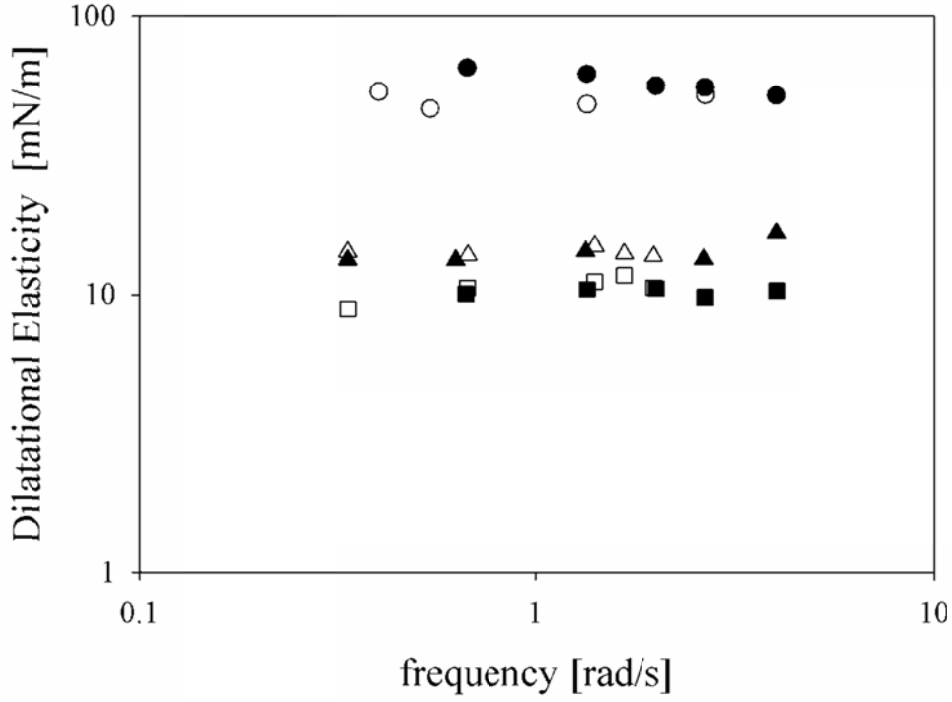

Figure 9.9. Elasticity as a function of frequency for homopolymer, HGD and LGD particles measured at the xylene-water interface (filled symbols) and air-water interface (open symbols). The symbols correspond to HGD particles, ■ 0.02 wt% □ 0.033 wt%, LGD particles, ▲ 0.1 wt% △ 0.1 wt%, and PDMAEMA homopolymer, ● 0.0066 wt% ○ 0.0044 wt%.

The results at the xylene-water interface are very similar to those measured at the air-water interface. For the HGD and LGD particles show no dependence on frequency. The average modulus for both particles is 10.2 ±0.3 and 14.2 ±1.5 mN/m, respectively. The modulus for homopolymer at the xylene-water interface is shows a slight decrease with increasing frequency. The average modulus is 58.0 ±5.3 mN/m, which is higher than the modulus measured at the air-water interface.

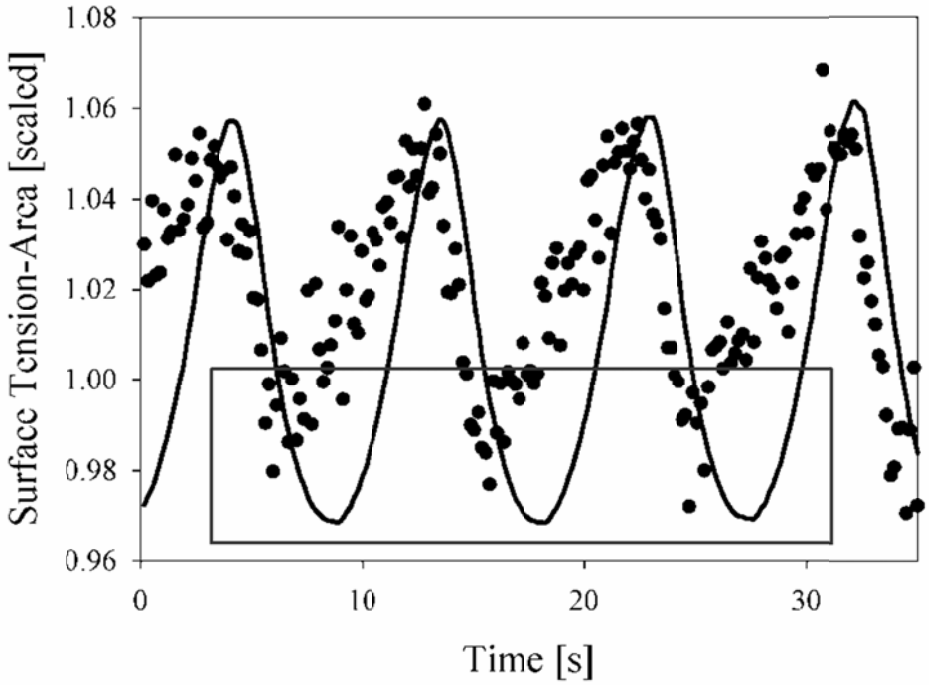

Figure 9.10. Surface tension (points) and area (solid curve) as a function of time for 0.08 wt% high grafting density particles. The area starts with an area expansion of the interface.

Note that elasticity measurements of HGD particles at both the xylene-water and the air-water interface could not be analyzed at a concentration larger

than 0.05 wt% since the measured surface tension response is nonlinear, i.e. not sinusoidal. In Figure 9.10, scaled surface tension and surface area are plotted as a function of time at the xylene-water interface. The points in Figure 9.10 represent the surface tension response of a solution of 0.08wt% HGD particles. The curve represents the area of the interface in scaled units. There is an obvious departure of the data from the traditionally observed sinusoidal response. It should be noted that this behavior is observed down to a ~1% strain amplitude, which is the limit of our instrument and implies that this behavior is not likely due to large amplitude strains.

There is a noticeable decrease in the measured dilatational modulus from the homopolymer covered surface to the grafted nanoparticle covered surface. As described previously in Eqns (9.13) and (9.15), a decrease in dilatational modulus is expected when the contact angle is close to *0* or the ratio of $\varepsilon_{LF}/\gamma_{LF}$ or $\varepsilon_{LF}\Big/\left(\gamma_{LF}-\tau\Big/\left(r\tan^2\theta\right)\right)$ are very large. If we assume line tension is not important and that γ_{LF} and ε_{LF} correspond to the measured equilibrium surface tension and elasticity of homopolymer at the interface, then the ratio of $\varepsilon_{LF}/\gamma_{LF}$ for HGD and LGD particles is greater than 1 for both the air-water and xylene-water interface. Thus, Eqn (9.13) predicts a decrease in the dilatational modulus when particles are present at the interface, which is what we observe in Figure 9.9.

9.6 DISCUSSION

The PDMAEMA acts to bring the grafted nanoparticles to the interface. Unmodified silica particles of this size (20 nm) do not strongly affect surface tension [4]. Measurements on bare silica nanoparticles show no change in the clean surface tension of air-water (data not shown). This is most likely because the nanoparticles do not spontaneously adsorb to the air-water interface. The free PDMAEMA homopolymer on the other hand does spontaneously adsorb to the air-water and xylene-water interface, c.f. Figure 9.3 and Figure 9.7. Both the low and high grafting density nanoparticles at the air-water and xylene-water interface show spontaneous adsorption, Figure 9.2 and Figure 9.6, and the equilibrium surface and interfacial tension values are much lower than the clean air-water surface and xylene-water interfacial tension, c.f. Figure 9.8.

The equilibrium surface and interfacial tensions for the HGD particles at the air-water and xylene-water interface are very similar to the homopolymer equilibrium surface and interfacial tension. Since the silica core of the HGD particles do not contribute to the surface tension, then the decrease in tension is due to the adsorption of tethered PDMAEMA chains. The available interface for PDMAEMA chains to adsorb to is $1-\phi_F$, where ϕ_F is the excluded volume of the silica core and depends on the contact angle, see Eqn (9.8). This suggests that the grafting density of 1.27 chains/nm^2 is approaching the maximum packing of PDMAEMA at the air-water and xylene-water interface because the equilibrium surface tensions are comparable for homopolymer and HGD particles and packing for a grafted particle is confined to the grafting density.

The grafting density of PDMAEMA on the silica nanoparticle impacts the rate of transport of particles to the interface. For example, in both Figure 9.2 and Figure 9.6 the HGD particles reach equilibrium faster than LGD particles at similar molar concentrations of PDMAEMA. This is despite the slower bulk diffusion of the HGD particles, see Table 9.1. If we assume that the transport mechanism for particles to the interface is diffusion limited, then the time scale for diffusion is proportional to the diffusion coefficient [8]. When one grafted nanoparticle adsorbs to the interface it brings with it all the PDMAEMA grafted to the surface of the nanoparticle. There are 1596 and 515 molecules of PDMAEMA per HGD and LGD particle, respectively. The flux of amphiphilic molecules to an interface, j, is a function of several variables,

$$j = f\left(\mathrm{C}_{bulk}, \mathrm{D}, \mathrm{b}, \Gamma_{\mathrm{eq}}\right), \tag{9.17}$$

where C_{bulk} is the bulk concentration, D is the diffusion coefficient, b is the radius of the interface, and Γ_{eq} is the equilibrium surface concentration. If we consider the same C_{bulk} and assume that the packing of HGD and LGD particles at equilibrium is the same, $\Gamma_{eq}^{HGD} = \Gamma_{eq}^{LGD}$, then the ratio of the flux to an interface with radius b of HGD to LGD particles is the ratio of their diffusion coefficients, 0.582. However, the ratio of the flux of PDMAEMA molecules is the ratio of number of tethered chains per particle multiplied by the ratio of the diffusion coefficients, 1.80. This means that the rate of transport of PDMAEMA to the interface is ~2 times larger for HGD particles than for LGD particles despite the lower flux of particles. Therefore, the grafting density acts to adjust the rate of

transport and the equilibrium surface tension value. Note that the assumption that $\Gamma_{eq}^{HGD} = \Gamma_{eq}^{LGD}$ is supported by ellipsometry data, where both LGD and HGD particles are measured to have similar surface concentrations [24].

Bare silica particles do not stabilize xylene-water emulsions and homopolymer stabilizes xylene-water emulsion droplets for only a short time, no more than three days [3]. Both the LGD and HGD particles stabilize emulsions down to concentrations as low as 0.05 wt% for more than 6 months. There does not seem to be a correlation between equilibrium surface tension and stabilization properties, since all three systems HGD, LGD, and homopolymer lower the surface and interfacial tension. In fact, homopolymer and HGD both lower the surface and interfacial tension more than LGD, yet emulsions stabilized by homopolymer break in less than three days.

It has been suggested in the literature that large dilatational moduli are responsible for stabilizing emulsion droplets [25, 26]. A comparison of dilatational elasticity, Figure 9.9, shows that homopolymer has the highest elasticity of all three systems for both fluid studies, which would suggest that it should stabilize emulsions better than the HGD and LGD particles. It appears that dilatational elasticity is required to stabilize emulsions, however it does not explain why homopolymer stabilized emulsions do not remain stable. One possible explanation is that the dilatational modulus for homopolymer at the air-water and xylene-water interface may be a function of time. Another possibility is that a correlation between interfacial shear viscosity and emulsion stability may be more pertinent than dilatational moduli for these systems. Biswas and Haydon

demonstrate that a correlation between interfacial shear viscosity and emulsion stability exists for macromolecular species [6, 16, 27].

An interesting observation from Figure 9.9 is that dilatational elasticity measurements at the air-water and xylene-water interface yield the same magnitudes. This implies that the contact angle for the two interfaces have to be different to compensate for the differences in the ratio of $\varepsilon_{LF}/\gamma_{LF}$ at the air-water and xylene-water interface in Eqn (9.13). This introduces the question whether the contact angle between different fluid pairs is such that the modulus is constant regardless of the fluids that make up the interface. If this proves true then this facilitate dilatational measurements by measuring the modulus at the air-water interface, a much easier experiment than at the oil-water interface, and extrapolating air-water measurements to oil-water studies.

It was mentioned in the results section that elasticity measurements at concentrations above 0.05wt% of HGD particles could not be analyzed since the response is nonlinear. The observed behavior seems to occur because the surface tension reaches a point whereby it cannot be decreased further, see outlined region in Figure 9.10. At the start of the compression cycle the surface tension decreases as expected, however, towards the end of the compression cycle the surface tension increases even though the interface is still compressing. One possible explanation is a sudden loss of particles at the interface to balance the change in area. Sudden compression tests at equilibrium (not shown) show that the lower value of surface tension acts as a limit that cannot be further lowered. At the instant the interface is compressed the interface yields a constant interfacial

tension equal to the lower value regardless of the amplitude of the area change. We hypothesize that this sudden loss of particles could be induced by the contact angle going to zero below a critical surface tension value causing the particles to desorb.

We measured the equilibrium surface tension and dilatational modulus of HGD particles solubilized in xylene at 0.05wt% and adsorbing to the interface from inside the drop. We found that the nonlinear response in modulus was not observed and the measured modulus was larger, an average value of $\varepsilon = 20.9 \pm 2.5$ mN/m compared to $\varepsilon = 10.2 \pm 0.3$ mN/m, and the equilibrium surface tension was slightly lower, $\gamma_{LF} = 7.2$ mN/m compared to $\gamma_{LF} = 7.9$ mN/m. Equation (9.13) suggests that if all other quantities except ε and θ are the same in both the HGD solubilized in water and in xylene, then the contact angle must be larger for the larger value of ε, which corresponds to the HGD particles solubilized in xylene. The fact that the contact angle is larger for HGD in xylene and no nonlinear response is observed supports the hypothesis that the contact angle could be responsible for the observation of a nonlinear response.

9.7 SUMMARY

Using the microtensiometer, we have demonstrated that PDMAEMA grafted to the surface of a silica nanoparticle acts to spontaneously drive the grafted nanoparticles to the air-water and oil-water interface. The grafting density affects the rate of change of surface tension and the equilibrium surface and interfacial tension values. The dilatational modulus measured at the air-water and xylene-water interface are quantitatively similar. It appears that a dilatational

modulus is required to create stable emulsions, but the dilatational modulus alone cannot explain why homopolymer stabilized emulsions break after a short period of time.

[1] B.P. Binks, "Particles as surfactants - similarities and differences," Current Opinion in Colloid & Interface Science, 7 (2002), 21-41.

[2] N. Saleh, et al., "Oil-in-water emulsions stabilized by highly charged polyelectrolyte-grafted silica nanoparticles," Langmuir, 21 (2005), 9873-9878.

[3] T. Saigal, et al., "Pickering Emulsions Stabilized by Nanoparticles with Thermally Responsive Grafted Polymer Brushes," Langmuir, 26 (2010), 15200-15209.

[4] T. Okubo, "Surface-Tension of Structured Colloidal Suspensions of Polystyrene and Silica Spheres at the Air-Water-Interface," Journal of Colloid and Interface Science, 171 (1995), 55-62.

[5] N.P. Ashby and B.P. Binks, "Pickering emulsions stabilised by Laponite clay particles," Physical Chemistry Chemical Physics, 2 (2000), 5640-5646.

[6] D.A. Edwards, H. Brenner, and D.T. Wasan, *Interfacial transport processes and rheology* (Butterworth-Heinemann, Boston, Mass., 1991).

[7] N.J. Alvarez, L.M. Walker, and S.L. Anna, "A Microtensiometer To Probe the Effect of Radius of Curvature on Surfactant Transport to a Spherical Interface," Langmuir, 26 (2010), 13310-13319.

[8] N.J. Alvarez, L.M. Walker, and S.L. Anna, "Diffusion-limited adsorption to a spherical geometry: The impact of curvature and competitive time scales," Physical Review E, 82 (2010).

[9] J.Q. Ding, et al., "Magnetic needle viscometer for Langmuir monolayers," Langmuir, 18 (2002), 2800-2806.

[10] W.E. Ewers and R.A. Sack, "A New Surface Viscometer," Nature, 168 (1951), 964-964.

[11] H.O. Lee, T.S. Jiang, and K.S. Avramidis, "Measurements of Interfacial Shear Viscoelasticity with an Oscillatory Torsional Viscometer," Journal of Colloid and Interface Science, 146 (1991), 90-122.

[12] A.R. Deemer, et al., "Measuring Liquid-Liquid Interfacial Behavior with the Deep-Channel Surface Viscometer," Journal of Colloid and Interface Science, 78 (1980), 87-99.

[13] H. Fruhner and K.D. Wantke, "A new oscillating bubble technique for measuring surface dilational properties," Colloids and Surfaces A-Physicochemical and Engineering Aspects, 114 (1996), 53-59.

[14] R.L. Kao, et al., "Measurement of the Dynamic Interfacial-Tension and Interfacial Dilatational Viscosity at High-Rates of Interfacial Expansion Using the Maximum Bubble Pressure Method .2. Liquid Liquid Interface," Journal of Colloid and Interface Science, 148 (1992), 257-260.

[15] L. Liggieri, et al., "Measurement of the surface dilational viscoelasticity of adsorbed layers with a capillary pressure tensiometer," Journal of Colloid and Interface Science, 255 (2002), 225-235.

[16] D.A. Edwards and D.T. Wasan, "Surface Rheology .3. Stress on a Spherical Fluid Surface," Journal of Rheology, 32 (1988), 473-484.

[17] J. Lucassen, "Dynamic Dilational Properties of Composite Surfaces," Colloids and Surfaces, 65 (1992), 139-149.

[18] J. Lucassen, "Capillary Forces between Solid Particles in Fluid Interfaces," Colloids and Surfaces, 65 (1992), 131-137.

[19] J. Eastoe and J.S. Dalton, "Dynamic surface tension and adsorption mechanisms of surfactants at the air-water interface," Advances in Colloid and Interface Science, 85 (2000), 103-144.

[20] T. Gilanyi, et al., "Adsorption of poly(ethylene oxide) at the air/water interface: A dynamic and static surface tension study," Journal of Colloid and Interface Science, 301 (2006), 428-435.

[21] L.A. Girifalco and R.J. Good, "A Theory for the Estimation of Surface and Interfacial Energies .1. Derivation and Application to Interfacial Tension," Journal of Physical Chemistry, 61 (1957), 904-909.

[22] D.L. Lord, A.H. Demond, and K.F. Hayes, "Effects of organic base chemistry on interfacial tension, wettability, and capillary pressure in multiphase subsurface waste systems," Transport in Porous Media, 38 (2000), 79-92.

[23] R. Meszaros, et al., "Adsorption of poly(ethylene oxide) at the air/water interface: A dynamic and static surface tension study," Journal of Colloid and Interface Science, 301 (2006), 428-435.

[24] T. Saigal, PhD thesis: Carnegie Mellon University, (2011).

[25] A. Prins, C. Arcuri, and Vandente.M, "Elasticity of Thin Liquid Films," Journal of Colloid and Interface Science, 24 (1967), 84.

[26] A. Prins and Vandente.M, "Composition and Elasticity of Thin Liquid Films," Journal of Physical Chemistry, 73 (1969), 2828.

[27] B. Biswas and D.A. Haydon, "Rheology of Some Interfacial Adsorbed Films of Macromolecules .1. Elastic and Creep Phenomena," Proceedings of the Royal Society of London Series A-Mathematical and Physical Sciences, 271 (1963), 296.

CHAPTER 10

CONCLUSIONS

Kinetic rate parameters can only be measured when the rate of kinetics is comparable or slower than the rate of diffusion. However, there was previously no independent method of determining the relative rates of the two mechanisms from equilibrium or dynamic surface tension data. Therefore, researchers were required to analyze dynamic surface tension data considering both kinetics and diffusion. This led to unphysical trends in diffusion coefficients and kinetic rate parameters. In this thesis we overcame these challenges. In Chapter 4, we outlined a scaling analysis that directly identifies the relevant transport mechanisms in dynamic surface tension data: allowing for the correct quantitative analysis of diffusion coefficients and kinetic rate parameters.

The functional form of the spherical diffusion time scale is fundamental to our scaling analysis. In Chapter 4, we validated using experiment and theory the correct dependence of the diffusion time scale on curvature and bulk concentration. The experimental confirmation of the dependence of the diffusion time scale on curvature introduced a new experimental technique, a microtensiometer, described in Chapter 5 to study and quantify surfactant transport parameters.

It was previously thought that measuring dynamic surface tension as a function of concentration was the only experimental method to analyze surfactant transport. However, in Chapter 4 we show that bubble radius is a more relevant parameter to differentiate between diffusion-limited and kinetic-limited dynamics.

The spherical diffusion time scale depends on the radius of the interface while the kinetic time scale does not. Furthermore, in Chapter 4 and 6 we showed that one is more likely to observe kinetic-limited transport at smaller radii than higher surfactant bulk concentrations.

For highly surface active species (i.e. surfactants with large adsorption rate constants), it is difficult to experimentally reach a condition using either concentration or radius where the rate of kinetics is comparable or slower than the rate of diffusion: thus limiting the magnitude of measurable kinetic rate constants using available dynamic surface tension techniques. In Chapter 8, we introduced an additional time scale analysis to characterize surfactant transport in the presence of flow. Flow increases the rate of diffusion relative to the rate of kinetics and thus increases the range of measurable kinetic rate parameters. We showed that the dependence of dynamic surface tension data on Peclet number is another powerful experimental tool to determine and increase the importance of kinetics in dynamic surface tension data.

Together the dependence of the diffusion time scale on radius, concentration and Peclet number results in a new methodology of analyzing surfactant dynamic surface tension data to determine appropriate transport parameters. For example, the literature suggests that the adsorption rate constants for $C_{12}E_8$ and $C_{14}E_8$ is $\beta \sim 5$ $m^3/(mol \cdot s)$. For this magnitude of β one should observe kinetic-limited transport of these surfactants at experimentally feasible conditions. However, our findings show that $C_{12}E_8$ and $C_{14}E_8$ follow diffusion-limited dynamics down to very small radii and high Peclet numbers. In fact, our

analysis shows that the rate constant for these two surfactants must be significantly greater than 5 $m^3/(mol \cdot s)$. Furthermore, these two surfactants can be described solely by molecular diffusion for all transport situations to and from the air-water interface below the critical micelle concentration and for radii greater than a micron.

The above demonstration of identifying dominant surfactant transport mechanisms results in a new methodology of analyzing dynamic surface tension data, outlined in Chapter 7. Given a new surfactant that has not been previously characterized, the following is a procedure to correctly quantify relevant transport parameters. First, a measurement of dynamic surface tension for a range of bulk surfactant concentrations, C_{bulk}, is necessary to determine the dependence of γ_{eq} on C_{bulk}. Second, γ_{eq} vs. C_{bulk} data is fit to an equation of state, which determines thermodynamic parameters, such as the ratio of rate constants and the maximum packing of surfactant on the interface. Third, these parameters are used to perform a time scale analysis on dynamic surface tension data as a function of radius, concentration, and/or Peclet number.

Deviation of the experimental time scale from the theoretical spherical diffusion time scale is characteristic of a shift in transport mechanisms, c.f. Chapters 4, 7, and 8. If no deviation is observed, such as in the analysis of $C_{12}E_8$ data in Chapter 6, then the dynamics are completely described by diffusion-limited transport for the conditions studied. However, if a deviation from the diffusion-limited time scale is observed and is in agreement with expected trends for kinetic-dominated dynamics, then direct measurement of the rate constants are

determined from a simple one parameter fit to dynamic surface tension data, c.f. Chapter 7. In addition, because of the distinct difference in the dependence of the kinetic time scale on bubble radius and concentration, two different types of experiments can be performed to definitively confirm the presence of kinetic-dominated dynamics.

This scaling analysis was used to show that there is a transition in the surfactant transport mechanism for $C_{12}E_8$ and $C_{14}E_8$ from low concentration to high concentration at the silicone oil-water interface. Adsorption and desorption rate constants for $C_{12}E_8$ and $C_{14}E_8$ and a lower bound for $C_{10}E_8$ are reported. Comparisons of oil-water results with studies at the air-water interface show that dynamics are strongly dependent on the fluids that make up the interface.

The microtensiometer developed in this thesis and described in Chapter 5 is responsible for the experimental confirmation of the spherical diffusion time scale and the study of dynamic surface tension as a function of curvature. This device on its own possesses numerous advantages over conventional surface tension measurement techniques and plays a crucial role in analyzing surfactant dynamics. The advantages of the microtensiometer include: in-situ dynamic surface tension measurements, less volume, faster measurement times, direct measurement of pressure, and in-situ surface tension measurements in the presence of bulk flow.

Furthermore, the microtensiometer was modified to function as an interfacial dilatational rheometer. In Chapter 9, this apparatus was used characterize the transport and rheological properties of PDMAEMA grafted silica

nanoparticles at the air-water and xylene-water interface. These particles are known to be efficient emulsifiers. However, there stabilization mechanism is not yet known. Our dilatational and dynamic surface tension results show that the behavior of these particles at the air-water and xylene-water interface bring us to a better understanding of how these particles adsorb to interfaces and the configuration that they take once adsorbed.

In summary, this work contributes to the understanding of the role of curvature on diffusion-limited surfactant transport at fluid-fluid interfaces and how this relationship can be used to quantitatively and accurately analyze dynamic surface tension measurements. This work presents an array of new tools both experimental and analytical to properly measure and quantify surfactant transport and interfacial rheological parameters. These tools will be instrumental in understanding the relationship between surfactant structure and interfacial behavior and dynamics.

APPENDIX

SURFACTANT DYNAMICS AND EQUILIBRIUM IN CONFINED VOLUMES

A.1 INTRODUCTION

In Chapter 4 we discussed the time scale associated with surfactant dynamics in a semi-infinite volume. There are many fields of research that are concerned with surfactant transport in finite volumes (confined volumes), such as: multiphase flow in porous media [1], emulsification and coalescence [2, 3], biological processes [4], surface tension studies [5-14], tipstreaming [15, 16], wetting [17-19], and Marangoni flows [20, 21]. Confined volume situations are also prevalent for studies involving microfluidic systems whereby the volumes under considerations are in the nanoliter to picoliter range and the available surface area is large enough that adsorption of surfactant molecules to interfaces reduces the concentration of surfactant in the bulk volume, i.e. the surfactant is depleted from the bulk and the remaining concentration is less than the initial bulk concentration [17, 20-23].

Depletion effects are not always correctly accounted for in the analysis of dynamic and equilibrium surface tension measurements. The pendant drop technique is often used to measure dynamic surface tension of surfactant solutions. Surface tension is determined by fitting the Young-Laplace equation to the profile of a hanging drop [24]. Many studies using the pendant drop technique compare data to a model developed for surfactant dynamics from a semi-infinite

volume to a planar interface or a spherical interface. However, a pendant drop does not have a semi-infinite volume to draw surfactant from.

Surfactants do not only adsorb at fluid-fluid interfaces, but also at solid-fluid interfaces [27-29]. When the volume of solution is small and the surface area in contact with the surfactant solution is large, e.g. microfluidic studies or the inside of a pendant drop, then depletion can be caused by adsorption of surfactant molecules to the solid walls [30]. The large surface area acts as a sink for surfactant; reducing the overall concentration in the bulk. In some cases, the problem is avoided altogether by modifying the surface of the container, e.g. glass or plastic, to reduce adsorption of the solute species to the container [30]. This is not always possible in all systems. Regardless, it is important to know when depletion effects are important.

A number of theoretical studies have addressed the dependence of dynamic surface tension and equilibrium surface tension on confined volume. Rubin and Radke computationally modeled surfactant dynamics to and from a sphere considering mass transport across the interface into another immiscible phase [31]. Fillipov and Fillipova developed an analytical theory to describe surfactant dynamics for a liquid drop submerged in a semi-infinite immiscible fluid, a liquid drop surrounded by a spherical shell of immiscible fluid, and a liquid drop [32]. Yang and Gu calculated the difference between a planar interface and a pendant drop shape (non-spherical) considering a finite volume of solution [33]. In some cases the authors find substantial differences between the

planar model and their results and in other cases find that the two models are very similar.

Although these contributions have been very useful in understanding and acknowledging the differences between the semi-infinite volume and confined volume cases, there is currently no general criterion for determining when depletion is important to equilibrium and/or dynamic surfactant studies. A criterion that depends on a straightforward parameter would aid in the design of experiments to avoid depletion effects or in some cases to determine when depletion effects are important and should be included in any analysis. This criterion should also extend to applications where surface tension is calculated using models from the literature, such as an isotherm and surface equation of state, EOS. The isotherm and EOS is only valid if the bulk concentration is constant and depletion is not important.

The purpose of this chapter is to determine a criterion that quantifies the importance of depletion effects. We first present a theory that is general to any geometry and then focus on the case of a spherical droplet where the surfactant is solubilized in the droplet phase and is immiscible in the outside phase (i.e. no diffusion of surfactant across the boundary). This chapter is limited to analysis concerning diffusion-limited transport and the Langmuir isotherm. However, the trends are general to any isotherm. Recently, we have shown that the spherical diffusion time scale depends on the normalized bubble radius, b/h_p, where b is the bubble radius and $h_p = \Gamma_{eq}/C_\infty$ is the planar intrinsic length scale dependent on the equilibrium surface coverage, Γ_{eq}, and the bulk surfactant concentration,

C_∞ [25]. This ratio of length scales is derived from a mass balance, i.e. a ratio of the number of surfactant molecules available in the bulk volume to the number of surfactant molecules adsorbed on the available surface area. In this chapter, we show that depletion effects are quantified by the same mass conservation ratio which for an arbitrary system is represented by a ratio of volumes, $\left(C_\infty V\right)/\left(\Gamma_{eq} A\right) = V/\left(h_p A\right)$, where V is the volume of solution and $h_p A$ is the volume of surfactant required to populate the interface(s), with surface area A, to equilibrium. For a spherical drop, i.e. liquid-liquid or liquid-gas interface, depletion effects are quantified in terms of $V/\left(h_p A\right) = b/\left(3h_p\right)$.

This chapter is organized into two sections. The first section describes the effect of depletion on equilibrium surface tension. We quantify using simulations the ratio of volumes, $3V/\left(h_p A\right)$, for which depletion effects are minimized, i.e. do not affect the bulk surfactant concentration. The results of this study are put in the context of experiments conducted on pendant drops/bubbles [8, 34], recent experiments conducted on nanoscopic droplets [23]. The second section describes the effect of depletion on dynamic surface tension measurements. For the case of a spherical droplet, the time scale governing surfactant transport from inside the drop is determined from numerical simulations and analytical expressions are presented for the upper and lower bounds. Theoretical dynamic surface tension curves in the presence of depletion for the inside drop and outside drop cases are compared in order to characterize the effect of curvature on dynamic surface tension.

A.2 CONFINED AND INFINITE VOLUME MODEL

The transport problem considering surfactant dynamics from inside and outside the droplet phase are depicted in Figure A.1a and b, respectively. The transport problem considering surfactant dynamics from outside the interface was given previously [25]. The diffusion of surfactant from the bulk solution is modeled using Fick's law in spherical coordinates

$$\frac{\partial C}{\partial t} = \frac{D}{r^2}\frac{\partial}{\partial r}\left(r^2 \frac{\partial C}{\partial r}\right), \tag{A.1}$$

where C is the bulk surfactant concentration and D is the surfactant molecular diffusion coefficient. Only the diffusion-limited case is considered and therefore the surface concentration of surfactant is always in equilibrium with the concentration of surfactant immediately adjacent to the interface. The model does not account for partitioning of surfactant across the interface. We assume that the surfactants follow a Langmuir isotherm, given by

$$\frac{\Gamma_{eq}}{\Gamma_{\infty}} = \frac{C_s}{C_s + a}, \tag{A.2}$$

where C_s is the concentration of surfactant at $r = b$, the radius of the interface, Γ_{eq} is the equilibrium surfactant surface concentration, Γ_{∞} is the maximum surfactant surface concentration, and $a = \alpha/\beta$ is the ratio of the desorption rate constant, α, to that of the adsorption rate constant, β. The flux of surfactant at the interface for the outside and inside are given by

$$\frac{\partial \Gamma}{\partial t} = D\frac{\partial C}{\partial r}\bigg|_{r=b} \tag{A.3}$$

and

$$\frac{\partial \Gamma}{\partial t} = -D \frac{\partial C}{\partial r}\bigg|_{r=b}, \tag{A.4}$$

respectively. The second boundary condition is that of spherical symmetry at $r = R_f$ for the outside case, where R_f is the radius away from the interface that encompasses a fixed volume of solution, and at $r = 0$ for the inside case, i.e.

$$\frac{\partial C}{\partial r}\bigg|_{r=R_f} = 0 \tag{A.5}$$

and

$$\frac{\partial C}{\partial r}\bigg|_{r=0} = 0, \tag{A.6}$$

respectively. Note that the equations governing diffusion from inside a drop is equivalent to one of the cases analyzed asymptotically in [32].

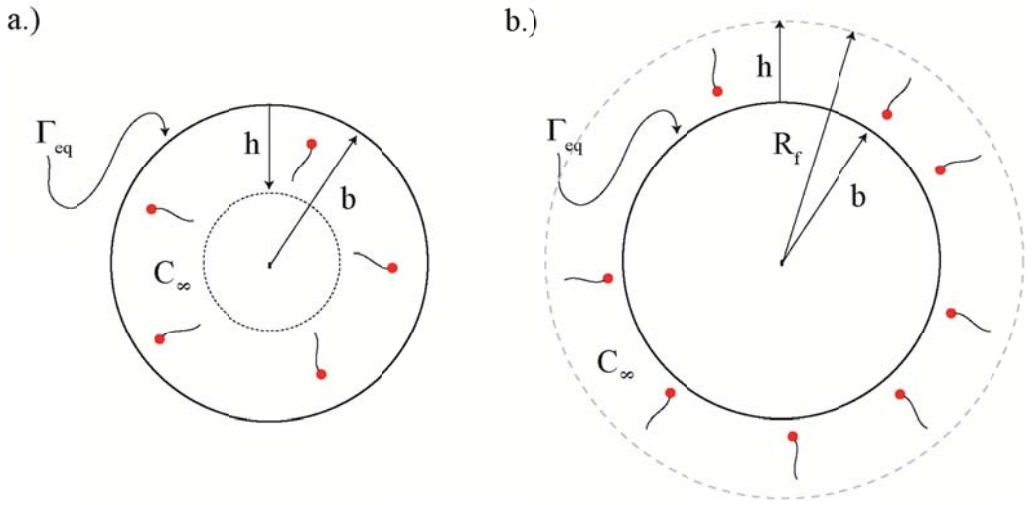

Figure A.1. Schematic diagram of geometry for the case a.) inside the drop and b.) outside the drop, where C_∞ is the bulk surfactant concentration, h the length scale over which diffusion occurs, Γ_{eq} is the equilibrium surface concentration, b is the radius of the interface, and R_f is the radius encompassing a volume from the interface.

We solve the governing equations using a spectral analysis method to obtain the complete time-dependent concentration profile for diffusion-limited dynamics. The spectral analysis was performed using Chebyshev grid points and an implicit Euler scheme for discretization in time. The details of the method are explained elsewhere [25, 26]. The outside transport case is represented by solving Eqns (A.1) and (A.2) simultaneously subject to boundary conditions (A.4) and (A.6). The inside transport case is represented by solving equations (3.7) and (A.2) simultaneously subject to boundary conditions (A.3) and (A.5).

Using theoretical dynamic surface tension profiles calculated from the above inside transport model, we perform a scaling analysis to determine the relevant time scale for diffusion in the case of transport from inside the droplet phase. Using simulated surface concentration profiles, $\Gamma(t)$, we determine the time, τ_{num}, required to reach a given fraction, ϕ, of the equilibrium surface concentration, $\phi = \Gamma(\tau_{num})/\Gamma_{eq} = const$. The same analysis was used previously to determine the time scale for diffusion-limited transport to a spherical interface from a semi-infinite volume [25, 26].

A.3 MATERIALS AND METHODS

Two types of sample preparation methods were performed for equilibrium surface tension measurements on $C_{14}E_8$. The first method was to equilibrate 10 ml samples of different concentrations of $C_{14}E_8$ in 20 ml borosilicate glass scintillation vials for 24 hours before measuring surface tension. The second method was to prepare 10 ml samples of the same concentrations immediately prior to taking measurements of surface tension. Dynamic and equilibrium

surface tension values were measured using a microtensiometer described elsewhere [26]. The error in surface tension of this technique is less than 0.5 mN/m. Note that the value of V/A is kept constant and the value of h_p depends on C_i. Care was taken to ensure that the walls of the microtensiometer measurement cell were pre-equilibrated with surfactant solution before surface tension measurements were taken.

A.4 RESULTS AND DISCUSSION

A.4.1. EFFECT OF DEPLETION ON EQUILIBRIUM SURFACE TENSION

A.4.1.1. CASE OF A SINGLE DROPLET AND SAMPLE PREPARATION

Once a solution containing surfactant comes into contact with a surface such as a glass/plastic container or a fluid-fluid interface, the molecules in the bulk begin to adsorb to the surface in order to minimize the surface energy of the system. The surfactant molecules will continue to adsorb until equilibrium with the bulk surfactant concentration is reached. This equilibrium is governed by an isotherm and depends on the bulk concentration, the nature of the interface, the surfactant molecules, and the solvent. If the number of molecules in the bulk volume is small enough such that the adsorption of molecules to any type of surface in the system considerably reduces the overall number of molecules in the bulk and changes the bulk concentration, then the bulk concentration is said to be depleted. This translates to the bulk concentration and other variables that depend on bulk concentration changing with time until equilibrium is established.

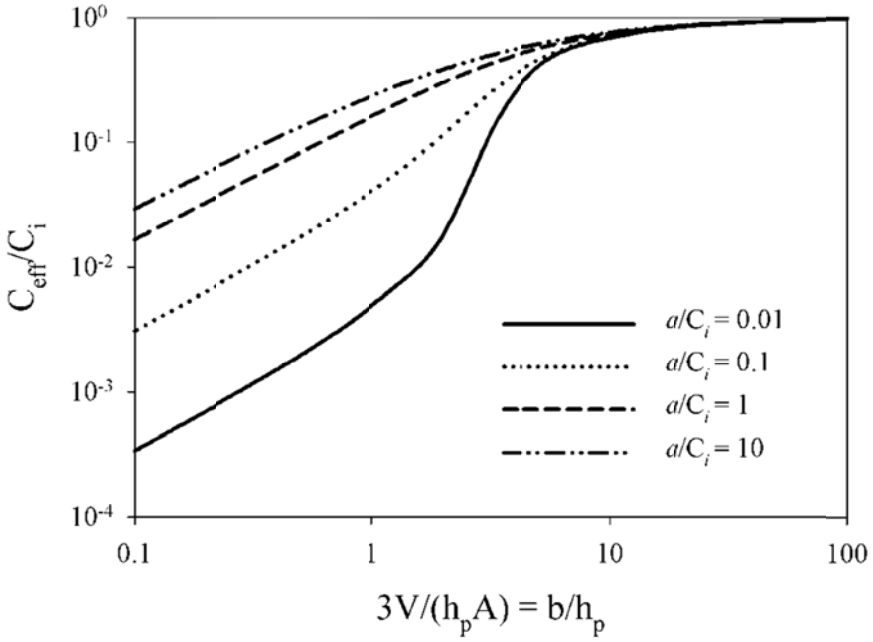

Figure A.2. Normalized effective bulk surfactant concentration as a function of different b/h_p for different ratios of a/C_i .

Through a mass balance one can determine a relationship between bulk surfactant concentration and the surface area to volume ratio. For example, if we consider a bulk surfactant solution of volume, V , in contact with a solid or fluid interface of area, A , with an initial bulk and surface concentration, C_i and Γ_i , respectively, the mass balance for the system is

$$C_i V + \Gamma_i A = C_{eff} V + \Gamma_{eq} A, \tag{A.7}$$

where C_{eff} and Γ_{eq} are the effective concentration and equilibrium surface concentration, respectively. For the case of an initially clean surface, i.e. $\Gamma_i(t=0) = 0$, then the mass balance reduces to

$$C_i V = C_{eff} V + \Gamma_{eq} A\,, \tag{A.8}$$

where Γ_{eq} is related to C_{eff} through an isotherm, such as the Langmuir isotherm given by (4.6), where $C_s = C_{eff}$ when $t \to \infty$, i.e.,

$$\Gamma_{eq} = \frac{C_{eff}\Gamma_\infty}{C_{eff} + a}. \tag{A.9}$$

Solving equations (A.8) and (A.9) for C_{eff} and an arbitrary geometry yields $C_{eff} = f\left(h_p A/V, a/C_i\right)$, i.e.

$$\frac{C_{eff}}{C_i} = \frac{\left(1 - \frac{h_p A}{V} - \left(\frac{h_p A}{V} + 1\right)\frac{a}{C_i}\right) - \sqrt{\left(1 - \frac{h_p A}{V} - \left(\frac{h_p A}{V} + 1\right)\frac{a}{C_i}\right)^2 + \frac{4a}{C_i}}}{2} \tag{A.10}$$

and for a spherical interface where $A = 4\pi b^2$ and $V = \frac{4}{3}\pi b^3$, the concentration ratio becomes,

$$\frac{C_{eff}}{C_i} = \frac{\left(1 - \frac{3h_p}{b} - \left(\frac{3h_p}{b} + 1\right)\frac{a}{C_i}\right) - \sqrt{\left(1 - \frac{3h_p}{b} - \left(\frac{3h_p}{b} + 1\right)\frac{a}{C_i}\right)^2 + \frac{4a}{C_i}}}{2}. \tag{A.11}$$

From Eqn (A.11), it is obvious that C_{eff} is dependent on the ratios of b/h_p and a/C_i, where $b/h_p = b\Gamma^i_{eq}/C_i$, and $\Gamma^i_{eq} = \Gamma_{eq}\left(C_{eff} = C_i\right)$. Figure A**.2** shows the ratio of C_{eff}/C_i as a function of $3V/\left(h_p A\right)$ and b/h_p for different values of a/C_i calculated from Eqns (A.10) and (A.11). The factor of three appears in $3V/\left(h_p A\right)$ because we calculate the effect of C_{eff}/C_i on b/h_p not $b/\left(3h_p\right)$. It is evident

from Figure A**.2** that at very large values of the normalized bubble radius $b/h_p > 10$, regardless of the ratio of a/C_i, C_{eff} is approximately equal to the initial bulk concentration, C_i. Given that the equilibrium surface concentration depends directly on the value of C_{eff}, the impact of depletion on both the equilibrium surface tension and the bulk surfactant concentration becomes minimized for $b/h_p >> 10$ or in more general terms with respect to geometry when $3V/(h_p A) >> 10$.

For fluid-fluid interfaces, the surface concentration is not directly measured in an experiment. Instead the surface tension is measured and related to the surface concentration through an equation of state. The equation of state for the Langmuir isotherm is given by

$$\gamma = \gamma_0 + RT\Gamma_\infty \ln\left(1 - \frac{\Gamma_{eq}}{\Gamma_\infty}\right), \tag{A.12}$$

where R is the gas constant, T is the temperature, and γ_0 is the initial surface tension of the fluid-fluid pair. It is relevant to determine at what value of $3V/(h_p A)$ or in the case of pendant drops at what values of b/h_p does $\gamma_{eq}(C_{eff}) = \gamma_{eq}(C_i)$. Figure A**.**3 shows the dependence of surface tension as a function of time for different values of b/h_p for a fixed value of $a/C_i = 1$. These theoretical curves are comparable to measuring dynamic surface tension at different radii of curvature in a pendant drop experiment at the water-air interface at fixed surfactant concentration. For very small values of b/h_p, it is evident

from Figure A.3 that the equilibrium surface tension is approximately equal to the clean interfacial tension value, even though the initial bulk surfactant concentration is relatively high. For example, short chain alcohols, such as butanol, have Langmuir rate constant ratios $a \approx 0.1\,\text{mol/m}^3$, which yields an initial concentration, $C_i \approx 100\,\mu\text{M}$ for $a/C_i = 1$ [25]. As the ratio b/h_p increases, the equilibrium surface tension value approaches the semi-infinite volume case, i.e. $b/h_p \to \infty$. Specifically, the curve representing a ratio of $b/h_p = 100$ is indistinguishable from the semi-infinite volume curve. As in Figure A.**2**, when $b/h_p >> 10$ the effect of depletion on surface tension is minimized. This is more clearly presented in Figure A.4, which shows equilibrium surface tension as a function of b/h_p. The dotted line corresponds to the equilibrium surface tension of the infinite volume case, i.e. no depletion $\gamma_{eq}(C_i)$. Note that for $b/h_p > 100$, the equilibrium surface tension is indistinguishable from the infinite volume case and for $b/h_p = 20$, the equilibrium surface tension is $> 99\%$ of the infinite volume case.

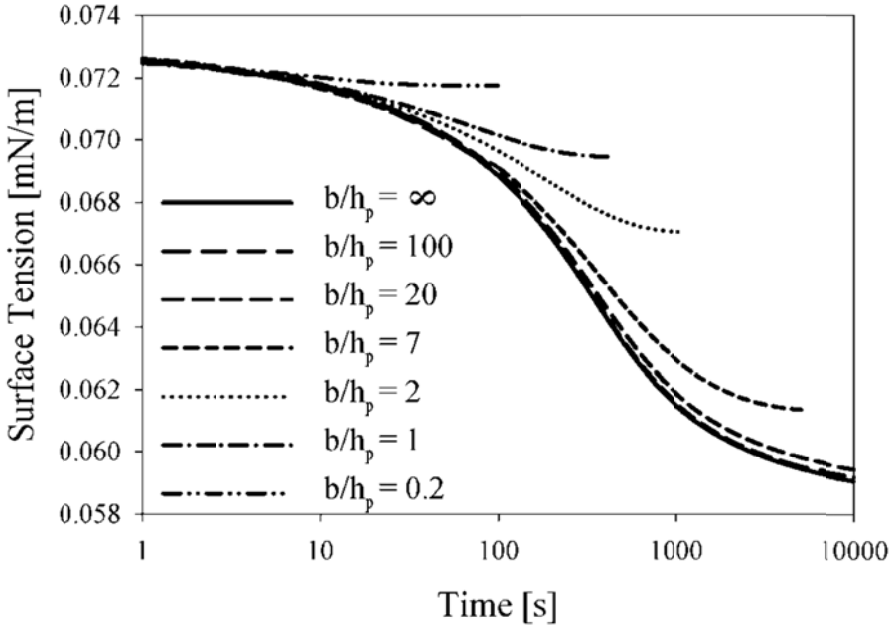

Figure A.3. Surface tension as a function of time for a ratio of $a/C_i = 1$ for different values of b/h_p.

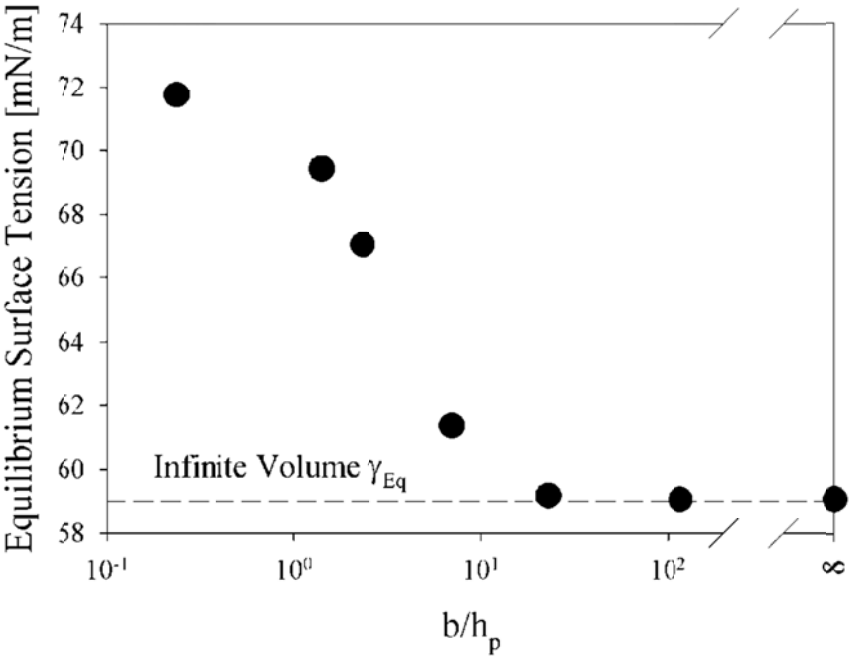

Figure A.4. Equilibrium surface tension as a function of b/h_p for a fixed value of $a/C_i = 1$.

Regardless of the surfactant under consideration, the impact of depletion can be quantified using b/h_p or more generally $3V/(h_p A)$. Using this relationship, experiments can be presented in a scaled form that explicitly show whether depletion is important or not. For example, recently Fainerman *et al.* compared equilibrium and dynamic surface tension results studied using a pendant drop and a pendant bubble apparatus [8]. For the concentrations studied, there is a significant difference between equilibrium surface tension measurements from the two techniques. Figure A.5 shows the equilibrium surface tension from measurements using a pendant bubble apparatus, γ_{eq}^{PB}, normalized by pendant drop measurements, γ_{eq}^{PD}, for the corresponding values of b/h_p calculated using the parameters for $C_{14}E_8$ [26]. The points in Figure A.5 were taken from Figure 3 of [8]. From Figure A.5, it is evident that the pendant drop experiments show a systematically larger surface tension than pendant bubble experiments, $\gamma_{eq}^{PB}/\gamma_{eq}^{PD} < 1$, regardless of C_i. Since all cases $b/h_p < 10$ for Figure A.5, it is no surprise that the equilibrium surface tension for pendant drop experiments is consistently higher than pendant bubble experiments. As the value of $b/h_p \to 10$ the ratio $\gamma_{eq}^{PB}/\gamma_{eq}^{PD} \to 1$, which is what is expected from the analysis above.

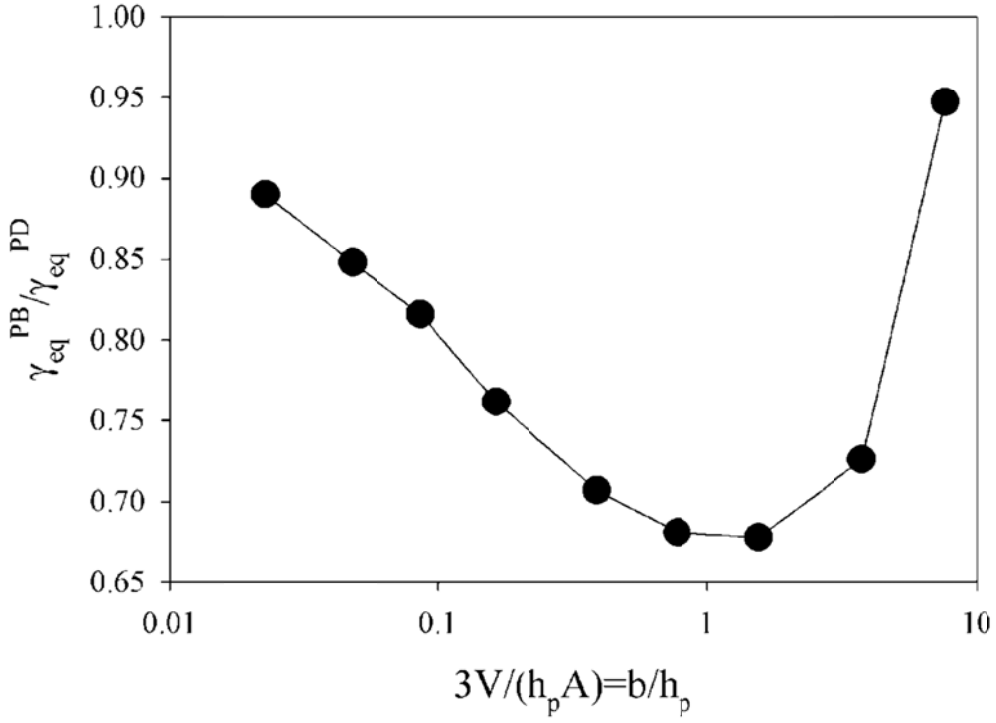

Figure A.5. Ratio of equilibrium surface tension measured from pendant drop experiments normalized by pendant bubble measurements as a function of b/h_p.

To test the theoretical criterion, $3V/(h_pA) >> 10$, further and more generally, experiments were conducted over a large range of $3V/(h_pA)$ values, specifically around the transition region. Since C_iE_j surfactants adsorb to silica, $\Gamma_\infty \approx 2\times10^{-6}$ mol/m^2 at $C_\infty \approx 100$ μM [28, 29], we measured interfacial tension of a sample that had time to allow depletion to occur by adsorption to the silica-fluid interface and the fluid-fluid interface and a sample that had little or no time to deplete. The depleted samples were prepared by leaving 10 mL $C_{14}E_8$ surfactant solutions of known concentrations in glass scintillation vials for 24 hours. The experiments were designed such that depletion effects were measured at constant

ratios of V/A at varying $C_{14}E_8$ concentrations, i.e. different values of h_p. The "non-depleted" samples were prepared immediately prior to measuring interfacial tension. The depleted samples were stored in cylindrical scintillation vials with an I.D. of 22.8 mm. The surface area of silica in contact with a 10 mL sample in the scintillation vial is 21.7 cm^2. The surface area of the air-water interface is 4.05 cm^2. Figure A**.6**a shows equilibrium surface tension for the two sample preparation methods as a function of bulk surfactant concentration. Note that there is a considerable difference in equilibrium surface tension measured by the two samples at low surfactant concentrations. At high concentrations, there is no difference in equilibrium surface tension.

As in the case of comparing measurements using the pendant drop and pendant bubble apparatus, it is insightful to plot the ratio of γ_{eq} as a function of $3V/(h_p A)$. The surface coverage of $C_{12}E_5$ and $C_{12}E_{10}$, surfactants similar to $C_{14}E_8$, on silica in the concentration range considered here is between $\Gamma_{eq} = 1\times10^{-9} - 2\times10^{-6}$ mol/m^2 over a concentration range C_∞ = 1-100 μM [28, 29, 35]. For these calculations, we assume that the isotherm governing adsorption to the silica-solution interface is approximated by the isotherm for the air-water interface, i.e. h_p for the solid-fluid interface is equal to h_p for the fluid-fluid interface. This assumption is supported by the similar maximum surface coverage values between the air-water and solid-liquid interface. Figure A.6b shows a ratio of equilibrium surface tension for the freshly made case to the 24 hour case as a function of $3V/(h_p A)$. At small values of $3V/(h_p A)$, the surface tension

measured after 24 hours is up to 8% higher than the freshly made case. At large values of $3V/(h_p A)$, the ratio of surface tensions is approximately unity, i.e. no depletion. From our theoretical analysis, the ratio of equilibrium surface tensions should approach unity for values $3V/(h_p A) >> 10$. From Figure A.6b it is evident that when the ratio of $3V/(h_p A) > 22$, the equilibrium surface tension for both sample preparation methods are indistinguishable. This suggests that a value of $3V/(h_p A) > 20$ is sufficient to avoid depletion effects and confirms our theoretical analysis above.

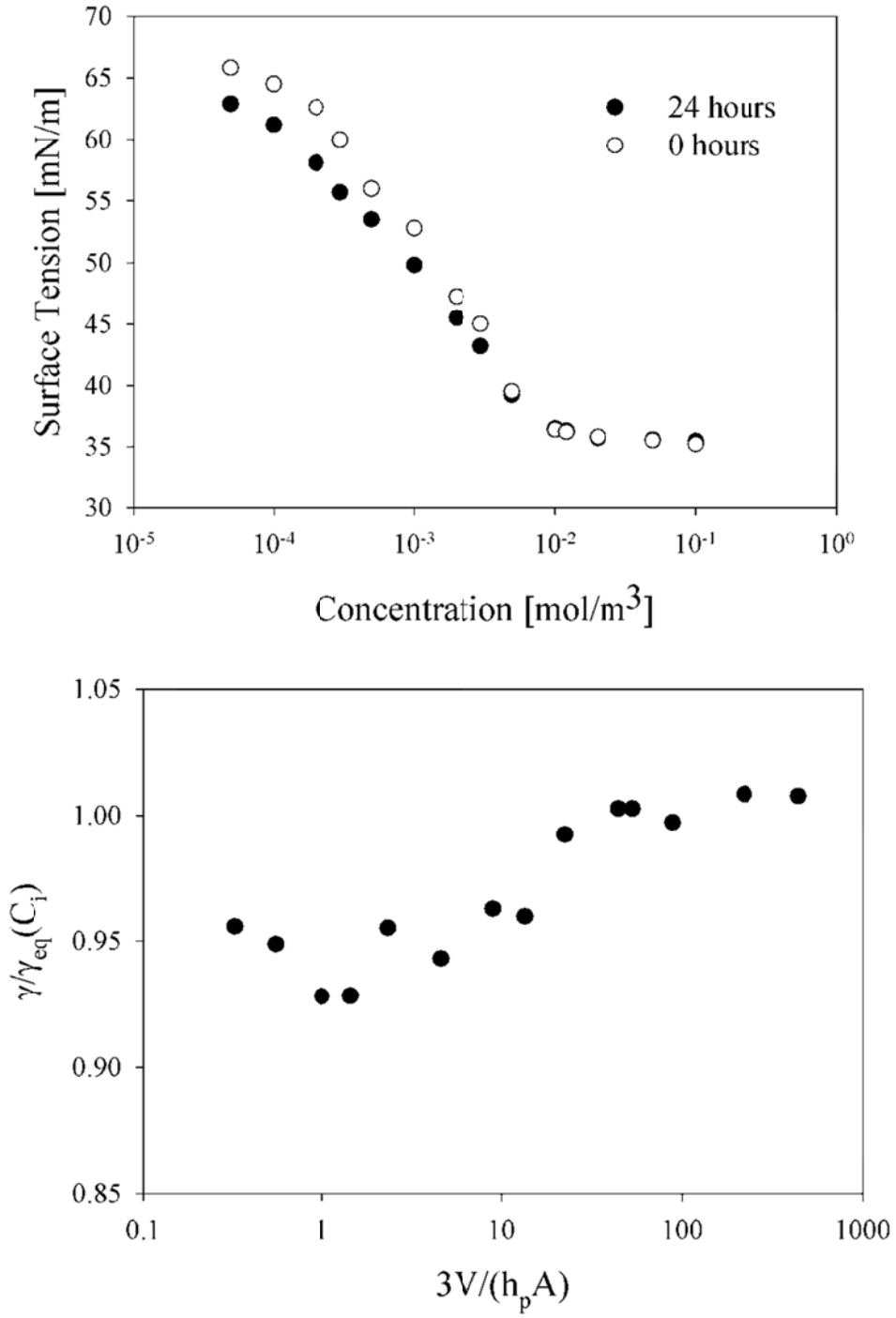

Figure A.6. a.) Equilibrium surface tension as a function of different concentrations of $C_{14}E_8$ solutions measured 24 and 0 hours after sample preparation, b.) Ratio of equilibrium surface tension 24 hours after sample preparation to surface tension measured 0 hours after sample preparation as a function of $3V/(h_pA)$ for $C_{14}E_8$.

The implications of these experimental results are three fold. Sample preparation is important when constructing surface tension isotherms. If samples containing amphiphilic species are to be prepared and stored for a long period of time, it should be stored such that $3V/(h_p A) > 22$. In light of these findings, we have re-examined previously published data [26]. The isotherm measured in ref. [26] for $C_{12}E_8$ was done so using previously prepared samples of different concentrations in 100 ml volumetric flasks. The majority of the low concentration experiments have values of $3V/(h_p A) < 20$. The difference in isotherm parameters between previously reported [36] and the ones fit in [26] are not due solely to a difference in temperature as postulated in [26], but also because of depletion effects. This means that some of the concentrations reported in the figures and the parameters in Table 1 of [26] are not correct since $C_{eff} \neq C_i$. Note that the conclusions drawn from the model predictions in [26] are not affected by the small change in parameters.

Pendant bubble experiments are almost always approximated as semi-infinite volume cases since the volume of surfactant solution is upwards of 15 ml. However, the value of $3V/(h_p A)$ for dilute surfactant concentrations, e.g. $C_i < 10$ μM in the case of $C_{14}E_8$, is far from 20. Much larger volumes of solution are required to ensure that depletion effects do not affect both dynamic and equilibrium surface tension measurements. For example, the dimensions of the square sample cuvette required to ensure that $3V/(h_p A) > 22$ for $C_{12}E_8$, another well studied surfactant [26] , at $C_i \sim 0.1\,\mu M$ ($h_p \sim 0.01$ m) must be greater than or

equal to $50\ \text{cm} \times 50\ \text{cm}$ ($3V/\left(h_p A\right) = 25$): a total solution volume of 125 L. This is obviously an experimentally impractical sample holder size. Instead this calculation implies that a sample cell with traditional dimensions, e.g. $2.5\ \text{cm} \times 4.0\ \text{cm}$, must be pretreated with either a higher surfactant concentration or multiple aliquots of the desired surfactant concentration. Each method has advantages and disadvantages. For example, titrating with a higher concentration could cause the concentration to go up due to desorption of surfactant from the cuvette surface. Treating with multiple aliquots could take a long period of time.

Regardless of which method, if we assume that the walls of the sample cell have been properly treated in some cases a sample cell of $2.5\ \text{cm} \times 4.0\ \text{cm}$ is inappropriate to measure dynamic or equilibrium surface tension for dilute surfactant concentrations using a pendant bubble if the top of the cuvette is left open. If a mass balance between the surface area of the bubble and free surface and the volume of solution in the cuvette is taken into account, then for a traditional pendant drop experiment, i.e. assuming a concentration of $C_{12}E_8$ surfactant $C_i \sim 0.1\,\mu\text{M}$ ($h_p \sim 0.01$ m) the value of $3V/\left(h_p A\right) = 0.7$, which fails to meet the criteria for which depletion does not occur. The only way to achieve dynamic and equilibrium surface tension independent of depletion effects is to properly equilibrate a $2.5\ \text{cm} \times 4.0\ \text{cm}$ with no more than 0.22 cm^2 (the surface area of a pendant bubble with $b = 1.2\,\text{mm}$ is $A = 0.18\,\text{cm}^2$), i.e. essentially a pre-equilibrated closed cell. This criteria is very useful in designing pendant bubble experiments to minimize depletion effects.

A.4.1.2. MULTIPLE DROPLETS

In many microfluidic experiments, there is no single bubble/drop interface but rather a large number of droplets/bubbles such as in emulsions and foams. This slightly changes the mass balance by introducing a new variable, N, which corresponds to the number of droplets/bubbles. Eqn (A.7) assuming $\Gamma_i = 0$ becomes

$$C_i V = C_{eff} V + N\Gamma_{eq} A. \tag{A.13}$$

This in turn changes equation (A.10) to

$$\frac{C_{eff}}{C_i} = \frac{\left(1 - \frac{Nh_p A}{V} - \left(\frac{Nh_p A}{V} + 1\right)\frac{a}{C_i}\right) - \sqrt{\left(1 - \frac{Nh_p A}{V} - \left(\frac{Nh_p A}{V} + 1\right)\frac{a}{C_i}\right)^2 + \frac{4a}{C_i}}}{2}. \tag{A.14}$$

The impact of this slight change is quite dramatic for large values of N even for systems with relatively large volumes of solution. The same critical point still holds from the previous section, i.e., $3V/\left(h_p A\right) >> 10$. However, neglecting depletion to the walls of the container, the critical limit for a solution containing N bubbles/droplets with surface area A_R is $3V/\left(h_p N A_R\right) >> 10$. This implies that for a large value of N extremely large volumes are required to minimize the effect of depletion, i.e. small volume fractions of the dispersed phase.

Recently it was reported that the isotherm for the well-studied surfactant sodium dodecylsulfate, SDS, is different for nanoscopic droplets than for a planar interface. Under the conditions studied, it is not possible to decouple changes in surface tension due to depletion with changes due to geometrical restrictions. For example, the experiments presented in [23] were conducted at 1% by volume with

83 nm emulsion droplets. If we neglect contributions of the sample cell wall and partitioning of surfactant into the oil phase, $3V/\left(h_p N A_R\right) \sim 2$ for a 1% by volume dispersion of 83 nm droplets at the highest concentration reported and $3V/\left(h_p N A_R\right) < 2$ for lower concentrations. Thus for all cases considered it cannot be assumed that $C_{eff} = C_i$, i.e. depletion effects are important, $C_{eff} \neq C_i$. In fact, the sample would have to be prepared at $\text{vol}\% < 0.1$ to ensure that depletion effects are minimized assuming that the walls of the sample chamber were properly equilibrated to the desired surfactant concentration. Therefore, the fact that the equilibrium surface tension is higher for experiments conducted at the oil droplet interface than at the planar interface supports that depletion effects are a factor and it is unlikely that the cause was due to the size of the emulsion droplets (the main conclusion of Ref. [23]).

A.4.2. EFFECT OF DEPLETION AND CURVATURE ON DYNAMIC SURFACE TENSION INSIDE/OUTSIDE A DROP/BUBBLE

In addition to equilibrium surface tension, Figure A**.3** also depicts the effect of depletion on dynamic surface tension. For example at very low values of b/h_p, the time to reach equilibrium is two orders of magnitude faster than the infinite volume case. This happens because the initial bulk concentration is much higher than the effective bulk concentration. Therefore at early times there is a large flux of molecules to the interface, such as in the infinite volume case. Note how all values of b/h_p have very similar early time dynamics. However, when b/h_p is small the bulk is quickly depleted of surfactant, the flux goes to zero and

the system reaches equilibrium. Therefore, the time required to reach the reduced equilibrium surface concentration is shortened because of the initially high bulk surfactant concentration. On the other hand at large values of b/h_p, e.g. $b/h_p \geq 100$, the dynamic surface tension curve is indistinguishable from the semi-infinite volume (planar) case, i.e. $b/h_p \to \infty$.

In a previous paper, we determined the dependence of the spherical diffusion-limited time scale for surfactant adsorbing/desorbing from outside a spherical interface from a semi-infinite volume. To see the dependence of the dynamic surface tension time scale on b/h_p for surfactant adsorbing/desorbing from inside a droplet, we perform a similar analysis as reported in the numerical procedure section and previously [25, 26]. Figure A.7 is a result of the time scale analysis and shows the theoretical diffusion-limited time scale for the semi-infinite planar and exterior spherical cases, and numerically calculated points for the finite interior spherical case normalized by the theoretical planar time scale and plotted versus b/h_p. It is obvious from Figure A.7 that for large values of b/h_p, $b/h_p > 10$, the time scale approaches the planar diffusion time scale, as described by Figure A.3. As the value of b/h_p decreases, it is evident that the time scale is orders of magnitude smaller than the planar case. In fact the time scale quickly approaches a functional form that is captured by $\tau_{Ds}^{I} = b^2/D$ or $\tau_{Ds}^{I}/\tau_{Dp} = \left(b/h_p\right)^2$, superscript *I* denotes the time scale for the inside diffusion case, whereby the characteristic length scale for diffusion is equivalent to the bubble radius, $l = b$. This is expected since the radius is the maximum length

scale over which diffusion can occur and since at small values of b/h_p depletion is important, the diffusion process happens over the entire radius.

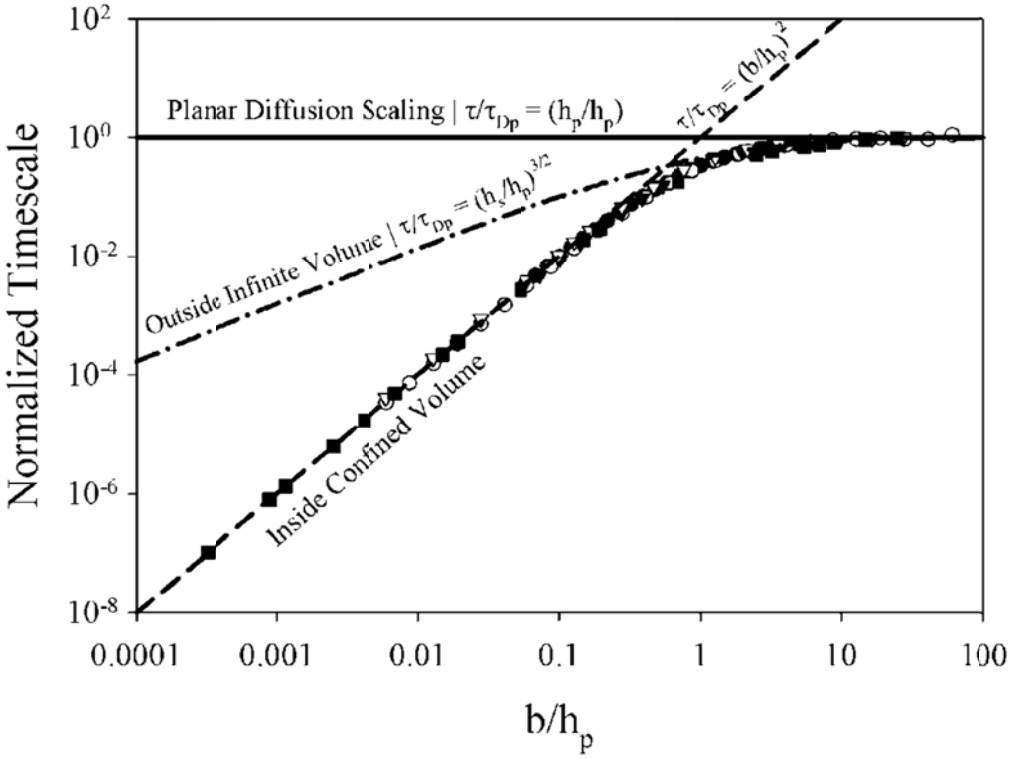

Figure A.7. A time scale analysis of theoretical diffusion-limited dynamics at different values of b/h_p for different geometrical considerations. The different symbols correspond to analysis at different fractional coverage (ϕ) for the interior confined volume case.

This argument is made clearer by examining the normalized depth of the concentration front during the dynamic process as a function of normalized time for a large and small value of b/h_p. The concentration front was defined to be the depth away from the interface that corresponds to $C(r,t) = 0.9 \cdot C\left(r = 0, t\right)$. Figure A.8 shows the position of the concentration front away from the interface normalized by the interface radius for two values of b/h_p. The curve

corresponding to $b/h_p \sim 0.1$ shows that the depletion depth reaches a critical depth and cannot penetrate further. The $b/h_p \sim 10$ case shows a maximum depth at a unique time. This demonstrates how the $b/h_p << 10$ case follows the scaling $\tau_{Ds}^{I} = b^2/D$.

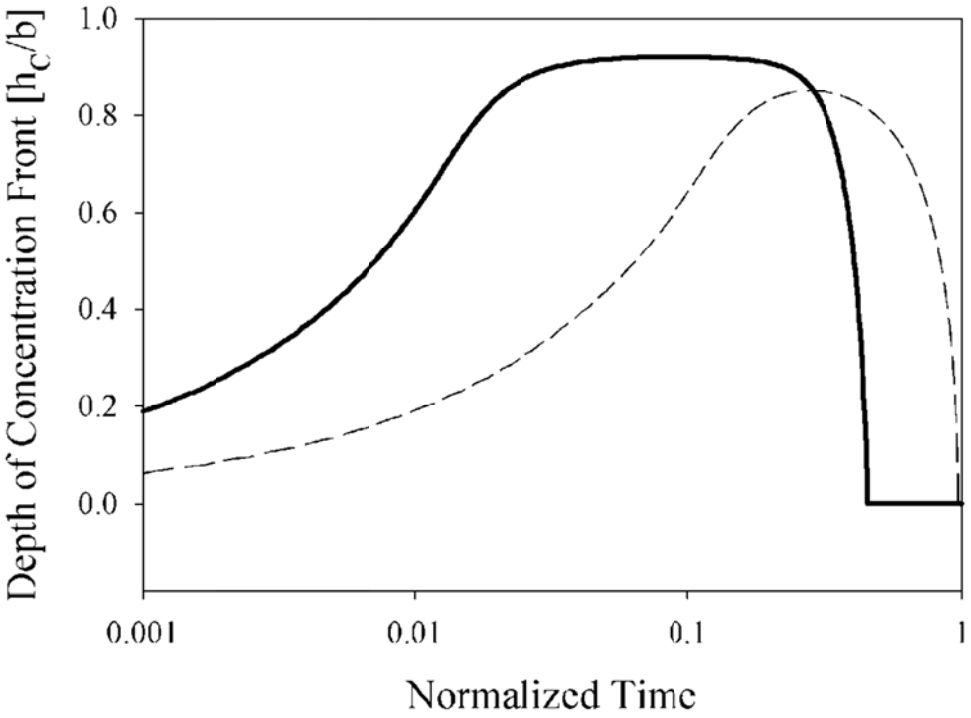

Figure A.8. Location of concentration front as a function of time for small [solid line] $b/h_p \sim 0.1$ and large [dashed line] $b/h_p \sim 10$.

These results have implications for the wide range of microfluidic experiments that consider emulsion studies where surfactant is solubilized in the droplet phase. If the value of b/h_p is very small then determining the time scale to reach equilibrium is easily calculated using $\tau_{Ds}^{I} = b^2/D$, which is considerably faster than previously thought. In addition to the faster time scale, the bulk surfactant concentration and the equilibrium surface concentration will be a

fraction of the initial quantities. To avoid having depletion confound mass transport, experiments should be conducted at $b/h_p >> 10$, whereby the planar diffusion time scale is the appropriate scaling.

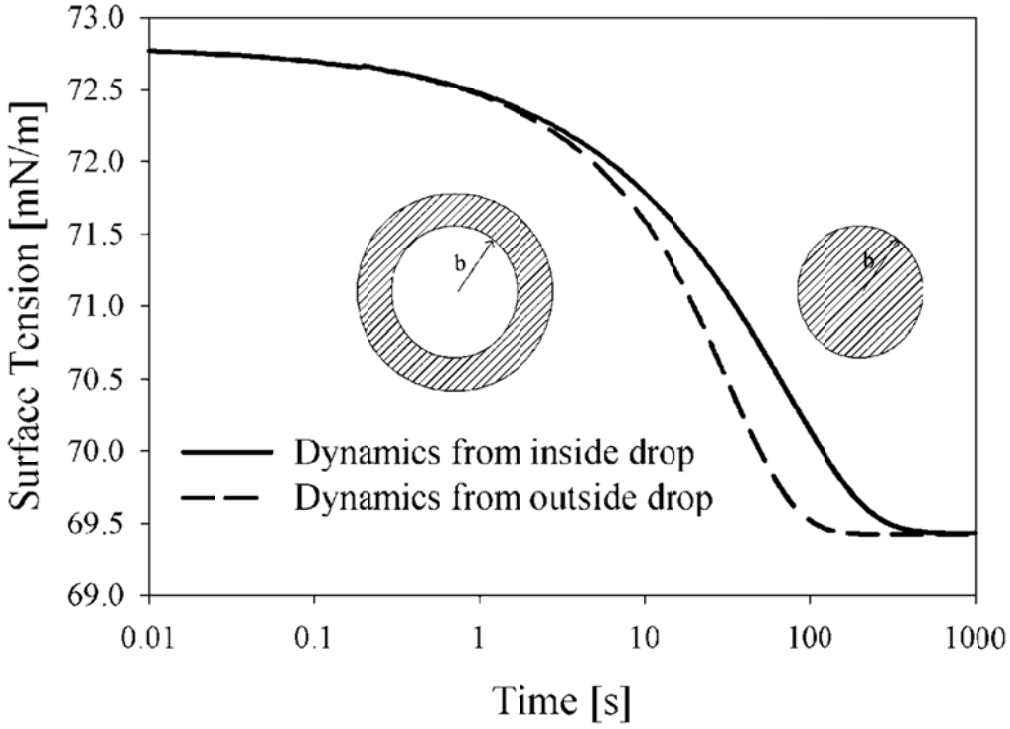

Figure A.9. Dynamic surface tension for the same surfactant inside and outside the drop for a fixed finite volume V=0.9 μL and b/h_p=1.4

We have only considered the effect of depletion on dynamic surface tension from inside the drop. We now examine the effect of curvature on the dynamic and equilibrium surface tension. In other words, how do dynamic time scales in the presence of depletion (fixed volume of surfactant solution) compare for inside and outside the drop. Dynamic surface tensions for the inside and outside drop cases are numerically calculated for constant surfactant concentration and radius, i.e. fixed $3V/(h_p A) = 1.4$, and volume of surfactant

solution. Figure A.9 shows the effect of curvature in the presence of depletion, i.e. $3V/(h_p A) < 10$. Since the volume of surfactant solution in both cases is equal, the effect of depletion is equal and both dynamic curves reach the same equilibrium surface tension, i.e. surface concentration and effective bulk concentration. However, the dynamic surface tension curve for the outside case is considerably faster to reach equilibrium than the inside case. This is directly related to the difference in curvature for the two systems. For the outside case, the volume to surface area ratio is much larger than for the inside case. At any given time, there is more surfactant surrounding the droplet to undergo adsorption than inside the droplet [25]. For large values of $3V/(h_p A) >> 10$, depletion is not important and both cases have the same time scale, which is equal to the planar time scale.

A.5 SUMMARY

The effect of depletion on equilibrium surface tension and dynamic surface tension depends on the value of $3V/(h_p A)$. For values of $3V/(h_p A) >> 10$, the equilibrium surface tension and dynamic surface tension are indistinguishable from the semi-infinite volume case. For values of $3V/(h_p A) < 10$, depletion has a considerable effect on both dynamic and equilibrium surface tension measurements. The equilibrium surface tension is always larger than the semi-infinite volume case and the dynamics are always faster. Depletion can be caused by adsorption to available free surface as well as solid surfaces in the system such as containers and sample cells.

In some cases the interface is not a sphere and/or multiple interfaces are present. In such cases, depletion is unimportant when $3V/\left(Nh_pA\right) >> 10$ and the system is approximated using a semi-infinite volume model. When $3V/\left(Nh_pA\right) < 10$ depletion effects are important and must be considered.

For a spherical droplet at very small values of b/h_p, i.e. $b/h_p << 10$, the dynamics for transport to the interface from inside the droplet follow the time scale given by $\tau_{Ds}^{I} = b^2/D$. Furthermore, the time scale to reach equilibrium is dependent on which side of the droplet interface the surfactant is adsorbing from. The time scale to reach equilibrium is smaller for the outside case then the inside case when depletion is important. This is due to higher availability of surfactant directly adjacent to the interface outside the droplet/bubble.

The results presented in this chapter allow one to quickly determine the importance of depletion from a simple calculation of $3V/\left(Nh_pA\right)$, where $h_p = \Gamma_{eq}/C_i$. If depletion cannot be avoided, then the results must be interpreted considering effects due to depletion.

[1] R. Aveyard, B.P. Binks, and J.H. Clint, "Emulsions stabilised solely by colloidal particles," Advances in Colloid and Interface Science, 100 (2003), 503-546.

[2] P. Sherman, *Emulsion science* (Academic Press, London, 1968).

[3] K. Malysa, R. Miller, and K. Lunkenheimer, "Relationship between Foam Stability and Surface Elasticity Forces - Fatty-Acid Solutions," Colloids and Surfaces, 53 (1991), 47-62.

[4] P.M. Reis, et al., "Influence of Surfactants on Lipase Fat Digestion in a Model Gastro-intestinal System," Food Biophysics, 3 (2008), 370-381.

[5] M.L. Pollard, et al., "Phase behavior of sparingly soluble polyethoxylate monolayers at the air-water surface and its effect on dynamic tension," Langmuir, 14 (1998), 7222-7234.

[6] C.Y. Chao, et al., "Drop-shape analysis of receptor-ligand binding at the oil/water interface," Langmuir, 24 (2008), 2472-2478.

[7] J.K. Ferri, et al., "Desorption kinetics of surfactants at fluid interfaces by novel coaxial capillary pendant drop experiments," Colloids and Surfaces A-Physicochemical and Engineering Aspects, 319 (2008), 13-20.

[8] V.B. Fainerman, et al., "C14EO8 adsorption characteristics studied by drop and bubble profile tensiometry," Colloids and Surfaces A-Physicochemical and Engineering Aspects, 323 (2008), 56-62.

[9] J.K. Ferri, C. Kotsmar, and R. Miller, "From surfactant adsorption kinetics to asymmetric nanomembrane mechanics: Pendant drop experiments with subphase exchange," Advances in Colloid and Interface Science, 161 (2010), 29-47.

[10] R.S. Hansen and J.A. Mann, "Propagation Characteristics of Capillary Ripples .I. Theory of Velocity Dispersion + Amplitude Attenuation of Plane Capillary Waves on Viscoelastic Films," Journal of Applied Physics, 35 (1964), 152.

[11] P.A. Harvey, et al., "Influence of sodium dodecyl sulphate and Dowfroth frothers on froth stability," Minerals Engineering, 18 (2005), 311-315.

[12] H. Luo, et al., "Interfacial tension of ethylene and aqueous solution of sodium dodecyl sulfate (SDS) in or near hydrate formation region," Journal of Colloid and Interface Science, 297 (2006), 266-270.

[13] G. Para, E. Jarek, and P. Warszynski, "The surface tension of aqueous solutions of cetyltrimethylammonium cationic surfactants in presence of bromide and chloride counterions," Colloids and Surfaces a-Physicochemical and Engineering Aspects, 261 (2005), 65-73.

[14] T. Smith, "Monolayers on Water .I. A Theoretical Equation for Liquid Expanded State," Journal of Colloid and Interface Science, 23 (1967), 27.

[15] S.L. Anna and H.C. Mayer, "Microscale tipstreaming in a microfluidic flow focusing device," Physics of Fluids, 18 (2006), 121512.

[16] J.P. Millette, et al., "An apparatus for the measurement of surface tensions at high pressures and temperatures," Canadian Journal of Chemical Engineering, 80 (2002), 126-134.

[17] C. Brumaru and M.L. Geng, "Interaction of Surfactants with Hydrophobic Surfaces in Nanopores," Langmuir, 26 (2010), 19091-19099.

[18] N.T. Nguyen, et al., "Thermally mediated droplet formation in microchannels," Applied Physics Letters, 91 (2007).

[19] K. Medrzycka, E. Hallmann, and S. Pastewski, "Evaluation of Surfactant and Biosurfactant Mixture Usefulness in Oil Removal from Soil, Based on Physicochemical Studies and Flushing Experiments," Environment Protection Engineering, 35 (2009), 191-205.

[20] P.G. Dommersnes, et al., "Marangoni transport in lipid nanotubes," Europhysics Letters, 70 (2005), 271-277.

[21] A.A. Darhuber and S.M. Troian, "Principles of microfluidic actuation by modulation of surface stresses," Annual Review of Fluid Mechanics, 37 (2005), 425-455.

[22] J.D. Martin and S.D. Hudson, "Mass transfer and interfacial properties in two-phase microchannel flows," New Journal of Physics, 11 (2009), 115005.

[23] H.B. de Aguiar, et al., "The Interfacial Tension of Nanoscopic Oil Droplets in Water Is Hardly Affected by SDS Surfactant," Journal of the American Chemical Society, 132 (2010), 2122.

[24] N.J. Alvarez, L.M. Walker, and S.L. Anna, "A non-gradient based algorithm for the determination of surface tension from a pendant drop: Application to low Bond number drop shapes," Journal of Colloid and Interface Science, 333 (2009), 557-562.

[25] N.J. Alvarez, L.M. Walker, and S.L. Anna, "Diffusion-limited adsorption to a spherical geometry: The impact of curvature and competitive time scales," Physical Review E, 82 (2010).

[26] N.J. Alvarez, L.M. Walker, and S.L. Anna, "A Microtensiometer To Probe the Effect of Radius of Curvature on Surfactant Transport to a Spherical Interface," Langmuir, 26 (2010), 13310-13319.

[27] M.J. Rosen, "Relationship of Structure to Properties in Surfactants .3. Adsorption at Solid-Liquid Interface from Aqueous-Solution," Journal of the American Oil Chemists Society, 52 (1975), 431-435.

[28] P. Somasundaran, et al., "Effect of Adsorption of Nonionic Surfactant and Nonionic Anionic Surfactant Mixtures on Silica Liquid Interfacial Properties," Colloids and Surfaces, 63 (1992), 49-54.

[29] P. Somasundaran and S. Krishnakumar, "Adsorption of surfactants and polymers at the solid-liquid interface," Colloids and Surfaces a-Physicochemical and Engineering Aspects, 123 (1997), 491-513.

[30] C.H. Suelter and M. Deluca, "How to Prevent Losses of Protein by Adsorption to Glass and Plastic," Analytical Biochemistry, 135 (1983), 112-119.

[31] E. Rubin and C.J. Radke, "Dynamic Interfacial-Tension Minima in Finite Systems," Chemical Engineering Science, 35 (1980), 1129-1138.

[32] L.K. Filippov and N.L. Filippova, "Dynamic surface tension and adsorption kinetics in finite systems," Journal of Colloid and Interface Science, 187 (1997), 352-362.

[33] C.D. Yang and Y.G. Gu, "Modeling of the adsorption kinetics of surfactants at the liquid-fluid interface of a pendant drop," Langmuir, 20 (2004), 2503-2511.

[34] M. Reichert, et al.,*Unpublished Results* (2011).

[35] A. Thibaut, et al., "Adsorption of an aqueous mixture of surfactants on silica," Langmuir, 16 (2000), 9192-9198.

[36] S.Y. Lin, et al., "Adsorption kinetics of C12E8 at the air-water interface: Adsorption onto a clean interface," Langmuir, 12 (1996), 6530-6536.